

ANNUAL REPORT

2005

and list of publications



Bayerisches Forschungsinstitut
für Experimentelle Geochemie und Geophysik
Universität Bayreuth

Bayerisches Geoinstitut
Universität Bayreuth
D-95440 Bayreuth
Germany

Telephone: +49-(0)921-55-3700
Telefax: +49-(0)921-55-3769
e-mail: bayerisches.geoinstitut@uni-bayreuth.de
www: <http://www.bgi.uni-bayreuth.de>

Editorial compilation by: Stefan Keyssner and Petra Buchert
Section editors: Andreas Audétat, Tiziana Boffa Ballaran, Leonid Dubrovinsky,
Dan Frost, Florian Heidelbach, Hans Keppler, Catherine McCammon,
Dave Rubie, Friedrich Seifert, Gerd Steinle-Neumann, Michael Terry



Staff and guests of the Bayerisches Geoinstitut in **July 2005**:

Die Mitarbeiter und Gäste des Bayerischen Geoinstituts im **Juli 2005**:

First row, from left (1. Reihe, v. links) Yuki Asahara, Jun Liu, Ashima Saikia, Kanani Lee, Ute Mann, Claudia Romano, Gerti Gollner, Micaela Longo, Deborah Schmauß-Schreiner, Anastasia Kantor

Second row, from left (2. Reihe, v. links) Hubert Schulze, Jérôme Rouquette, Catherine McCammon, Natalia Dubrovinskaia, Eva Holbig, Fabrizio Nestola, Craig Tennant, Polina Gavrilenko, Kiyoshi Fujino

Third/fourth row, from left (3./4. Reihe v. links) Alexander Kurnosov, Brent Poe, Dave Rubie, Dan Frost, Nico Walte, Florian Heidelberg, Mike Terry, Sven Linhardt, Alexander Kanschak, Alexei Kuznetsov, Andreas Audétat, Gerd Ramming, Emil Stoyanov, Stefan Keyssner, Lydia Kison-Herzing

Background, from left (Hintergrund v. links) David Dolejš, Vladimir Solozhenko, Hans Keppler, Friedrich Seifert, Oleksandr Kurakevych, Gerd Steinle-Neumann, Detlef Krauß, Heinz Fischer, Kurt Klasinski, Innokenty Kantor, Stefan Übelhack

Absent (Es fehlten) Ulrich Böhm, Tiziana Boffa Ballaran, Petra Buchert, Leonid Dubrovinsky, Ahmed El Goresy, Holger Kriegel, Oskar Leitner, Anke Potzel, Oliver Rausch

Contents

Foreword/Vorwort	9/I
1. Advisory Board and Directorship	11
1.1 Advisory Board	11
1.2 Leadership	11
2. Staff, Funding and Facilities	13
2.1 Staff	13
2.2 Funding	13
2.3 Laboratory and office facilities	16
2.4 Experimental equipment	16
3. Forschungsprojekte - Zusammenfassung in deutscher Sprache.....	III
3. Research Projects	19
3.1 <i>Earth's Structure and Geodynamics</i>	19
a. The effect of water on the olivine to wadsleyite transformation (D.J. Frost) ..	20
b. The effect of ferric iron on the olivine to wadsleyite transformation (D.J. Frost and C.A. McCammon)	22
c. The formation of calcium perovskite from majorite garnet: Implications for splitting of the 520 km seismic discontinuity (A. Saikia, D.J. Frost and D.C. Rubie).....	23
d. The origin of the Earth's asthenosphere (K. Mierdel/Tübingen, in collaboration with H. Keppler, J.R. Smyth/Boulder and F. Langenhorst/Jena)	25
e. Effect of Al on the sharpness of the MgSiO ₃ perovskite to post-perovskite transition (S. Akber-Knutson/San Diego, G. Steinle-Neumann and P.D. Asimow/Pasadena)	28
f. Mantle mineral model for geodynamics simulations (A.S. Piazzoni/München, G. Steinle-Neumann and D. Dolejš)	30
3.2 <i>Geochemistry</i>	32
a. Early evolution of oxygen isotopes in the protosolar nebula (J. Aléon/Vandoeuvre-les-Nancy, in collaboration with A. El Goresy and E. Zinner/St. Louis)	33
b. Oxygen partitioning between magnesiowüstite and liquid Fe-rich metal at high pressure and high temperature (Y. Asahara, D.J. Frost, D.C. Rubie and F. Langenhorst/Jena)	35
c. Beating the miscibility barrier between iron group elements and magnesium by high-pressure alloying (L.S. Dubrovinsky, N.A. Dubrovinskaia and I.Yu. Kantor, in collaboration with W.A. Crichton/Grenoble, L. Vitos and R. Ahuja/Uppsala, and I.A. Abrikosov/Linköping)	37

d.	High-pressure alloying of iron and xenon: ‘Missing’ Xe in the Earth’s core? (K.K.M. Lee/Pasadena, in collaboration with G. Steinle-Neumann)	39
e.	Partitioning of trace elements among silicate, sulfide and metal under high pressure and high temperature (V. Malavergne, S. Berthet and R. Combes/ Marne-La-Vallée, D.J. Frost)	42
f.	Metal-silicate partitioning of nominally lithophile elements (Ta, Ga, In, Zn) – new constraints on existing core formation models (U. Mann, D.J. Frost and D.C. Rubie)	44
g.	Accretion and core formation of terrestrial planets: Insights from experimentally determined solubility behaviour of siderophile elements in silicate liquids (P. Kegler and H. Palme/Köln, A. Holzheid/Münster, D.C. Rubie and D.J. Frost)	46
h.	Partitioning and valence state of titanium in oxide-metal assemblages at upper mantle conditions (E. Stoyanov, F. Langenhorst/Jena and D.J. Frost) ..	48
i.	Origin of the negative niobium tantalum anomaly in subduction zone magmas (J. Baier/Tübingen, A. Audétat and H. Keppler)	50
3.3	<i>Mineralogy, Crystal Chemistry and Phase Transformations</i>	52
a.	Crystal-structure refinement of high-pressure and high-temperature natural Na-bearing clinopyroxenes (F. Nestola, M. Longo, C.A. McCammon and T. Boffa Ballaran)	52
b.	Equation of state of the jadeite (NaAlSi ₂ O ₆) – aegirine (NaFe ³⁺ Si ₂ O ₆) and the jadeite – hedenbergite (CaFe ²⁺ Si ₂ O ₆) solid solutions (F. Nestola and T. Boffa Ballaran, in collaboration with C. Liebske/Zurich)	54
c.	High-temperature behaviour of clinopyroxenes along the joins jadeite-aegirine and jadeite-hedenbergite (F. Nestola, M. Tribaudino/Parma, M. Bruno/Torino and T. Boffa Ballaran).....	55
d.	Iron site partitioning in clinopyroxene determined using Mössbauer spectroscopy: A new approach (C.A. McCammon, M. Longo and F. Nestola)	56
e.	High-pressure behaviour of analcime (G.D. Gatta, F. Nestola and T. Boffa Ballaran)	57
f.	High-pressure behaviour of 10 Å phase: An <i>in situ</i> Raman and X-ray powder diffraction study (P. Comodi/Perugia, F. Cera/Perugia and L.S. Dubrovinsky)	59
g.	Fe solubility and symmetry reduction in CaSiO ₃ perovskite at lower mantle conditions (K. Fujino, F. Langenhorst/Jena, D.C. Rubie and H. Izumi/Sapporo)	60
h.	High-pressure study of K-Na hollandite solid solution (J. Liu, T. Boffa Ballaran, L.S. Dubrovinsky and D.J. Frost).....	62
i.	Electronic configuration of iron in cold compressed olivine Mg _{1.8} Fe _{0.2} SiO ₄ (J. Rouquette, I. Yu. Kantor, C.A. McCammon and L.S. Dubrovinsky)	63

j.	Mössbauer study of a spin crossover in ferropericlaase: Compositional, pressure and temperature dependence (I.Yu. Kantor, L.S. Dubrovinsky and C.A. McCammon)	65
k.	Phase transitions in MnO and FeO at low temperatures: A neutron powder diffraction study (A.P. Kantor, L.S. Dubrovinsky, N.A. Dubrovinskaia and I.Yu. Kantor, in collaboration with I.N. Goncharenko/Gif-sur-Yvette)	67
3.4	<i>Physical Properties of Minerals</i>	70
a.	Crystal structure and compression of an iron-bearing Phase A to 33 GPa (C.M. Holl and J.R. Smyth/Boulder; D.J. Frost, in collaboration with M.H. Manghnani, G.M. Amulele and M. Sekar/Honolulu; V.B. Prakapenka and G. Shen/Chicago)	70
b.	Compressional behaviour and P-induced structural evolution of topaz, Al ₂ SiO ₄ (F,OH) ₂ (G.D. Gatta, F. Nestola and T. Boffa Ballaran).....	71
c.	Microstructural control of Fe-Mg interdiffusion in magnesiowüstite (F. Heidelbach, M.P. Terry, C.A. McCammon, in collaboration with M. Bystricky/Toulouse and C. Holzapfel/Saarbrücken)	73
d.	Lamellar magnetism in titanohaematite: A Mössbauer study (C.A. McCammon, in collaboration with S.A. McEnroe and P. Robinson/Trondheim)	75
e.	<i>In situ</i> combined X-ray diffraction and conductivity measurements of Fe-Ni alloy (20 wt.% Ni) (A.Yu. Kuznetsov, Y. Volkova/Yekaterinburg, A.V. Kurnosov, I.Yu. Kantor, N.A. Dubrovinskaia and L.S. Dubrovinsky, in collaboration with V.P. Dmitriev/Grenoble)	77
f.	Absence of charge ordering in Fe ₃ O ₄ magnetite under pressure (M.J. Wenzel/Berkeley and G. Steinle-Neumann)	79
g.	MnO high-pressure phase diagram: Magnetic ordering and lattice distortion (I.Yu. Kantor and L.S. Dubrovinsky, in collaboration with I.N. Goncharenko/Saclay)	80
h.	Preliminary study of iron behaviour during the breakdown reaction of (Mg,Fe) ₂ SiO ₄ to (Mg,Fe)SiO ₃ perovskite + (Mg,Fe)O (J. Rouquette, D.J. Frost, C.A. McCammon, I.Yu. Kantor and L.S. Dubrovinsky)	82
3.5	<i>Fluids and their Interaction with Melts and Minerals</i>	84
a.	Quartz solubility in fluorine-bearing aqueous fluids (D. Dolejš)	84
b.	Solubility of tin in magmatic-hydrothermal fluids (Q. Duc-Tin/Tübingen, A. Audétat and H. Keppler)	86
c.	Thermodynamic modeling of granite-fluid interaction: Gibbs free energy minimization by convex programming (D. Dolejš and T. Wagner/Tübingen)	89
d.	Carbon solubility and speciation in mantle minerals (S.S. Shcheka, H. Keppler, M. Wiedenbeck/Potsdam and D.J. Frost).....	91

e.	The hydration of olivine at 12 GPa (J.R. Smyth/Boulder, D.J. Frost, F. Nestola, C.M. Holl/Boulder and G.D. Bromiley/Cambridge)	93
f.	Hydration of stishovite and the fate of subducting slabs (G.D. Bromiley and F.A. Bromiley/Cambridge, D.W. Bromiley/Bristol)	95
3.6	<i>Physics and Chemistry of Melts and Magmas</i>	98
a.	Viscosity of peridotite liquid up to 24 GPa predicted from self-diffusion coefficients (B. Schmickler and D.C. Rubie, in collaboration with C. Liebske/Zurich, C. Holzappel/Saarbrücken and B.T. Poe/Rome)	98
b.	Aluminium coordination and density of 4 and 5 component high-pressure aluminosilicate glasses (J.R. Allwardt, J.F. Stebbins and L.-S. Du/Stanford, D.J. Frost, in collaboration with M.M. Hirschmann and A.C. Withers/Minnesota)	100
c.	CO ₂ speciation in silicate melts (A. Korschak and H. Keppler)	102
d.	Adsorption of SO ₂ onto volcanic ashes (D. Schmauß-Schreiner and H. Keppler)	103
e.	High-pressure melting curve of methane hydrates: Implications for Titan's interior (A.V. Kurnosov and L.S. Dubrovinsky)	104
3.7	<i>Rheology</i>	107
a.	Remobilisation of old faults by transformation from olivine to wadsleyite (D.P. Dobson, A. DeRonde and P. Meredith/London, F. Heidelbach)	108
b.	Lattice preferred orientation of olivine in the presence of metallic melt (J. Hustoft and D. Kohlstedt/Minneapolis, F. Heidelbach)	110
c.	Olivine-FeS melt deformation experiments with the D-DIA (N.P. Walte, D.J. Frost and D.C. Rubie)	113
d.	<i>In situ</i> observation of high-temperature textural processes with the Moissanite cell (N.P. Walte and H. Keppler)	115
e.	Stress induced changes in slip systems in natural olivine from the Kvalvika peridotite lens, Western Norway (M.P. Terry and F. Heidelbach)	117
f.	Inherited fabric in a symplectite: A key to deformation history (F. Heidelbach and M.P. Terry)	118
g.	Intra- and intergranular dynamic recrystallisation and accompanied geochemical diffusion processes in deformed garnets (M. Bestmann, G. Habler and M. Thoeni/Vienna, F. Heidelbach)	120
h.	New constraints on the evolution of the Bayerischer Pfahl shear zone (E. Galadi-Enriquez and G. Zulauf/Frankfurt, F. Heidelbach)	121
3.8	<i>Metamorphism</i>	124
a.	Coarse-grained graphite calc-silicate rock enclosed in microdiamond-bearing garnet gneiss, Fjærtøft, Norway (P. Robinson and M.P. Terry)	124

b.	Metamorphic conditions of olivine c-slip in the Kvalvika peridotite, Norway (M.P. Terry, F. Heidelbach, H. Couvy/Stony Brook, G.D. Bromiley/Cambridge, T. Krogh/Toronto)	126
c.	Omphacite textures in eclogites of the Tauern Window: Implications for the exhumation of the Eclogite Zone (Austrian Alps) (K. Neufeld and A. Kühn/Mainz, U. Ring/Christchurch, F. Heidelbach)	128
d.	Assessing the tectonothermal evolution of a large-scale shear zone in the western Pan-African belt of central Africa (G. Njiekak and G. Zulauf/Frankfurt, F. Heidelbach)	130
3.9	<i>Materials Science</i>	133
a.	Aggregated diamond nanorods, the densest and least compressible form of carbon (N.A. Dubrovinskaia, L.S. Dubrovinsky, W.A. Crichton/Grenoble, F. Langenhorst/Jena and A. Richter/Wildau).....	134
b.	Processing and characterization of heat resistant polycrystalline diamond with calcium carbonate as sintering aid (J.E. Westraadt, J.H. Neethling/Port Elizabeth, N.A. Dubrovinskaia and I. Sigalas/Johannesburg)	136
c.	Synthesis of new fullerene materials by extreme hydrogenation at high-pressure/high-temperature conditions and their characterization (A.V. Talyzin, A. Dzwilewski and B. Sundqvist/Umeå; Y.O. Tsybin, J.M. Purcell and A.G. Marshall/Tallahassee; Y. Shulga/Chernogolovka, C.A. McCammon and L.S. Dubrovinsky)	138
d.	Reaction of metallic iron with C ₆₀ : Possible implications for “magnetic carbon” (A. Talyzin and A. Dzwilewski/Umeå; L.S. Dubrovinsky; A. Setzer and P. Esquinazi/Leipzig)	139
e.	High-pressure/high-temperature behaviour of graphite-like B–C phases (V.L. Solozhenko and O.O. Kurakevych/Villetaneuse, N.A. Dubrovinskaia and L.S. Dubrovinsky)	140
f.	Turbostratic graphite-like BC ₄ under pressure: Raman scattering (V.L. Solozhenko and O.O. Kurakevych/Villetaneuse, A.Yu. Kuznetsov)	140
g.	Synthesis and properties of new materials in the B–C system (N.A. Dubrovinskaia and L.S. Dubrovinsky; G. Eska and H. Braun/Bayreuth; G.A. Sheshin/Kharkov)	142
h.	Stacking faults and internal strains in DHCP phase of La (A.Yu. Kuznetsov, F. Langenhorst/Jena and L.S. Dubrovinsky, in collaboration with E. Estevez-Rams/Habana, V.P. Dmitriev/Grenoble and H.-P. Weber/Lausanne)	144
i.	Finite-size and pressure effects on the Raman spectrum of nanocrystalline anatase TiO ₂ (V. Swamy and B.C. Muddle/Clayton, A.Yu. Kuznetsov, L.S. Dubrovinsky, R.A. Caruso/Melbourne and D.G. Shchukin/Potsdam)	147
j.	Size effects on the structure and phase transition behaviour of baddeleyite TiO ₂ (V. Swamy/Clayton, L.S. Dubrovinsky, N.A. Dubrovinskaia and F. Langenhorst/Jena)	149

k.	Size-dependence of pressure-induced amorphization in nanoscale TiO ₂ (V. Swamy and B.C. Muddle/Clayton, A.Yu. Kuznetsov and L.S. Dubrovinsky, P.F. McMillan/London)	151
l.	Sol-gel synthesis of amorphous and nanocrystalline ZrO ₂ -TiO ₂ (E. Holbig, L.S. Dubrovinsky, T. Boffa Bollaran and N. Miyajima, in collaboration with P. Löbmann and M. Bockmeyer/Würzburg)	153
m.	ZrO ₂ -TiO ₂ phase equilibria at high pressures and temperatures (E. Holbig, L.S. Dubrovinsky, C.A. McCammon and D.J. Frost)	154
n.	Semiconductor-metal transition and crystal structure of LaCoO ₃ at high pressure probed by Raman spectroscopy and X-ray diffraction (D.P. Kozlenko/Dubna, L.S. Dubrovinsky, Z. Jiráček and B.N. Savenko/Prague)	156
o.	Structural changes and pressure-induced chemical decomposition of boric acid (A.Yu. Kuznetsov, L.S. Dubrovinsky and A. Shiryayev)	157
p.	Synthesis of hexagonal nickel nitride using high pressures and temperatures (C. Guillaume, G. Serghiou and J.P. Morniroli/Edinburgh; D.J. Frost)	160
q.	Synthesis and properties of new (oxide)-nitride-ceramics: spinel-nitrides and -sialons (T. Gross, T. Locherer, R. Riedel and H. Fuess/Darmstadt; E. Kroke and M. Schwarz/Freiberg, in collaboration with D.J. Frost)	162
r.	Mixing and reactivity across the semiconducting to metal transition in group IV alloys (C. Guillaume, G. Serghiou, J.P. Morniroli and A. Thomson/Edinburgh; D.J. Frost)	163
3.10	<i>Methodological Developments</i>	165
a.	Ferric iron determination at high pressures using micro-XANES analysis (I.Yu. Kantor, L.S. Dubrovinsky and C.A. McCammon)	165
b.	New experimental setup for high-pressure/high-temperature gigahertz ultrasonic interferometry (A.P. Kantor, I.Yu. Kantor and L.S. Dubrovinsky, in collaboration with S.D. Jacobsen/Washington DC and H.-J. Reichmann/Potsdam)	168
c.	High-brilliance X-ray system for <i>in situ</i> high-pressure studies: New developments (A.Yu. Kuznetsov, A.V. Kurnosov and L.S. Dubrovinsky)	169
d.	Raman spectroscopy in laser-heated diamond anvil cells (L.S. Dubrovinsky, A.V. Kurnosov, I.Yu. Kantor and A.Yu. Kuznetsov)	171
e.	Synthesis of large MgSiO ₃ perovskite samples for use in shock-wave equation-of-state measurements (J. Mosenfelder/Pasadena, D.J. Frost, D.C. Rubie, P. Asimow/Pasadena and T. Ahrens/Pasadena)	173
f.	Development of a goniometer stage for single crystal Mössbauer measurements (C. Tennant, C.A. McCammon and F. Nestola, in collaboration with H. Spiering/Mainz)	174
g.	A preparation method for TEM specimens using combined techniques of Focused Ion Beam milling and conventional Ar-milling (N. Miyajima, Y. Asahara, L.S. Dubrovinsky, D.J. Frost and D.C. Rubie, in collaboration with C. Holzapfel/Saarbrücken)	175

h.	Preparation of a natural hemo-ilmenite sample for magnetic experiments using a combination of crystallographic, magnetic and polishing techniques (S.A. McEnroe and P. Robinson/Trondheim, A. Hirt/Zurich and F. Heidelbach)	177
4.	International Graduate School "Structure, Reactivity and Properties of Oxide Materials"	181
5.	Publications, Conference Presentations, Seminars	185
5.1	Publications (published)	185
a.	Refereed international journals	185
b.	Monographs	190
5.2	Publications (submitted, in press)	190
5.3	Presentations at scientific institutions and at congresses	193
5.4	Lectures and seminars at Bayerisches Geoinstitut	202
5.5	Conference organization	204
6.	Visiting scientists	205
6.1	Visiting scientists funded by the Bayerisches Geoinstitut	205
6.2	Visiting scientists supported by other externally funded BGI projects	206
6.3	Visitors (externally funded)	211
7.	Additional scientific activities	213
7.1	Patents	213
7.2	Ph.D. theses	213
7.3	Honours and awards	213
7.4	Editorship of scientific journals	213
7.5	Membership of scientific advisory bodies	213
8.	Scientific and Technical Personnel	215
	Index	218

Foreword

The main research aims of the Bayerisches Geoinstitut are to understand the structure, composition, evolution and dynamics of the Earth's interior. Such aims are achieved by studying the chemical and physical properties of Earth materials experimentally at high pressures and temperatures. In addition, first-principles computational approaches are used to understand material properties at extreme conditions that cannot be achieved experimentally. A sound knowledge of material properties at high pressures and temperatures is crucial for other key areas of the Earth sciences, including geodynamical modelling, cosmochemistry and seismology. Some of the research areas and the approaches used overlap strongly with the fields of solid-state physics and chemistry and materials science and scientists from these disciplines are also represented strongly at the Bayerisches Geoinstitut.

The contributions contained in this Annual Report describe the results of experimental and computational studies as applied to a wide range of problems in the Earth Sciences. The research reports cover a broad spectrum of topics such as the early differentiation of the Earth, the present structure of the silicate mantle, the incorporation and transport of water in the Earth's mantle, the composition of the Earth's core and chemical interactions at the core-mantle boundary. Of relevance to shallower parts of the Earth, there are also contributions on topics such as volcanism and its influence on the Earth's atmosphere, the origin of ore deposits and crustal metamorphism.

Many contributions shed light on large-scale aspects of the Earth's structure. For example, a new model for the lithosphere and asthenosphere is presented, based on water solubilities in mantle minerals measured experimentally at high pressures and temperatures. A minimum in bulk water solubility occurs over the depth range of the asthenosphere and is the likely cause of the partial melt that is considered to make this layer relatively weak and ductile. Other contributions are concerned with details of major seismic discontinuities, such as those that are present at depths of 410 km, 520 km and 2900 km (the core-mantle boundary). For example, a perplexing observation from seismology is the *occasional* presence of a double discontinuity at a depth of around 520 km. New experimental results now suggest that the presence or absence of this double discontinuity could depend on whether or not the mantle has been chemically depleted by partial melting. This result leads to the possibility of being able to map out depleted regions of the mantle using seismological observations.

The decision was made in 2005 to extend the research activities at Bayerisches Geoinstitut into the field of geodynamical modelling. This development will lead to exciting possibilities for collaboration between scientists in the fields of experimental geosciences and geodynamics, with major synergistic effects. A proposal to create a Tenure-Track Junior Professorship in Geodynamical Modelling, with funding from the *Stifterverband für die Deutsche Wissenschaft*, was submitted in 2005; we have recently heard (early 2006) that the proposal has been successful. Through the efforts of Catherine McCammon as a coordinator,

a new *EU Marie Curie Training Site* proposal under the title “Atomic to Global” has been granted. On the instrumentation side it can be reported that a proposal for a laser-ablation ICP-MS has been approved, and that the TEM laboratory is again fully operational through the hiring of Nobuyoshi Miyajima as a successor to Falko Langenhorst.

As in previous years, external funding from various research programmes has made a major contribution to our research activities. An International Graduate School under the Elitenetzwerk Bayern programme on the theme “Structure, Reactivity and Properties of Oxide Materials” commenced in January 2005 and is funded initially for four years. The partners involved in this interdisciplinary Graduate School are the Bayerisches Geoinstitut, the Institute for Inorganic Chemistry (University of Bayreuth) and the Fraunhofer-Institut für Silicatforschung (ISC) in Würzburg. The first year of the Graduate School has been very successful, as reported below in Section 4. The EU Marie Curie Training Site and Research Infrastructure (Transnational Access) programmes have also been very successful and have enabled a large number of both junior and senior scientists from other European States to work at the Bayerisches Geoinstitut and take advantage of our laboratory and computational facilities.

As in previous years, and also on behalf of my colleagues, I would like to thank the *Free State of Bavaria* as represented by the *Bayerisches Staatsministerium für Wissenschaft, Forschung und Kunst* as well as the *Kommission für Geowissenschaftliche Hochdruckforschung* of the *Bavarian Academy of Sciences* for their continuing support and strong commitment to the Bayerisches Geoinstitut. We also gratefully acknowledge generous support from external funding agencies, in particular the *Alexander von Humboldt Foundation*, the *European Union*, the *German Science Foundation*, and the *European Science Foundation* which have also contributed greatly to the development and success of the Institute.

Bayreuth, March 2006

David C. Rubie

Vorwort

Die Forschungsarbeiten des Bayerischen Geoinstituts dienen dem Verständnis von Struktur, Zusammensetzung, Entwicklung und Dynamik des Erdinneren. Hierzu werden die Eigenschaften von geologisch relevanten Materialien unter hohem Druck und hoher Temperatur im Labor experimentell untersucht. Zusätzlich werden zunehmend quantenmechanische Berechnungen verwendet, um Materialeigenschaften unter extremen Bedingungen zu bestimmen, die im Labor nicht leicht zugänglich sind. Solide Kenntnisse über Materialeigenschaften bei hohen Drücken und Temperaturen sind für viele Kernbereiche der Geowissenschaften wie die geodynamische Modellierung, die Kosmochemie und die Seismologie essenziell. Einige Forschungsfelder und wissenschaftliche Ansätze überschneiden sich mit der Festkörper-Physik, der Chemie und den Materialwissenschaften. Wissenschaftler dieser Disziplinen sind daher am Bayerischen Geoinstitut zahlreich vertreten.

Der vorliegende Bericht enthält neue Ergebnisse experimenteller und rechengestützter Forschungsarbeiten zu offenen Fragen in verschiedenen geowissenschaftlichen Teildisziplinen. Die einzelnen Artikel decken ein weites Themenspektrum ab, das von der frühen Differenziation der Erde über den heutigen Aufbau des silikatischen Erdmantels, die Speicherung und den Transport von Wasser im Erdmantel und die Zusammensetzung des Erdkerns bis zu chemischen Wechselwirkungen an der Kern/Mantel-Grenze reicht. Andere Beiträge beschäftigen sich mit oberflächennäheren Phänomenen. Sie stellen Ergebnisse zum Vulkanismus und dessen Einfluss auf die Erdatmosphäre, sowie zur Entstehung von Erzlagerstätten und zur Metamorphose in der Erdkruste vor.

Zahlreiche Beiträge erhellen großräumige Phänomene im Aufbau der Erde. So wird zum Beispiel ein neues Modell der Lithosphäre und Asthenosphäre präsentiert. Es basiert auf der Löslichkeit von Wasser in Mineralen des Erdmantels, die unter hohen Drücken und Temperaturen experimentell bestimmt wurde. Ein Minimum in der Wasserlöslichkeit fällt genau zusammen mit dem Tiefenbereich der Asthenosphäre. Dies führt wahrscheinlich zur Bildung von Teilschmelzen, die diese Lage des Erdmantels mechanisch schwach und leicht verformbar machen. Andere Beiträge befassen sich mit Details der markanten seismischen Diskontinuitäten in Tiefen von 410 und 520 km sowie an der Kern-Mantel-Grenze in 2900 km Tiefe. Eine verblüffende Beobachtung aus der Seismologie ist zum Beispiel das *gelegentliche* Vorhandensein einer Doppel-Diskontinuität in Tiefen um 520 km. Neue experimentelle Ergebnisse lassen vermuten, dass das Auftreten oder das Fehlen der doppelten Diskontinuität vom Grad der chemischen Verarmung des Erdmantels durch partielle Schmelzen abhängen könnte. Die Ergebnisse eröffnen die Möglichkeit, verarmte Regionen des Erdmantels eventuell mit Hilfe von seismologischen Daten zu kartieren.

Im Jahre 2005 fiel die Entscheidung, die Forschungsaktivitäten des Bayerischen Geoinstituts auf das Gebiet „Geodynamische Modellierung“ auszuweiten. Dies wird eine fruchtbare Zusammenarbeit zwischen experimentell arbeitenden Wissenschaftlern und Modellierern aus

der Geodynamik mit wesentlichen Synergieeffekten ermöglichen. Im Zusammenhang damit wurde im Jahre 2005 bei dem *Stiferverband für die Deutsche Wissenschaft* ein Antrag zur Einrichtung einer Junior-Professur („*tenure-track*“) für das Fachgebiet „Geodynamische Modellierung“ eingereicht. Wir wurden vor kurzem informiert, dass der Antrag Erfolg hatte. Aufgrund der Bemühungen von Catherine McCammon als Koordinatorin wurde ein neues *EU Marie Curie Training Site*-Programm unter dem Titel „*Atomic to Global*“ bewilligt. Auch der Antrag auf ein Laser-Ablation-ICP-MS im HBEF-Verfahren wurde bewilligt. Schließlich ist das TEM-Labor durch die Einstellung von Nobuyoshi Miyajima als Nachfolger Falko Langenhorsts wieder vollständig einsatzbereit.

Wie in früheren Jahren wurden die Forschungsaktivitäten des Geoinstituts wesentlich durch die Einwerbung von Drittmitteln verschiedener Wissenschaftsprogramme unterstützt. Ein Internationales Doktorandenkolleg im Elitenetzwerk Bayern lief im Jahre 2005 unter dem Thema „Struktur, Reaktivität und Eigenschaften von oxidischer Materie“ an. Partner im Doktorandenkolleg, in dem vorerst für die Dauer von 4 Jahren Finanzmittel zur Verfügung stehen, sind das Bayerische Geoinstitut, das Institut für Anorganische Chemie der Universität Bayreuth und das Fraunhofer-Institut für Silicatforschung (ISC) in Würzburg. Über das erfolgreiche erste Jahr des Internationalen Doktorandenkollegs wird im Kapitel 4 des Jahrbuchs berichtet. Auch die EU-Programme *Marie Curie Training Site* und *Research Infrastructure (Transnational Access)* wurden erfolgreich fortgesetzt. Diese Programme haben zahlreichen sowohl jüngeren als auch erfahrenen Wissenschaftlern aus Europa das Arbeiten am Bayerischen Geoinstitut und die Nutzung der Labor- und Rechnereinrichtungen ermöglicht.

Wie in den vorangegangenen Jahren möchte ich auch im Namen meiner Kollegen dem *Freistaat Bayern*, vertreten durch das *Bayerische Staatsministerium für Wissenschaft, Forschung und Kunst*, als auch der *Kommission für Geowissenschaftliche Hochdruckforschung* der *Bayerischen Akademie der Wissenschaften* meinen Dank für ihre fortwährende Unterstützung und ihre enge Verbundenheit mit dem Bayerischen Geoinstitut aussprechen. Wir sind auch sehr dankbar für die großzügige Förderung durch externe Geldgeber, insbesondere durch die *Alexander von Humboldt-Stiftung*, die *Europäische Union*, die *European Science Foundation* und die *Deutsche Forschungsgemeinschaft*, die ebenfalls wesentlich zur Entwicklung und zum Erfolg des Bayerischen Geoinstituts beigetragen haben.

Bayreuth, im März 2006

David C. Rubie

1. Advisory Board and Directorship

1.1 Advisory Board

The *Kommission für Geowissenschaftliche Hochdruckforschung der Bayerischen Akademie der Wissenschaften* advises on the organisation and scientific activities of the Institute. Members of this board are:

Prof. Dr. Drs. h. c. E. ALTHAUS ^{*)}	Emeritus, Mineralogisches Institut der Universität Karlsruhe
Prof. Dr. U. CHRISTENSEN	Max-Planck-Institut für Aeronomie, Katlenburg-Lindau
Prof. Dr. R. KNIEP	Institut für Chemische Physik fester Stoffe der Max-Planck-Gesellschaft, Dresden
Prof. Dr. H. PALME	Institut für Mineralogie und Geochemie der Universität zu Köln
Prof. Dr. R. RUMMEL	Institut für Astronomische und Physikalische Geodäsie der TU München
Prof. Dr.-Ing. G. SACHS (Chairman)	Lehrstuhl für Flugmechanik und Flugregelung der Technischen Universität München
Prof. Dr. E. SALJE	Department of Earth Sciences, University of Cambridge
Prof. Dr. Drs. h. c. W. SCHREYER ^{†)}	Emeritus, Institut für Mineralogie der Ruhr-Universität Bochum
Prof. Dr. H. SOFFEL	Emeritus, Institut für Allgemeine und Angewandte Geophysik der Universität München

^{*)} resigned from the *Kommission* December 31, 2005

^{†)} deceased February 12, 2006

The Advisory Board held meetings in Bayreuth (07.-08.04.2005) and in Munich (18.11.2005).

1.2 Leadership

Prof. Dr. David C. RUBIE (Director)

Prof. Dr. Friedrich SEIFERT

Prof. Dr. Hans KEPPLER

2. Staff, Funding and Facilities

2.1 Staff

At the end of 2005 the following staff positions existed in the Institute:

- Scientific staff: **12**
- Technical staff: **13**
- Administrative staff: **2**
- Administrative officer: **1**

During 2005, 11 scientific (56 months) and 2 technical (19 months) positions were funded by grants raised externally by staff members of the institute.

In addition 12 long-term scientific positions (76 months) were funded by the resources of the BGI Visiting Scientists' Program (see Sect. 8) which also supported short-term visits for discussing future projects or presenting research results (see Sect. 6). Positions for 5 young scientists (50 months) were funded under the BGI International Graduate School under the Elitenetzwerk Bayern "Structure, Reactivity and Properties of Oxide Materials" (see Sect. 4). 7 scientists (32 months) were funded by personal grants (stipends).

2.2 Funding

In 2005, the following financial resources were available from the Free State of Bavaria:

- Visiting Scientists' Program: 416.000 €
- Consumables/investment: 441.000 €
- Internat. Graduate School/Elitenetzwerk Bayern 339.000 €

The total amount of national/international external funding ("*Drittmittel*") used for ongoing research projects in 2005 was 518.000 € (Positions: 266.000 €; equipment, consumables and travel grants: 252.000 €).

	positions	equipment, consum- ables, travel grants	total
• AvH	64.000 €	43.000 €	107.000 €
• DAAD		1.000 €	1.000 €
• DFG	169.000 €	44.000 €	213.000 €
• EU	25.000 €	134.000 €	159.000 €
• Others	8.000 €	30.000 €	<u>38.000 €</u>
			518.000 €

(AvH = Alexander von Humboldt Foundation; DAAD = German Academic Exchange Program; DFG = German Science Foundation; EU = European Union)

In the following list only the BGI part of the funding is listed in cases where joint projects involved other research institutions. Principal investigators and duration of the grants are listed in brackets.

Funding institution	Project, Funding	Total Project Funding
BCTC*	Travel funding (G. Steinle-Neumann, S. Akber-Knutson) for project "Computer Modelling of deep Earth Mineralogy and Geochemistry"	6.500 €
DFG	Bo 2550/1-1 (T. Boffa Ballaran, D.J. Frost, L.S. Dubrovinsky – 8.05 - 7.07) Positions: BAT IIa/2, 24 months 58.800 € Consumables and travel funding: 6.000 €	64.800 €
DFG	Fr 1555/1-2 (D.J. Frost, D.C. Rubie – 9.03 - 8.05) Positions: BAT IIa/2, 12 months 29.400 € Consumables and travel funding: 6.125 €	35.525 €
DFG	Fr 1555/2-1 (D.J. Frost, F. Heidelbach, F. Langenhorst, D.C. Rubie – 1.04 - 8.05) Positions: BAT IIa/2, 12 months 29.400 € Consumables and travel funding: 5.000 €	34.400 €
DFG	Ja 1122/1-1 (S.D. Jacobsen, L.S. Dubrovinsky – 2.04 - 1.06) Positions: BAT IIa/2, 24 months 58.800 € Consumables and travel funding: 21.000 €	79.800 €
DFG	Gottfried Wilhelm Leibniz-Preis Ke 501/6-1 (H. Keppler – 12.04 - 9.06) Positions, consumables, equipment, travel:	240.000 €
DFG	ESF-Verbundprojekt "Hydrogen in Minerals" KE 1351/1-1 (H. Keppler – 12.05 - 11.08) Positions: BAT IIa/2, 36 months 88.200 € Consumables and travel funding: 15.000 €	103.200 €
DFG	Ma 801/7-1 (A. Magerl and M. Göbbels/Erlangen, F. Seifert/Bayreuth) Positions: BAT IIa, 24 months: 117.600 € (Erlangen) Consumables and travel funding: 18.400 € (Erlangen)	
DFG	Mc 3/13-3 (C.A. McCammon, L.S. Dubrovinsky – 1.05 - 12.06) Positions: BAT IIa/2, 24 months 58.800 € Consumables and travel funding: 33.810 €	92.610 €

DFG	Ru 437/6-2 (D.C. Rubie, D.J. Frost, F. Langenhorst, A. Holzheid – 4.04 - 3.06) Positions: BAT IIa, 24 months 117.600 € Consumables and travel funding: 12.100 €	129.700 €
DFG	Ru 437/7-2 (D.C. Rubie – 2.04 - 8.05) Positions: BAT IIa, 12 months 58.800 € Consumables and travel funding: 18.200 €	77.000 €
DFG	Ru 437/8-1 (D.C. Rubie, D.J. Frost, F. Langenhorst – 11.05 - 11.07) Positions: BAT IIa, 24 months 117.600 € Consumables and travel funding: 12.750 €	130.350 €
DFG	Travel funding (G. Steinle-Neumann) for Post-Perovskite Workshop, Tokyo Institute of Technology, Japan	926 €
ESF	ESF PESC Exploratory Workshop on Novel Superhard Materials, Bayreuth, 16.-20.11.05 (L.S. Dubrovinsky, N.A. Dubrovinskaia)	14.000 €
EU	"Research Infrastructures – Transnational Access" Programme (D.C. Rubie – 1.05 - 12.08)	960.000 €
EU	Marie Curie Fellowships (Training Center) (S. Mackwell/D. Rubie – 01.02. - 01.06) Positions, consumables, equipment, travel:	150.000 €

* Bavaria California Technology Center

2.3 Laboratory and office facilities

The institute occupies an area of

ca. 1200 m ²	laboratory space
ca. 480 m ²	infrastructural areas (machine shops, computer facilities, seminar room, library)
ca. 460 m ²	office space

in a building which was completed in 1994.

2.4 Experimental equipment

The following major equipment is available at Bayerisches Geoinstitut:

I. High-pressure apparatus

- 5000 tonne multianvil press (25 GPa, 3000 K)
- 1200 tonne multianvil press (25 GPa, 3000 K)
- 1000 tonne multianvil press (25 GPa, 3000 K)
- 500 tonne multianvil press (20 GPa, 3000 K)
- 500 tonne press with a deformation DIA apparatus
- 3 piston-cylinders (0.5" and 0.75"; 4 GPa, 2100 K)
- Cold-seal vessels (700 MPa, 1100 K, H₂O), TZM vessels (300 MPa, 1400 K, gas), rapid-quench
- Internally-heated autoclave (1 GPa, 1600 K)

II. Structural and chemical analysis

- 2 X-ray powder diffractometers
- 1 X-ray powder diffractometer with furnace and cryostat
- Single-crystal X-ray cameras
- 2 automated single-crystal X-ray diffractometers
- High-brilliance X-ray system
- 1 Mössbauer spectrometer (1.5 - 1300 K)
- 3 Mössbauer microspectrometers
- 2 FTIR spectrometers with IR microscope
- FEG transmission electron microscope, 200 kV analytical, with EDS and PEELS
- FEG scanning electron microscope with BSE detector, EDS, EBSD and CL
- 2 Micro-Raman spectrometers
- JEOL JXA-8200 electron microprobe; fully-automated with 14 crystals, 5 spectrometer configuration, EDX, capability for light elements
- Cameca SX-50 electron microprobe

193 nm Excimer Laser-Ablation ICP-MS
ICP-AES sequential spectrometer
Water content determination by Karl-Fischer titration

III. In situ determination of properties

1 calorimeter (77 - 1000 K) scanning

Diamond anvil cells for powder and single crystal X-ray diffraction, Mössbauer, IR, Raman, optical spectroscopy and electrical resistivity measurements up to at least 100 GPa

Facility for in situ hydrothermal studies in DAC

Externally electrically heated DACs for in situ studies at pressures to 100 GPa and 1200 K
1-atm furnaces to 1950 K, gas mixing to 1600 K, zirconia fO_2 probes

1-atm high-temperature creep apparatus

Gigahertz ultrasonic interferometer and an interface to resistance-heated diamond-anvil cells

Heating stage for fluid inclusion studies

Impedance/gain-phase analyser for electrical conductivity studies

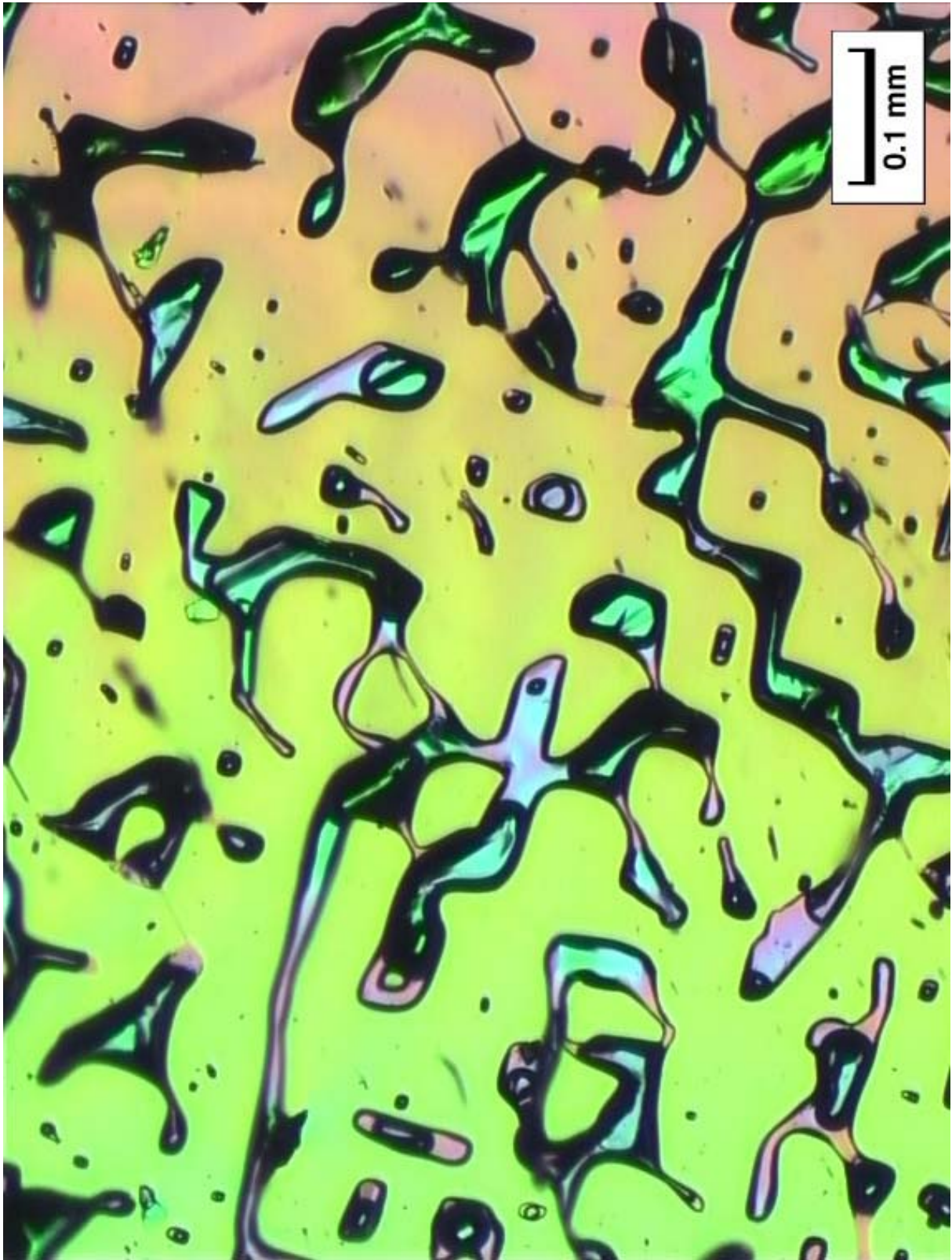
Apparatus for in situ measurements of thermal diffusivity at high P and T

Laser-heating facility for DAC

The Geoinstitut is provided with well equipped machine shops, electronic workshop and sample preparation laboratories. It has also access to the university computer centre.

The picture on page 18 shows synthetic fluid inclusions in quartz, photographed in the microscope using transmitted light and crossed polarizers. Each inclusion contains small amounts of a NaCl-bearing fluid that was in equilibrium with cassiterite (SnO_2) and was trapped in quartz at 700 °C and 1400 bar. The supercritical fluid unmixed into a gas and a liquid phase during subsequent cooling to room temperature. Using laser ablation ICP-MS, it is now possible to chemically analyze such inclusions individually, and thereby obtain information on the solubility of tin in ore-forming fluids.

Das Bild auf Seite 18 zeigt synthetisch hergestellte Flüssigkeitseinschlüsse in Quarz, aufgenommen im Durchlichtmikroskop bei gekreuzten Polarisatoren. Jeder Einschluss enthält eine kleine Menge an NaCl-haltigem Fluid welches im Gleichgewicht mit Kassiterit (SnO_2) stand und bei 700 °C und 1400 bar im Quarz eingefangen wurde. Das superkritische Fluid entmischte sich während der Abkühlung auf Raumtemperatur in eine Gas- und eine Flüssigphase. Mittels Laser-Ablation ICP-MS ist es heutzutage möglich, einzelne solcher Einschlüsse chemisch zu analysieren, und somit Informationen über die Löslichkeit von Zinn in erzbildenden Fluiden zu gewinnen.



3. Forschungsprojekte

Es wird an dieser Stelle nur über die wichtigsten, derzeit laufenden Projekte berichtet. Informationen über abgeschlossene Teilprojekte sind in den Abschnitten 5.1 und 5.2 in Form von Literaturzitationen angegeben. Die Beiträge des Kapitels 3 sollen nicht zitiert werden.

3.1 Aufbau und Geodynamik der Erde

Detaillierte Kenntnisse über die physikalischen Eigenschaften von Materialien des Erdinneren sind erforderlich, um den Aufbau und die Dynamik unseres Planeten zu erforschen. Dies gilt sowohl für die Hochdruckphasen der Silikat- und Oxidminerale des Erdmantels als auch für Metalllegierungen des Erdkerns. Mit solchen Daten kann man auf komplexere Fragestellungen aus der Geophysik und der Geochemie eingehen. So können zum Beispiel lateral unterschiedliche elastische Eigenschaften der Materie des Erdmantels sowohl durch chemische als auch durch thermische Inhomogenitäten der Materie hervorgerufen werden. Die wirksame Ursache lässt sich nur durch sorgfältige mineralphysikalische Untersuchungen identifizieren. Die Bereitstellung derartiger Daten, und ihre Integration in Modelle für den Erdaufbau und die thermische und chemische Entwicklung der Erde, ist eine zentrale wissenschaftliche Aufgabe des Bayerischen Geoinstituts. Fortschritte in experimentellen Methoden und Modellierung ermöglichen heute eine erfolgreiche Erforschung physikalischer Eigenschaften von Mineralen des Erdinneren unter Druck, Temperatur und chemischer Zusammensetzung.

Ergebnisse aus der Mineralphysik haben die Interpretation von seismischen Diskontinuitäten im Erdinneren als Phasenübergänge erst ermöglicht. So werden die Tiefen dieser Reflektoren mit Phasenübergängen in Hauptmineralen des Erdmantels korreliert. Hervorzuheben ist hier die Diskontinuität zwischen dem oberen Mantel und der Übergangszone in 410 km Tiefe, die von dem Phasenübergang in $(\text{Mg,Fe})_2\text{SiO}_4$ von Olivin nach Wadsleyit verursacht wird. Während sich im Experiment dieser Phasenübergang scharf begrenzt zeigt, erstreckt sich die seismische Diskontinuität in manchen Regionen über einen relativ großen Tiefenbereich. Die Ursache dafür ist zur Zeit noch nicht geklärt, es könnten aber chemische Inhomogenitäten eine Rolle spielen. Die ersten beiden Beiträge dieses Kapitels befassen sich mit dieser offenen Frage und erkunden zwei potentielle chemische Einflüsse: Wasser und dreiwertiges Eisen. Die Übergangszone zwischen 410 und 660 km Tiefe wird als ein potentielles Wasserreservoir in der festen Erde angesehen, da Wasser in Form von OH-Gruppen in Wadsleyit, dem Hauptmineral dieser Zone, löslicher ist als in Olivin. Der Einfluss dieser Affinität auf Druckübergänge und auf die Kontrastschärfe zwischen den beiden Mg_2SiO_4 -Modifikationen wird hier mit Hilfe von Experimenten untersucht. Ein ähnliches Projekt befasst sich mit dreiwertigem Eisen, das ebenfalls eine größere Affinität zu Wadsleyit aufweist.

Während der Übergang von Olivin zu Wadsleyit ein deutliches elastisches Signal im Erdmantel hervorruft, ist der Übergang von Wadsleyit zu Ringwoodit (in ca. 520 km Tiefe)

hinsichtlich der seismischen Eigenschaften kontrastarm und kann durch seismologische Untersuchungen nur schwer erfasst zu werden. Jüngere Fortschritte in der seismischen Inversion zeigen lokale Reflektoren, hinterlassen jedoch ein rätselhaftes Bild für den zentralen Bereich der Übergangszone: dort zeigt sich in einigen Regionen ein seismischer Reflektor in ungefähr 520 km Tiefe, während an anderen Stellen keine Reflektionen zu erkennen sind. In wiederum anderen Regionen zeigen sich komplexe Strukturen von Doppel-Reflektoren. Da die Entmischung von CaSiO_3 -Perowskit aus der Granatkomponente des Erdmantels bei vergleichbaren Druck- und Temperaturbedingungen wie der Wadsleyit/Ringwoodit-Übergang beginnt, könnte dieser Prozess ebenfalls einen Reflektor im Zentrum der Übergangszone erzeugen, wie der dritte Beitrag des Abschnitts verdeutlicht.

Weitere geophysikalisch interessante Forschungsziele im Erdinneren stellen obere und untere Grenzflächen dar. Thermische und chemische Grenzflächen spielen in zahlreichen geophysikalischen Prozessen eine wesentliche Rolle (Plattentektonik, Subduktion). Die Lithosphäre ist von der unter ihr ablaufenden Mantelkonvektion durch eine mechanische Schwächezone (Asthenosphäre) teilweise entkoppelt. Die Natur dieser Schwächezone wird im vierten Beitrag dieses Kapitels untersucht. Dabei steht der Wasseranteil von Mantelgesteinen im Mittelpunkt. Es werden neue Daten zur Wasserlöslichkeit von Pyroxen mit denen von Olivin zur Analyse der mechanischen Eigenschaften kombiniert.

Ähnlich wie die Lithosphäre weist die D'' -Schicht an der Untergrenze des Mantels starke laterale Variationen in Mächtigkeit und physikalischen Eigenschaften auf, was Geophysikern seit Jahrzehnten Rätsel aufgibt. Jüngste Forschungsergebnisse zum Phasenübergang von Perowskit zum Post-Perowskit in MgSiO_3 unter Bedingungen des unteren Erdmantels können zur Klärung der Inhomogenitäten in D'' beitragen. Der fünfte Beitrag dieses Kapitels behandelt den Einfluss von Al_2O_3 auf Druck und Ausdehnung dieses Phasenübergangs mit Hilfe von *ab initio*-Modellierungen.

Der abschließende Beitrag dieses Kapitels führt uns zur primären Fragestellung zurück, physikalische Mineraleigenschaften in ein globales Modell der festen Erde zu integrieren. Ähnlich wie die inverse Fragestellung aus der Seismologie, mit der elastische Daten interpretiert werden, hängen Modelle zum thermischen Zustand und der Entwicklung des Erdinneren (Geodynamik) von qualitativ ausgereiften Modellen der Mineraleigenschaften ab. Hier wird ein thermodynamisches und physikalisches Modell der Mineralogie des Erdmantels präsentiert, das in der Geodynamik, und letztlich auch der Modellierung von Wellenfortbewegung im Erdinneren (Forward-Seismologie), Einsatz finden wird.

3.2 Geochemie

Ein wichtiges Ziel der Geochemie ist das Verständnis und die Vorhersage der Fraktionierung chemischer Elemente bei der Auftrennung geochemischer Reservoirs. Wichtige Faktoren bei einem Fraktionierungsereignis sind die Gesamtzusammensetzung des Ausgangssystems, die

Zusammensetzungen der neu gebildeten Systeme sowie die Bedingungen, unter denen Fraktionierung stattfand. In vielen Fällen sind einer oder mehrere dieser Parameter im System Erde nur ungenau bekannt. In Laborexperimenten ist es jedoch häufig möglich, die physikalischen Bedingungen zu simulieren, unter denen diese Vorgänge abliefen sowie die Zusammensetzung unbekannter Reservoirs zu ermitteln. Alle in diesem Kapitel beschriebenen Projekte befassen sich mit bestimmten Aspekten von Fraktionierungsprozessen und führen zu einem besseren Verständnis der Bildung und Zusammensetzung geochemischer Reservoirs in der Erde.

Man nimmt häufig an, dass die Erde eine Gesamtzusammensetzung ähnlich den chondritischen Meteoriten hat, wobei es jedoch offenbar keinen Chondriten gibt, der sowohl in seiner chemischen als auch isotopischen Zusammensetzung genau mit der Erde übereinstimmt. Im Sonnennebel und der daraus entstandenen Akkretionsscheibe müssen noch vor der Entstehung der Planeten Fraktionierungsprozesse abgelaufen sein. Diese Prozesse führten zu unterschiedlichen chemischen und isotopischen Zusammensetzungen verschiedener Meteorit-Typen und auch der Planeten. Wenn wir verstehen, wann und wie derartige Fraktionierungsprozesse ablaufen, sind wir eventuell in der Lage die Gesamtzusammensetzung der Erde enger einzugrenzen.

Ein Haupt-Fraktionierungsereignis in der Entwicklungsgeschichte der Erde war die Abtrennung des metallischen, eisenreichen Erdkerns aus dem silikatischen Erdmantel. Hier ist uns die Zusammensetzung des Reservoirs „Erdmantel“ recht gut bekannt. Außerdem wissen wir, dass die Gesamtzusammensetzung der Erde wahrscheinlich in etwa chondritisch ist. Die Zusammensetzung des Erdkerns kennen wir dagegen nur ungenau; wir wissen lediglich, dass er eisen- und nickelreich ist und einen bis zu 10 %igen Anteil aus einem oder mehreren leichteren Elementen aufweist. Die Bedingungen, unter denen die Kern/Mantel-Trennung ablief, sind ebenfalls nicht bekannt; sie könnten ein weites Spektrum von Temperaturen, Drücken und Sauerstoff fugazitäten umfassen. Durch Hochdruck- und Hochtemperaturexperimente lässt sich die Elementverteilung zwischen Silikaten des Erdmantels und Schmelzen des Erdkerns untersuchen. Auf diese Weise können die Bedingungen der Bildung des Erdkerns und seine Zusammensetzung eingegrenzt werden.

Fluide, die an konvergenten Plattenrändern aus subduzierter ozeanischer Kruste freigesetzt werden, sind an einem weiteren Fraktionierungsprozess beteiligt. Dieser Prozess führt im Bereich von Inselbögen zur Bildung neuer kontinentaler Kruste aus dem Erdmantel. An diesen Orten läuft die Fraktionierung komplexer ab, da die entstehenden Magmen eine Mischung aus Komponenten zweier Reservoirs im Erdmantel sind; sie stammen teilweise aus der abtauchenden Platte selbst, teilweise aus dem überlagernden Mantelkeil. Genaue Informationen über die bei Subduktionen ablaufenden Fraktionierungsprozesse sind sowohl für das Verständnis der geochemischen Transportprozesse unterhalb von Inselbögen wichtig als auch für die Bestimmung der Zusammensetzung der abtauchenden Platte, die ein wichtiges Reservoir im Erdmantel darstellt.

3.3 Mineralogie, Kristallchemie und Phasenübergänge

Die Arbeiten zur Mineralogie und Kristallchemie im vergangenen Jahr waren weiterhin auf die Struktur-Eigenschaftsbeziehungen in wichtigen Mineralgruppen fokussiert. Durch das Studium der „Antwort“ der Kristallstrukturen auf geänderte Bedingungen von Druck und Temperatur und Vergleich mit der Änderung physikalischer Eigenschaften lassen sich die Ursachen von Eigenschaftsänderungen bestimmen. Dieser Ansatz war in der Vergangenheit für das Studium von chemisch einfachen Endgliedern sehr erfolgreich. Der kontrollierte chemische Ersatz z. B. einzelner Kationen durch andere stellt neben Druck und Temperatur eine weitere „Stellschraube“ zur gezielten Veränderung einer Kristallstruktur dar und es lassen sich gleichzeitig die komplexeren chemischen Zusammensetzungen natürlicher Minerale annähern.

Für den Geowissenschaftler ist die Zustandsgleichung eines Minerals eine der wichtigsten Eigenschaften, da sie z. B. in die seismischen Wellengeschwindigkeiten und die Druckabhängigkeit von Mineralreaktionen oder Phasentransformationen eingeht. Gleichzeitig ist sie sehr eng mit der Änderung der Kristallstruktur mit Druck und Temperatur verknüpft. Hierzu werden im folgenden neue Daten zu Pyroxen-Mischkristallen, zum Zeolit Analcim und zur sog. 10Å-Phase (einem wasserreichen Mg-Silicat) berichtet. Der Ersatz von K durch Na im Hochdrucksilicat Hollandit führt zu einer starken Reduktion seines Molvolumens. Die Fe³⁺-Konzentrationen und dessen Verteilung über Gitterplätze im Klinopyroxen geben Aufschluss über die Redox-Bedingungen im oberen Erdmantel.

In jüngerer Zeit wird verstärkt den elektronischen und magnetischen Eigenschaften von Mantelmineralen Aufmerksamkeit geschenkt: Der für hohe Drucke postulierte Spinübergang der Fe²⁺ von „low-spin“ zu „high-spin“ könnte drastische Einflüsse auf Molvolumina einzelner Erdmantelphasen und auf die Fe-Mg-Verteilungskoeffizienten zwischen ihnen haben, der Effekt ist aber im Detail noch nicht ganz verstanden. Erste Daten werden für das Spinverhalten bei Kompression von (metastabilem) Olivin und für Ferropervit, dem zweitwichtigsten Mineral des tieferen Erdmantels, angegeben. Ein wichtiges Ergebnis ist, dass die Änderung dieser Eigenschaft über ein großes Druck- (bzw. Tiefen-) Intervall hinweg erfolgt, also keine ausgeprägte Diskontinuität zu erwarten ist. Im Endglied FeO wird mit Hilfe von Neutronenbeugung nachgewiesen, dass der magnetische (Néel-) Phasenübergang und der strukturelle Phasenübergang von kubisch zu rhomboedrisch um ca. 40 °C auseinanderliegen, also nicht direkt miteinander verknüpft sind.

3.4 Physikalische Eigenschaften von Mineralen

Spektakuläre Ereignisse an der Erdoberfläche wie Vulkanausbrüche und Erdbeben werden hauptsächlich von Prozessen im Erdinneren angetrieben, die wiederum durch die physikalischen und chemischen Eigenschaften der beteiligten Minerale gesteuert werden. Somit

bleiben experimentelle Untersuchungen von physikalischen Eigenschaften im Brennpunkt der Forschung am Bayerischen Geoinstitut.

Materie, die unter kontrollierten Bedingungen synthetisiert wurde, ermöglicht die Bestimmung ihres Gefüges und ihrer physikalischen Eigenschaften in Abhängigkeit experimenteller Variablen (Temperatur, Druck und/oder Zusammensetzung), ohne jedoch komplexe Störeinflüsse wie Verunreinigungen, Defekte oder eine unbekannt thermische Vorgeschichte einbeziehen zu müssen. Andererseits können bei natürlicher Materie Merkmale wie z. B. das Mikrogefüge untersucht werden. Ein weiterer Ansatz zur Bestimmung von Mineralkenngrößen ist die Computer-Modellierung von Gefüge und Eigenschaften. Mit dieser Methode lassen sich zahlreiche experimentelle Grenzen überwinden.

Kompressionsuntersuchungen mit Hilfe der Röntgendiffraktometrie sind eines der wichtigsten Instrumente bei der Bestimmung elastischer Eigenschaften durch Messungen von Zustandsgleichgewichten. Solche Untersuchungen liefern nicht nur die Parameter, die zur Modellierung des Erdinneren unter Verwendung seismischer Daten notwendig sind, sondern sie erlauben auch Einblicke in Kompressionsmechanismen für ein weites Spektrum von Verbindungen (u. a. wasserhaltige Minerale). Durch seine Mikrostruktur lässt sich ein Stoff mit Hilfe einer Längenskala oberhalb des atomaren Maßstabs (zumeist im Bereich Mikrometer bis mehrere Hundert Mikrometer) beschreiben; das Mikrogefüge kann die physikalischen Eigenschaften wie Diffusion und Magnetismus stark beeinflussen. Durch akkurate Bestimmungen zum Beispiel mit Hilfe der Röntgenbeugung mit rückgestreuten Elektronen und der Mössbauer-Spektroskopie lassen sich Beziehungen zwischen Mikrogefüge und Gesamtverhalten aufzeigen. Oxide, Silikate und Legierungen aus Übergangsmetallen sind einerseits Hauptbestandteile des Erdinneren; jedoch können sie bereits in geringen Anteilen aufgrund der zahlreichen Übergangsmöglichkeiten ihrer Elektronenstruktur physikalische Eigenschaften gravierend beeinflussen.

Die vorgestellten Untersuchungen konzentrieren sich sowohl auf Hauptbestandteile des Erdmantels als auch auf Modellverbindungen, deren ungewöhnliche Eigenschaften relevant für ein weites Spektrum ähnlicher Phasen sein könnten.

3.5 Fluide und ihre Wechselwirkung mit Mineralen und Schmelzen

Obwohl Wasser- und CO₂-haltige Fluide nur in sehr kleinen Mengen im Erdinneren vorkommen, spielen sie eine große Rolle bei chemischen Transportprozessen. Viele alltägliche Gebrauchsmetalle sind nur deshalb kommerziell verfügbar, da sie durch Fluide in Erzlagerstätten extrem angereichert wurden. Manche Typen von Erzlagerstätten, beispielsweise von Zinn, sind sehr eng verknüpft mit Anreicherungen von Fluor. Sowohl die Natur der Fluorhaltigen Spezies in hydrothermalen Fluiden als auch der Einfluss von Fluor auf den Transport von Haupt- und Spurenelementen sind jedoch wenig verstanden. Im letzten Jahr wurde daher

der Effekt von Fluor auf die Löslichkeit von Quarz und von Cassiterit (SnO_2) in hydrothermalen Lösungen experimentell untersucht. Zur Untersuchung der Löslichkeit von Cassiterit wurde eine neue Technik entwickelt, um im Labor synthetische Einschlüsse von mit Cassiterit gesättigten Fluiden in Quarz zu erzeugen. Fluor erhöht sowohl die Löslichkeit von Cassiterit als auch die Löslichkeit von Quarz in hydrothermalen Lösungen drastisch. Eine thermodynamische Analyse der Daten deutet darauf hin, dass $\text{Si}(\text{OH})_2\text{F}_2$ der Hauptträger von Fluor in diesen Fluiden ist. Die Untersuchungen zeigen weiterhin, dass Zinn in der Gegenwart von Fluor in Fluiden zu extrem hohen Konzentrationen angereichert werden kann.

Die Löslichkeit von Wasser in nominal wasserfreien Mineralen ist mittlerweile ein gut etabliertes Forschungsgebiet mit großer Bedeutung für Geodynamik und den globalen Wasserkreislauf. Bis vor wenigen Jahren war dagegen die Löslichkeit von Kohlenstoff in normalen Mantelmineralen praktisch unbekannt. Dies hat sich geändert durch die Entwicklung neuer experimenteller und analytischer Methoden am Geoinstitut, mit denen die Kohlenstoff-Löslichkeit in Mineralen bis zu Konzentrationen von weniger als einem ppm gemessen werden kann. Diese Methoden wurden nun benutzt, um die Kohlenstoff-Löslichkeit in allen wichtigen Mineralen des Erdmantels zu bestimmen, einschließlich der Phasen des unteren Mantels und der Übergangszone. Die Löslichkeit von Kohlenstoff in all diesen Mineralen ist extrem niedrig. Praktisch der gesamte Kohlenstoff im Erdmantel muss daher als Karbonat vorliegen.

3.6 Physik und Chemie von Schmelzen und Magmen

Die Erde und andere Planeten unseres Sonnensystems haben sich während der vergangenen 4,5 Milliarden Jahren vor allem durch die Bildung und Kristallisation von Magmen verändert. Es gilt als sehr wahrscheinlich, dass die Erde in ihrer Frühzeit bis in große Tiefen aufgeschmolzen war. Dafür waren zahlreiche große Impakt-Ereignisse verantwortlich, durch die während der Akkretion der Erde große Mengen an kinetischer Energie freigesetzt wurden. Als Konsequenz davon bildete sich ein möglicherweise über 1000 km tiefer „Magma-Ozean“, in dem die Abscheidung einer eisenreichen Metallschmelze aus einem silikatischen Magma gefördert wurde und zur Bildung von Erdkern und Erdmantel führte. Die nachfolgende Kristallisation des tiefen Magma-Ozeans legte die frühe Struktur des Planeten fest und könnte zur Ausbildung chemisch unterschiedlicher Lagen im Mantel geführt haben. In den vergangenen 4,5 Milliarden Jahren schufen und formten magmatische Prozesse und Vulkanismus die ozeanische Kruste und die Kontinente. Der Transport flüchtiger Bestandteile aus dem Inneren des Planeten in die Atmosphäre durch Vulkane ist ein Hauptfaktor für die Entwicklung der Atmosphäre und für klimatische Veränderungen.

Um Auswirkung und Einfluss magmatischer Prozesse auf die chemische Differenzierung der Erde und der terrestrischen Planeten zu verstehen, müssen die physikalischen und chemischen Eigenschaften von Magmen und Schmelzen bekannt sein. Mit einem breiten Spektrum dieser

Eigenschaften befassen sich die Beiträge in diesem Abschnitt. Viskositätsmessungen an einer Silikatschmelze bei Drücken bis 25 GPa sind wichtig, um das Konvektionsverhalten und die Abkühlungsgeschwindigkeit eines Magma-Ozeans zu verstehen. Druck beeinflusst die Viskosität in sehr komplexer Weise über Veränderungen in der atomaren Struktur der Schmelzen. Mit der Kernresonanz-Spektroskopie wurde die Struktur von Gläsern untersucht, die aus Schmelzen bei sehr hohem Druck abgeschreckt wurden. Flüchtige Bestandteile im Magma bestimmen weitgehend den Mechanismus von Vulkaneruptionen. Der Einfluss von gelöstem CO₂ auf die Schmelzstruktur und auf Schmelzeigenschaften wurde mit Hilfe von spektroskopischen Methoden untersucht. In einer weiteren Arbeit zu vulkanischen Phänomenen werden Ergebnisse zur Absorption von Schwefeldioxid durch Vulkanasche vorgestellt. Ohne eine Quantifizierung dieses Effektes ist es unmöglich, den Einfluss von Vulkaneruptionen auf das Klima korrekt vorherzusagen. Auch die Struktur und die Entwicklung des größten Saturnmonds Titan ist Ziel von Untersuchungen. Durch Schmelzversuche an Methan-Gashydraten unter hohen Drücken lassen sich der Vulkanismus auf der Titan-Oberfläche sowie die hohen Methangehalte in der Atmosphäre von Titan erklären.

3.7 Rheologie

Die Erde ist ein dynamischer Planet, dessen Inneres durch Deformationsprozesse auf unterschiedlichen Zeitskalen geprägt ist. Das rheologische Verhalten der Gesteine ist bei hohen Spannungen und schnellen Verformungsraten typischerweise bruchhaft (z. B. Erdbeben) und bei niedrigen Spannungen und langsamen Verformungsraten duktil (z. B. die Konvektionsprozesse im Erdmantel). Sogenannte Fließgesetze, die dieses mechanische Verhalten beschreiben, können in mechanischen Testverfahren ermittelt werden, wobei jedoch eine Vielzahl von Variablen auftritt. Neben äußeren Einflussgrößen wie Temperatur, Druck, Fugazität/Aktivität verschiedener chemischer Komponenten müssen auch intrinsische, probenspezifische Materialeigenschaften wie Kristalldefekte und kristallographische Vorzugsrichtungen (Textur) in Betracht gezogen werden. Daneben verändert auch die plastische Materialverformung selbst diese spezifischen Eigenschaften. In den Geowissenschaften wird die Mikrostruktur verformter natürlicher Gesteine daher häufig ausgewertet, um ihre Deformationsgeschichte abzuleiten. Während sich der eigentliche Deformationspfad natürlicher Gesteine oft relativ erfolgreich rekonstruieren lässt, bleibt die Bestimmung der Spannung, die zur Verformung führte, weiterhin extrem schwierig. Hier bietet bisher zumeist nur die Messung und Extrapolation von Daten aus mechanischen Versuchen eine Möglichkeit, quantitative Ergebnisse zu erzielen.

Die Rheologie von Olivin und seinen Hochdruckpolymorphen (Wadsleyit, Ringwoodit) ist von großer Wichtigkeit für das Verständnis des Auftretens von Erdbeben in Tiefenbereichen, wo normalerweise bruchhafte Verformungen durch die hohen Umschließungsdrücke und Temperaturen ausgeschlossen sind. Der Prozess des Phasenübergangs selbst sowie Unterschiede in der Festigkeit der verschiedenen Phasen können möglicherweise bruchhafte

Verformung auslösen bzw. auch durch duktilen Verhalten verhindern. Gerichtete Spannungen auf vorgezeichneten Störungsflächen können umgekehrt auch die Phasenübergänge erleichtern. Erkenntnisse über den Einfluss einer Zugabe von Schmelze auf die Verformung von Olivin sind von Bedeutung, da der oberste Erdmantel unter mittelozeanischen Rücken und über abtauchenden Krustenplatten wahrscheinlich bis zu 10 % Schmelze aufweist. Die Anwesenheit einer Schmelze führt zu einer Verformungstextur, die sich drastisch von einer Olivinprobe ohne Schmelze unterscheidet, und damit auch zu einem sehr unterschiedlichen Muster in der physikalischen Anisotropie. Die Deformation eines schmelzhaltigen Gesteins führt umgekehrt auch zu drastisch veränderter Schmelzverteilung im Gestein sowie anderen Permeabilitäten. Ob eine Schmelze in einem Gestein eingeschlossen bleibt oder ein Netzwerk bildet, das der Schmelze erlaubt, sich durch den Festkörper hindurch zu bewegen, ist stark davon abhängig, welcher Verformung der schmelzhaltige Gestein unterworfen ist. Experimentelle Ansätze, bei denen diese dynamischen mikrostrukturellen Vorgänge untersucht werden, sind problematisch, wenn die Proben nicht *in situ*, d. h. bei den entsprechenden Drücken und Temperaturen beobachtet werden können. Experimente in der Moissanit-Stempelzelle bieten einen Ausweg aus diesem Problem, da sie direkte Beobachtung der Proben bei hohen Drücken und Temperaturen erlauben.

Die Rheologie subduzierter Platten relativ zu der des umgebenden Erdmantels ist sehr wichtig für das Verständnis der Bildung sogenannter Hochdruckterrains, die sich in nahezu allen Gebirgszügen der Welt finden. Während die absolute Festigkeit natürlicher Gesteine unter hohem Druck und Temperatur oft nur mit sehr großen Fehlern abgeschätzt werden kann, können Geländebeobachtungen und Mikrostrukturen in solchen Hochdruckterrains es erlauben, zumindest relative Festigkeiten zu bestimmen (z. B. in gemeinsam deformiertem Eklogit und Peridotit). Die Rekonstruktion des Deformationsverhaltens eines bestimmten Gesteins bei bestimmten Druck- und Temperaturbedingungen kann dabei aber durch nachfolgende Überprägungsvorgänge und Mineralumwandlungen verschleiert werden (z. B. in Symplektiten).

Natürliche Beispiele duktiler Deformation in Granat sind in neuerer Zeit häufiger in der Literatur dokumentiert worden, da durch die Verwendung der Beugung rückgestrahlter Elektronen (EBSD) im Rasterelektronenmikroskop die Analyse von Deformationsstrukturen in Granaten möglich gemacht wird. Ein wichtiger Aspekt dieser Messungen ist, dass die intrakristalline Deformation auch einen Einfluss auf Diffusionsprozesse und chemische Gleichgewichte hat, so dass z. B. Wachstumszonierungen verändert werden können, die gerade im Granat oft zur Bestimmung der p,T-Bedingungen verwendet werden. Quarz ist eines der wichtigsten Minerale in Krustengesteinen, das zur Rekonstruktion von Deformationsverhalten und p,T-Bedingungen der Deformation herangezogen wird. Eine detaillierte Texturanalyse des Quarzes in granitischen Gesteinen erlaubt es, sowohl die Kinematik von unterschiedlichen Deformationsphasen als auch die Temperaturentwicklung während der Deformation von Krustengesteinen und der Bildung von Gebirgsgürteln einzugrenzen.

3.8 Metamorphose

Metamorphe Gesteine machen circa 85 % des Volumens der Erde aus. Fast alle wurden in der Unterkruste und im Erdmantel gebildet; sie sind das Ergebnis tektonischer Prozesse wie Subduktion an Plattengrenzen, Krustenverdickung im Bereich kontinentaler Gebirgsgürtel, Grabenbildung bei der Entstehung neuer Krustenplatten sowie Konvektion im Erdinneren. Metamorphe Gesteine entstehen durch eine Überprägung ihrer Ausgangsgesteine unter veränderten Druck- und Temperaturbedingungen entsprechend des jeweiligen tektonischen Umfeldes. Ihre Bildung beinhaltet physikalische und chemische Veränderungen des Materials im festen Zustand. Physikalische Veränderungen ergeben sich durch Gesteinsverformung und durch Bildung neuer Minerale; chemische Veränderungen werden durch kontinuierliche und diskontinuierliche metamorphe Reaktionen hervorgerufen, die zu neuen, stabilen Mineralen und/oder neuen chemischen Zusammensetzungen der Minerale führen.

Experimentelle Untersuchungen zu den Stabilitätsbedingungen verschiedener metamorpher Minerale und dazu, wie diese Bedingungen als Funktion der chemischen Zusammensetzung variieren können, liefern uns wichtige Erkenntnisse über Druck- und Temperaturbedingungen in einem speziellen tektonischen Umfeld. Experimente ermöglichen weiterhin Einblicke in die Art und Weise wie und in die Bedingungen (z. B. Druck, Temperatur, Spannung, Fluidaktivität), unter denen metamorphe Minerale als Folge verschiedener Mechanismen verformt werden. Die Verknüpfung beider experimentellen Ansätze mit sorgfältigen Untersuchungen stabiler Minerale und ihrer chemischen Zusammensetzung in natürlichen metamorphen Gesteinen führt zu entscheidenden Erkenntnissen über thermo-mechanische Prozesse in unterschiedlichen tektonischen Bildungsräumen.

Die in diesem Kapitel des Jahresberichts zusammengeführten Beiträge befassen sich sowohl mit der Erforschung der tektonischen Entwicklungsgeschichte als auch mit den thermo-mechanischen Prozessen, die mit Metamorphose-Ereignissen in verschiedenen Tiefenabschnitten (bis in 125 km Tiefe) in den Wurzelzonen sehr alter sowie junger Gebirgsketten in Verbindung stehen. Es wird die tektonische Entwicklung von Mikro-Diamant-führenden Gneisen in Westnorwegen vorgestellt, die durch das ungewöhnliche Auftreten von faserigem Pumpellyit in einem metamorphen Spätstadium auffallen. Die Wechselwirkung zwischen Erdkruste und Mantel sowie unterschiedliche Metamorphosebedingungen in diesem Grenzbereich werden durch Veränderungen der chemischen Zusammensetzung der Minerale in einem Peridotiteinschluss in Eklogit untersucht. Weitere Beiträge befassen sich mit der Verformung und kristallographischen Vorzugsorientierung von Mineralen durch gebirgsbildende Prozesse. Die Texturen von Omphazit und Granat in Eklogiten der österreichischen Alpen erlauben Rückschlüsse darüber, wie während der Bildung der Alpen schon subduzierte ozeanische Kruste an die Erdoberfläche zurücktransportiert wurde. Die Analyse von Quarz-texturen im panafrikanischen Gebirgsgürtel Zentralafrikas dagegen erlaubt, die metamorphen Bedingungen und die Kinematik von Störungen zu bestimmen, die für die Gebirgsbildung eine entscheidende mechanische Funktion in der Kruste hatten. Die Beiträge dieses Kapitels liefern Beispiele dafür, wie physikalische und chemische Veränderungen im Verlauf

metamorpher Prozesse können für das Verständnis dieser Prozesse und die Bildung von Gebirgsketten genutzt werden können.

3.9. Materialwissenschaften

Durch die großen Fortschritte bei der Konstruktion und Leistungsfähigkeit von Hochdruck-Hochtemperatur-Apparaturen hat sich die Hochdrucktechnik als eine weit verbreitete, relativ kostengünstige Methode etabliert, um in grundlegenden physikalischen Experimenten die Eigenschaften von Festkörpern, insbesondere Volumen, Kristallstruktur, elektronische und magnetische Kenngrößen usw. zu bestimmen. Außerdem zeichnen sich in der angewandten Forschung vielversprechende Synthesen neuartiger Materialien ab. Am Bayerischen Geoinstitut werden Hochdruckmethoden und -techniken nicht nur angewandt sondern auch weiterentwickelt, und es ist somit in der Materialforschung unter extremen Bedingungen engagiert. Hier werden die Ergebnisse von Untersuchungen an unterschiedlichen Feststoffen vorgestellt – an Kohlenstoff und Materialien auf Kohlenstoffbasis, Metallen und Legierungen, grob- und nanokristallinen Oxiden und Keramiken auf Nitridbasis.

Diamant findet wegen seiner Kombination einzigartiger physikalischer und chemischer Eigenschaften (Härte, hohe thermische Leitfähigkeit, breite Energieband-Lücke, hohe Mobilität von Elektronen und Elektronenlöchern, chemische Stabilität) ein weites Anwendungsspektrum in der modernen Wissenschaft und Technologie. In der Elektronik besteht auf der Anwenderseite ein wachsender Bedarf an diamantähnlicher Materie. Es ist wohl nicht zu erwarten, dass mikroelektronische Bauteile aus diamantähnlicher Materie Silicium vollständig verdrängen werden. Aber es ist Tatsache, dass Bauteile aus Diamant noch unter Bedingungen einsetzbar sind, wo solche aus Silicium bereits versagen. So erfüllen elektronische Bauteile aus Diamant noch bei Temperaturen von mehreren Hundert Grad ihre Aufgaben, während Siliciumchips oberhalb ca. 450 °K ausfallen. Elektrochemische Einsatzbereiche für Filme auf Diamantbasis wurden in den letzten Jahren kontinuierlich weiterentwickelt und werden als vielversprechendes Forschungsgebiet angesehen. Reiner Diamant wirkt als perfekter Isolator. Aber, genau wie Silicium, kann Diamant durch geringste Beimengungen von Bor oder Stickstoff in einen Halbleiter umgewandelt werden. Am Geoinstitut durchgeführte Untersuchungen bei erhöhten Drücken und Temperaturen im System Bor/Kohlenstoff haben hinsichtlich der Synthese von stark mit Bor dotierten Diamanten neue Perspektiven eröffnet und gezeigt, dass dieses Material eine extrem hohe Härte mit einzigartigen elektronischen Eigenschaften, insbesondere Supraleitfähigkeit, vereinigt.

Die nanokristalline Form der Materie kann positive Eigenschaften ihres makrokristallinen Pendant noch verstärken. In den jüngsten Jahren waren Synthesen und Untersuchungen verschiedener Nanomaterialien (Kohlenstoff- Röhren, Drähte, Stäbe und Whisker) besonders attraktiv. Obwohl sich die Produktion von Nanostäbchen aus verschiedenen Ausgangsmaterialien als sehr erfolgreich erwiesen hat, wurde bisher nicht über experimentelle

Erfahrungen mit Diamant-Nanostäbchen berichtet. Dabei wurden doch sowohl ihre Existenz als auch ihre überragenden physikalischen Eigenschaften von Theoretikern vorhergesagt. Das Geoinstitut kann nun in diesem Jahr über eine gelungene Synthese von aggregierten Diamant-Nanostäbchen (ADNRs) berichten, die aus C₆₀-Fullerenen in einer Multianvil-Pressen synthetisiert wurden. Einzelne Diamant-Nanostäbchen weisen einen Durchmesser von 5 bis 20 nm und eine Länge von mehr als 1 µm auf. Die Dichte der ADNRs ist ca. 0,2 bis 0,4 % höher als die gewöhnlicher Diamanten. Durch *in situ*-Röntgenbeugungsmessungen wurde ein extrem hoher isothermaler Kompressionsmodul nachgewiesen, der deutlich über dem von Diamant liegt. Von allen bekannten Materialien aus Kohlenstoff weisen ADNRs die größte Dichte und die geringste bisher experimentell bestimmte Kompressibilität auf.

Zu den bekannten und potentiellen Anwendungsmöglichkeiten von nanokristallinem Titandioxid/Titandioxid-Zirkondioxid-Mischkristallen gehören Pigmente, Kunststoffe, Kosmetika, elektronische Bauteile und Katalysatoren. Experimentelle Hochdruck-Untersuchungen am Geoinstitut ermöglichten nicht nur Synthesen neuartiger Phasen von (Ti,Zr)O₂, sondern zeigten weiterhin neue Phänomene, wie zum Beispiel die Partikelgrößenabhängigkeit der druckinduzierten Amorphisierung von Titandioxid.

Eines der Hauptprobleme der Hochdruckforschung in den Materialwissenschaften liegt in der Synthese von Probenmengen in der Größenordnung einiger Kubikmillimeter. Die Aufgabe wird noch schwieriger, wenn keine Niedrigdruck-Pendants der entsprechenden Substanzen verfügbar sind. Neuartige Experimente zur Synthese von Nitriden (insbesondere Nickelnitrid) unter Verwendung von Kaliumazid als Stickstofflieferant könnten eine Lösung dieses Problems darstellen.

3.10 Methodische Entwicklungen

Die Entwicklung neuartiger experimenteller und analytischer Verfahren ist eine fundamentale Vorbedingung, um auf hohem wissenschaftlichen Standard konkurrieren und eine Führungsrolle in einer wissenschaftlichen Disziplin spielen zu können. Dies gilt auch für das Bayerische Geoinstitut, das teilweise als eine „Forschungseinrichtung für Europa“ dient. Methodenentwicklung ist eine zeitaufwändige Herausforderung, die einem Forschungsinstitut hohen technischen und finanziellen Einsatz abfordert. Im vergangenen Jahr wurden Verfahren entwickelt, getestet und verbessert, die sich zwei Kategorien zuordnen lassen: (1) *in situ*-Methoden zur Probencharakterisierung bei hohen Drücken und Temperaturen und (2) *ex situ*-Verfahren zur Probencharakterisierung bei Umgebungsbedingungen. In die erste Kategorie fallen die ersten vier Projektbeschreibungen dieses Kapitels.

Ein wichtiger Schritt für das Verständnis der Redox-Bedingungen im Erdmantel ist die Anwendung der Mikro-XANES Methode der Fe³⁺/ΣFe-Bestimmung auf *in situ*-Bedingungen in der Diamantstempelzelle und die Kalibrierung des Druckeffektes auf derartige Messungen.

Durch den Einsatz der Rubin-Fluoreszenz-Methode bei Gigahertz-Ultraschall-Interferometrie in einer Diamantstempelzelle kann jetzt der Druck wesentlich genauer bestimmt werden. Die Leistungsfähigkeit des Röntgensystems mit hoher Brillianz wurde durch einen drehbaren Probenstisch erhöht. Dieser wird für die Erzeugung hochqualitativer Beugungsmuster schwachstreuender Proben wie Eis oder Gashydrate/Clathrate in der Diamantstempelzelle benötigt. Weiterhin wurde eine Methode entwickelt, die simultane Röntgenbeugungsmessungen und Bestimmungen des elektrischen Widerstands ermöglicht. Die *in-situ* Raman-Spektroskopie ist nun auch in laserbeheizten Diamantstempelzellen einsetzbar, um Phasengleichgewichte und Schmelzprozesse bei hohen Drücken zu ermitteln.

Eine neuartige Technik ermöglicht die Synthese großvolumiger Perowskitproben für die Bestimmung von Zustandsgleichungen durch Schockwellen-Experimente. Für diese Technik, mit der die wahrscheinlich größte je synthetisierte MgSiO_3 -Perowskit-Probe erzeugt wurde, kommt die 5000 Tonnen-Presse des Bayerischen Geoinstituts zum Einsatz. Die Leistungsfähigkeit der Mössbauer-Spektroskopie wurde durch einen neuen Goniometer-Probenstisch vergrößert, mit dem Einkristalle bei konstanter Absorber-Dicke analysiert werden. Mit dem neuen Versuchsaufbau sind zum Beispiel elektrische Feldgradienten oder die Anisotropie der rückstoßfreien Fraktion messbar. Diese Kenngrößen sind zur Entfaltung stark überlappender Mössbauer-Spektren erforderlich. Mit einer anderen neuen Technik lassen sich extrem dünne, kontaminationsfreie Probenträger-Folien für die hochauflösende Transmissionselektronenmikroskopie und EELS herstellen. Weiterhin berichtenswert ist die Identifizierung eines natürlichen, kristallographisch homogenen Hämatit-Ilmenits, der in einer spezifischen Orientierung präpariert wurde, um die Theorie des lamellaren Magnetismus zu überprüfen.

3. Research Projects

In this section an overview of the most important ongoing projects is given. Information concerning recently-completed projects can be obtained from the publication lists of sections 5.1 and 5.2. Please note that the following contributions should not be cited.

3.1 Earth's Structure and Geodynamics

Studying Earth's structure and dynamics requires a detailed understanding of the physical properties of the material that comprises the interior of our planet, both the high pressure silicate and oxide phases of the Earth's mantle, and the metals found in the core. Many long standing open questions in the study of Earth's interior, and new complex observations, may be linked to limited characterization of Earth materials. For example, lateral differences in elastic properties as observed by seismic tomography may be caused by chemical or thermal differences between such regions, and only careful studies in mineral physics can provide the data that will ultimately help to differentiate between the two causes. Providing such data and integrating them into Earth models is one of the central scientific missions of the Bayerisches Geoinstitut, and advances in experimental and computational studies make it now possible to efficiently explore physical properties in the thermodynamic space of pressure, temperature, and chemistry, that is at the focus of deep Earth structure.

It is mineral physics that did provide the unchallenged interpretation of seismic discontinuities in the Earth's interior by correlating pressures at depths of these reflectors with phase transitions in major mantle minerals. In particular, the discontinuity at 410 km between the upper mantle and the transition zone has been associated with the phase transition of $(\text{Mg, Fe})_2\text{SiO}_4$ olivine to wadsleyite. While this phase transition is very sharp in experiments, recent seismic observations reveal a broad discontinuity at 410 km in some regions, with unknown cause. The transition zone has caught recent attention as a potential major water reservoir in the solid Earth, as water in the form of OH^- groups is more soluble in wadsleyite compared to olivine. The effects of this affinity on transition pressure and sharpness between the two Mg_2SiO_4 polytypes are investigated in the first contribution to this section. In the second contribution, a similar study is performed for ferric iron which also has a stronger affinity to wadsleyite.

While the transition of olivine to wadsleyite leaves a clear elastic signature in the mantle, the transition from wadsleyite to ringwoodite does not provide enough contrast in terms of seismic properties to be visible to global seismology. However, recent advances in seismic inversion yields a puzzling picture of seismic reflectors in the mid transition zone. Some regions show a discontinuity with a varying depth around 520 km. Other regions show no signature at all, while yet different regions reveal complex patterns of double reflectors. As the exsolution of CaSiO_3 perovskite from the garnet component of mantle mineralogy starts at comparable pressures and temperatures to the wadsleyite to ringwoodite transition, this process provides a second possibility for a mid transition zone reflector, explored in the third contribution of this section.

In addition to the discontinuities the boundary layers at the top and bottom of the Earth's mantle are zones of great geophysical interest. These thermal and chemical boundary layers play a crucial role in many geophysical processes, including plate tectonics, subduction, or possible zones for plume origin. At the top, the lithosphere is to some degree decoupled from the underlying convecting mantle by a mechanically weak zone, the asthenosphere. The origin of this weak zone is explored in the fourth contribution of this section by looking at water in mantle rocks, integrating newly obtained data of water solubility in pyroxenes with data in olivine. Similar to the lithosphere on the top, the D'' layer at the base of the mantle shows laterally strongly varying thickness and physical properties, the interpretation of which has puzzled geophysics for decades. The recent discovery of the perovskite to post-perovskite phase transition in MgSiO_3 at lower mantle conditions has added two possible causes for D''. In the fifth contribution in this section the influence of Al_2O_3 on the transition pressure and the sharpness of the phase transition is explored by means of *ab initio* computations.

The final contribution of this section brings us back to the overarching goal to integrate physical properties of minerals into global Earth models. In addition to the inverse problem of interpreting seismic properties revealed by tomography, forward models of the temperature field (geodynamics) and seismic wave propagation, as well as the relation of temperature field in the Earth to physical properties, depend strongly on high quality models of mineral properties. Here, a thermodynamic and physical model of mantle mineralogy is presented that will ultimately be used in forward modelling of geodynamics and seismology.

a. The effect of water on the olivine to wadsleyite transformation (D.J. Frost)

The "410" km mantle seismic discontinuity results from the transformation of $(\text{Mg,Fe})_2\text{SiO}_4$ olivine to wadsleyite. Recent studies of seismic waves that are reflected and converted at the "410" seem to indicate that in some regions of the mantle the "410" can occur over a depth interval of between 20 and 30 km. Simple petrological models indicate, however, that in mantle of typical bulk silicate earth composition the two-phase divariant transformation region between olivine and wadsleyite should be no more than 5 km thick or up to 9 km in regions of rapid adiabatic upwelling. On the other hand, it has been proposed that as H_2O has a stronger affinity for the wadsleyite structure over olivine, relatively small concentrations of H_2O in the mantle will stabilize the wadsleyite polymorph, lower the pressure of the transformation and broaden the transformation interval. If the effect of H_2O on the transformation can be experimentally calibrated it may be possible to draw firm conclusions about the chemical and thermal nature of the mantle on a regional scale from local estimates of the discontinuity width, position and velocity jump.

The H_2O saturated olivine to wadsleyite transformation has been investigated in the Mg_2SiO_4 - H_2O system. By excluding Fe from the system the influence of H_2O can be separated from that of ferric Fe, which is unavoidably present in H_2O saturated Fe-bearing systems at these conditions. Platinum capsules containing forsterite and enstatite with 10 wt.% H_2O were placed inside outer platinum capsules of dry forsterite and ReO_2 to ensure oxidizing conditions. Below this capsule a multichamber Al_2O_3 sample holder with four $(\text{Mg,Fe})_2\text{SiO}_4$

compositions of varying Fe/(Fe+Mg) ratios was placed. These samples are ground with metallic Fe to ensure reducing conditions. Both capsules are run in a large 25 mm edge length multianvil assembly in a 5000 tonne press at conditions of the “410” discontinuity between 1200 and 1600 °C. Temperature differences between the two capsules are less than 50°.

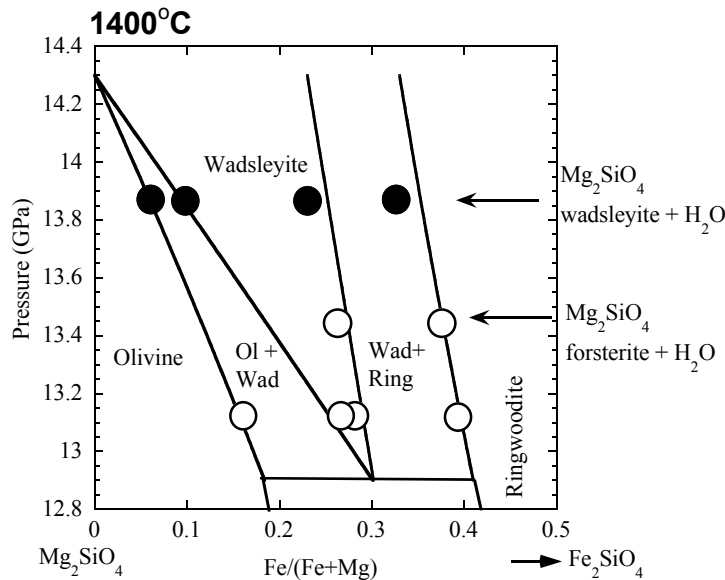


Fig. 3.1-1: Three experimental results from 1400 °C. Coexisting $(\text{Mg,Fe})_2\text{SiO}_4$ compositions from the lower capsule (shown as open and closed circles) are used to determine the pressure in the experiment using the phase relations in the dry Mg_2SiO_4 - Fe_2SiO_4 system. Open symbols indicate conditions where forsterite was observed in the upper H_2O -saturated Pt capsule and closed symbols indicate conditions where H_2O -saturated wadsleyite formed.

Recovered experiments were analyzed to bracket the pressure at which the Mg_2SiO_4 forsterite to wadsleyite transition occurs under water saturated conditions. Pressure is determined using the divariant phase relations from the dry $(\text{Mg,Fe})_2\text{SiO}_4$ samples. The results at 1400°C show the known phase relations in the $(\text{Mg,Fe})_2\text{SiO}_4$ system (Fig. 3.1-1). Three experiments are shown where the pressure is accurately determined using the phase diagram in conjunction with coexisting $(\text{Mg,Fe})_2\text{SiO}_4$ olivine and wadsleyite and wadsleyite and ringwoodite compositions from the lower Al_2O_3 experimental capsule. Filled symbols indicate conditions where the upper Pt capsule contained hydrous wadsleyite and melt, while the open symbols indicate where forsterite and melt were observed. H_2O -saturated Mg_2SiO_4 wadsleyite is therefore stable at a pressure that is approximately 0.5 GPa lower than the dry Mg_2SiO_4 end member. At 1200°C hydrous wadsleyite forms at pressures that are approximately 0.8 GPa lower than in the dry system, while at 1600°C the stabilization is less than 0.5 GPa. These measurements have been combined with a thermodynamic model for the Fe-Mg phase relations to calculate the effect of water on the “410” km discontinuity. To broaden the “410” to over 20 km requires temperatures in the mantle to be below 1400°C and H_2O contents close to olivine saturation. Mantle water contents of less than 300 ppm have negligible influence on the “410”.

b. The effect of ferric iron on the olivine to wadsleyite transformation (D.J. Frost and C.A. McCammon)

It has been proposed that the strong affinity of H₂O for wadsleyite over olivine should broaden the olivine to wadsleyite transformation and lower the pressure at which wadsleyite appears in the Earth's mantle. This has important implications for the "410" km seismic discontinuity that also appears to be broader and shallower in some regions of the mantle. In addition to H₂O, however, ferric iron also readily dissolves in the wadsleyite structure whereas it is almost totally excluded from olivine. Under relatively oxidizing conditions the presence of ferric iron may therefore also expand the stability field of wadsleyite.

Multianvil experiments have been performed to test the effect of varying redox conditions on the olivine to wadsleyite transformation. Two multichamber capsules of Re and Al₂O₃ were employed, each with 4 sample chamber holes of 300 microns diameter. In the Al₂O₃ capsule (Mg,Fe)₂SiO₄ samples were placed with varying Fe/Mg ratios coexisting with 20 wt.% metallic Fe. In the Re capsule similar samples were placed but mixed with Re and ReO₂ as opposed to Fe. Each 0.5 mm long capsule was placed in a multianvil assembly with the junction between the capsules in the hot spot. Samples were run at 1600 °C over the pressure interval of the olivine-wadsleyite divariant loop (Fig. 3.1-2).

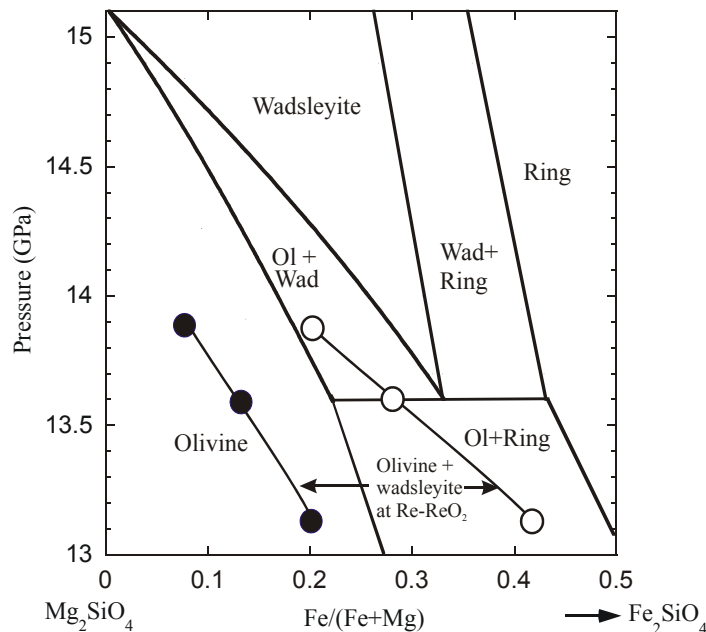


Fig. 3.1-2: The effect of redox state on the (Mg,Fe)₂SiO₄ olivine to wadsleyite transformation at 1600 °C. Phase relations for the olivine-wadsleyite-ringwoodite stability fields are shown determined from experiments performed under reducing conditions in equilibrium with metallic Fe, where ferric iron contents of all phases are minimal. Open and closed symbols indicate coexisting wadsleyite and olivine compositions from experiments performed at the oxidising conditions of the Re-ReO₂ buffer. All iron is plotted as Fe²⁺.

Coexisting olivine and wadsleyite compositions from the oxidised Re-ReO₂ experiments are indicated by the closed and open symbols and can be compared to the phase relations determined under the reducing conditions of metallic Fe saturation. Under oxidising conditions wadsleyite becomes stable at much lower pressures in comparison to the phase relations at more reduced conditions. Under reducing conditions olivine with a Fe/(Fe+Mg) ratio of 0.1 starts to break down to wadsleyite at 14.5 GPa. Under the more oxidising conditions for the same bulk composition wadsleyite appears at a pressure that is approximately 1 GPa lower. Mössbauer measurements indicate that olivine with Fe/(Fe+Mg)=0.1 synthesized in the Re-ReO₂ experiments has a Fe³⁺/ΣFe content that is below detection limits (< 2 %), while wadsleyite with the same Fe/Mg ratio has a Fe³⁺/ΣFe content of 9 % which rises to 13.9 % for Fe/(Fe+Mg)=0.2. Because ferric Fe will strongly partition into wadsleyite as it first forms, even low Fe³⁺/ΣFe ratios that seem to be typical for the upper mantle (< 3 %) will likely have a measurable effect on the “410”. In oxidized regions of the mantle the “410” km discontinuity would be shallower by up to 20 km and may be significantly broadened. These results also have consequences for previous experimental studies where the redox state of the samples was not controlled.

c. The formation of calcium perovskite from majorite garnet: Implications for splitting of the 520 km seismic discontinuity (A. Saikia, D.J. Frost, D.C. Rubie)

A weak seismic velocity discontinuity has been observed in a number of global seismic studies from a depth of 520 km in the transition zone of the mantle. In some regions of the mantle, however, this discontinuity seems to be split into two discontinuities. The wadsleyite to ringwoodite transition at this depth is often implicated as the cause of this discontinuity. However, the exsolution of calcium perovskite from majorite garnet that also occurs at a similar depth in the transition zone could cause the observed split in the 520 km discontinuity. A major question, however, is whether this reaction occurs over a narrow enough pressure interval to cause an observable discontinuity.

We have performed high pressure and temperature experiments in order to investigate whether the CaSiO₃ perovskite forming reaction can cause a mid transition zone discontinuity. Four calcium free majorite-pyrope garnet glass compositions were presynthesised with varying Al/Si contents in order to study garnet compositions that are relevant to a range of potential mantle bulk compositions. These starting garnet glasses were mixed with calcium silicate wollastonite (CaSiO₃) and equilibrated in multianvil experiments in the pressure and temperature range of 17-24 GPa and 1200-1600 °C. During the experiments CaSiO₃ perovskite and majorite garnet crystallize rapidly from the starting compositions and CaSiO₃ dissolves into the garnet until saturation is reached. We measured the CaO solubility in the different majorite garnets as a function of pressure and temperature. Reversal experiments were also performed to check the equilibrium in the experiments using presynthesised Ca bearing majorite garnet, which exsolves CaSiO₃ during the experimental run. Reaction kinetics are sluggish, so a boron oxide (B₂O₃) flux was employed to promote equilibrium in the experiments. Re multi capsules with 4 sample chambers were employed so that several

compositions with varying majorite contents could be run in the same experiment. Olivine compositions with varying Mg/(Mg+Fe) are included in each experimental run in one of the 4 chambers. From the Fe/(Fe+Mg) ratio of coexisting phases (*i.e.*, ringwoodite, wadsleyite or magnesiowüstite) the pressure can be accurately calculated for each run from the previously constrained phase relations in this system.

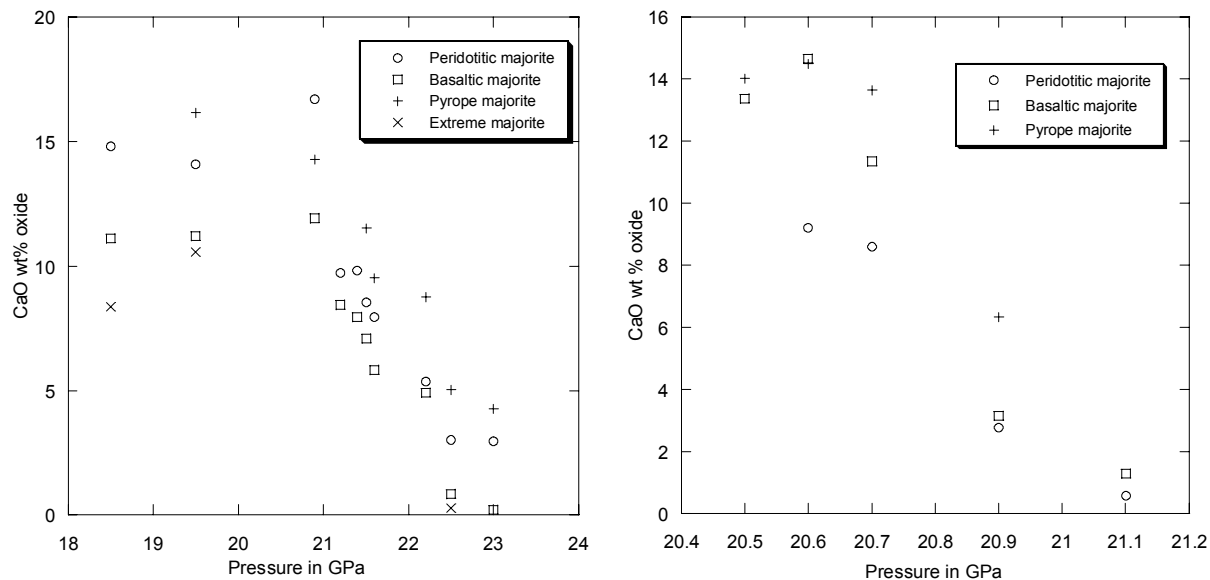


Fig. 3.1-3: Pressure dependence of CaO solubility in majorite garnet at 1600 °C (left) and 1400 °C (right).

The samples recovered from the experiment are analyzed using the electron probe and micro-Raman spectroscopy. Results show that the CaO solubility in the majorite garnet decreases with increasing majorite component, *i.e.*, Al/(Mg+Si) at a constant pressure and temperature (Fig. 3.1-3). This implies that garnet CaO saturation, or the initiation of CaSiO₃ perovskite exsolution, will occur at higher pressures for garnets with a smaller majorite component at transition zone pressure-temperature conditions. For a peridotite garnet composition with about 8 wt.% CaO, the reaction of majorite garnet to form calcium perovskite is accomplished within a pressure interval of 1 GPa, which corresponds to a coexistence width of ~ 30 km. This is a similar depth interval to the wadsleyite-ringwoodite transformation and is sharp enough for the reflection of seismic waves.

Elasticity studies imply that the changes in P and S wave velocity across the wadsleyite to ringwoodite transition are comparable to the change expected as majorite garnet exsolves calcium perovskite. Consequently, both these reactions should be capable of producing a detectable seismic discontinuity at 520 km depth. Variation in mantle temperature cannot account for the observed split in this discontinuity, as there is no realistic pressure-temperature condition where these two reactions converge at the same depth in the transition zone (Fig. 3.1-4).

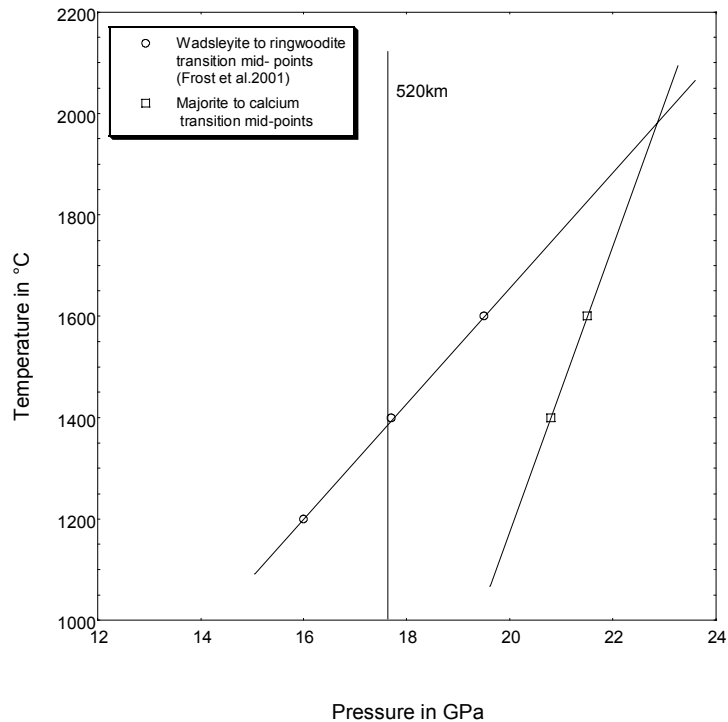


Fig. 3.1-4: Comparison of the transition pressure for wadsleyite-ringwoodite (diamonds) and majorite-CaSiO₃ perovskite (squares) as a function of mantle temperature with line fits to guide the eye. The solid line indicates the pressure at the depth of the 520 km discontinuity based on the seismic PREM model.

A plausible explanation is that a single discontinuity is observed arising from the wadsleyite to ringwoodite transition at 520 km depth in mantle regions that are relatively depleted in CaO. Such depletions would occur in mantle that has undergone melt extraction at mid oceanic ridge settings, leaving the residual mantle depleted in calcium, *e.g.*, relatively refractory harzburgite composition. But for fertile mantle peridotite two discontinuities would occur at mid-transition zone depth for the two transitions, wadsleyite to ringwoodite and majorite exsolving calcium perovskite. The splitting of the 520 km discontinuity may therefore be an indicator of the varying fertility of the mantle and implies that the mantle is heterogeneous on a regional scale in terms of basalt forming components.

d. *The origin of the Earth's asthenosphere (K. Mierdel/Tübingen, in collaboration with H. Keppler, J.R. Smyth/Boulder and F. Langenhorst/Jena)*

Plate tectonics implies that rigid plates of the lithosphere are able to slide over a mechanically weak asthenosphere in the upper mantle. Since the asthenosphere coincides with a zone of low seismic velocities, it has often been suggested that the weakness of the asthenosphere may be related to the presence of a small fraction of melt. However, the mechanism that may cause melting in the asthenosphere is not well understood.

Water is known to strongly affect melting in the mantle and most of the water in the mantle is probably locked up in nominally anhydrous minerals such as olivine or pyroxenes. While the water solubility in olivine is relatively well studied and is known to increase continuously with pressure and temperature, there are only limited data on water solubility in aluminous orthopyroxene, the second most abundant mineral in the mantle. Therefore, we investigated the solubility of water in enstatite saturated in aluminium, *i.e.*, coexisting either with $MgAl_2O_4$ spinel or with $Mg_3Al_2(SiO_4)_3$ pyrope. Experiments were carried out in a piston cylinder apparatus at pressures between 1.5 and 3.5 GPa and temperatures between 800 and 1100 °C. Water contents were determined by measuring polarized infrared spectra of clear and inclusion free crystals (Fig. 3.1-5).

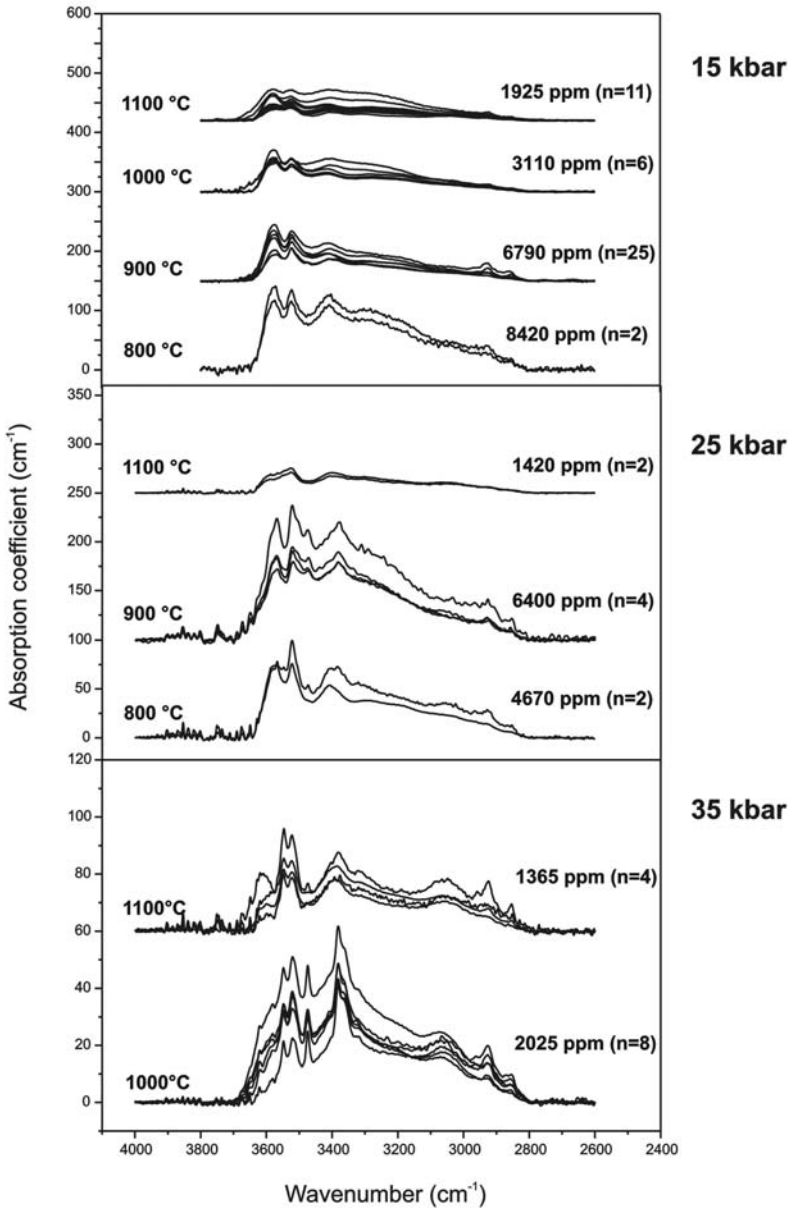


Fig. 3.1-5: Polarized FTIR spectra (polarized parallel to c) and bulk water contents of Al-saturated enstatite synthesized between 1.5 and 3.5 GPa and 800-1100 °C.

Water solubility in aluminous orthopyroxene is strikingly high, reaching values close to 1 wt.% at 1.5 GPa and 800 °C (Fig. 3.1-5). TEM studies confirmed that these high water contents are indeed due to chemically dissolved water in the pyroxene lattice; no evidence for guest phases or planar or linear defects hosting the water was found. Interestingly, water solubility in aluminous orthopyroxene was found to rapidly decrease both with temperature and with pressure, in striking contrast to olivine.

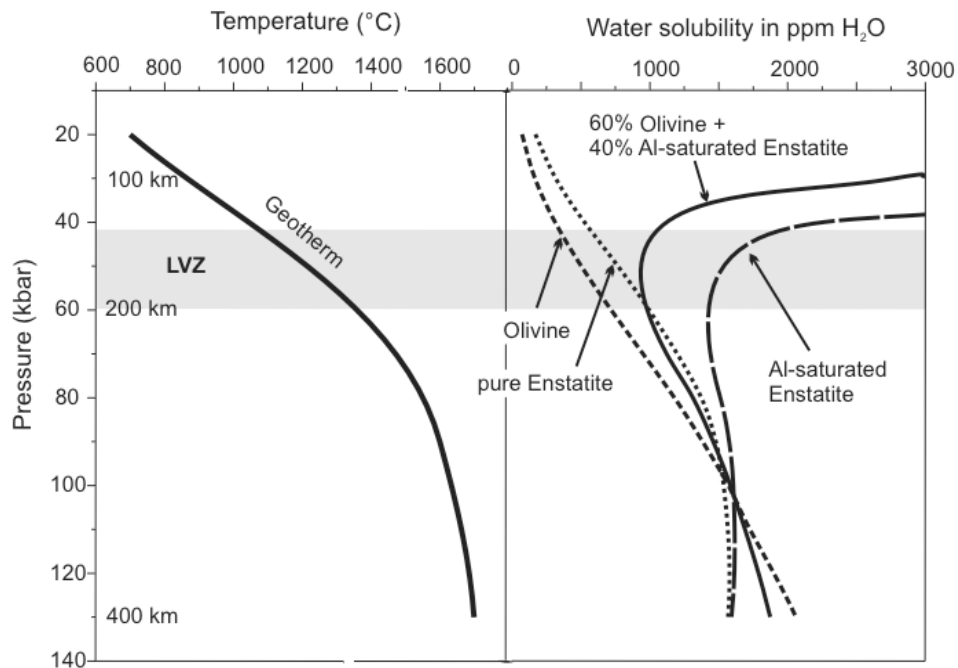


Fig. 3.1-6: Water solubility (in ppm by weight) in upper mantle minerals as a function of depth for a continental shield geotherm. The low-velocity zone (LVZ) is shaded in gray.

Figure 3.1-6 shows the calculated water storage capacity of a model mantle consisting of 60 % olivine and 40 % aluminous orthopyroxene. The water storage capacity has a pronounced minimum right at the depth of the seismic low velocity zone. This implies that at the depth of the minimum and at a bulk mantle water content of about 1000 ppm, solid mantle minerals would coexist with a free hydrous fluid with a water activity of 1. However, at the respective depth, mantle temperatures are already above the hydrous peridotite solidus. Accordingly, not a free hydrous fluid, but a hydrous silicate melt will form. In this phase, water activity is reduced to values of about 0.1-0.3. At these reduced water activities, the equilibrium water content in the minerals of the mantle would be reduced to a few hundred ppm, comparable to estimates of bulk mantle water contents. Accordingly, the data suggest that melting in the asthenosphere is directly related to a minimum in water solubility in nominally anhydrous minerals (Fig. 3.1-6), with the excess water available forming a partial melt. As water solubility in minerals increases both above and below the minimum, water increasingly partitions into the minerals and the melt solidifies. The sharp increase in water solubility at

shallow depths is consistent with the observed sharp seismic discontinuity on top of the asthenosphere. Similarly, the gradual increase in water solubility below the asthenosphere correlates well with the diffuse nature of the lower boundary of the seismic low velocity zone.

e. Effect of Al on the sharpness of the MgSiO₃ perovskite to post-perovskite transition (S. Akber-Knutson/San Diego, G. Steinle-Neumann and P.D. Asimow/Pasadena)

At the base of the Earth's mantle lies a distinct layer a few hundred kilometers thick. Known as D'', it serves as a thermal and chemical boundary between silicate mantle rock and molten iron alloy outer core. It exhibits large lateral heterogeneity in seismic properties, including sharp discontinuities in density and shear wave in some places, and low velocity zones in others, as well as shear wave splitting. Such features potentially provide valuable constraints on the nature of D'' and may be attributed to core-mantle reactions, subduction debris, a phase change in mantle minerals, or a combination of the above.

The discovery of MgSiO₃ post-perovskite, stable at lowermost mantle conditions, has led to numerous efforts to integrate this phase into the current view of D''. Work has focused largely on pure MgSiO₃, for which the univariant transition is sharp; realistic mantle compositions should involve partitioning of other elements, such as Al and Fe, between the two phases, and affect phase equilibria. In particular, the transition would not occur univariantly in the system, and chemical heterogeneity would yield to coexistence of perovskite and post-perovskite. This divariant phase loop may have a strong influence on geophysical interpretation and a thorough investigation is warranted.

Here we conduct static, 0 Kelvin first-principles calculations to explore the effects of Al₂O₃ incorporation on the perovskite to post-perovskite transition. Internal energies are computed from first-principles calculations based on density functional theory, using fixed volume cell optimizations with respect to cell shape, atomic positions, and electronic wave functions. We test the method by computing equations of state for relevant pure MgSiO₃ and Al₂O₃ polymorphs and find good agreement with previously published ab-initio results. Equations of state are obtained from fitting internal energy versus volume curves to the third-order Birch-Murnaghan equation of state. From this we have static Helmholtz free energy and volume as functions of pressure. Thus we may calculate the static Gibbs free energy and relative stabilities of the phases.

We consider several types of Al incorporation mechanisms into MgSiO₃: MgSi → AlAl (charge coupled mechanism: CCM), SiSiO → AlAl□ (oxygen vacancy forming substitution: OVM), and Si → AlH (hydrous Al substitution: AlHM). In each case, an 80-atom cell is used. For CCM, we calculate equations of state and static enthalpies for Al₂O₃ concentrations of 6.25 and 100 mol.%, whereas for OVM, only the case for 6.25 mol.% is included. For AlHM, one Si is substituted, resulting in an Al₂O₃ concentration of 3.125 mol.%. Enthalpies

of solution for Al incorporation into perovskite and post-perovskite structures indicate that oxygen vacancy substitution is highly unfavorable in both phases. In the anhydrous case, one need only consider charge coupled substitution. From the CCM enthalpies of solution it is apparent that at a fixed concentration of 6.25 mol.%, Al_2O_3 is more soluble in perovskite than in post-perovskite. Thus Al stabilizes perovskite with respect to post-perovskite and increases the transition pressure. In particular, CCM, at 6.25 and 100 mol.% Al_2O_3 , increases the transition pressure to 112 and 113 GPa, respectively.

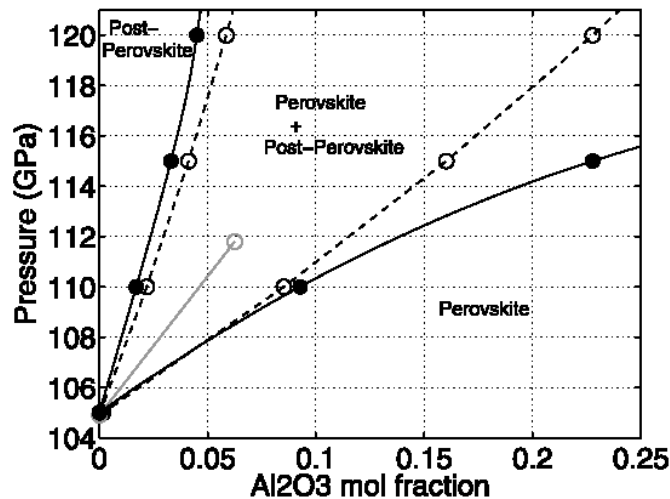


Fig. 3.1-7: Phase diagram of Al containing MgSiO_3 for the CCM substitution. The dashed curves are derived from Henry's law; whereas the solid black curves are from regular solution theory. The grey curve corresponds to the pseudo-univariant phase transition. A temperature of 2500 K was assumed.

Calculations are carried out with equal Al concentrations in the two phases; we call an equilibrium pressure determined by this means "pseudo-univariant". However, the endmember equilibria in pure MgSiO_3 and Al_2O_3 and one pair of such calculations for Al-bearing perovskite and post-perovskite at equal concentration are sufficient to determine the divariant phase loop of Al-bearing MgSiO_3 , if a reasonable model about the form of the solution is made. We examine two such models for both phases: Henry's Law for dilute Al_2O_3 concentrations, and symmetric regular solutions for the whole binary. For CCM we find that with even a small amount of Al_2O_3 , MgSiO_3 perovskite and post-perovskite coexist over a large range in pressure (~ 109 - 122 GPa at 0 K) (Fig. 3.1-7). Assuming that the Clapeyron slope for pure MgSiO_3 applies to the whole phase loop, the pressure range at 2500 K becomes ~ 127 - 140 GPa. If we limit the upper pressure to that of the core-mantle boundary (136 GPa), then the phase coexistence region spans a depth range of ~ 2740 - 2890 km. However, the mole fractions of the two coexisting phases vary nonlinearly with pressure, with most of the change occurring at the lower pressures, which in turn may reduce the apparent phase transition width for seismic observations. A forward modelling of seismic wave propagation shows that even with the broad coexistence region we predict here, a discontinuity in shear wave velocity is still present.

There are additional issues to consider regarding the phase transition width. Increasing the lower mantle temperature decreases the width of the phase loop, but increases the transition depth. In addition, our calculations do not account for the effects of Fe in any oxidation or spin state. While it seems unlikely that adding more components and increasing the variance of the coexistence region would narrow the transition, this needs to be tested.

f. Mantle mineral model for geodynamics simulations (A.S. Piazzoni/München, G. Steinle-Neumann and D. Dolejš)

Over the past two decades geophysical studies of deep Earth structure have become increasingly sophisticated and now provide considerable insight into the physical state of our planet. On the one hand, geodynamics helps us understand mantle processes by modelling mantle convection; on the other hand, seismic tomography yields a picture of ever increasing resolution of mantle structure in terms of acoustic wave velocity. Obviously, the temperature field obtained from geodynamics and the physical properties observed in seismology are related through material properties of mantle minerals. This connection has not yet been fully explored, and interpretation of seismic data is hampered by the tradeoffs between thermal and chemical effects on material properties. As density differences are the driving force for mass transport in the mantle through the Navier-Stokes equation, a coupling of realistic density fields with a geodynamic model is highly desirable to obtain a self-consistent picture of mantle structure.

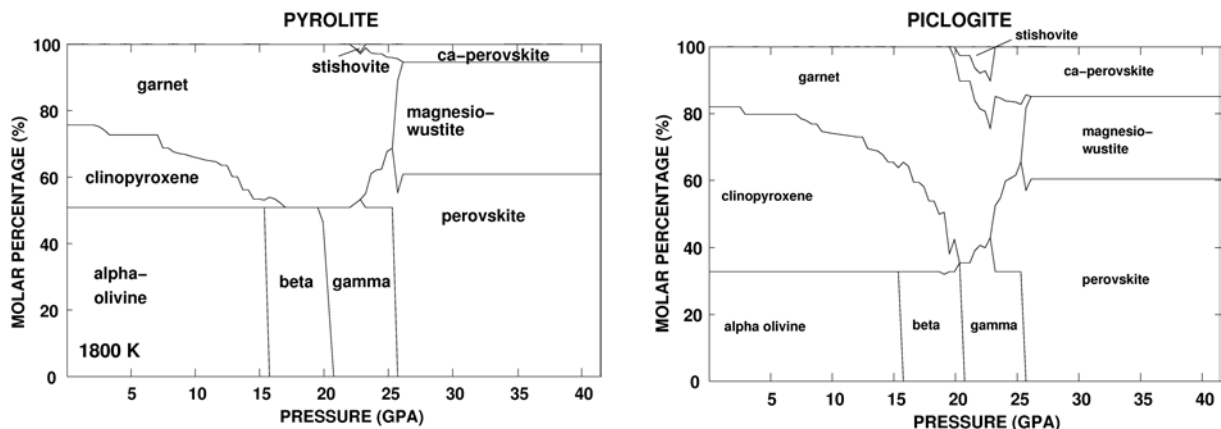


Fig. 3.1-8: Mantle mineralogy for a pyrolite (left) and piclogite (right) model of mantle composition along a 1800 K isotherm. Molar percentages of the phases in the $ASiO_3$ and A_2SiO_4 based minerals in the upper mantle, and the $ASiO_3$ and AO systems in the lower mantle are indicated (A being any cation).

Advances in high-pressure mineralogy make it now possible to build a self-consistent model of mineral phases of the mantle. Such a model can be based on laboratory experiments of the thermal equations of state, measurements of phase equilibria, and calorimetric data. With such data for mantle relevant minerals one can in principle obtain the stable phase assemblage, and

hence the physical properties at a given point of pressure-temperature-composition (P-T-X) by minimizing the Gibbs free energy of the system. Here we have built a thermodynamic model of the CMASF system (CaO-MgO-Al₂O₃-SiO₂-FeO) including phases that occur close to a pyrolite chemical model of the mantle at reasonable mantle temperatures. In this system we perform Gibbs free energy minimization, including pure end-member phases and a non-ideal formulation for solid solutions where excess properties are treated by asymmetric Redlich-Kister polynomials. Solid solutions were subdivided into discrete pseudo-compounds with 1 mol.% spacing and treated as pseudo-endmembers during computation of chemical equilibrium by the simplex method. In addition to density and compressibility, we have included shear elastic properties in our model that only recently have become available by applying a finite strain theory to a compilation of experimental and computational elastic properties. From the minimization we obtain the stable mineral assemblage, and using a Voigt-Reuss-Hill averaging scheme the associated density, compressibility, and shear modulus. Figure 3.1-8 shows the stable phase assemblage for both a pyrolitic and piclogitic composition along a 1800 K isotherm for pressures of the Earth's mantle.

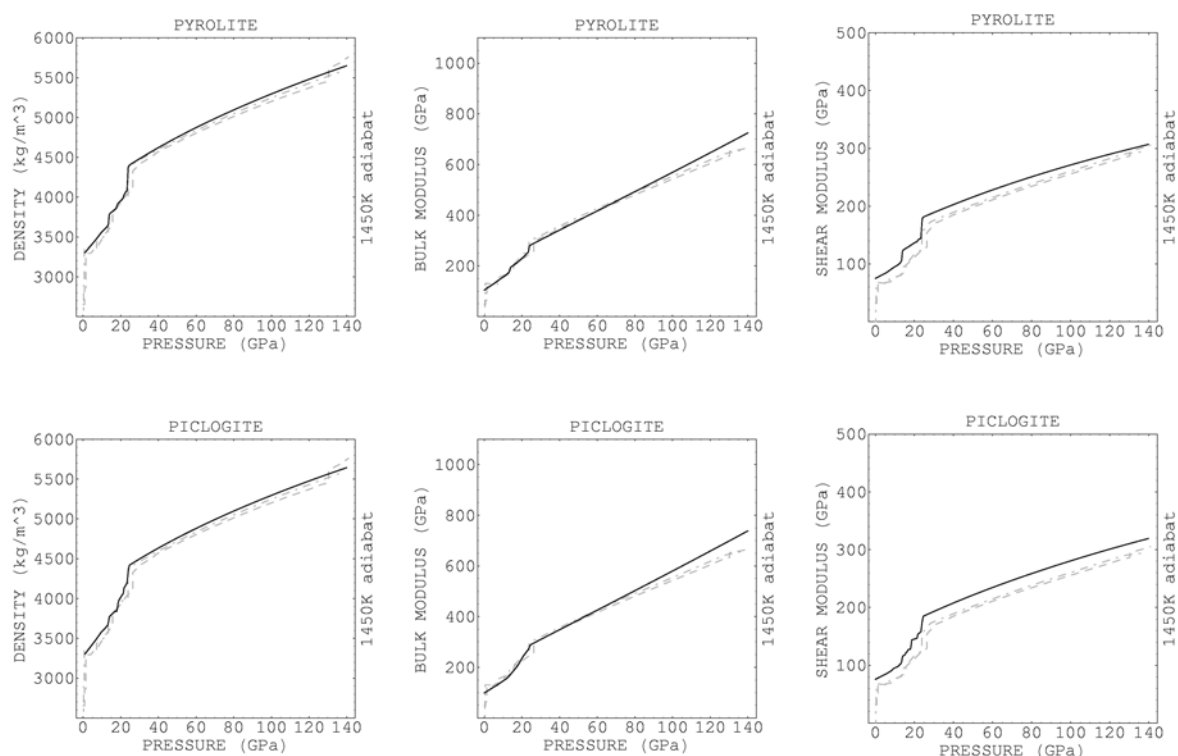


Fig. 3.1-9: Density (left), bulk (middle), and shear modulus (right) from two mantle mineralogy models along a 1450 K isotherm (solid lines). The upper and lower panels show results for pyrolite and piclogite mantle models, respectively. For comparison seismic models PREM (dashed lines) and AK135 (dashed-dotted lines) are shown.

3.2 Geochemistry

A major goal of geochemistry is to understand and predict how elements are fractionated during the separation of geochemical reservoirs. The factors of interest in a fractionation event are the bulk composition, the compositions of the two or more ensuing reservoirs and the conditions at which the fractionation event took place. In most instances when we study the Earth one or more of these factors is poorly understood. Through experimental studies of fractionation events, however, it is often possible to establish the physical conditions at which such processes took place and to place constraints on unknown compositional factors. The projects in this section have all been performed to investigate some aspect of fractionation processes and help us to understand the formation and composition of the Earth's geochemical reservoirs.

It is often assumed that the material that formed the Earth had a close genetic relationship with chondritic meteorites, but no meteorite seems to be a perfect chemical or isotopic match for the Earth. Fractionation events appear to have occurred in the solar nebular and subsequent accretionary disk prior to planetary formation. These events led to chemical and isotopic variations between meteorite types and ultimately between planets. By trying to understand when and how such fractionation processes took place, we may be able to place tighter constraints on the material from which the Earth formed.

One of the major fractionation events in Earth's history was the segregation of the Earth's metallic Fe-rich core from its silicate mantle. In this instance we know the composition of one of the ensuing reservoirs relatively well, *i.e.*, the mantle, and we know that the bulk composition of the Earth is probably similar to some chondritic meteorites. We have relatively little information on the composition of the core, however, other than it is FeNi-rich with approximately 10 % of a light alloying element or elements. The conditions at which core mantle segregation took place are also unknown but could potentially span a wide range of temperature, pressure and oxygen fugacity. Through high pressure and temperature experiments on the partitioning of elements between silicate materials and core forming liquids we can start to constrain the conditions at which core formation took place and elucidate the core's composition.

Fluids leaving subducting slabs in the mantle at convergent plate boundaries take part in another fractionation event, which results in the formation of new continental crust from the mantle at island arcs. Here the fractionation is more complicated because the crust-forming magmas are a mixture of components from two mantle sources, *i.e.*, the slab itself and the overlying mantle wedge. Understanding how elements are fractionated during subduction zone processes is crucial for understanding the geochemical exchange that takes place beneath island arcs and for identifying the composition of the subducting slab, which ultimately forms a distinct geochemical reservoir within the Earth's mantle.

a. *Early evolution of oxygen isotopes in the protosolar nebula (J. Aléon/Vandoeuvre-les-Nancy, in collaboration with A. El Goresy and E. Zinner/St. Louis)*

Refractory inclusions rich in calcium and aluminium (CAIs), were presumably the first solids formed in the solar system and are the most ^{16}O -rich materials in meteorites. CAIs probably preserve the composition of the initial solar gas enriched in ^{16}O , while chondrules and planetary materials formed in a late, evolved gaseous reservoir depleted in ^{16}O . However, the exact mechanisms and the timing of the event leading to the ^{16}O -depletion are still debated. Igneous inclusions from CV3 carbonaceous chondrites show a dichotomy in the oxygen isotopic composition of their minerals. While spinel and Al- (Ti)-rich clinopyroxene are usually ^{16}O -rich, anorthite and melilite are commonly ^{16}O -poor. Deciphering the origin of this dichotomy is essential to unravelling the evolution of the oxygen isotopic composition in the early solar system.

We conducted a systematic study of oxygen isotopic composition of E49, a compact and composite type A CAI from the reduced CV3 chondrite Efremovka. A previous study has revealed the presence of an enclosed xenolith characterized by mineralogy and trace element patterns different from those of the host CAI. Petrography indicates that the xenolith was injected in the host melt prior to condensation of the outer rim layers of the host. The host inclusion is a fragment of an initially round CAI, probably ~ 4 mm in diameter. It is dominated by melilite with variable Mg content. The host inclusion exhibits a rim sequence consisting, from the inside to the outside, of monomineralic layers of perovskite, spinel, melilite ($\sim \text{Åk}_{20}$) and Al-rich clinopyroxene. The xenolith is dominantly composed of fractured coarse-grained spinel (\pm perovskite) surrounded by convoluted pyroxene ranging in composition from diopside with little Al to very Ti-rich fassaite and associated andradite \pm wollastonite. Textures and mineralogy indicate that the xenolith experienced partial melting upon injection into an extensively molten host. Oxygen isotopes were measured of spinel, pyroxene, anorthite and melilite from the host inclusion and the xenolith. Isotopic ratios are reported as per mil deviations from Standard Mean Ocean Water ($\delta^{\text{X}}\text{O} = [^{\text{X}}\text{O}/^{16}\text{O}_{\text{sample}} - ^{\text{X}}\text{O}/^{16}\text{O}_{\text{SMOW}}] / [^{\text{X}}\text{O}/^{16}\text{O}_{\text{SMOW}}] \times 1000$). ^{16}O excesses are reported as ^{17}O deviations from the terrestrial mass fractionation line ($\Delta^{17}\text{O} = \delta^{17}\text{O} - 0.52 \times \delta^{18}\text{O}$). All errors are 2σ .

Spinel and pyroxene from both inclusions and from the rim are systematically enriched in ^{16}O by 4 to 5 % (Fig. 3.2-1a). Melilite in the xenolith is enriched in ^{16}O to varying degrees (Fig. 3.2-1a); it is moderately ^{16}O -rich in the rim ($\Delta^{17}\text{O} = -12.0 \pm 2.7$ ‰, Fig. 3.2-1b). In contrast, oxygen isotopic ratios in the host melilite span the whole range of previously reported compositions (Fig. 3.2-1b). These variations are correlated with the location within the inclusion (Fig. 3.2-2a). Immediately below the host rim, melilite is ^{16}O -rich, but the ^{16}O -excess decreases towards the centre of the inclusion and reaches its lowest values 300 μm inwards from the rim (Fig. 3.2-2a). The O isotopic compositions are correlated with the Åk content of the melilite (Fig. 3.2-2b): ^{16}O -rich melilite below the host rim is nearly pure gehlenite (down to Åk₁) and ^{16}O -poor melilite is typically Åk₂₀₋₃₀. Oxygen isotope variations were thus probably acquired during the crystallization of the inclusion from the outside

inwards. Chemical zonation of melilite is also indicative of fractional crystallization from a melt commencing at the rim.

The oxygen isotopic zoning observed in E49 thus reflects the change of oxygen isotopic composition of the gas during fractional crystallization of the host inclusion. However, 5 to 200 hours seems too short to allow the oxygen isotopic composition of an entire nebular region to change by 5 ‰. It is thus likely that the CAI crystallization occurred during transport between two isotopically different nebular regions. If the Sun was initially ^{16}O -rich, this suggests that, at the time E49 was formed, the ^{16}O -rich reservoir was restricted to regions close to the proto-Sun and a ^{16}O -poor planetary oxygen gas reservoir already existed at planetary distances. The initial $^{26}\text{Al}/^{27}\text{Al}$ determined from the measurements of melilite is $4.1 \pm 0.6 \times 10^{-5}$, which corresponds to an age of 5×10^5 years assuming that ^{26}Al was homogeneously distributed in the early solar system and that the initial ratio in the Solar System was 7×10^{-5} . This age implies that as early as 5×10^5 years both ^{16}O -rich and ^{16}O -poor regions existed in the protosolar nebula. Taken all together, these results suggest that CAIs, chondrules and early planetesimals were coexisting before our Solar System was 1 Myr old.

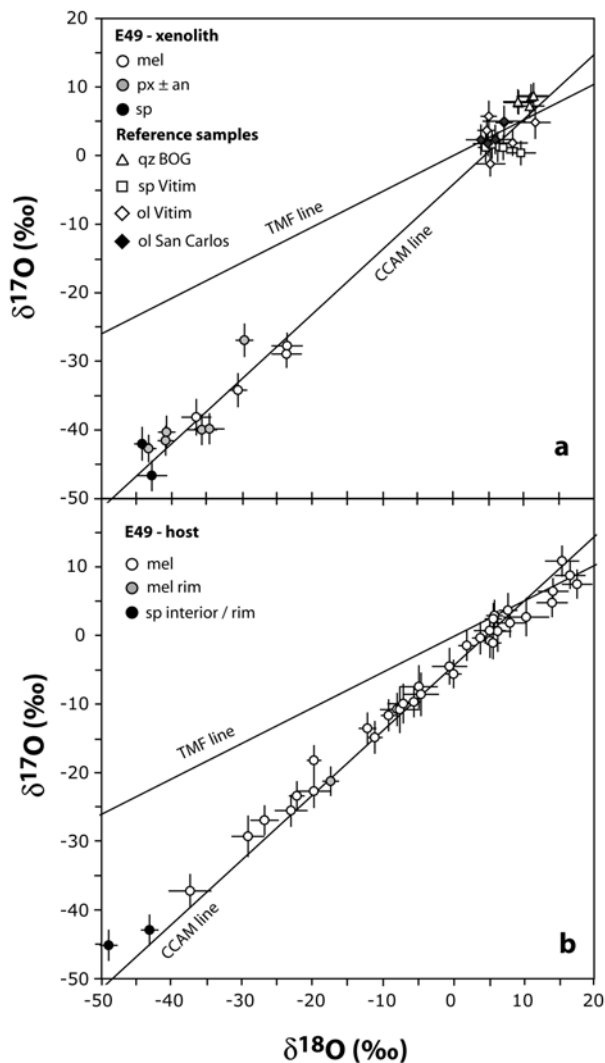


Fig. 3.2-1: Oxygen isotopic compositions in E49. All error bars are 2σ and take into account analytical error and uncertainty in instrumental mass fractionation. TMF stands for Terrestrial Mass Fractionation and CCAM for Carbonaceous Chondrite Anhydrous Minerals. **a.** Oxygen isotopic compositions of minerals in the xenolith and of reference samples used as standards. **b.** Oxygen isotopic compositions of melilite and spinel in the host and the rim.

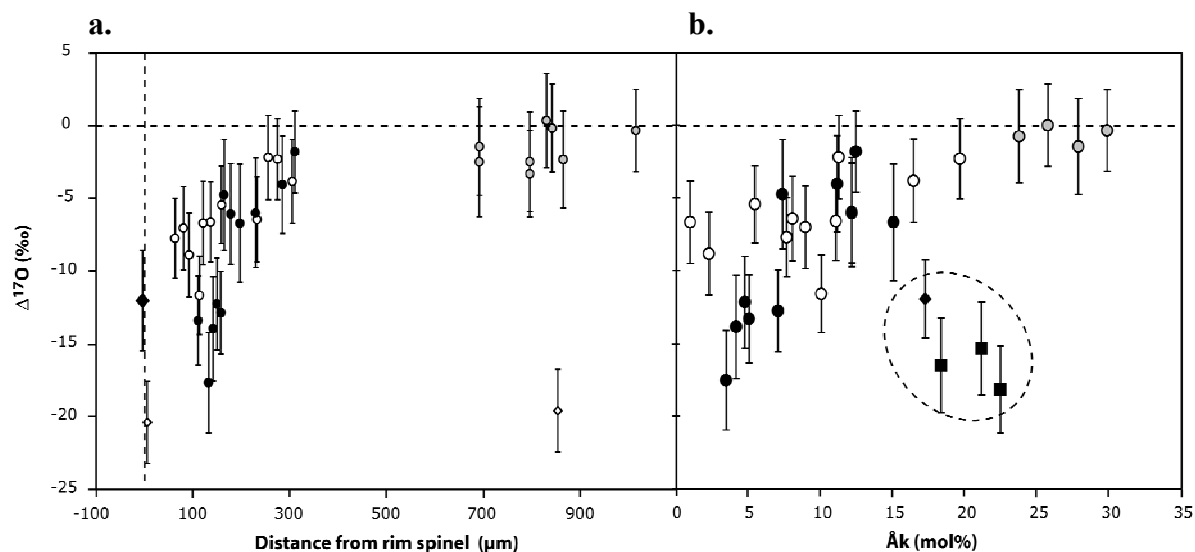


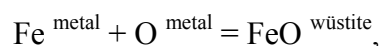
Fig. 3.2-2: Oxygen isotopic deviations from the terrestrial mass fractionation line in melilite and spinel. Error bars are 2σ . **a.** $\Delta^{17}\text{O}$ as a function of distance to the rim. **b.** $\Delta^{17}\text{O}$ of melilite as a function of Åk content. Melilite from the rim and the xenolith are grouped in the encircled area.

b. *Oxygen partitioning between magnesiowüstite and liquid Fe-rich metal at high pressure and high temperature (Y. Asahara, D.J. Frost, D.C. Rubie and F. Langenhorst/Jena)*

Oxygen is a strong candidate for the light-alloying element (or elements) in the Earth's core. The pressure effect on oxygen solubility in metallic iron is controversial. From phase relations in the Fe-FeO system, it has been suggested that oxygen solubility in liquid iron increases with increasing pressure. However, from partitioning studies between magnesiowüstite and liquid metal, it has been proposed that oxygen solubility in liquid iron decreases with increasing pressure. Here we report new data on oxygen partitioning between magnesiowüstite and liquid iron in the Fe-FeO-MgO system over a wide pressure and temperature range (3-25 GPa and 2273-3173 K), performed with the aim of resolving this inconsistency.

High pressure and temperature experiments were performed using a Kawai-type multianvil apparatus. The starting materials were mixtures of Fe metal powder and Fe_2O_3 oxide powder with various bulk oxygen contents. We used MgO single crystals as sample containers. Temperatures were monitored with a W3%Re-W25%Re thermocouple in experiments below 2400 °C, and above 2400 °C temperature was estimated using a temperature-power relation. Chemical analysis and imaging analysis of the recovered samples were conducted with an electron microprobe and a scanning electron microscope.

If we consider the reaction between metal and magnesiowüstite as:



then the distribution coefficient, Kd , of the reaction is expressed as:

$$K_d = X_{\text{O}}^{\text{met}} X_{\text{Fe}}^{\text{met}} / X_{\text{FeO}}^{\text{mw}},$$

where $X_{\text{O}}^{\text{met}}$, $X_{\text{Fe}}^{\text{met}}$, $X_{\text{FeO}}^{\text{mw}}$ are the mol fractions of oxygen in metal, Fe in metal and FeO in magnesiowüstite, respectively. Our experiments show that $\ln Kd$ increases with increasing temperature over the range of experimental conditions examined (Fig. 3.2-3), and $\ln Kd$ has an almost linear relationship with $1/T$ at 15-24.5 GPa and 2273-3173 K. We observe, however, that $\ln Kd$ decreases with increasing pressure up to approximately 10 GPa, but reaches a minimum between 10-15 GPa. This means that the volume change of the reaction (ΔV) is strongly pressure dependent, being negative at pressure below 10 GPa but becoming positive at higher pressures. This can be easily explained by a difference in the compressibility between the FeO components of magnesiowüstite and liquid Fe.

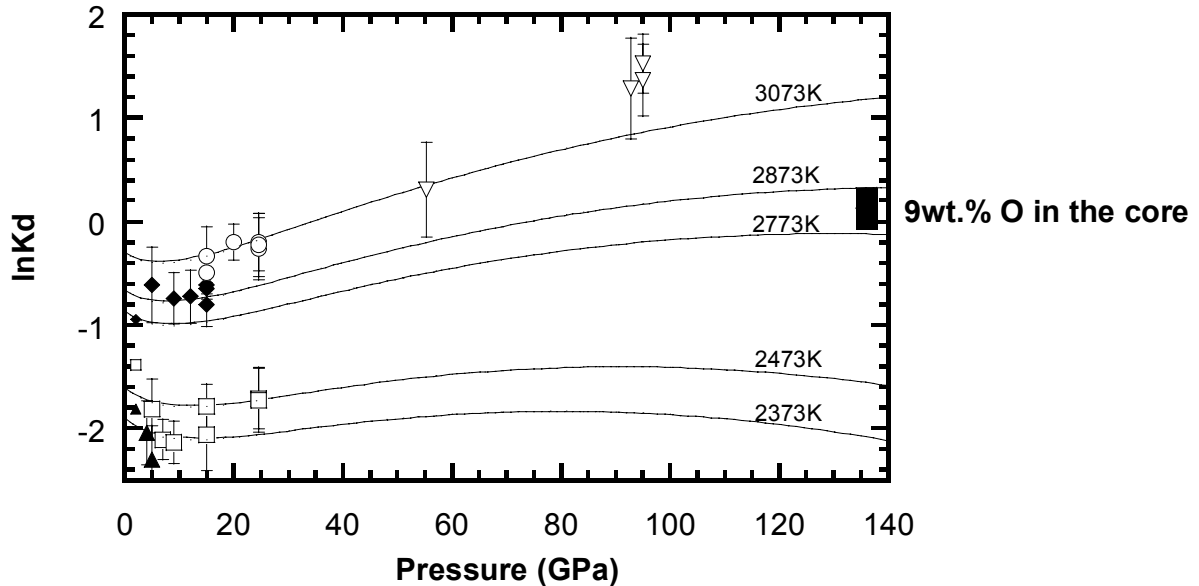


Fig. 3.2-3: The relationship between $\ln Kd$ and pressure up to 140 GPa. The data from this study are plotted at various temperatures as filled triangles, 2373 K; open squares, 2473 K; filled diamonds, 2873 K; and open circles, 3073 K. The data of Ohtani and Ringwood (EPSL, 71, 85, 1984) are also shown as a small filled triangle, 2373 K. Open triangles are the calculated Kd using the data from Takafuji *et al.* (GRL, 32, 6313, 2005) and the partitioning coefficient of Fe between magnesiowüstite and Mg-perovskite reported by Kesson *et al.* (PEPI, 131, 295, 2002). The solid curves show the fit of the equation described in the text at various temperatures. The solid rectangular symbol shows the hypothetical Kd for the core with 9wt.% oxygen in equilibrium with mantle magnesiowüstite with $X_{\text{FeO}}^{\text{mw}} = 0.15-0.18$.

We have examined the present experimental data and higher pressure partitioning data reported by Takafuji *et al.* (GRL, 32, 6313, 2005) by applying the following equation:

$RT \ln K_d = -\Delta H + T\Delta S - \int \Delta V dP$, where ΔH , ΔS and ΔV are the changes in enthalpy, entropy and volume, respectively, for the oxygen exchange reaction and R is the gas constant. Activity coefficients of oxygen in metal, Fe in metal and FeO in magnesiowüstite are assumed to be unity. $\Delta H_{0,2000K} = 1.66 (\pm 0.07) * 10^5$ J/mol and $\Delta S = 52 (\pm 2)$ J/K/mol are obtained by the fit.

Our new partitioning data provide a solution to the previous arguments over the pressure effect on oxygen solubility between Fe-FeO phase relation studies and Fe-FeO-MgO partitioning studies. Oxygen solubility in metallic Fe decreases with increasing pressure at lower pressure conditions, but increases with increasing pressure above about 15 GPa as observed in studies of phase relations. The previous partitioning studies with multianvil apparatus overlooked the ΔV change because of the limited set of pressures examined. The present results suggest that the metallic liquid could contain 1 - 10 wt.% oxygen in a deep terrestrial magma ocean during core formation. As temperatures at the core-mantle boundary are in excess of 3500 K, there is a possibility that the core may even be under-saturated with respect to oxygen. Oxygen may very well be the light element in the core.

c. Beating the miscibility barrier between iron group elements and magnesium by high-pressure alloying (L.S. Dubrovinsky, N.A. Dubrovinskaia and I.Yu. Kantor, in collaboration with W.A. Crichton/Grenoble, L. Vitos and R. Ahuja/Uppsala, and I.A. Abrikosov/Linköping)

Studies of the combined effect of alloying and compression on the phase stabilities and properties of materials attract increasing interest in the geophysical community, and are also important for other research fields, including materials science and physics. In particular, they are of direct relevance for the description of the composition of the Earth's core. Indeed, the chemical composition of the Earth's outer core is a geochemical parameter that is crucial for understanding the evolution and current dynamics of our planet. Since it was recognized that the liquid metallic outer core is about 10 % less dense than pure iron, different elements lighter than iron, including Si, S, O, C, and H, have been proposed as major or at least significantly abundant in Earth's core. However, a combination of experimental results with theoretical and geochemical considerations shows that it is unlikely that any one of these elements can account for the density deficit on its own.

In order to study the miscibility of iron and magnesium at high pressures and temperatures, we have combined novel experimental techniques and state-of-the-art theoretical calculations. We present for the first time an experimental technique for studying alloying in the megabar pressure range. Metal alloying experiments in diamond anvil cells are difficult – external electrical heating does not supply high enough temperatures, while laser heating cannot ensure the homogeneous heating of a mixture of metals at high pressures. Our methodology overcomes these limitations (Fig. 3.2-4). The pressure range (over 125 GPa) at which alloying experiments can be performed for the solid-state physics and chemistry, geophysics and

geochemistry communities is now increased by about 4 to 5 times in comparison with common multi-anvil apparatuses.

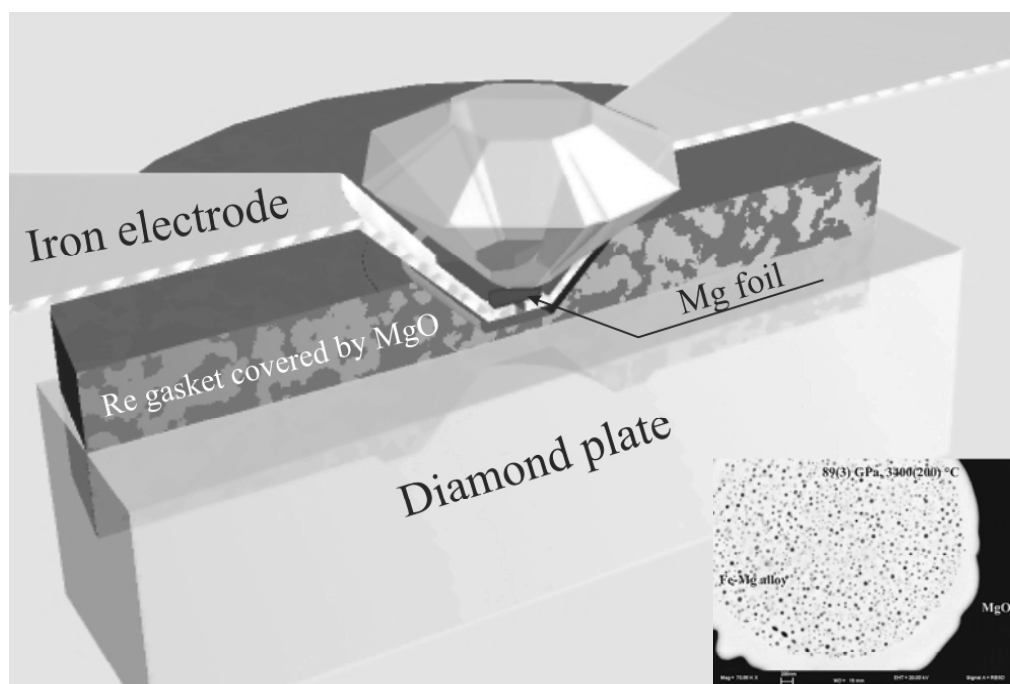


Fig. 3.2-4: A schematic diagram of the internal electrical heating assemblage for alloying experiments in the megabar pressure range. A rhenium gasket of 250 μm thickness was indented to 25-30 μm between diamond anvils with 250 or 300 μm culets. The gasket was covered by periclase-based cement and pure periclase and was placed into the indentation, around the Mg foil. Iron foils of 0.2 mm thickness flattened to a thickness of less than 10 μm at the end were used as electrical leads. The magnesium foil was heated by DC current with a stabilized power supply operating in the region of 25 V/25 A. The inset shows a back-scattering electron image of the metal droplet in the sample recovered after the experiment in the internally electrically heated diamond anvil cell at 89(3) GPa and 3400(200) $^{\circ}\text{C}$. On average the droplet contains 7.8(5) at.% Mg.

We have observed Fe metal droplets in the experiments containing on average 7.8 at.% Mg. One of the most important (and actually not trivial) results of our combined theoretical and experimental study is that the Hume-Rothery atomic size factor rule, which states that alloys form when the atomic radii of the two elements differ by $< 15\%$, are applicable for alloying elements at high pressure once the alloy compressibility is considered. This provides a new way of estimating the extent of alloying at high pressure, without any complex quantum mechanical calculations or expensive experiments. In order to show the generality of our concept to high-pressure alloying between immiscible elements, we investigated the extent of alloying between Mg and two of the close chemical analogues of iron, namely nickel and cobalt. Though the latter form intermetallic compounds with magnesium, the solubility of Mg in these metals is negligibly low. We conducted experiments on alloying Ni and Mg at 86(5)

GPa and 3300(200) K, and Co and Mg at 105(5) GPa and 3450(250) K, and found that at the conditions of our experiments, about 9 at.% Mg could dissolve in Ni and more than 12 at.% Mg in Co.

Our main result, the possibility of alloying between Fe and Mg at multimegabar pressures, suggests that magnesium can be an important light element in Earth's outer core. The assumption that Mg cannot alloy with Fe based on ambient pressure behaviour is clearly incorrect.

d. High-pressure alloying of iron and xenon: 'Missing' Xe in the Earth's core? (K.K.M. Lee/Pasadena, in collaboration with G. Steinle-Neumann)

With its inherent chemical inertness, the noble gas xenon (Xe) has been used to study the evolution of Earth and its atmosphere through investigation of the daughter products from short-lived radioactive isotopes. However, the Earth is 'missing' Xe in its atmosphere: Xe is depleted compared to chondritic abundances and lighter noble gases. More than 90 % of the Earth's Xe budget has been concluded to be missing; however the mechanism by which it has been lost is less obvious. Many models have attempted to explain Earth's Xe depletion. Hydrodynamic escape or impact vaporization is not enough to account for the missing Xe since even lighter rare gases like argon and neon are less depleted than xenon. Additionally, extensive searches for surface Xe reservoirs (*e.g.*, in ice or sediments) have been conducted but none have been found. Instead, the missing Xe may be hidden deep in the Earth's interior where there is little communication with the surface.

Here we consider the likelihood of xenon being in the Earth's core as a result of high-pressure alloying with iron. In light of recent experimental and theoretical results on high-pressure alloying of iron with various elements, the insulator-metal transition in Xe at pressures above ~ 125 GPa and the close-packed nature of Fe and Xe at high pressure support the possibility of Xe forming a solid solution with the high-pressure form of iron, hcp ϵ -Fe. While ϵ -Fe is only expected to be stable and present in the solid inner core, liquid iron, present in the outer core, is predicted to be also close packed. In this study, therefore, we have focused on ϵ -Fe and assumed the solubility of Xe into the crystalline structure will be similar to that of the liquid. To investigate the plausibility of a Fe-Xe solid solution, we use the Vienna *ab-initio* simulation package (VASP), a density functional theory-based method to evaluate the ground-state energetics of hcp Fe-Xe alloy supercells with varying Xe abundance.

We examine the enthalpy of the equilibrium reaction: $x\text{Fe} + (1-x)\text{Xe} \leftrightarrow \text{Fe}_x\text{Xe}_{(1-x)}$ where x is a value between 0.9688-0.9958 (32-240 -atom supercells) (Fig. 3.2-5). At 0 K, we find that at the lowest Xe concentration tested, ~ 0.4 mol.% Xe abundance level in Fe (240-atom supercell), xenon substitution into iron becomes favourable relative to the constituent elements above ~ 300 GPa, a pressure corresponding to the deep outer core (Fig. 3.2-5). If we

assume that the only difference is the entropy of mixing, stemming from the large number of positions that Xe can be substituted in the supercell, the alloy is even more favoured (*i.e.*, stability will be achieved at lower pressures) by entropic effects at high temperatures (Fig. 3.2-6). Therefore, including temperature and the entropy of mixing, xenon substitution into iron at 350 GPa increases from less than 0.3 (± 0.1) mol.% Xe at static conditions to more than ~ 0.6 (± 0.2) mol.% at 5000 K (Fig. 3.2-6).

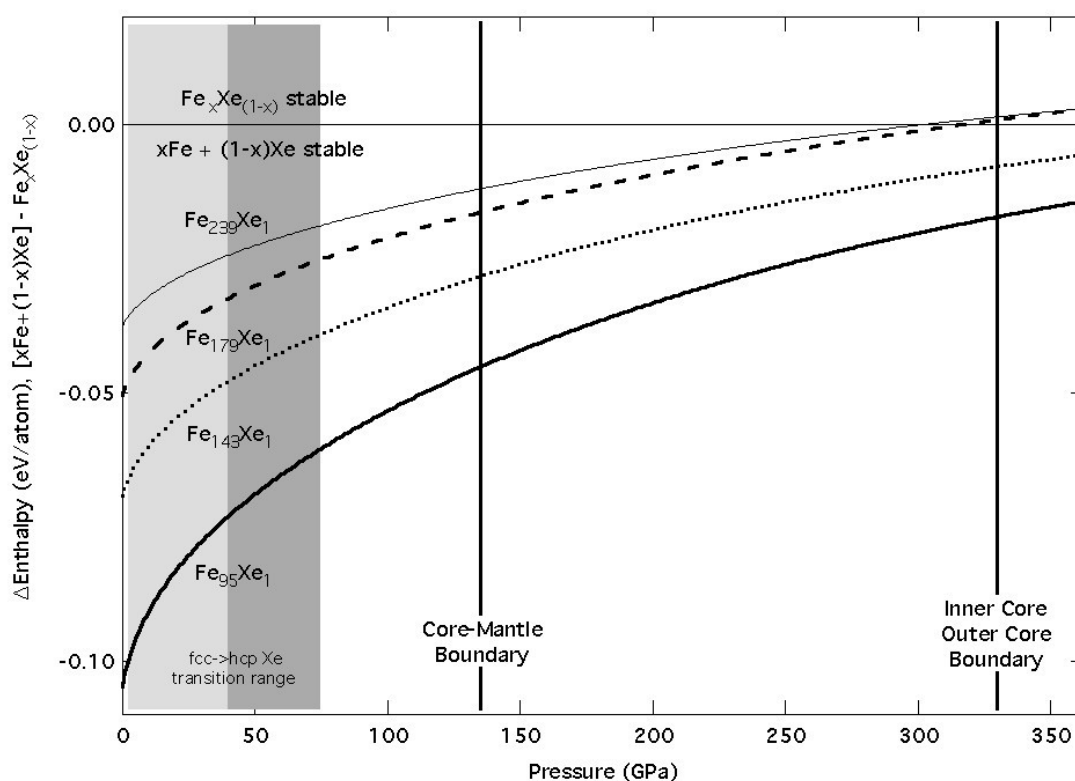


Fig. 3.2-5: The difference in the enthalpy of the pure elements Fe and Xe compared with Fe-Xe alloy versus pressure. Curves are labelled for the different Xe concentrations: $\text{Fe}_{0.9958}\text{Xe}_{0.0042}$ ($\text{Fe}_{239}\text{Xe}_1$, $\sim 9,700$ ppm, thin); $\text{Fe}_{0.9944}\text{Xe}_{0.0056}$ ($\text{Fe}_{179}\text{Xe}_1$, $\sim 13,000$ ppm, dashed); $\text{Fe}_{0.9931}\text{Xe}_{0.0069}$ ($\text{Fe}_{143}\text{Xe}_1$, $\sim 16,000$ ppm, dotted); and $\text{Fe}_{0.9896}\text{Xe}_{0.0104}$ ($\text{Fe}_{95}\text{Xe}_1$, $\sim 24,000$ ppm, thick). For positive values, the $\text{Fe}_x\text{Xe}_{(1-x)}$ alloy is energetically favoured over the pure elements. The shaded areas represent the fcc-to-hcp phase transition pressure regime for Xe from two different studies. Pressures for the core-mantle and inner core boundary are shown for reference.

Our results can readily explain the ‘missing’ Xe problem in the Earth as cosmochemical constraints only require that $\sim 10^{-1}$ ppm (equivalently 100 ppb, by weight) Xe to be in the Earth’s core, compared to the solubility limit of $\sim 10^4$ ppm (by weight) that the ϵ -Fe unit cell can actually accommodate at core conditions (Fig. 3.2-5, Fig. 3.2-6). Although our results can resolve the ‘missing’ Xe problem by placing Xe in the core, we do not constrain the isotopic core abundances of the Xe daughter isotopes, namely ^{129}Xe (from ^{129}I) and $^{131,132,134,136}\text{Xe}$ (from ^{244}Pu and ^{238}U). However, due to the vastly different electronic structures of iodine,

plutonium and uranium, we can imagine a preferred partitioning into the Earth's core of one parent over another. Indeed a better understanding of the partitioning of Xe, I, Pu and U between metal and silicates at high pressures and temperatures are necessary to better constrain the Earth's bulk and isotopic xenon budget.

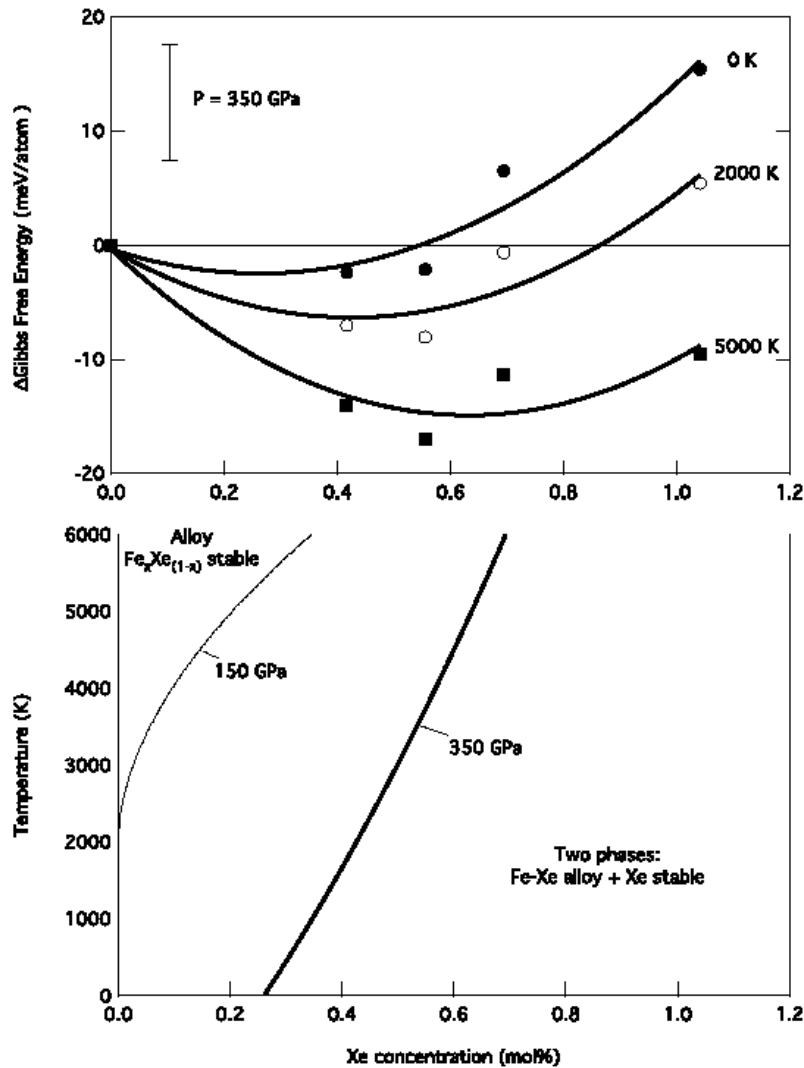


Fig. 3.2-6: Top. The difference in the Gibbs free energy of the pure elements Fe and Xe compared to the Fe-Xe alloy versus Xe concentration (mol.%) at 350 GPa: $x\text{Fe} + (1-x)\text{Xe} \Leftrightarrow \text{Fe}_x\text{Xe}_{(1-x)}$ where x is a value between 0.9896-1.000 at 0 K (filled circles), 2000 K (empty circles) and 5000 K (filled squares). Labelled curves through the data are third-order polynomial fits. The minima of each polynomial fit are used to construct the phase diagram below. A representative error bar is shown for energy convergence uncertainty ($\pm \sim 5$ meV). Bottom. Fe-Xe alloy phase diagram of temperature versus Xe concentration. The thick curve delineates the stability boundary between the Fe-Xe alloy and a two-phase space at 350 GPa. For comparison, we also include the boundary at 150 GPa (thin curve). To the left of each curve, the Fe-Xe alloy is stable; whereas to the right of each curve, a mixed region of Fe-Xe alloy and Xe phases are stable. The curvature of the phase boundaries are determined by the quality of the polynomial fit from above.

e. *Partitioning of trace elements among silicate, sulfide and metal under high pressure and high temperature (V. Malavergne, S. Berthet and R. Combes/Marne-La-Vallée, D.J. Frost)*

Determining the composition of the Earth's core is essential for understanding the internal structure, evolution, and present day dynamics of the Earth. Studying how and to what degree elements are partitioned into either metal or silicate is essential for understanding the processes in which the Earth differentiated and for determining the composition of the core. Multianvil experiments at high pressure (HP) and high temperature (HT) have been performed in order to provide better constraints on this topic.

In this project we have investigated the partitioning of trace elements between liquid metal and silicates between 20 GPa and 25 GPa at 2000-2400 °C and at different oxygen fugacities. All the samples have been characterized by optical microscopy, scanning electron microscopy and Raman spectroscopy. The concentrations of trace elements in metal and in silicates were measured by electron microprobe. In the samples of this study, the metallic phases were always liquid during heating, but both solid and liquid silicates were investigated. It is possible to determine the distribution coefficient $D_{\text{metal-silicate}}^X$ (X is a trace element) which is defined as the wt.% of element X in the metal divided by the wt.% of X in the silicate.

The first part of this study was performed to examine the reaction:



This reaction leads to the formation of MgS at high pressures and reducing conditions, and is potentially important as MgS could have been retained in the mantle rather than separating into the core. In addition a series of transition metals (Cr, Mn, Fe, Co, Ni and W) were added to the starting materials in order that their partitioning behaviour could be studied over a range of P, T and oxygen fugacity. A second goal of this work is to examine the validity of Henry's law in these types of experiments to see if the initial level of dilution might interfere with the partition coefficients. This may be very important, as the majority of previous partitioning studies have employed initial element concentrations that are in the 1-10 wt.% range, *i.e.*, well above natural concentration levels for most elements.

In Figure 3.2-7 we present preliminary results for Mn, a slightly siderophile element, as a function of oxygen fugacity. Our data are in good agreement with previous studies. The level of dilution of Mn in the starting material (wt.% or ppm) does not seem to significantly influence $D_{\text{metal-silicate}}^{\text{Mn}}$. From the $f\text{O}_2$ dependence the valence state of Mn in the silicate phases is determined as 2+, as already observed in previous studies.

In the second part of this study phase relations and partitioning between phases forming from a natural enstatite chondrite (EH) at high pressure and high temperature have been examined. Several studies have proposed that enstatite chondrites, highly reduced primitive meteorites,

could have comprised or contributed to the material from which the Earth formed. However, up to now, these models have never been experimentally tested and moreover, the phase diagram and the HP-HT metal-silicate partitioning of siderophile and lithophile elements in these chondrites are still unknown. Thus, experimental studies at HP-HT on a material of EH-type composition are required in order to model planetary differentiation. A finely ground powder of a natural EH4 chondrite (Indarch), doped with trace elements, was used as the starting material. The doping elements covered a range from highly siderophile elements to slightly siderophile elements, as well as rare Earth elements. No more than 0.1 wt.% per element or oxide was added. The main features of Indarch are that : (1) its major phase is Fe-free enstatite $MgSiO_3$, (2) around 33 wt.% of Fe-S and Fe-Si-Ni metallic phases are present. These observations are good indicators of the highly reduced conditions (around $\Delta IW-5$) that prevailed during its formation.

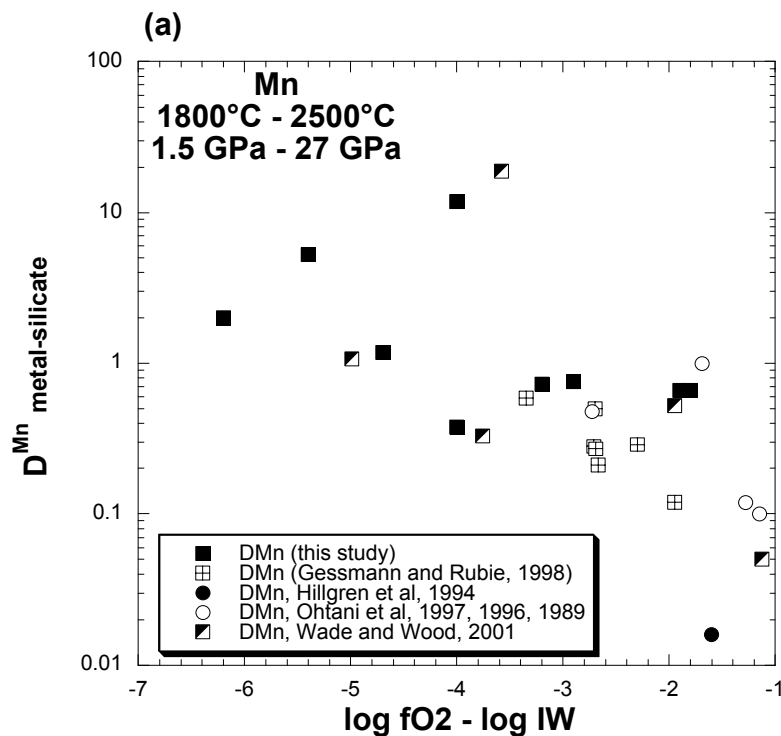


Fig. 3.2-7: $D^{\text{Mn}}_{\text{metal-silicate}}$ is plotted against fO_2 relative to the IW buffer at different pressures. The data are compared with previous studies Gessmann and Rubie (GCA, 62, 867, 1998), Hillgren *et al.* (Science, 264, 1442, 1994), Ohtani *et al.* (CMP 103, 263, 1989), Ohtani *et al.* (GRL, 23, 1993, 1996), Ohtani *et al.* (PEPI 100, 97, 1997), Wade and Wood (Nature, 409, 75, 2001).

The first results of this study indicate an oxidation of the samples at HP-HT, since almost no Si was found in the metallic phases and up to 7 wt.% of FeO were observed in the silicate. An oxygen fugacity fO_2 around $\Delta IW-2$ is obtained. Up to three different phases could be present in one sample (Fig. 3.2-8) allowing the determination of partition coefficients between metallic liquid, solid silicates (garnet or perovskite, depending on P-T) and silicate liquid.

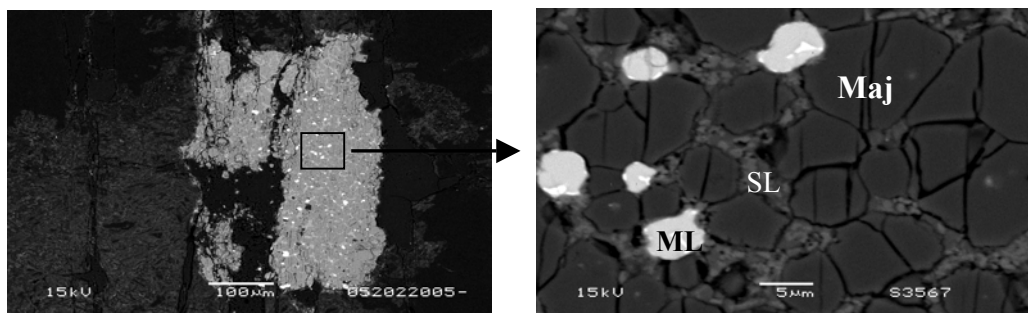


Fig. 3.2-8: Back-scattered electron images of the an enstatite chondrite sample equilibrated at 20 GPa and 2000°C for 5 min. The Fe-S metallic liquid (ML) has an inhomogeneous structure due to quench crystallisation. Two silicate phases are present, majorite (Maj) and a silicate glass (SL) between the grain boundaries of the majorite.

f. Metal-silicate partitioning of nominally lithophile elements (Ta, Ga, In, Zn) – new constraints on existing core formation models (U. Mann, D.J. Frost and D.C. Rubie)

The formation of the Earth is discussed in terms of two end-member models - homogeneous and heterogeneous accretion. While homogeneous models assume a single-stage equilibration process, many heterogeneous models propose a stepwise increase in oxidation state during accretion resulting from a stepwise change in the composition of the accreting material. In most heterogeneous models an initial quite reducing step is an important aspect, as redox conditions have a strong influence on the metal-silicate partitioning behaviour of many elements. A low oxygen fugacity would have favoured not only the extraction of relatively siderophile but also of several weakly siderophile and possibly even moderately lithophile elements from the Earth's mantle during early core formation. This could for example explain the relative depletion of Si and confirm the assumption of Si (~ 7 wt.%) being a principal light element in the Earth core. On the other hand there are certain lithophile elements like Ta, Ga, In and Zn that are believed to be not at all depleted in today's Earth's mantle as a result of core formation. Studying their partitioning behaviour enables us to place constraints on the initial very reducing stage of such heterogeneous models. Experimental data on Ta metal/silicate partitioning, for example, are lacking but simple thermodynamic calculations show that Ta should behave very similarly to Si.

In order to investigate the liquid metal-liquid silicate partitioning behaviour of Ta, Ga, In and Zn we have performed a number of multianvil experiments over a pressure range of 6 - 20 GPa, at temperatures between 2100-2250 °C and a range of redox conditions below IW. In each experiment the starting material was mixed from 56 wt.% of synthetic primitive mantle composition and 40 wt.% of Fe-alloy and doped with 4 wt.% of the indicator elements (as oxides). The metallic component always contained 2 wt.% Ni and 1 wt.% Co and was mixed from varying proportions of Fe powder and Fe₈₄Si₁₆ or Fe₇₁Si₂₉. The amount of Si metal was adjusted in order to achieve various redox conditions. Graphite and MgO single crystal capsules were employed. During heating liquid metal and silicate melts separated from each

other with the metal forming a discrete blob. Both metal and silicate phases show heterogeneous quench textures and were analyzed with EMP using a defocused electron beam. Moreover, SIMS was employed for some silicate phase measurements.

In Figure 3.2-9 partition coefficients (D) of Si, Ta, Ga, In and Zn at 6 GPa and 2100 °C are plotted against logarithmic values of oxygen fugacity which were calculated relative to the IW buffer from the Fe - FeO equilibrium between metal and silicate phase. All these elements show a good correlation between $\log f_{O_2}$ and $\log D$. Among them Si is the least siderophile element maintaining its lithophile character over the whole redox range. Ga and In on the other hand are always siderophile. A comparison of Si with Ta shows that over the entire redox range Ta is always more siderophile than Si and therefore would be massively depleted from the mantle at any conditions where significant Si would be in the core.

The valences of elements in the silicate liquid can be derived from the slopes of the lines in Fig. 3.2-9. This yields very reasonable values of, for example, a 5^+ state for Ta and a 1^+ state for In.

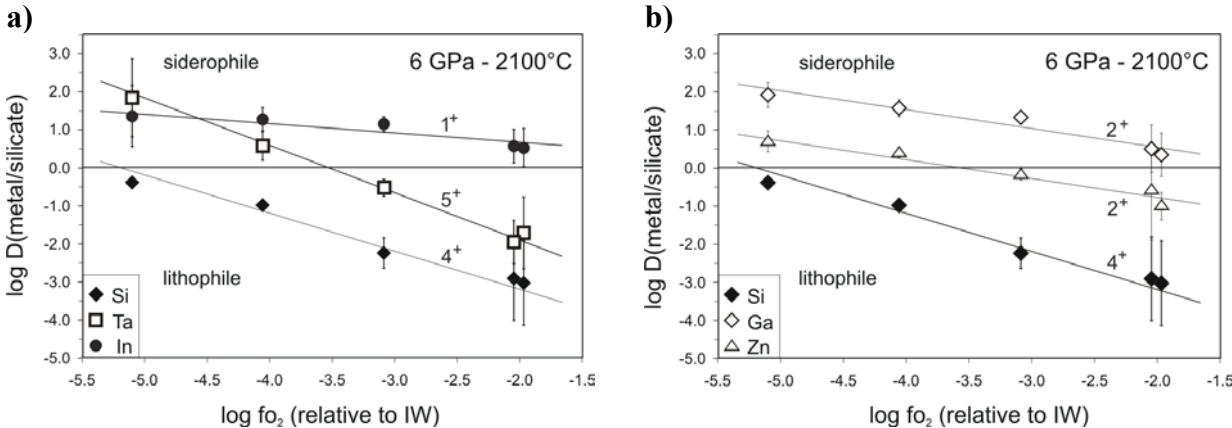


Fig. 3.2-9: Partitioning behaviour of **a)** Si, Ta, In and **b)** Si, Ga and Zn between metal and silicate melt at 6 GPa, 2100 °C. For each element the estimated valence state as derived from the slopes of the correlation trend is indicated.

The effects of higher P and T on the metal-silicate partitioning behaviour of Si and Ta are demonstrated in Fig. 3.2-10. For both elements an increase in P from 6 to 20 GPa at 2100 °C does not have a significant influence on the partition coefficient. At a higher T of 2250 °C at 18 GPa we have performed only one experiment so far. However, this preliminary result indicates that T has a significant effect on the geochemical character of Si and Ta, as in both cases the partition coefficients are increased by at least one order of magnitude. Moreover, for Si the data point fits well into the trend found by Wade and Wood (Nature, 409, 75, 2001) at similar HP and HT conditions (Fig. 3.2-10a). Even at these HP-HT conditions Ta still shows a more siderophile character than Si and would always be extracted into a core forming Fe-alloy to a greater extent than Si.

From our partitioning data for Ta we can derive additional information on another important geochemical topic. Wade & Wood (2001) have recently suggested that one reason for the observed low Nb-Ta ratio in the Earth's mantle could be that under higher P and low redox conditions Nb becomes moderately siderophile comparable to the geochemical behaviour of V. This would have allowed for a certain extraction of Nb to the core in an early reducing stage of accretion. Now the new data for Ta of this study can be compared with their experimental data for Nb (Fig. 3.2-10b). At lower pressure the Nb data plot within the error range of the Ta correlation trend. And also at around 20 GPa our Ta data point seems to fit well into the Nb trend found by Wade & Wood (2001). So based on these datasets a separation of these two elements by metal-silicate partitioning can be excluded if core formation happened at pressures up to 25 GPa and temperatures between 2100-2300 °C. Our aim is to confirm this observation with further HT experiments on Ta.

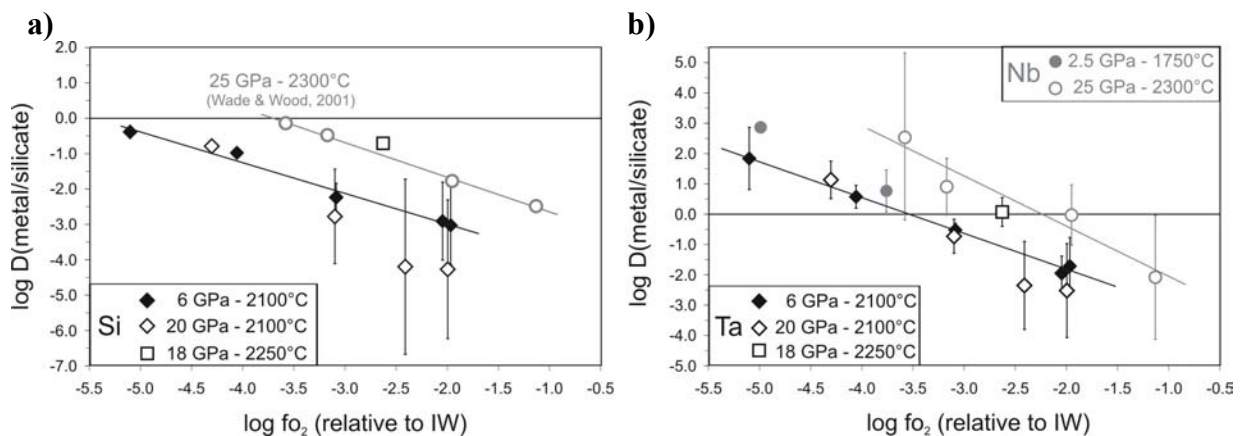


Fig. 3.2-10: Influence of pressure and temperature on the metal-silicate partitioning behaviour of Si and Ta. **a)** For comparison, Si experimental data from Wade & Wood (Nature, 409, 75, 2001) are added. **b)** In the investigated P and T range the partition coefficients of Ta (this study) and Nb (after Wade & Wood, 2001) are very similar, excluding a significant separation of these elements during core formation.

g. Accretion and core formation of terrestrial planets: Insights from experimentally determined solubility behaviour of siderophile elements in silicate liquids (P. Kegler and H. Palme/Köln, A. Holzheid/Münster, D.C. Rubie and D.J. Frost)

The formation of an iron-rich metallic core is one of the most important events in the history of the terrestrial planets. A key for understanding core formation processes is the partitioning behaviour of siderophile elements (e.g., Ni, Co, Ge, PGEs) between metal and silicate phases. The metal/silicate partitioning behaviour of nickel and cobalt play a special role among the siderophile elements. Both elements are not only overabundant in the Earth's mantle compared to what one would expect from experimentally determined metal/silicate partition coefficients at one atmosphere, but they also occur in nearly chondritic ratios in the Earth's mantle (Ni/Co: Earth's mantle = 18.2, chondrites = 21.2), although Ni is considerably more

siderophile at one bar than Co. Based upon high-pressure studies Ni-Fe and Co-Fe metal - liquid silicate exchange partition coefficients, K_D^{Ni-Fe} and K_D^{Co-Fe} , appear to converge at pressures of about 28 GPa corresponding to a depth of about 800 km in the Earth. It is therefore generally assumed that absolute abundances of Ni and Co as well as the chondritic Ni/Co ratio in the Earth's mantle are consistent with metal - silicate equilibrium at the base of a 750 to 1200 km deep magma ocean. We have performed new experiments over a wide range of pressures (1 atm to 25 GPa) and temperatures (1300-2300 °C) to better define the pressure and temperature dependence of the metal/silicate partitioning behaviour of Ni and Co.

The results of these experiments show that the pressure and the temperature dependence of Ni-Co partition coefficients both depend on pressure. From 1 atmosphere to a pressure of about 2.5 GPa the partition coefficients of Ni and Co depend strongly on temperature, while above 5 GPa the decrease of the metal-silicate partition coefficients with temperature is much weaker. The same behaviour is observed for the pressure gradient, a strong increase of Ni and Co partition coefficients at pressures below 3.5 GPa and a weak increase above 5 GPa (see Fig. 3.2-11 and Fig. 3.2-12).

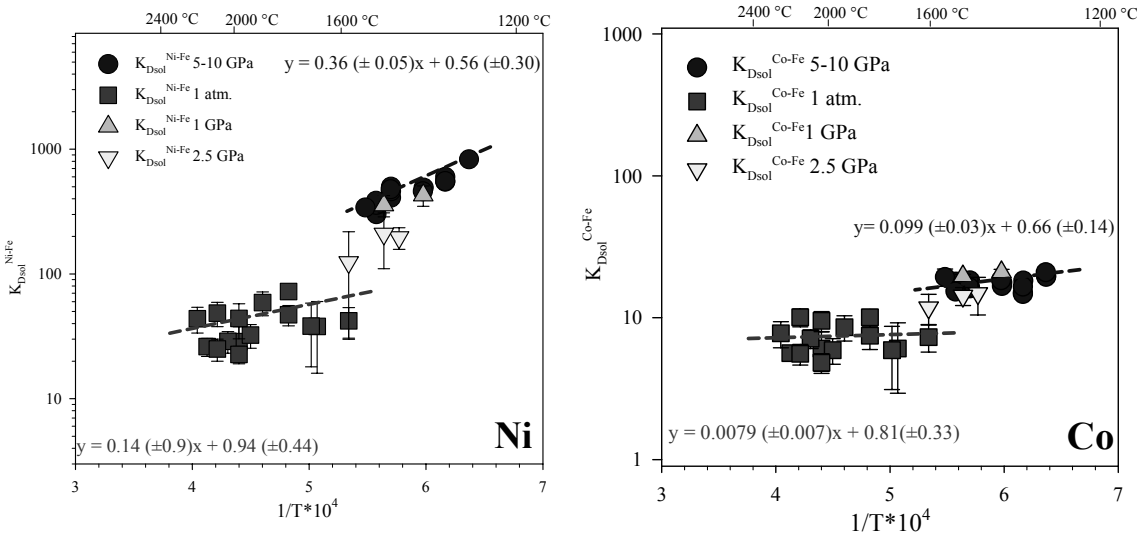


Fig. 3.2-11: Temperature dependence of the exchange partition coefficient (K_D) of Ni and Co at 1 atm, 1 GPa, 2.5 GPa and the pressure regime from 5-10 GPa.

A single extrapolation of Ni and Co partition coefficients experimentally determined at low and at high pressures is not justified. Our data show that it is very likely that a single pressure where both partition coefficients have the same value does not exist within the Earth. Therefore, neither the absolute Ni abundance nor the chondritic Ni/Co ratio in the Earth's mantle may be explained by simple metal/silicate equilibration at the conditions of a deep and hot magma ocean. Possible explanations for the present Ni and Co concentrations in the Earth's mantle are inhomogeneous accretion (change of the oxidation state of accreting

material) or inefficient core formation (later oxidized remnants of core forming metal in the mantle). Similar high-pressure experiments are being conducted for Ge and Cu.

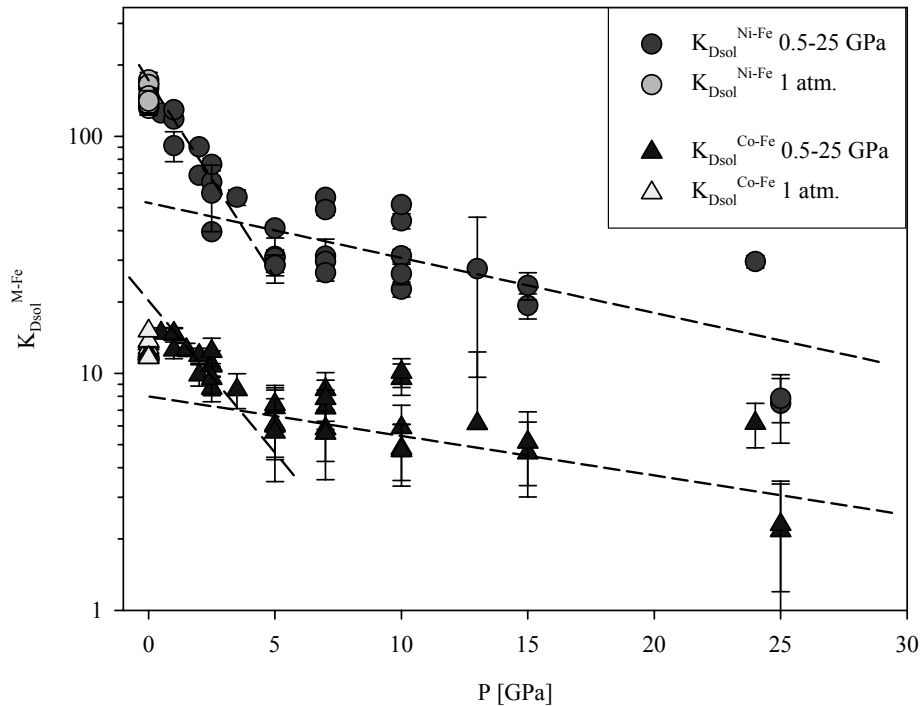


Fig. 3.2-12: Pressure dependence of the exchange partition coefficient (K_D) of Ni and Co.

h. Partitioning and valence state of titanium in oxide-metal assemblages at upper mantle conditions (E. Stoyanov, F. Langenhorst/Jena and D.J. Frost)

At conditions of the Earth's surface titanium (Ti) occurs dominantly in the 4+ oxidation state. However, there are some minerals in which titanium can be in the 3+ (armalcolite) or even 2+ (honquiiite) valence state. Armalcolite is present as an accessory mineral in lunar and some terrestrial rocks. The cubic phase TiO, known as "hongquiiite", is found in platinum ores associated with high-temperature rocks of the garnet-hornblende-pyroxenite facies in Tao district, Hongqui, China. Understanding titanium incorporation into high-pressure minerals is particularly important to gain insight into the oxidation state and element partitioning in the Earth's mantle. Thus we have studied the partitioning and valence state of titanium in oxide-metal assemblages at upper mantle conditions, establishing a fingerprint technique for the study of mantle-derived samples.

To this avail we have performed multianvil experiments on the MgO-Ti-Fe system with increasing FeO content in the MgO phase. The experiments were done at a temperature of 1700 °C and 5 GPa pressure in MgO capsules. The so prepared specimens were analyzed using transmission electron microscopy and electron energy-loss spectroscopy (EELS). In

order to understand the signals in collected EELS spectra we compared them with EELS spectra of Ti-standards with known coordination of the titanium and known $\text{Ti}^{4+}:\text{Ti}^{3+}$ ratio. We found in our experiments that the formation of Ti-bearing phases depends largely on the FeO content in ferropericlase and thus on the oxidation state. The results of Ti L ELNES measurements are summarized in Fig. 3.2-13a. In the case of the pure MgO starting composition we observed epitaxial growth of cubic $\text{Ti}^{[2+]}\text{O}$ nanocrystals (Fig. 3.2-13b). Increasing the FeO content by 10 % leads to the formation of two Ti-bearing phases – cubic $\text{Ti}^{[2+]}\text{O}$ and armalcolite $(\text{Mg,Fe, Ti}^{3+})(\text{Ti}^{3+}, \text{Ti}^{4+})_2\text{O}_5$. Applying our recent quantification technique for the Ti^{4+} concentration of armalcolite yields $\text{Ti}^{4+}/\Sigma\text{Ti}=0.58$. In the sample with 40 % FeO we found an epitaxial relationship between ferropericlase $\text{Mg}_{0.7}\text{Fe}_{0.3}\text{O}$ and ulvöspinel $\text{Ti}^{[4+]}\text{Fe}_2\text{O}_4$ (Fig. 3.2-13c). According to our quantification technique ulvöspinel contains only Ti^{4+} . In all samples the titanium content in the metal (Fe) phase is up to 2.0 wt.%. Increasing the FeO content of magnesiowüstite in equilibrium with metallic Fe raises the $f\text{O}_2$ which seems to be matched by a progressive change in Ti oxidation state from dominantly 2+ to 4+. Comparing the obtained EELS spectra with the spectra from Ti-standards we find that the titanium coordination in the analyzed Ti-bearing phases is six-fold. The presence of the observed phases is also proved by electron diffraction. The cell parameters of TiO and TiFe_2O_4 are doubled in comparison with MgO, which suggests the possibility of an epitaxial relationship between the host (MgO) and growing nanocrystals of TiO or TiFe_2O_4 .

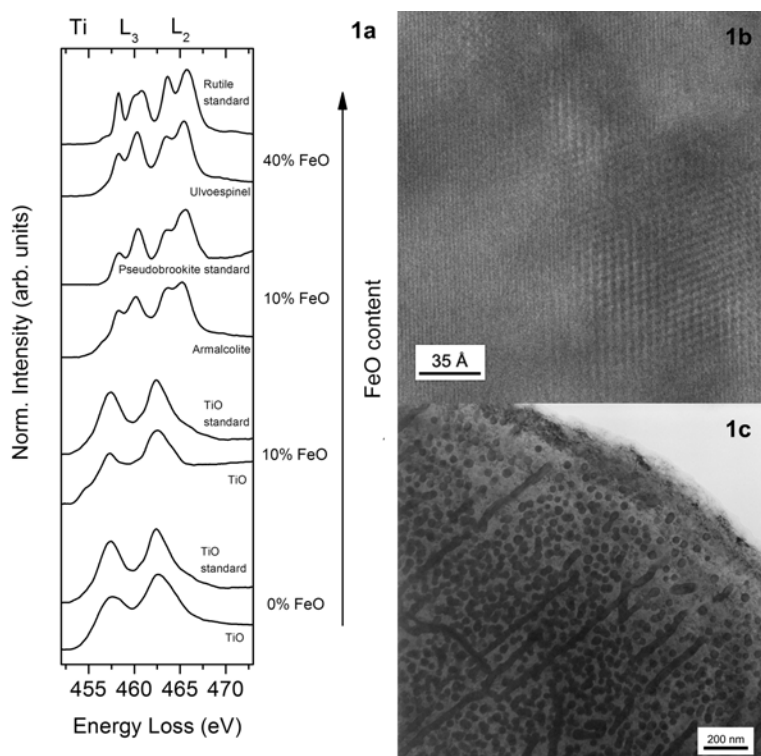


Fig. 3.2-13: a – comparison between Ti standards and measured EELS spectra; b – TiO crystal in MgO matrix; c – exsolution of ulvöspinel crystals in $\text{Mg}_{0.7}\text{Fe}_{0.3}\text{O}$ matrix

We have carried out high-pressure experiments on titanium partitioning as a function of FeO content. Three titanium-bearing phases were found - TiO, armalcolite and ulvöspinel. One of

them (armalcolite) is also found in meteorites. Our results demonstrate the advantages of the EELS technique for fingerprinting minerals. The measurements demonstrate the capability of ELNES to provide insight into the valence states and site geometry of Ti in terrestrial and planetary materials.

i. Origin of the negative niobium tantalum anomaly in subduction zone magmas (J. Baier/Tübingen, A. Audétat and H. Keppler)

When compared to magmas from other tectonic settings, arc-related magmas are characterized by a low content of Nb and Ta relative to other trace elements. This is referred to as the “negative niobium tantalum anomaly”. An often-invoked explanation for this phenomenon is the retention of Nb and Ta by rutile in the subducting slab. Rutile is a common accessory mineral in eclogites, and although it seldom makes up more than 1-2 % of the rock’s volume, it is so rich in Nb and Ta that it usually is the dominant carrier (> 90 %) of the rock’s Nb/Ta budget. Rutile therefore controls the behaviour of these elements during slab dehydration, and since rutile/fluid partition coefficients of Nb and Ta are extremely high, any fluid emanating from a rutile-bearing lithology should be strongly depleted in Nb and Ta. However, before these fluids can reach the site where arc magmas are generated, they need to travel through large volumes of mantle rocks that are essentially devoid of rutile. Hence, if rutile was the only mineral to produce the negative Nb-Ta anomaly, this geochemical signature would long have disappeared by the time the fluids had reached the melting zone. A second mechanism is therefore required to maintain low Nb and Ta-concentrations (relative to other elements) in the fluid during its percolation through the mantle wedge. One possibility is Nb and Ta incorporation in clinopyroxene. Clinopyroxene contains far less Nb and Ta than rutile, but due to its far higher modal abundance it nevertheless might be able to dominate the Nb and Ta budget of mantle rocks and, as a consequence, the behaviour of these elements during fluid-rock interaction.

For this reason, experiments were conducted to explore the partitioning behaviour of Nb and Ta between clinopyroxene and aqueous fluid. Because precise determination of large mineral/fluid partition coefficients in runs involving only mineral + fluid is difficult, an indirect approach was chosen in which the solubility of Nb (or Ta) in clinopyroxene and aqueous fluid was measured in two separate experiments that both contained excess CaNb_2O_6 (or CaTa_2O_6). The solubility of Nb in clinopyroxenes was investigated in the system $\text{CaMgSi}_2\text{O}_6$ - $\text{NaAlSi}_2\text{O}_6$ - Nb_2O_5 - H_2O at 1.5 GPa and 900-1100 °C. At these conditions, clinopyroxene coexists with hydrous melt and CaNb_2O_6 . The solubility of niobium in the pyroxene was found to increase strongly with its aluminium content. While the solubility of niobium is on the order of 100 ppm by weight for Al-poor clinopyroxenes, it reaches 4 wt.% for clinopyroxenes containing 10 wt.% Al_2O_3 . Microprobe analyses suggest that Nb is incorporated in the clinopyroxene as a $\text{NaNbAl}_2\text{O}_6$ component. The solubility of CaNb_2O_6 in aqueous fluid was determined by direct visual observation of dissolving CaNb_2O_6 crystals of

known volume in an externally heated hydrothermal diamond anvil cell. At 1.5 to 1.7 GPa and 800-1000 °C, an aqueous fluid saturated with diopside dissolves only 20-100 ppm by weight of CaNb_2O_6 , *i.e.*, niobium solubility in the fluid is orders of magnitude lower than that in aluminous clinopyroxenes. Reconnaissance experiments on the solubility of CaTa_2O_6 in clinopyroxenes and in aqueous fluid suggest that Ta generally behaves similar to Nb, with the notable exception that the solubility of CaTa_2O_6 in aqueous fluid is even lower than that of CaNb_2O_6 . Our results imply that fluid/clinopyroxene partition coefficients of Nb and Ta are $\ll 1$ for pyroxene compositions typical of the subducted slab or the subarc mantle. Only for very Al-poor clinopyroxenes, the partition coefficient may approach unity. The relative depletion of Nb and Ta in subduction zone magmas is therefore primarily a result of the intrinsically low solubility of Nb and Ta in the fluid and does not require the presence of HFSE-rich accessory phases in the rock. Previous studies have underestimated the role of clinopyroxenes in sequestering Nb and Ta because they were conducted in Al-poor systems.

3.3 Mineralogy, Crystal Chemistry and Phase Transformations

Studies in the fields of mineralogy and crystal chemistry focused, also in the year 2005, on structure-property relations in important mineral groups. By studying the response of a crystal structure to changed conditions of pressure and temperature, and by comparison with the changes in physical properties, the underlying causes of changes in properties may be understood. The approach has been very successful in the past for the study of chemically simple end members of solid solutions. The controlled chemical substitution in simple systems may be used as an additional “set screw” for changing the crystal structure. At the same time, the complex natural compositions can be more closely approximated by synthetic samples.

For the geoscientist the equation of state is one of the most important properties, because it is a controlling factor, *e.g.*, for seismic properties and for the pressure dependence of mineral reactions and phase transformations. At the same time, the equation of state is directly linked to changes in the crystal structure with pressure and temperature. In this context, new data for pyroxene solid solutions, the zeolite analcite and the 10Å phase are reported here. For the high-pressure silicate hollandite it is shown that substitution of K by Na leads to a strong reduction in molar volume. The Fe³⁺ concentration and its distribution over lattice sites in clinopyroxenes gives indications of redox conditions in the upper mantle of the Earth.

More recently, electronic and magnetic properties of mantle minerals have received increasing attention: the postulated low-spin to high-spin transition of Fe²⁺ could have drastic effects on molar volumes of individual mantle phases and on the Fe-Mg distribution coefficients between them, but the effect and its consequences are still poorly understood. The first data are reported on spin behaviour during compression of olivine to pressures beyond its stability field. For ferropericlasite, the second most important mineral of the lower mantle, it is shown that the spin transition occurs over a wide range of pressures (or depths) and that no marked discontinuity in properties may be expected. In the end member FeO it is shown by neutron diffraction that the magnetic Néel phase transition and the structural phase transition from cubic to rhombohedral are separated by ca. 40 °C, so that these two transitions are not directly connected; whereas in the isostructural MnO they occur at practically the same temperature.

a. *Crystal-structure refinement of high-pressure and high-temperature natural Na-bearing clinopyroxenes (F. Nestola, M. Longo, C.A. McCammon and T. Boffa Ballaran)*

Omphacitic clinopyroxene and pyrope garnet represent the main constituents of mantle eclogite. The cation distribution in clinopyroxene is of particular interest due to the possible presence of vacancies at the M2 site, which may be related to the incorporation of OH. In the present work nine natural samples of Na-clinopyroxene primarily from the Udachnaya

diamond-bearing kimberlite were studied using single-crystal X-ray diffraction at ambient conditions. It is well known that accurate determination of the cation partitioning in natural pyroxene is not often a simple task. This is due to the wide range of elements present in the pyroxene structure, which results in several problems to be solved, *e.g.*, order-disorder of Mg-Fe²⁺ between the M2 and M1 structural sites, estimation of the Fe²⁺/Fe³⁺ ratio, the presence of vacancies, etc. In order to overcome all such problems a least-squares refinement to best match the parameters obtained from different investigation techniques (crystal-structure refinement, microprobe analysis and Mössbauer spectroscopy) was performed to obtain an accurate determination of cation partitioning. Our results show that out of the nine samples studied (all with space group *C2/c* and jadeite contents ranging between 25 and 58 %), six samples clearly show the presence of vacancies with concentrations between 0.025 and 0.054 p.f.u. (for six oxygen atoms).

Several previous studies have reported that vacancies cause a decrease of the unit-cell volume for samples with the same composition. We have plotted the Na content versus the unit-cell volumes of our samples compared to other *C2/c* clinopyroxenes from the literature not showing vacancies (Fig. 3.3-1). We also plotted literature data from a *C2/c* clinopyroxene from Bellsbank eclogite with 0.065 p.f.u. vacancies (for six oxygens). Even though the data shown are from a range of samples measured with different instruments and different Bragg reflection centering procedures, it is clear that the data form two different trends: those containing vacancies, and those without vacancies. Results from the refinements, combined with FTIR measurements that show relatively low OH concentrations, will be used to describe the history of the eclogite xenoliths, particularly the environmental conditions under which they were formed.

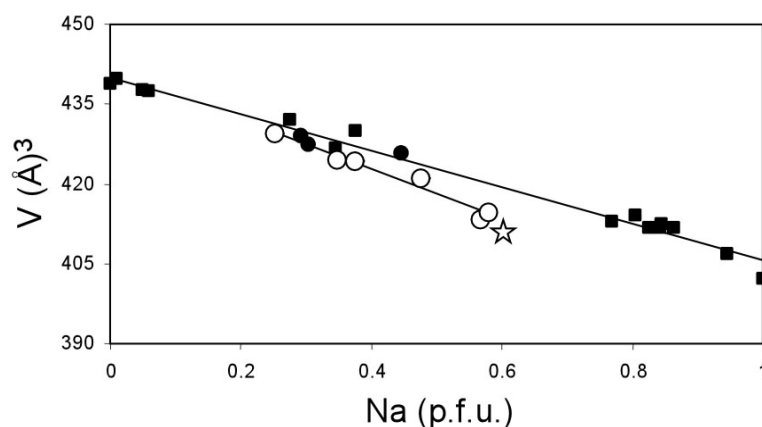


Fig. 3.3-1: Evolution of unit-cell volume with Na content for clinopyroxene. Squares indicate literature data showing no vacancies (Rossi *et al.*, 1983, *Contrib Mineral Petrol*, 83:247-258; Boffa Ballaran *et al.*, 1998, *Am Min*, 83, 419-433), while solid circles indicate our data showing no vacancies and open circles indicate our data where vacancies are present. The open star represents data from eclogitic clinopyroxene where vacancies were also found (McCormick, 1986, *Am Min* 71, 1434-1440). The two end-members with 0 and 1 Na content are diopside and jadeite, respectively.

b. Equation of state of the jadeite ($\text{NaAlSi}_2\text{O}_6$) – aegirine ($\text{NaFe}^{3+}\text{Si}_2\text{O}_6$) and the jadeite – hedenbergite ($\text{CaFe}^{2+}\text{Si}_2\text{O}_6$) solid solutions (F. Nestola and T. Boffa Ballaran, in collaboration with C. Liebske/Zurich)

Na-clinopyroxenes are the most common pyroxenes in high-pressure metamorphic rocks, not only in blueschist metamorphic terranes or in eclogites, but also in alkali-rich igneous rocks. They were found in the eclogites from Kokchetav massif, which are considered to be the highest-pressure metamorphic terrane due to the presence of abundant diamonds. Experimental investigations showed that Na-rich pyroxenes are stable throughout the temperature/pressure range of the subducting slabs in the upper mantle. Jadeite in particular is involved in one of the most studied geobarometers, which is based on the transformation of albite ($\text{NaAlSi}_3\text{O}_8$) to jadeite ($\text{NaAlSi}_2\text{O}_6$) + quartz (SiO_2), with a P - T line that can be described by $P = 0.35 + 0.0265T(^{\circ}\text{C}) \pm 0.50$ kbar. Cation substitution, very often present in natural samples, can affect the jadeite stability field and, therefore, shift the pressure of albite breakdown. The effect of aegirine ($\text{NaFe}^{3+}\text{Si}_2\text{O}_6$) and hedenbergite ($\text{CaFe}^{2+}\text{Si}_2\text{O}_6$) components, the most common substitutions in Na-clinopyroxenes, can be constrained if the thermo-elastic properties of pyroxenes along the jadeite – aegirine and jadeite – hedenbergite joins are known. To this end a compressional study (this report) and a high-temperature study (next report) have been undertaken on synthetic samples belonging to these two joins.

The clinopyroxenes used in this study have been synthesised at 6 GPa and ~ 1400 - 1600 K with a multianvil press using glasses of corresponding compositions as starting materials. The crystals obtained have a size ranging between 50 and 200 μm . Single crystals suitable for the X-ray diffraction measurements were selected and loaded in diamond anvil cells with quartz single crystals as an internal pressure standard. The evolution of the unit-cell parameters was followed up to 6-10 GPa. No phase transitions were found in the pressure ranges investigated. The pressure-volume data have been fitted using a third-order Birch-Murnaghan equation of state (BM3-EoS), refining simultaneously the unit-cell volume V_0 , the bulk modulus K_{T0} and its first derivative K' .

For the jadeite – aegirine solid solution the unit-cell volumes collected at room pressure for the different compositions indicate a slight deviation from linearity along the join in contrast with the suggestion that such joins behaves ideally. The bulk modulus, K_{T0} , varies from 134.0(7) GPa for pure jadeite to 116.1(5) GPa for pure aegirine. Its evolution with composition along the join is not linear and can be described with the 2nd order polynomial: $K_{T0} = 116.2(5) + [0.25(3) * (\text{mol.}\% \text{ Jd})] - [0.0008(3) * (\text{mol.}\% \text{ Jd})^2]$. The value of the first pressure derivative K' is close to 4 for all the samples investigated and can be used in a BM3-EoS to determine the volume variations of these pyroxenes up to 7-10 GPa.

For the jadeite – hedenbergite solid solution the bulk modulus K_{T0} decreases and K' increases with increasing hedenbergite component. The difference in K_{T0} between jadeite and hedenbergite is larger than between jadeite and aegirine, as expected due to the difference in unit-cell volumes at room pressure among the three end-members. The major difference

between the two solid solutions is, however, the fact that K' is constant along the jadeite – aegirine join; whereas it strongly depends on the hedenbergite component in the jadeite – hedenbergite system. We suggest that the value of K' is related to the crystal structure deformation mechanisms occurring at high pressure, which in the case of clinopyroxenes appears to be mainly controlled by the cations in the M2 sites. The cation substitution in the jadeite – aegirine join occurs at the M1 site ($\text{Al} \leftrightarrow \text{Fe}^{3+}$); whereas in the jadeite – hedenbergite join there is a double coupled substitution at the M2 ($\text{Na} \leftrightarrow \text{Ca}$) and at the M1 ($\text{Al} \leftrightarrow \text{Fe}^{2+}$) sites. The substitution at the M2 sites may cause a change of the response of the crystal structure of the jadeite – hedenbergite pyroxenes to the applied pressure. Crystal-structure determinations along the two joins are in progress in order to clarify the high-pressure behaviour of these clinopyroxenes.

c. High-temperature behaviour of clinopyroxenes along the joins jadeite-aegirine and jadeite-hedenbergite (F. Nestola, M. Tribaudino/Parma, M. Bruno/Torino and T. Boffa Ballaran)

Natural pyroxenes are in general complex chemical solid solutions of end member compositions; yet experimental data are mainly given for end members, in spite of the significant changes in the physical parameters with composition occurring in pyroxenes. Moreover the available experimental data in pyroxenes are affected by large experimental and systematic error and do not allow detailed modelling of the thermal expansion. The study reported here is part of a research project aimed to better constrain the thermo-elastic properties of Na-clinopyroxenes (see previous report).

New experimental data on the thermal expansion for intermediate clinopyroxenes along the joins jadeite – aegirine ($\text{NaAlSi}_2\text{O}_6 - \text{NaFe}^{3+}\text{Si}_2\text{O}_6$) and jadeite – hedenbergite ($\text{NaAlSi}_2\text{O}_6 - \text{CaFe}^{2+}\text{Si}_2\text{O}_6$), and for end members jadeite, aegirine and hedenbergite have been obtained by measuring using single-crystal X-ray diffraction the unit-cell parameters of the different samples between 25 and 800 °C at 100 °C intervals.

To improve the quality of the unit-cell parameters at each temperature, a preliminary peak centering on about 20 reflections was followed by subsequent data collection of about 200 strong reflections, then the peak profiles were fitted to determine experimental peak centre positions and to correct for $K\alpha_1$ - $K\alpha_2$ splitting. A decrease of one order of magnitude of the experimental error was observed with respect to the preliminary peak centering. The retrieved cell parameters were used to model the thermal expansion according to the equation:

$$\ln(V/V_0) = \alpha(T-T_0),$$

taking as V_0 the experimental value collected at room temperature T_0 . The calculated thermal expansion coefficients (α) are: $2.31(5) \cdot 10^{-5} \text{ K}^{-1}$ for $\text{Ae}_{60}\text{Jd}_{40}$, $2.68(8) \cdot 10^{-5} \text{ K}^{-1}$ for $\text{Ae}_{25}\text{Jd}_{75}$, and $2.78(5) \cdot 10^{-5} \text{ K}^{-1}$ for $\text{Jd}_{50}\text{Hd}_{50}$. The thermal expansions obtained for the end-members are:

$2.54 \cdot 10^{-5} \text{ K}^{-1}$ for jadeite, $2.12 \cdot 10^{-5} \text{ K}^{-1}$ for aegirine, and $2.92 \cdot 10^{-5} \text{ K}^{-1}$ for hedenbergite. It appears that the effects of aegirine and hedenbergite substitutions have an opposite effect on the thermal expansions of jadeite, so that the thermal expansion decreases with increasing aegirine component and increases with increasing hedenbergite component. An accurate determination of the uncertainties is in progress to elucidate if the asymmetric deviation from ideality observed for the jadeite – aegirine solid solution is real.

d. Iron site partitioning in clinopyroxene determined using Mössbauer spectroscopy: A new approach (C.A. McCammon, M. Longo and F. Nestola)

Clinopyroxene is an important rock-forming mineral that is a constituent of several thermometers and oxybarometers. Cation distribution is an important component of the formulations, particularly the site occupancy of iron. One of the methods traditionally applied to determining iron site distributions is Mössbauer spectroscopy, but results are compromised by the ambiguity arising from the heavily overlapped subspectral components. In this study we developed a new approach to fitting that involved simultaneous fitting of spectra of the same absorber recorded at different temperatures.

Samples were taken from a suite of Na-clinopyroxenes from xenoliths originating primarily from the Udachnaya diamond-bearing kimberlite in Siberia. Single-crystal grains from each sample were set aside for electron microprobe analysis and single-crystal X-ray refinement, and the remainder of the hand-picked grains were ground and mounted between pieces of Fe-free Al foil. Mössbauer spectra were recorded of all samples at both room temperature and 80 K using a conventional ^{57}Co source. Mössbauer spectra are similar to those in the literature, and consist of two broad absorption envelopes (Fig. 3.3-2). While $\text{Fe}^{3+}/\Sigma\text{Fe}$ is relatively well constrained by the difference in areas of the high- and low-velocity envelopes, the site distribution of Fe^{2+} cannot be unambiguously determined due to the strong overlap of components. However, the shape of the spectral envelope is different at room temperature compared to 80 K (Fig. 3.3-2), which results from the different temperature dependence of the hyperfine parameters of the various iron sites. If two assumptions are made regarding the spectra, namely (1) that the centre shifts corresponding to each site/environment change with temperature according to the second-order Doppler shift; and (2) that the only change to the relative areas with temperature arises from differences in recoil-free fraction, then the spectra can be fit simultaneously with these constraints to obtain robust estimates of iron site distribution.

We fitted all of the Mössbauer spectra using the above approach, and found that in three of the nine samples studied, there was an observable amount of Fe^{2+} occupying the M2 site. These results are in excellent agreement with single-crystal refinements where M1/M2 site distribution was determined independently (see report by Nestola in the same section). The detailed structure and composition data of the Na-clinopyroxenes provide the chance to

develop new probes (*e.g.*, geobarometers) to characterise the conditions under which they formed.

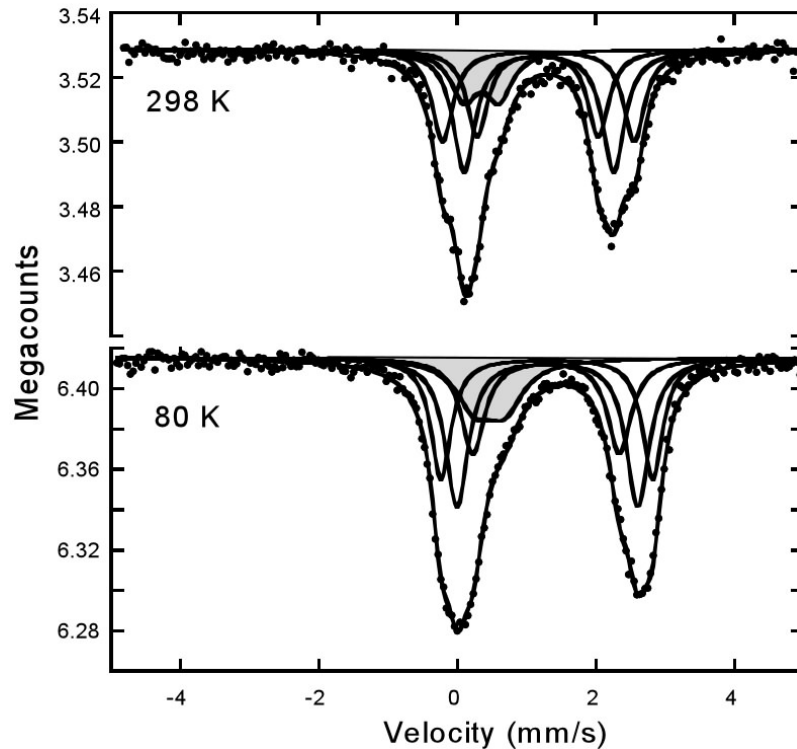


Fig. 3.3-2: Mössbauer spectra of the same clinopyroxene absorber at two different temperatures. The spectra were fitted simultaneously with constraints on relative areas and centre shifts applied according to the temperature shift, resulting in a more accurate determination of $\text{Fe}^{3+}/\Sigma\text{Fe}$ and the possibility to extract the M1/M2 site distribution. In these spectra all Fe^{2+} (unshaded) occupies the M1 site based on the temperature dependence of quadrupole splitting, and $\text{Fe}^{3+}/\Sigma\text{Fe}$ corrected for recoil-free fraction is $15.5 \pm 1.6 \%$.

e. High-pressure behaviour of analcime (G.D. Gatta, F. Nestola and T. Boffa Ballaran)

Analcime (or analcite) is a feldspathoid with ideal formula $\text{NaAlSi}_2\text{O}_6 \cdot \text{H}_2\text{O}$. Analcime occurs in a wide variety of geological environments and, during the last decades, it was the object of a debate concerning its genetic conditions and origin (primary or secondary). Natural occurrences and experimental evidence appear to confirm that both primary and secondary analcime exist. However, whereas primary analcime has rarely been found (in rocks such as blairmorites or minettes) a wide number of secondary analcimes has been observed as products of alteration of primary magmatic minerals, such as nepheline and leucite.

The crystal structure of feldspathoids is composed of corner-sharing $(\text{Al},\text{Si})\text{O}_4$ tetrahedra, linked in an infinite three-dimensional array, commonly defined as a “framework”. The framework contains large cavities or channels where the “extra-framework content”,

represented by monovalent or divalent cations and water molecules, lies in order to balance the deficit of charge of the Si/Al-framework. The framework topology of analcime shows the maximum symmetry ($I a\bar{3}d$). In cubic analcime there is a statistical Si/Al-distribution in the tetrahedral framework and the Na sites exhibit statistical occupancy of 2/3 (due to charge balance). The Na sites are 6-coordinated (with 4 oxygens belonging to the tetrahedral framework and 2 to the water molecules) and lie in the framework voids. Two different systems of channel can be observed in the crystal structure of analcime: irregular channels formed by highly distorted 8-membered rings (8mR) and regular channels formed by 6-membered rings (6mR) along the [111] direction of the cubic lattice. The lower symmetry structures found in nature show some Si/Al-ordering.

A limited number of studies has been devoted to analcime under pressure and they report that cubic (or tetragonal or orthorhombic) analcime undergoes reversible first-order phase transitions between 0.8 and 1.5 GPa. On the basis of the lattice parameter discontinuities at HP it also was suggested that such phase transitions are to monoclinic (at about 0.8-0.9 GPa) and to triclinic (at about 1.5 GPa) symmetry. However, the previous studies were limited to the compressional behaviour of analcime up to 2.5 GPa and, in addition, no structural refinement was performed. The aim of our study is to investigate the elastic behaviour and the HP-structural evolution of cubic analcime in the hydrostatic regime by *in situ* single-crystal X-ray diffraction. Current HP-facilities and improvements in diffractometers and detectors can now provide us with more accurate and precise data up to pressure values higher than those reached in the previous studies, allowing us to investigate the crystal structure of the HP-polymorphs, which is still unknown.

A crystal of natural analcime from Sardinia (Italy) was used for the HP-experiment. Accurate lattice parameters were measured with a Huber four-circle diffractometer up to 7.2 GPa with the crystal in a BGI-type diamond anvil cell (Fig. 3.3-3). Diffraction data were then collected on a Xcalibur-Oxford Diffraction at 0.0001, 0.91(5), 1.23(5), 2.12(5) and 5.04(5) GPa. A first-order phase transition is observed in the pressure range between 0.91(5) and 1.08(5) GPa. Unit-cell constants and reflection conditions confirm that the space group of the HP-polymorph is $P\bar{1}$. No further phase transition has been observed at least up to 7.14 GPa. Fitting the volume data of the cubic polymorph with a second-order Birch-Murnaghan equation of state (BM-EoS) we obtain: $V_0 = 2571.2(4)\text{\AA}^3$, $K_{T0} = 56(3)$ GPa and $K' = 4$ (fixed). For the triclinic polymorph, a third-order EoS gives: $V_0 = 2607(9)\text{\AA}^3$, $K_{T0} = 19(2)$ GPa and $K' = 6.8(7)$. The elastic behaviour of the HP-polymorph appears to be strongly anisotropic, with $K_{T0}(a):K_{T0}(b):K_{T0}(c) = 2.64:1.82:1.00$. The structural refinement performed at HP allows us to describe the relevant structural variations in response to the cubic \rightarrow triclinic phase transition, mainly due to tetrahedral tilting. The tetrahedral framework distortion gives rise to a change of the 8- and 6-ring channel ellipticities and of the extra framework topological configuration: it appears in fact that for the high-pressure triclinic polymorph the coordination number of part of the Na atoms is 7 (2H₂O + 5 framework oxygens) instead of 6 (2H₂O + 4 framework oxygens).

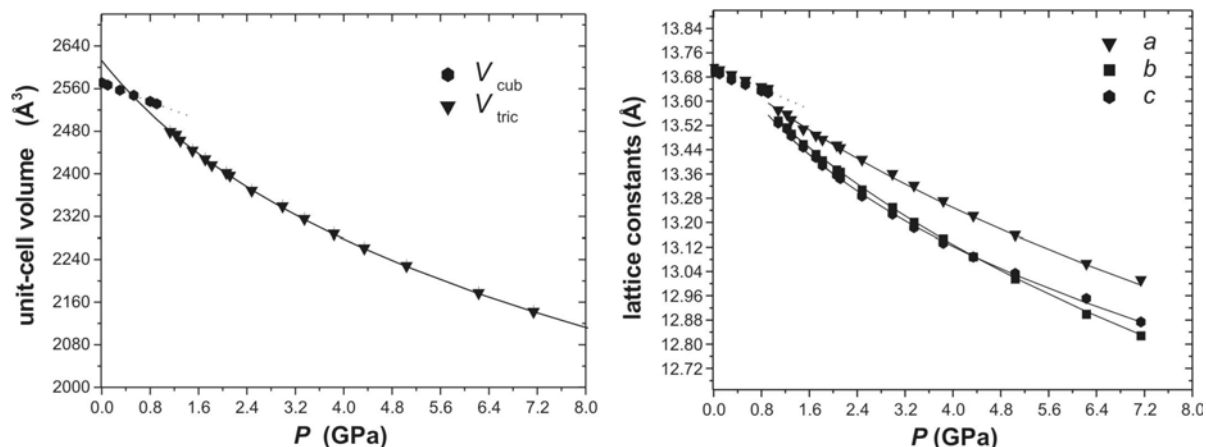


Fig. 3.3-3: Evolution of the lattice parameters of analcime with P and EoS-fit for cubic (dotted line) and triclinic polymorphs (solid line). For cubic analcime, the unrestrained cell constants are plotted. The estimated standard deviation values are slightly smaller than the size of the symbols.

f. *High-pressure behaviour of 10 Å phase: An in situ Raman and X-ray powder diffraction study (P. Comodi/Perugia, F. Cera/Perugia and L.S. Dubrovinsky)*

Subducting slabs undergo dehydration, and the water and volatiles released play a key role in many petrologic processes, such as metasomatism and partial melting inside the mantle wedge, acting in particular as trigger mechanisms for deep focus earthquakes. There are several hydrous phases indicated by experimental studies as possible candidates for carrying water deep into the Earth's mantle. Members of this group are the alphabet phases A, B, C, D, E, F and G, superhydrous B, 10 Å phase and 3.65 Å phase, phase X and EGG. So far very limited data are reported for the 10 Å phase [$\text{Mg}_3\text{Si}_4\text{O}_{10}(\text{OH})_2 \cdot \text{H}_2\text{O}$], which may represent an important phase for storage, transport and release of water in subducting slabs to depths exceeding the stability field of talc. This phase forms from talc at pressures between 3-5 GPa through the reaction: talc + H_2O \rightarrow 10 Å phase and at higher pressures through the fluid-free reaction: talc \rightarrow 10 Å + enstatite + coesite. Moreover the occurrence of the 10 Å phase is not restricted to the ternary MgO-SiO₂-H₂O system, given that an aluminous 10 Å phase was found in peridotitic systems. In complex ultramafic systems and at compositions approaching natural lherzolite, a 10 Å phase structure forms at the expense of chlorite, depending on the amount of undersaturated H₂O. Due to the thermal structure of the subducting slab the stability field of the 10 Å phase can reach that of phase A and transfer water deep into the mantle.

We studied the behaviour of the 10 Å phase at pressures up to 42 GPa and at room temperature by means of Raman spectroscopy and X-ray powder diffraction. The material remains chemically stable throughout the investigated pressure range and all observed changes in lattice diffraction patterns and Raman spectra are completely reversible. Fitting a third-order Birch-Murnaghan equation of state to the P - V data yields values of $V_0 = 492.9(3)$

\AA^3 , $K_0 = 39(3)$ GPa and $K' = 12.5(8)$. The linear compressibility coefficients of a and b and β parameters are $1.20(16) 10^{-3} \text{ GPa}^{-1}$, $1.72(9) 10^{-3} \text{ GPa}^{-1}$, $3.6(7) 10^{-4} \text{ GPa}^{-1}$, respectively. For the c lattice parameter an exponential decay is needed to describe the evolution with pressure: $c/c_0 = 0.876(2) + 0.116 e^{-P/6.7(5)}$.

The Raman frequencies of all lattice modes (low frequency region $< 1200 \text{ cm}^{-1}$) are observed to increase monotonically with increasing pressure and decrease with decompression. This behaviour is in agreement with that observed for other hydrous magnesium silicates. In contrast, the frequency of the stretching bands of the water molecules in the 10 Å phase are found to soften with pressure, possibly due to changes in the intermolecular hydrogen bonding between non-equivalent H atoms of the water molecules and oxygens of the tetrahedral layer induced by the significant distortion of the tetrahedral layers occurring with pressure. Such distortion can be expressed in terms of the tetrahedral Si-O-Si angle which shows a significant reduction as a function of pressure (Fig. 3.3-4).

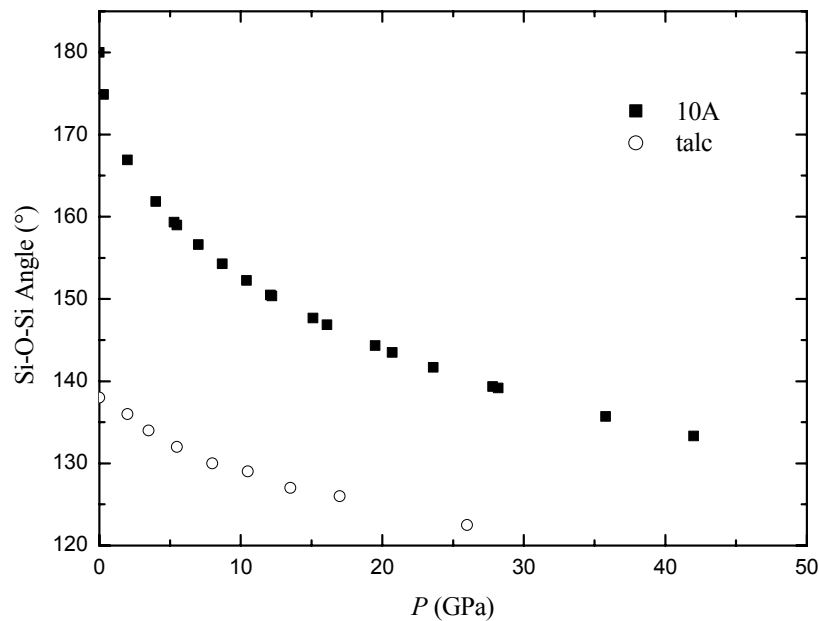


Fig. 3.3-4: Change of tetrahedral angle (calculated following Bailey's relationship) in the 10 Å phase as a function of pressure. The Si-O-Si values for talc (Stixrude, 2002, J. Geophys. Res. – Solid Earth, 107 (B12):2327) are shown for comparison.

g. *Fe solubility and symmetry reduction in CaSiO₃ perovskite at lower mantle conditions (K. Fujino, F. Langenhorst/Jena, D.C. Rubie and H. Izumi/Sapporo)*

CaSiO₃ perovskite is thought to be one of the major constituent minerals of the transition zone and the lower mantle, and even more abundant in subducting slabs. However, compared to Fe solubility in MgSiO₃ perovskite, Fe solubility in CaSiO₃ perovskite and its effect on the crystal structure and other physical properties are not well known. To clarify these issues, studies on high-pressure phase relations of the system CaSiO₃ - FeSiO₃ and characterization of

Fe-bearing CaSiO_3 perovskite were carried out using a combined method of a laser-heated diamond anvil cell (DAC), synchrotron X-ray diffraction and analytical transmission electron microscopy (ATEM).

Laser-heated DAC experiments using gel and powdered crystals of the system CaSiO_3 - FeSiO_3 were performed at around 30-137 GPa and 2000 K. A starting material was loaded in a hole of a rhenium gasket, sandwiched by diamond anvils and heated from both sides by a YAG or YLF laser. *In situ* X-ray diffraction experiments using a laser-heated DAC at the synchrotron radiation facilities in Japan show that CaSiO_3 perovskite is stable up to 137 GPa and has a Fe content between 0.1 and 0.15 per formula unit at 30-70 GPa, while for the end-member FeSiO_3 a mixture of FeO with a B1 structure and a high-pressure polymorph of SiO_2 is stable up to 137 GPa. In the intermediate composition region in CaSiO_3 - FeSiO_3 , the three phases of CaSiO_3 perovskite, FeO with a B1 structure and a high-pressure polymorph of SiO_2 are stable. All the Fe-bearing CaSiO_3 perovskite phases show tetragonal symmetry at high pressure and room temperature and the c/a ratios (< 1) of the refined cell parameters are smaller than those of pure CaSiO_3 perovskite with tetragonal symmetry at the same pressure. In addition, these ratios seem to further decrease with increasing pressure. These results indicate that Fe incorporation in CaSiO_3 perovskite along with pressure enhances the symmetry reduction from cubic to tetragonal.

Recovered samples were analyzed by ATEM. The analyzed compositions of the perovskite phases reveal that the Fe content in CaSiO_3 perovskite is around 0.11 per formula unit at ~ 40 GPa. It slightly increases to about 0.16 at about 72 GPa, indicating a slight increase of Fe solubility in CaSiO_3 perovskite with pressure. Electron energy loss spectroscopy (EELS) measurement of the sample synthesized at about 44 GPa and 1700 K (Fig. 3.3-5) indicates that Fe in the present CaSiO_3 perovskite is almost exclusively Fe^{2+} . This indicates that the predominant substitution scheme of Fe in CaSiO_3 perovskite using the starting materials of CaSiO_3 - FeSiO_3 is $\text{Ca}^{2+} \rightarrow \text{Fe}^{2+}$ at around this pressure. Thus it is unlikely that the substitution $\text{Si}^{4+} \rightarrow \text{Fe}^{3+} + \text{oxygen vacancy}$ will occur at the corresponding depth within the lower mantle, if the available Fe is Fe^{2+} . EELS measurements of Fe-bearing CaSiO_3 perovskites synthesized at higher pressures are now under way.

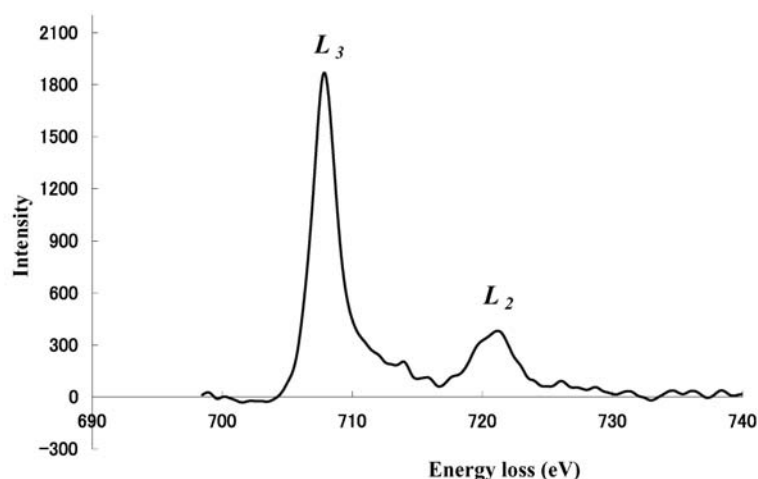


Fig. 3.3-5: Electron energy loss spectrum of $(\text{Ca}_{0.89}\text{Fe}_{0.11})\text{SiO}_3$ perovskite synthesized at 44 GPa and 1700 K. The calculated $\text{Fe}^{3+}/\sum\text{Fe}$ ratio was 0.09.

h. High-pressure study of K-Na hollandite solid solution (J. Liu, T. Boffa Ballaran, L.S. Dubrovinsky and D.J. Frost)

(Na,K)AlSi₃O₈ aluminosilicates with the hollandite-type structure are particularly dense phases in which all Si and Al are in six-fold coordination, and they are considered to be a possible repository of potassium and sodium in the Earth's lower mantle. Phase relations in the system KAlSi₃O₈ - NaAlSi₃O₈ have been examined so far at pressures of 5-23 GPa and temperatures of 700-1200 °C, indicating that the maximum solubility of NaAlSi₃O₈ component into the KAlSi₃O₈ hollandite-type structure at 1000 °C is about 40 mol.%. At higher Na content the high-pressure phase appears to be that of the calcium-ferrite type structure. However, in the last few years there have been a number of reports of natural occurrences of NaAlSi₃O₈ hollandite in shock-induced melt veins of chondrite. The aim of our research is to explore the phase relation of the K-Na system at different temperatures and pressures and to determine the physical-chemical properties and high-pressure behaviour of silicate hollandite-type structures containing K and Na in different concentrations.

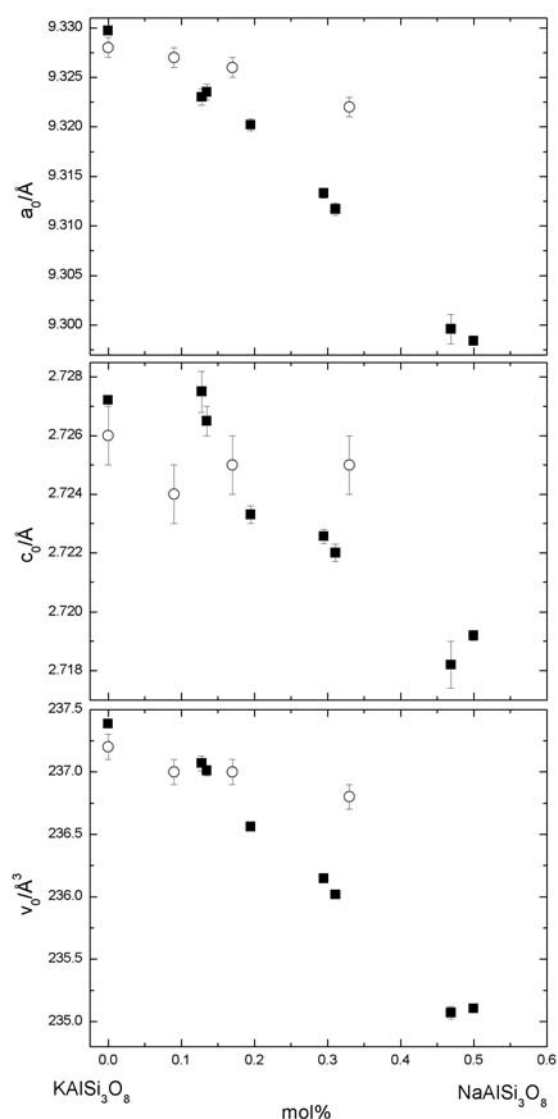


Fig. 3.3-6: Lattice parameters and unit cell volumes of KAlSi₃O₈ - NaAlSi₃O₈ hollandite solid solution. Solid squares are our data, and open circles are from a previous study by Yagi *et al.* (1994, *Phys Chem Minerals*, 21: 12-17) for samples synthesised at 1000 °C. Our results suggest a significant effect of Na on the lattice parameters of K_xNa_{1-x}AlSi₃O₈ hollandite.

A series of synthesis experiments has been done with the multianvil presses at the Bayerisches Geoinstitut in the pressure range 13-25 GPa and 1700 °C, using $K_xNa_{1-x}AlSi_3O_8$ ($x = 1, 0.7, 0.5, 0.4, 0$) glasses as the starting materials. Until now we have successfully synthesized materials containing up to 50 % Na at 22 GPa and 1700 °C. The cell parameters and cell volume of $KAlSi_3O_8$ hollandite decrease with increasing $NaAlSi_3O_8$ component (Fig. 3.3-6). Our results show that the solubility of the Na-component in hollandite silicate increases with increasing temperature. High-pressure X-ray powder and single-crystal diffraction and Raman spectroscopy experiments for samples recovered after multianvil experiments are in progress. Preliminary experiments using a $NaAlSi_3O_8$ end-member glass yield no hollandite-type structure at 22.5 GPa and 1700 °C. Further synthesis experiments are planned to determine the experimental P-T stability field of $NaAlSi_3O_8$ hollandite.

i. Electronic configuration of iron in cold compressed olivine $Mg_{1.8}Fe_{0.2}SiO_4$ (J. Rouquette, I. Yu. Kantor, C.A. McCammon and L.S. Dubrovinsky)

The electronic configuration of iron in mantle minerals strongly influences their physical and chemical properties. Since pressure and temperature cause significant changes to the structural environment of iron, there are numerous possibilities for transitions involving the electronic state of iron. These include changes of the spin state, valence state and band state, with consequent implications for mantle properties such as density, elasticity, rheology, partitioning behaviour and transport properties. Numerous electronic transitions have been observed in iron compounds at high pressure, including iron oxides [FeO , $(Mg,Fe)O$, Fe_3O_4 , Fe_2O_3] and iron-containing silicates [(Mg,Fe) SiO_3 perovskite], but the nature of some of the transitions remains controversial due to the multiple possible interpretations of spectroscopy data. Olivine is a popular starting material for high-pressure experiments, since it transforms at high pressures and temperatures to a mixture of (Mg,Fe) SiO_3 perovskite and (Mg,Fe) O , the dominant phases of the lower mantle. In diamond anvil cell experiments, the common P-T path to reach these conditions is isothermal compression at room temperature, followed by laser heating. To characterise the nature of the olivine starting material just before laser heating, as well as to expand the spectroscopic dataset of Fe^{2+} at high pressure, we recorded a sequence of room-temperature high-pressure Mössbauer and Raman spectra of iron-bearing olivine. Olivine is already known to undergo pressure-induced partial amorphisation and structural transformation (possibly to wadsleyite or an intermediate spineloid) during room-temperature compression, but no measurements of the electronic state of iron during these processes have previously been made.

We studied olivine with composition $Mg_{1.8}Fe_{0.2}SiO_4$ that was synthesised from ^{57}Fe -enriched starting materials. Powdered samples were loaded into a cylindrical hole drilled into a Re gasket, and pressure was generated using a miniature piston-cylinder diamond anvil cell with 250-300 μm diameter culet anvils. The samples were loaded under an argon atmosphere to avoid oxidising conditions, and pressure was measured using the ruby fluorescence technique. Mössbauer spectra at low pressure show a quadrupole doublet arising from Fe^{2+} in the M1 and M2 sites in the high-spin state (Fig. 3.3-7A). Above ~ 40 GPa the lines become broader and

the Raman peaks disappear, consistent with the previously reported partial amorphisation and structural transformation. Above ~ 50 GPa a new component with small centre shift and quadrupole splitting appears (Fig. 3.3-7B), whose intensity increases with increasing pressure. On decompression to atmospheric pressure the new component disappears, and the Mössbauer spectrum of the recovered sample is consistent with all iron occurring as high-spin Fe^{2+} , although in a range of different environments (Fig. 3.3.7C), consistent with the presence of an irreversible structural transformation.

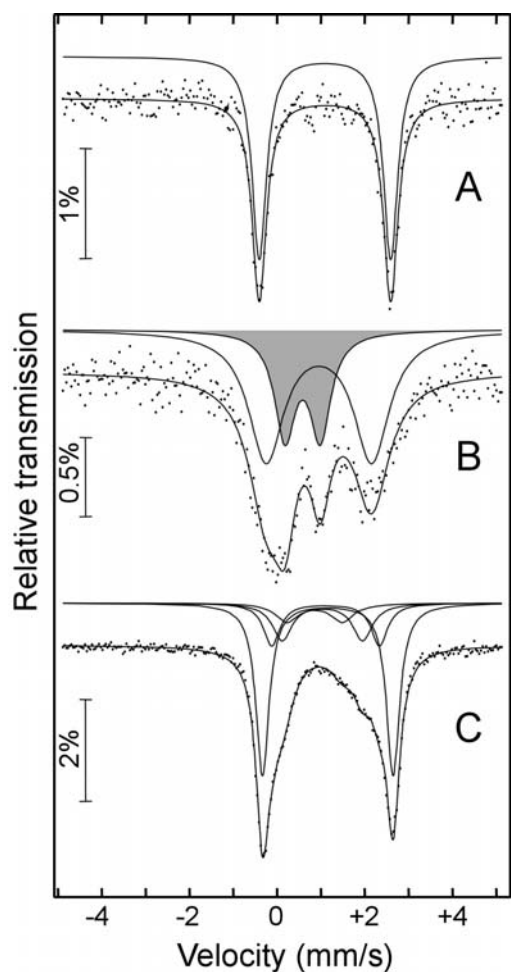


Fig. 3.3-7: Room-temperature Mössbauer spectra of $\text{Mg}_{1.8}\text{Fe}_{0.2}\text{SiO}_4$ synthetic olivine in the diamond anvil cell at: A) 12 GPa; B) 68 GPa; C) atmospheric pressure after the experiment. Components are shaded as follows: high-spin Fe^{2+} (unshaded); low-spin Fe^{2+} (grey). The additional peaks in spectrum C are due to high-spin Fe^{2+} in an amorphous or partially transformed phase.

The centre shifts of the high-spin and low-spin components vary consistently with pressure during both compression and decompression (Fig. 3.3-8), and combined with the observations above, suggest a high-spin to low-spin transition of Fe^{2+} in the range 40-50 GPa. This result has several important consequences. Literature compression data can be used to estimate polyhedral volumes and hence the effect of pressure on the crystal field, in order to better quantify the parameters of the Fe^{2+} spin transition. Such results provide useful insight for the interpretation of electronic transitions in other iron compounds. Also, the presence of low-spin Fe^{2+} in a metastable amorphous state in the starting material may influence the results of laser-heated diamond anvil cell experiments, particularly those reaching the pressures of the post-perovskite phase transition.

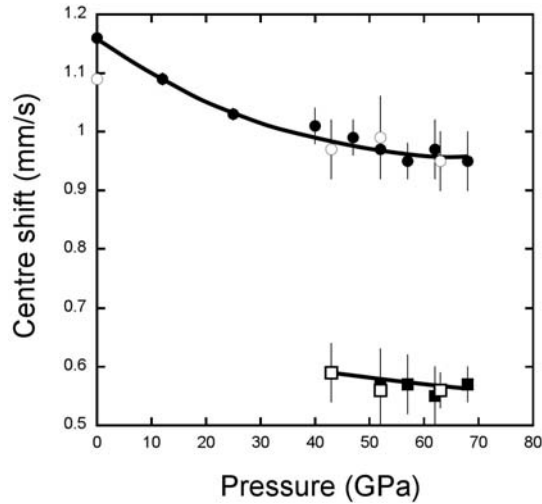


Fig. 3.3-8: Centre shift variation with pressure for high-spin Fe²⁺ (circles) and low-spin Fe²⁺ (squares) during compression (solid symbols) and decompression (open symbols).

j. *Mössbauer study of a spin crossover in ferropericlase: Compositional, pressure and temperature dependence (I.Yu. Kantor, L.S. Dubrovinsky and C.A. McCammon)*

Ferropericlase (Mg_{1-x}Fe_x)O with $x \sim 0.2$ is one of the main minerals constituting the Earth's lower mantle, and its high-pressure and high-temperature properties are of great importance for the Earth sciences. Spin state changes of Fe²⁺ in ferropericlase will influence many of its properties, including bulk density, elasticity, heat and electrical conductivity. For these reasons, a knowledge of the pressure dependence and characteristics of the spin crossover transition in ferropericlase is necessary for understanding the constitution and properties of the Earth's lower mantle.

Measurements were performed in a diamond anvil cell (DAC) equipped with internal resistive Pt heater. We used diamonds with 250 μm culet size and a Re gasket that was preindented to $\sim 25 \mu\text{m}$ and then drilled with a 125 μm diameter hole. Several small ($\sim 1 \mu\text{m}$ in diameter) ruby chips were loaded together with the sample for pressure calibration and evaluation of the pressure gradient. Three ferropericlase samples: (Mg_{0.8}Fe_{0.2})O (Fe20 sample), (Mg_{0.785}Fe_{0.125})O (Fe12 sample), and (Mg_{0.95}Fe_{0.05})O (Fe5 sample) with 60-90 % enrichment with ⁵⁷Fe were used in this study. We recorded conventional transmission Mössbauer spectra as a function of pressure, which show a quadrupole-split doublet at low pressure in agreement with existing data. The centre shift of the absorption is consistent with high-spin (HS) Fe²⁺. Above ~ 50 GPa a new spectral component appears whose relative area increases with pressure. The new component shows a significantly lower centre shift compared to HS Fe²⁺ and negligible quadrupole splitting, consistent with a low-spin (LS) state of Fe²⁺. The relative area of the LS component, which is related to its abundance, increases with increasing pressure. For the Fe5 sample the width of the spin transition is ~ 20 GPa and at 75 GPa a pure low-spin state was observed. For the Fe12 sample the transition is finished only at ~ 90 GPa, and for the Fe20 sample only at 105 GPa (Fig. 3.3-9).

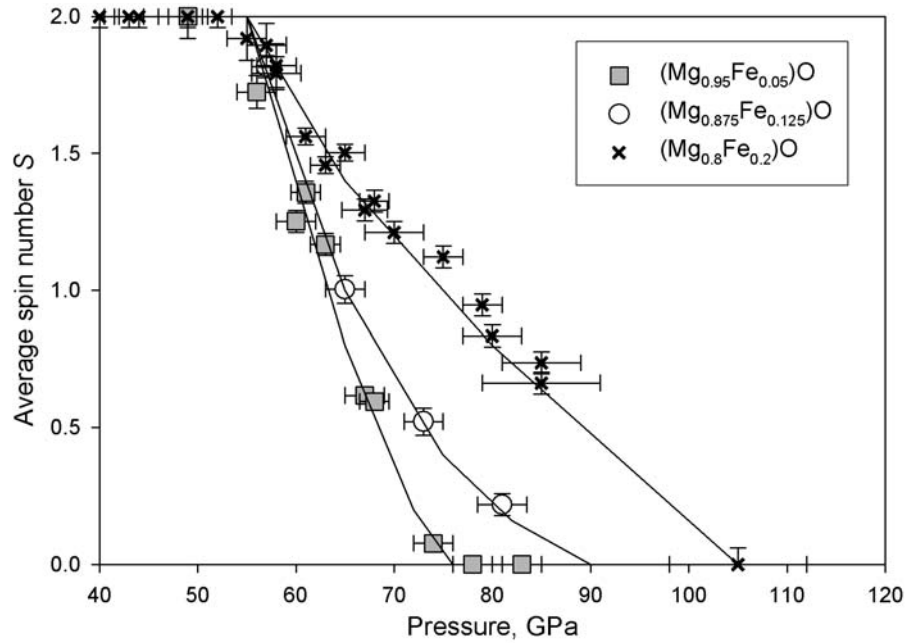


Fig. 3.3-9: Average spin number S of Fe^{2+} in ferropericlasite as a function of pressure. Gray squares – Fe5 sample, open circles – Fe12 sample, crosses – Fe20 sample.

High-temperature measurements (up to 750K) were performed for the Fe5 and Fe20 samples. The Fe5 sample shows a clear negative Clapeyron slope of about -0.03 GPa/K (Fig. 3.3-10). The width of the transition (region of high- and low-spin state coexistence) remains almost constant with temperature. For the Fe20 sample no temperature effect on low-spin abundance was observed, indicating zero Clapeyron slope in the studied temperature range. Assuming zero Clapeyron slope for the Fe20 (mantle composition) sample, the spin crossover in ferropericlasite occurs in a broad region of the Earth's lower mantle, from about 1400 to 2400 km depth. All changes of physical properties associated with this transition would occur gradually and smoothly throughout this wide depth interval in the Earth.

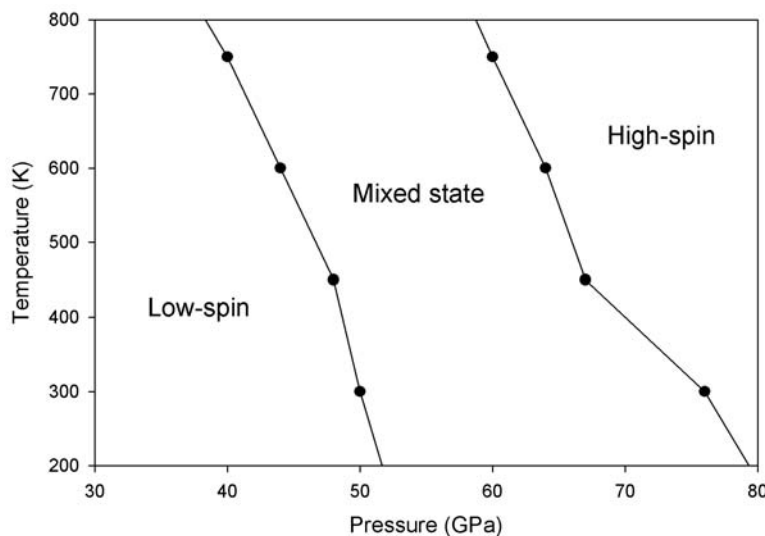


Fig. 3.3-10: Spin crossover in $(\text{Mg}_{0.95}\text{Fe}_{0.05})\text{O}$ ferropericlasite at high P and T – regions of low-, high- and mixed spin state of Fe^{2+} are shown.

k. *Phase transitions in MnO and FeO at low temperatures: A neutron powder diffraction study (A.P. Kantor, L.S. Dubrovinsky, N.A. Dubrovinskaia and I.Yu. Kantor, in collaboration with I.N. Goncharenko/Gif-sur-Yvette)*

A powder neutron diffraction study of MnO and Fe_{0.92}O was conducted at temperatures between 1.5 K and 298 K in order to establish the relationship between magnetic and structural phase transformations. MnO and FeO belong to the highly correlated transition metal monoxides group, and raise continuous interest due to their complex structural, electronic and magnetic properties. At ambient pressure these oxides are paramagnets with a NaCl-like *fcc* structure. A slight departure from cubic symmetry at low temperatures for these oxides can be described as a small contraction (for MnO) or elongation (for FeO) along the three-fold axis. Crystal symmetry, therefore, becomes trigonal (rhombohedral). It was suggested that these crystallographic deformations are a consequence of the exchange interactions that result from antiferromagnetic ordering. All theoretical approaches assume not only strong magneto-structural (or magneto-elastic) coupling, but also coincidence of these two transitions. For MnO the latter seems to be true. A recent study of FeO at high pressures revealed that the magnetic ordering transition occurs at about 5 GPa, while trigonal distortion occurs only above 12 GPa. The existence of a cubic magnetically ordered phase of FeO at high pressures raises the question of its possible existence at ambient pressure and low temperatures.

Powder neutron diffraction studies were performed on G6-1 cold neutron two-axis diffractometer in Laboratoire Léon Brillouin, Saclay, France. A monochromatic neutron beam was selected by a graphite monochromator with initial wavelength of 4.741 Å. The room-temperature lattice parameter *a* of MnO (of 99.99 % purity) was measured by powder X-ray diffraction to be 4.4455(4) Å. The measured cell parameter of FeO sample was 4.296(2) Å, corresponding to Fe_{0.92}O composition. About 150 mg of powder samples were loaded into vanadium capsule and placed in a liquid He cryostat for neutron diffraction measurements.

Figure 3.3-11 shows the temperature variation of the MnO lattice parameter *a* and angle α of the pseudo-cubic cell, calculated from two structural reflections (111) and ($\bar{1}$ 11). Our data are in good agreement with previous X-ray diffraction study results (Fig. 3.3-11). The integrated intensity of a magnetic reflection is proportional to the square of the spontaneous sublattice magnetization $(M/M_0)^2$. Experimentally observed magnetization curves for MnO and FeO are shown in Fig. 3.3-12.

Lattice parameters of cubic FeO are shown in Fig. 3.3-13. Note that in contrast to MnO (Fig. 3.3-11) almost no anomaly in thermal expansion is observed near the Néel transition (around 200 K). The absolute value of $\Delta\alpha$ for FeO is about six times smaller than that for MnO, resulting in higher relative uncertainties. A simple comparison of Figs. 3.3-12 and 3.3-13 shows that magnetic ordering does not coincide with structural distortion. The Ising fit of the FeO magnetization curve in the temperature interval from 150 to 200 K (solid line in Fig. 3.3-12) gives T_N equal to 201.6±0.1 K (expected value of T_N for this composition is about 201.9 K and $\beta = 0.1864$).

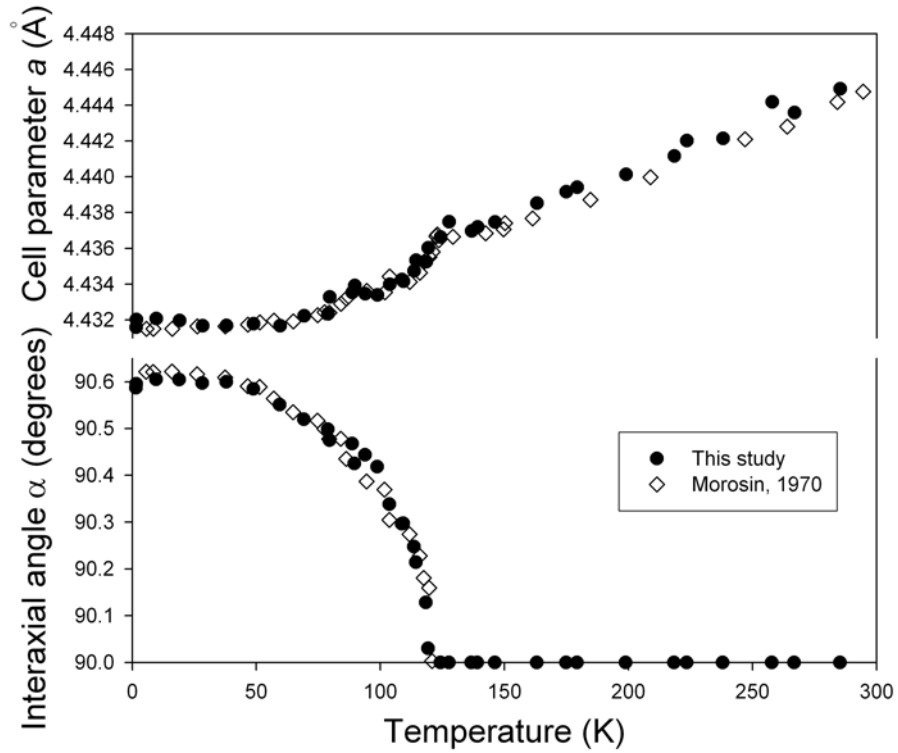


Fig. 3.3-11: Temperature dependence of the unit-cell parameter a (upper graph) and angle of the pseudo-cube cell α (lower graph) of MnO. Solid circles – this study, open diamonds – from Morosin, Phys. Rev. B 1, 236, 1970.

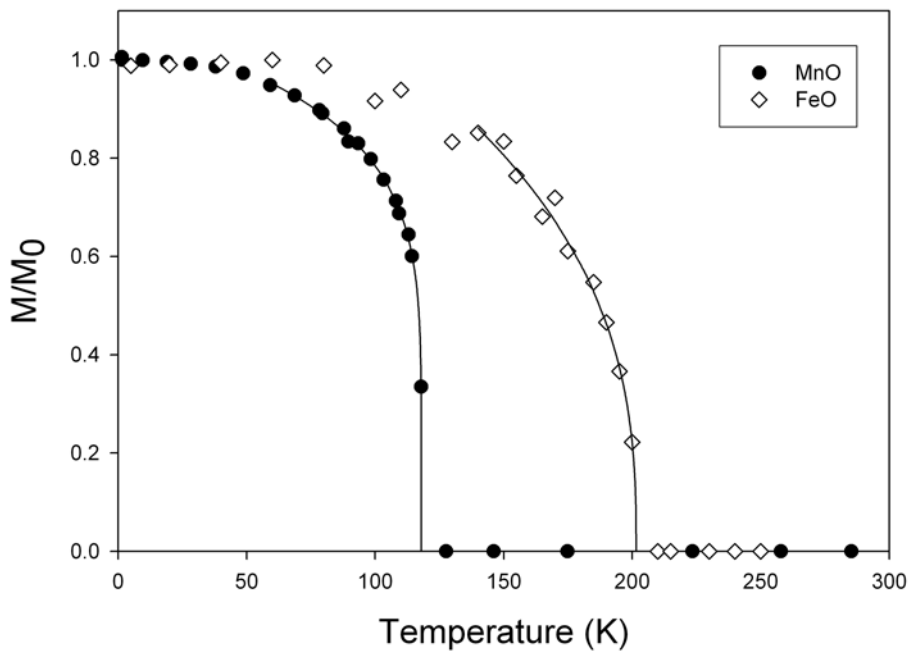


Fig. 3.3-12: Magnetization curves for MnO (solid circles) and FeO (open diamonds). Solid lines show fits to the Ising model. Temperature uncertainties are comparable with the size of the symbols.

In FeO a strong divergence between magnetic (Néel) transition and structural (cubic-to-rhombohedral) transition was observed: the transition temperatures were found to be 201.6 ± 0.1 K and 160 ± 5 K, respectively. Therefore, the magnetically ordered cubic phase of $\text{Fe}_{0.92}\text{O}$ observed at high pressures exists also at ambient pressure over a large temperature range. For MnO these two transitions coincide within the experimental uncertainty.

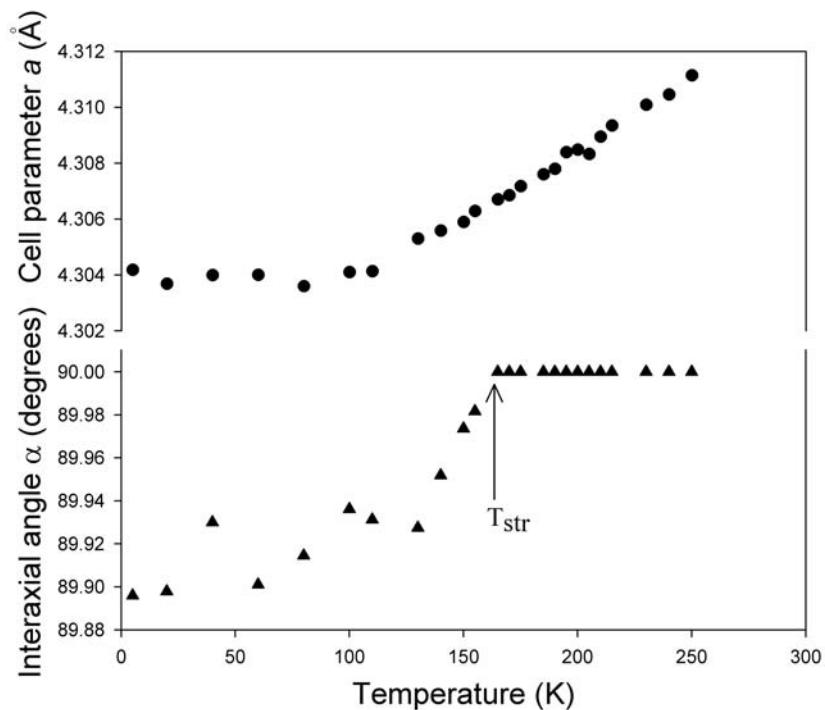


Fig. 3.3-13: Cell parameters a (circles) and α (triangles) of FeO as a function of temperature. T_{str} is a structure transition temperature.

3.4 Physical Properties of Minerals

Surface events such as volcanic eruptions and earthquakes are largely driven by processes occurring within the Earth's interior, which are in turn controlled by the physical and chemical properties of the relevant minerals. Consequently, studies of physical properties in the laboratory remain a focal point of research at Bayerisches Geoinstitut. The use of synthetic material produced under controlled conditions enables the determination of structure and physical property information as a function of the experimental variables (temperature, pressure and/or composition), without influence from complexities such as impurities, defects or unknown thermal history. On the other hand, the use of natural material allows the study of features such as microstructure, which cannot be reproduced in the experimental laboratory. A third approach involves computations of structure and properties, which overcome many of the limitations imposed by experiments.

Compression studies using X-ray diffraction are one of the main tools used for determining elastic properties through equation of state measurements. Such studies provide not only the parameters required for modelling the Earth's interior using seismic data, but also allow insight into compression mechanisms for large classes of compounds (for example, hydrous minerals). Microstructure describes a material on a length scale above the atomic level (often microns to hundreds of microns), and can have a strong influence on physical properties such as diffusion and magnetism. Detailed characterisation using methods such as electron backscattering diffraction and Mössbauer spectroscopy help to elucidate the link between microstructure and bulk behaviour. Transition metal alloys, oxides and silicates are not only abundant constituents of the Earth's interior, but also their presence, even as minor components, can have dramatic effects on physical properties due to the many transition possibilities of their electronic structure. Studies focus both on major constituents of the Earth's mantle as well as model compounds where unusual behaviour may be relevant for a large range of similar phases.

a. *Crystal structure and compression of an iron-bearing Phase A to 33 GPa (C.M. Holl and J.R. Smyth/Boulder; D.J. Frost, in collaboration with M.H. Manghnani, G.M. Amulele and M. Sekar/Honolulu; V.B. Prakapenka and G. Shen/Chicago)*

Phase A is a dense hydrous magnesium silicate phase that may be stable in the cold regions of subducting ultramafic lithosphere. It has an extremely high water content (~ 12 wt.% H₂O). Crystals of iron-bearing Phase A, Mg_{6.85}Fe_{0.14}Si_{2.00}O₈(OH)₆, up to 200 μm in diameter were grown in the 5000 tonne press at 12 GPa and 1250°C. The material was studied by single-crystal X-ray diffraction at ambient conditions and by high-pressure powder diffraction using synchrotron radiation to 33 GPa. Unit cell parameters at room temperature and pressure from single crystal measurements are $a = 7.8678(4) \text{ \AA}$, $c = 9.5771(5) \text{ \AA}$, and $V = 513.43(4) \text{ \AA}^3$. The crystal structure was refined from single X-ray diffraction data at ambient conditions. There is

no evidence of ordering of Mg and Fe among the three distinct octahedral sites in the structure.

Fitting of the pressure-volume data to a third-order Birch Murnaghan isothermal equation of state results in $V_0 = 512.54(43) \text{ \AA}^3$, $K_0 = 107.2(28) \text{ GPa}$ and $K_0' = 5.7(3)$. Compression is strongly anisotropic with the a -axis, which lies in the plane of the distorted close-packed layers, approximately 29 % more compressible than the c axis, which is normal to the plane. Compared to pure-Mg Phase A, unit cell parameters are larger and compressibilities are slightly lower. M2 and M3 octahedral volumes are 0.8 % and 0.6 % larger than in pure-Mg Phase A. The O2–O3 and O4–O3 polyhedral edges, which roughly correspond to the O-H bond directions, are longer, possibly indicating weaker H bonding in the Fe-bearing structure which may influence behaviour in subducting slab environments. These results are in excellent agreement with the elastic properties measured to 11 GPa by Brillouin spectroscopy at the University of Illinois which yield a bulk modulus K of 106 GPa and K_0' of 6.0.

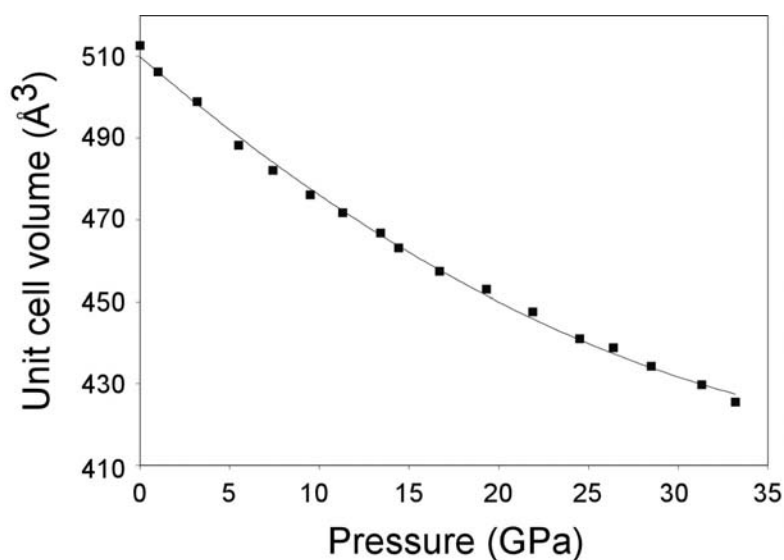


Fig. 3.4-1: Compression curve for Phase A measured in the diamond anvil cell. The symbols represent the data from the present powder XRD study, and the line is a best-fit polynomial curve to the data. Error bars based on internal instrument precision are smaller than the symbols.

b. Compressional behaviour and P -induced structural evolution of topaz, $\text{Al}_2\text{SiO}_4(\text{F},\text{OH})_2$
(G.D. Gatta, F. Nestola and T. Boffa Ballaran)

Topaz, $\text{Al}_2\text{SiO}_4(\text{F},\text{OH})_2$, is one of the most important F/OH-bearing silicates found in different geological environments: it occurs as an accessory mineral in F-rich granitic rocks, it is associated with pneumatolithic/hydrothermal events and it is found in ultra-high pressure terrains. Topaz may also be found in detrital sediments near areas of acid intrusive rocks. Due to its hardness (H8 on the Mohs scale), natural or synthetic topazes are used as materials for

ornamental purposes, and sometimes for the manufacture of abrasives, coated paper, grindstones, sharpening stones and scouring powders.

The crystal structure of topaz was first solved in the space group $Pbnm$. Later, the crystal chemistry of topaz has been an object of debate concerning the topological configuration of the OH group and the space group along the solid solution $Al_2SiO_4F_2-Al_2SiO_4(OH)_2$. It appears that for natural topazes with $OH/(OH+F)<0.4$, the crystal structure is well described in the $Pbnm$ space group with one H-site. In contrast, the crystal structure of the synthetic $Al_2SiO_4(OH)_2$ end-member is better described with the $Pbn2_1$ space group with two non-equivalent and partially occupied (50 %) H-sites. The thermal and pressure behaviour of a natural topaz ($Al_{2.01}Si_{1.00}O_4F_{1.57}(OH)_{0.43}$) was investigated by means of *in situ* X-ray single-crystal diffraction. The high-pressure lattice parameters have been measured up to about 6.8 GPa. The bulk modulus ($K_{T0} = -V_0(\partial P/\partial V)_{P0}$) was calculated on the basis of the volume data collected up to 6.2 GPa with a truncated second-order Birch-Murnaghan equation of state (BM-EOS), *i.e.*, with the bulk modulus P -derivative ($K'=(\partial K_{T0}/\partial P)_{P0}$) value fixed to 4. The calculated bulk modulus ($K_{T0} = 154(2)$ GPa) differs significantly from the elastic stiffness ($C=174.3$ GPa) reported in the literature measured by means of ultrasonic resonance experiments. Although the isothermal bulk modulus is always smaller than the elastic stiffness, such a large difference may also be due to the fact that the K' value was fixed to 4. The aim of this study was therefore to investigate the high-pressure elastic behaviour of a natural topaz by means of *in situ* single-crystal diffraction up to pressures in excess of 10 GPa for a better description of the elastic parameters of this hard material, and to describe on the basis of the high-pressure structural refinements the main deformation mechanisms that drive the P -induced structural evolution.

A natural single crystal of a pneumatolithic/hydrothermal topaz from Ouro Preto, Minas Geras, Brazil was used in this study. Electron microprobe analysis was performed and the chemical formula was $Al_{2.00}Si_{1.05}O_{4.00}(OH_{0.26}F_{1.75})$. Accurate lattice parameters were measured up to 10.55(5) GPa with the crystal in a BGI-type diamond anvil cell (methanol:ethanol:water 16:3:1 mix was used as hydrostatic pressure-transmitting medium) on a Huber four-circle diffractometer. Intensity diffraction data were collected on a Xcalibur-Oxford Diffraction diffractometer at pressures of 0.0001 (with the crystal in the DAC), 3.14(5), 5.79(5) and 8.39(5) GPa. The reflection conditions are in agreement with the space group $Pbnm$. The evolution of the lattice parameters with P shows that no phase transition occurs within the pressure range investigated (Fig. 3.4-2). Unit-cell volume data were fitted with a third-order BM-EOS. The third-order BM-EOS parameters, simultaneously refined using the data weighted by the uncertainties in P and V , are: $V_0= 345.57(7)$ Å³, $K_{T0}= 164(2)$ GPa and $K'= 2.9(4)$. The axial-EOS parameters are: $a_0=4.6634(3)$ Å, $K_{T0}(a)= 152(2)$ GPa, $K'(a)= 2.8(4)$ for the a -axis; $b_0=8.8349(5)$ Å, $K_{T0}(b) = 224(3)$ GPa, $K'(b)=2.6(6)$ for the b -axis; $c_0= 8.3875(7)$ Å, $K_{T0}(c) = 137(2)$ GPa, $K'(c) = 2.9(4)$ for the c -axis. The magnitude and the orientation of the principal Lagrangian unit-strain ellipsoid were determined. At $P-P_0= 10.55$ GPa, the ratio $\epsilon_1:\epsilon_2:\epsilon_3$ is 1.00:1.42:1.56, with $\epsilon_1\parallel b$, $\epsilon_2\parallel a$, $\epsilon_3\parallel c$ and $|\epsilon_3| > |\epsilon_2| > |\epsilon_1|$. The

four structural refinements performed at different pressures allowed a description of the structural evolution. The Al-O and Si-O bond distances decrease as a function of pressure with a consequent decrease of the Al-octahedral and Si-tetrahedral volumes. A minor effect of polyhedral tilting is observed between Al octahedra connected by a F-bridge. The angle Al-F(O)-Al is $143.5(2)^\circ$ under room conditions and decreases down to $139.9(5)^\circ$ at $8.39(5)$ GPa. The main structural deformation mechanism under pressure is therefore represented not by polyhedral tilting but rather by the shortening of the polyhedral bond distances, which implies a reduction of the polyhedral volumes as expected for a “dense” orthosilicate.

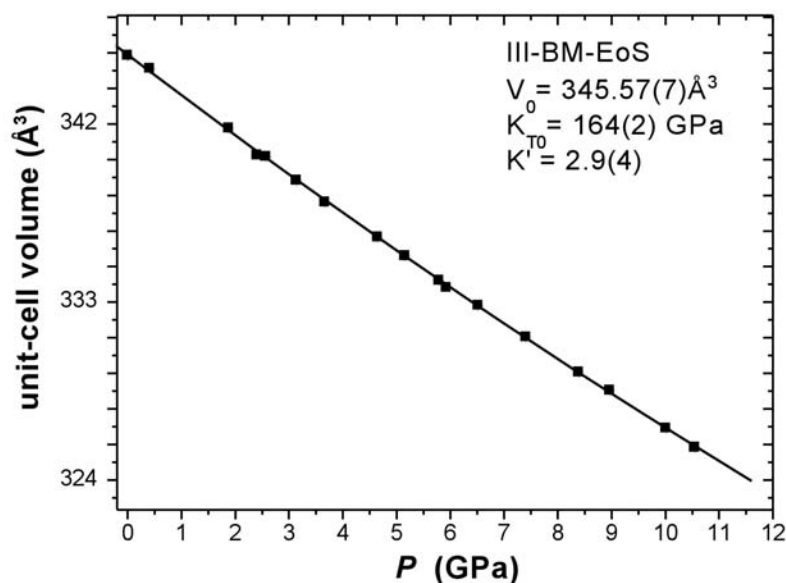


Fig. 3.4-2: Evolution of the unit-cell volume of topaz with P . The solid line represents a third-order Birch-Murnaghan equation-of-state fit. The *e.s.d.* values are slightly smaller than the size of the symbols.

c. *Microstructural control of Fe-Mg interdiffusion in magnesiowüstite (F. Heidelbach, M.P. Terry, C.A. McCammon, in collaboration with M. Bystricky/Toulouse and C. Holzappel/Saarbrücken)*

We examined the effects of deformation on a continuous Fe/Mg interdiffusion reaction between ferropericlase and periclase to provide insight into the interplay between metamorphic reactions and deformation. A torsion experiment was carried out on a diffusion couple of polycrystalline cylinders of periclase (MgO) and ferropericlase ($\text{Mg}_{0.6}\text{Fe}_{0.4}\text{O}$). A change in diffusion coefficient by a factor of 1.2 to 1.4 (between $X_{\text{FeO}} = 0.1$ and 0.3) as a function of increasing shear strain was observed (see BGI Annual Report 2004 and Fig. 3.4-3). In the diffusion direction there is no net strain, and the stress is equal to the confining pressure of the experiment such that the change in diffusion coefficient is unlikely to be caused by these parameters. Since varying oxygen fugacity (or point defect concentration) along the radius could cause a change in diffusion coefficient, the Fe^{3+} content was measured

with Mössbauer spectroscopy in three locations along the radius of the sample (in the centre, near the edge and at the edge) and was found to be constant at 5 % $\text{Fe}^{3+}/\Sigma\text{Fe}$ within the error of measurement.

The frequency of subgrain (misorientation angle $< 15^\circ$) and grain boundaries was measured as a function of shear strain by mapping the grain structure of the deformed ferropericlyase with electron backscattering diffraction (EBSD) in the scanning electron microscope (SEM). The frequency of both types of boundaries increases with increasing strain but only the frequency of grain boundaries shows a good correlation with the change in diffusion coefficient (Fig. 3.4-4), making it a likely candidate for the enhanced diffusion rates at higher strains. The diffusion coefficients may also be influenced by the density of dislocations which were introduced into the ferropericlyase by the deformation. The dislocation density is proportional to the stress, which in torsion experiments in dislocation creep increases rather rapidly from the centre and then flattens out toward the edge. In contrast the observed change in diffusion coefficient increases rather slowly in the centre and then rapidly near the edge, making dislocation density an unlikely candidate to cause this change.

The results of this study show that the frequency of grain boundaries (or grain size) has an influence on the diffusion coefficient. The effect is likely due to the enhanced diffusion along grain boundaries, which makes overall diffusion more efficient. Our attempts to show the enhanced diffusion along boundaries with high resolution element mapping in the electron microprobe were not truly conclusive, since the absolute differences in composition are small and effects of topography at the grain boundaries could not be excluded. Our results indicate also that subgrain boundaries as well as dislocations do not appear to form effective pathways for enhanced diffusion.

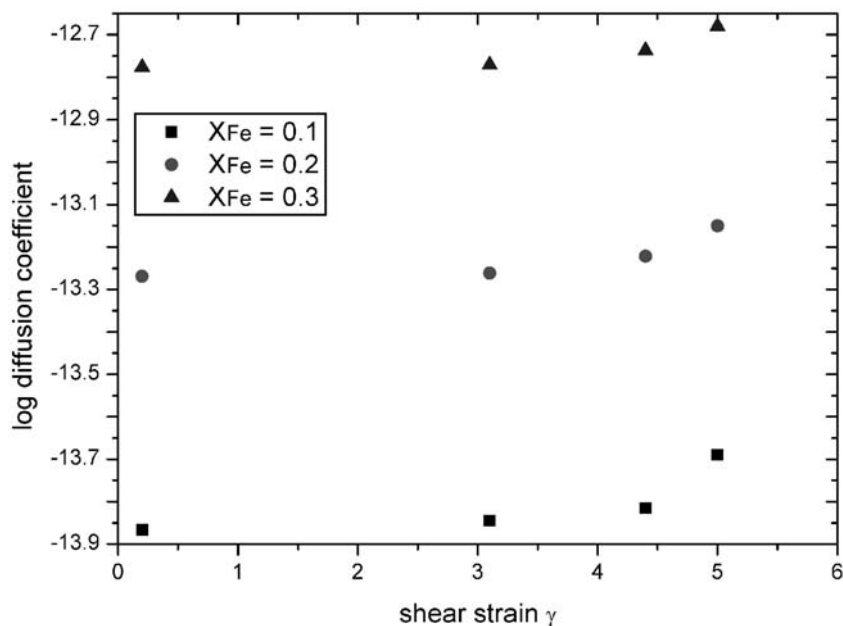


Fig. 3.4-3: Diffusion coefficients for different Fe contents as a function of shear strain.

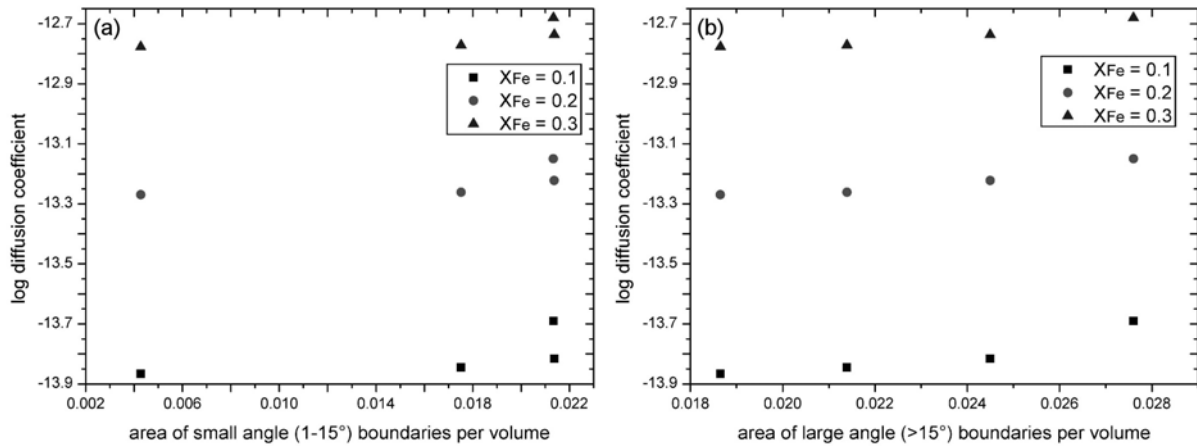


Fig. 3.4-4: Frequency of small (a) and large angle grain boundaries (b) with increasing shear strain as a function of diffusion coefficient for Fe in ferropericlase with different Fe contents.

d. Lamellar magnetism in titanohaematite: A Mössbauer study (C.A. McCammon, in collaboration with S.A. McEnroe and P. Robinson/Trondheim)

Nanosize lamellar structures that form in slowly cooled igneous and metamorphic rocks can have unusually high natural magnetic remanence that is stable over timescales of one billion years or more. This behaviour has been attributed to lamellar magnetism in the system hematite-ilmenite, where ferrimagnetic contact layers form between paramagnetic ilmenite and antiferromagnetic hematite. Such stable magnetic memory is of importance for planetary magnetism, particularly for planets such as Mars where the magnetic field is no longer present, and for potential industrial applications such as the development of highly stable magnetic storage units. Mössbauer spectroscopy provides a unique probe of the iron environment, enabling the quantitative determination of iron distribution and abundance, with insight into parameters that determine the magnetic properties. To investigate the role of iron in lamellar magnetism, we undertook a study of rocks from several different regions using Mössbauer spectroscopy.

Titanohaematite grains (Fig. 3.4-5) were identified optically on polished thin sections of slowly cooled rocks from Lerhuvud and Gödestad (both in southern Sweden) and the Russell Belt (Adirondack Mountains, USA). Grains were removed from thin sections with a microdrill, and mounted on a Mössbauer spectrometer fitted with a point source. Room-temperature Mössbauer spectra are dominated by magnetically ordered Fe^{3+} in hematite, with a smaller absorption corresponding to paramagnetic Fe^{2+} in ilmenite (Fig. 3.4-6). Minor absorption is also observed from magnetite and pyrite in some grains. There is no evidence for superparamagnetic hematite in any of the spectra. Comparison of Mössbauer spectra of the natural samples with those from synthetic hematite-rich titanohematite solid solutions provides a measure of the iron environment in natural titanohematite, showing that there is

only moderate deviation from the ideal hematite local environment. The absence of Fe^{3+} in ilmenite indicates that ilmenite lamellae are close to the endmember composition. All grains taken from the same thin sections show similar ilmenite:hematite area ratios, and the two different samples from Gödestad also show similar ratios, suggesting a similar bulk composition. Based on models of cation and magnetic ordering, the proportion of iron involved in the contact layers can be determined, and combined with information from the Mössbauer spectra, provide constraints on the density of lamellae, which effectively controls the magnetisation.

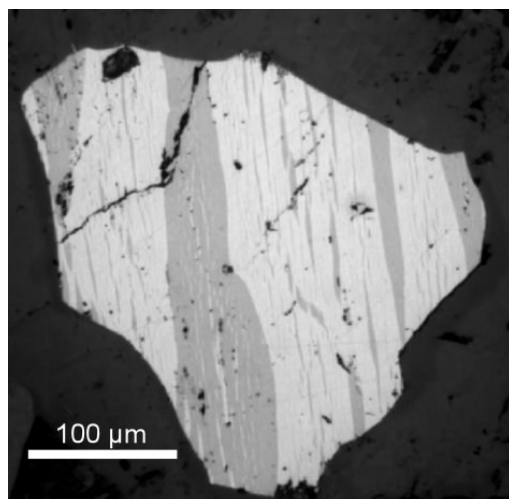


Fig. 3.4-5: Reflected light photomicrograph of a titanohaematite grain containing ilmenite lamellae. The lamellar structure can also be seen on a nanoscale as revealed by TEM measurements.

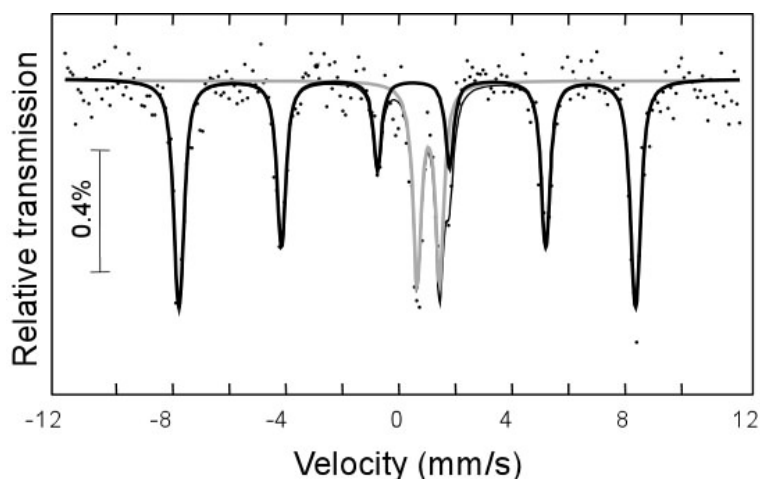


Fig. 3.4-6: Room-temperature Mössbauer spectrum of a 200 μm diameter grain of titanohaematite containing ilmenite lamellae. The subspectra arise from titanohaematite (outlined in black) and ilmenite (outlined in grey) with no evidence for superparamagnetic behaviour. The relative areas corrected for iron concentration provide constraints on the abundance of lamellae.

e. *In situ* combined X-ray diffraction and conductivity measurements of Fe-Ni alloy (20 wt.% Ni) (A.Yu. Kuznetsov, Y. Volkova/Yekaterinburg, A.V. Kurnosov, I.Yu. Kantor, N.A. Dubrovinskaia and L.S. Dubrovinsky, in collaboration with V.P. Dmitriev/Grenoble)

X-ray diffraction measurements and simultaneous X-ray diffraction and conductivity measurements of Fe-Ni alloy with 20 wt.% of nickel have been carried out in order to investigate phase relations of the Fe₂₀Ni alloy in the pressure-temperature range from ambient conditions up to 50 GPa and 700 K. Compressed samples of *bcc*-Fe₂₀Ni transformed to an *fcc* polymorph at ambient temperature, in contrast to the *bcc-hcp* phase transition observed in previous studies of Fe-Ni alloys with nearly the same Ni content. This shift to low pressures and temperatures of the stability field of the *fcc* phase in the phase diagram can be attributed to specific strain/stress conditions induced in the material in our study. Under these conditions, the generated elastic field shifts the stability limits of the phases and stabilises the *fcc* phase at essentially moderate pressures and temperatures compared to what would be expected based on previous high-pressure studies of Fe-Ni alloys.

A small flat chip (approximately 10 μm thickness and 50 μm diameter) of a single crystal of *bcc*-Fe₂₀Ni was loaded into a diamond anvil cell (DAC) together with LiF as a pressure medium. A sample chamber formed in a rhenium gasket had approximately 120 μm diameter and 40 μm thickness. The crystal was oriented with the [110] crystallographic direction parallel to the direction of the uniaxial force applied to the anvils of the DAC. For simultaneous X-ray diffraction and conductivity measurements, we used a specially developed sample setup with two halves of a rhenium gasket covered by gold and electrically isolated by nanocrystalline diamond powder (see Fig. 3.4-7). Ruby chips provided a pressure calibration using the standard ruby-fluorescence technique.

In situ X-ray diffraction data were measured at the Swiss-Norwegian beam lines of the European Synchrotron Radiation Facility using a monochromatic ($\lambda=0.7111 \text{ \AA}$) X-ray beam. Diffraction patterns were collected using an image plate detector (MAR-3450). Externally heated DACs developed at Bayerisches Geoinstitut were employed to generate high pressures and high temperatures.

The *bcc* phase of the starting sample transformed through a two-phase region into an *fcc* phase at about 14 GPa. Very weak diffuse spots at 2θ values expected for the *hcp* phase were present in the X-ray diffraction images together with the Debye-Scherrer diffraction rings of the *fcc* phase. On heating above 500 K, only the *fcc* phase was present in the diffraction patterns. The most interesting result of the experiments was the observation of a second *fcc* phase in a certain range of pressures and temperatures. The second *fcc* phase has a lower density and becomes the only phase present at higher pressures and temperatures.

The simultaneous conductivity and X-ray diffraction data are consistent with our conclusion about two density states of Fe₂₀Ni alloy and provide important information about

conductivity properties of the observed phases. From Figure 3.4-8 it is deduced that the resistance of the low-density *fcc* and the *bcc* phases decreases with increasing pressure, while the resistance of the high-density *fcc* phase has the opposite behaviour and gives an overall increase of the resistance at pressures above 10-12 GPa.

A fit of the experimental data to the Birch-Murnaghan equation of state gives the following parameters for the high-density *fcc* phase: $V_0=45.08(6) \text{ \AA}^3$, $K=160(5) \text{ GPa}$, $K'=5.0(3)$. These values are in excellent agreement with previous high-pressure studies of $\text{Fe}_{80}\text{Ni}_{20}$ alloy at room temperature. Our high-temperature data show, however, that in contrast to pure iron, the Fe_{20}Ni alloy has an increasing volume thermal expansivity as a function of pressure with the sign changing from negative at low pressure to positive above 15-20 GPa. Extension of our studies to higher pressures and temperatures is required in order to reduce the extrapolation needed to apply the experimental results to the P - T conditions of the Earth's core. A confirmation of the increased thermal expansivity in Fe-Ni alloy at higher pressures may have important implications for the structure and chemical composition of the Earth's inner core.

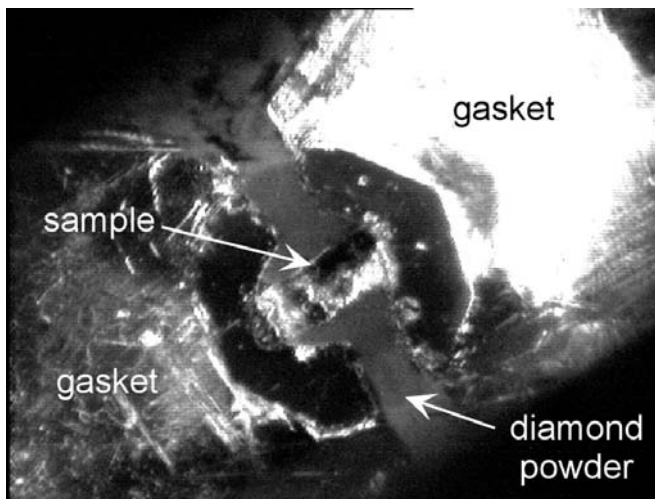


Fig. 3.4-7: The image of the sample arrangement in a DAC at 10 GPa and 420 K. The picture was taken looking through a diamond plate that was used as a second anvil during simultaneous conductivity and X-ray diffraction measurements.

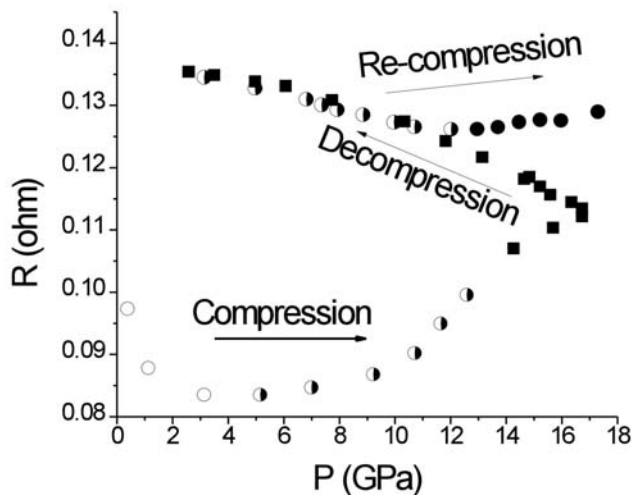


Fig. 3.4-8: Room-temperature behaviour of the electrical resistance of Fe_{20}Ni alloy. Open circles: *bcc* phase; half-open circles: mixture of *bcc* and high-density *fcc* phases; solid squares: mixture of high- and low-density *fcc* phases; solid circles: low-density *fcc* phase.

f. Absence of charge ordering in Fe_3O_4 magnetite under pressure (M.J. Wenzel/Berkeley and G. Steinle-Neumann)

Fe_3O_4 magnetite shows a number of interesting and unusual electronic properties that have only partly been understood to date. Of particular interest is the discovery of Verwey that electrical conductivity decreases by two orders of magnitude as Fe_3O_4 is cooled through a transition temperature T_V of ~ 120 K. At room temperature and pressure magnetite crystallises in the cubic spinel structure ($Fd\bar{3}m$) in which Fe ions occupy one tetrahedral (A) site and two octahedral (B) sites in a cubic close packed array of O atoms. In magnetite the A sites are nominally occupied by Fe^{3+} , while the B sites are nominally occupied by equal numbers of randomly distributed Fe^{3+} and Fe^{2+} ions, resulting in an inverse spinel structure. Magnetite is ferrimagnetically ordered with the Fe atoms on the A sublattice having opposite spin to the Fe on the B sites. The metallic conductivity of magnetite above T_V is attributed to electron hopping between octahedral sites; that is, the B sites are dynamically equivalent with an effective occupation of $Fe^{2.5+}$. The Verwey transition is then attributed to localisation and ordering of charge, or a structural transition.

With increasing pressure, T_V decreases, and the Verwey transition disappears at ~ 8 GPa. Fe_3O_4 undergoes a phase transition to a metallic orthorhombic structure at ~ 19 GPa at room temperature, although the exact structure is controversial. Additionally, charge localization has been proposed under compression based on *in situ* Mössbauer spectroscopy in the diamond anvil cell. Based on changes in the spectra, a transition at ~ 8 GPa and 300 K is proposed: from Fe^{3+} on the A site and two $Fe^{2.5+}$ on the B sites through a charge-localized inverse spinel state of Fe^{3+} on the A site and Fe^{2+} and Fe^{3+} on the B sites, to a state with the normal spinel structure with Fe^{2+} on the A site and two Fe^{3+} on the B sites. This charge transfer is supposed to occur at higher temperature with increasing pressure.

We use an all-electron DFT method, the linearised augmented plane wave (LAPW) method as implemented in the Wien2k code. We use both the generalised gradient approximation (GGA) to the exchange and correlation potential and the GGA+U approximation. Here we adopt a value of $U=4.6$ eV, consistent with previous work on both FeO and Fe_3O_4 , but also consider smaller values of U . Computations are performed for a cell setup in which the two octahedral (B) Fe sites in Fe_3O_4 (crystallographically equivalent) are split, resulting in an orthorhombic description of the magnetite structure. This allows charge transfer to take place between the two B sites. We perform reciprocal space sampling with a $4\times 4\times 4$ k -point mesh for the full Brillouin zone. $R\cdot K_{\max}=7.0$ is chosen, determining the size of the basis set. Computations are performed for a volume range of 0.80 to 1.05 times the experimental zero pressure volume V_0 . In order to analyse magnetic moments and electric states on the sites, we choose touching muffin tin radii to capture a maximum extent of charge density difference within the muffin tin spheres.

A third-order Birch-Murnaghan equation of state fit to the resulting energies yields a bulk modulus (K) of 175.5 GPa and a pressure derivative of the bulk modulus (K') of 3.6. The

value for K is within the range of those determined by experiment. In Figure 3.4-9 we show the magnetic moment versus volume (V) per atom for $0.8 < V/V_0 < 1.05$ for each cation site using GGA and GGA+U. The highest compression is equivalent to a pressure of 61 GPa. In agreement with experiment, the octahedral sites are equivalent at zero pressure. We are unable to observe any significant differences between octahedral sites in the magnetic moment or electronic field gradient. A lack of charge localisation is consistent with measurements that show magnetite to be metallic with increasing conductivity up to ~ 20 GPa. Consequently, the Mössbauer measurements remain unexplained. We are expanding our study to include characterisation of the hyperfine field and a detailed analysis of the electronic density of states, which may provide additional insights.

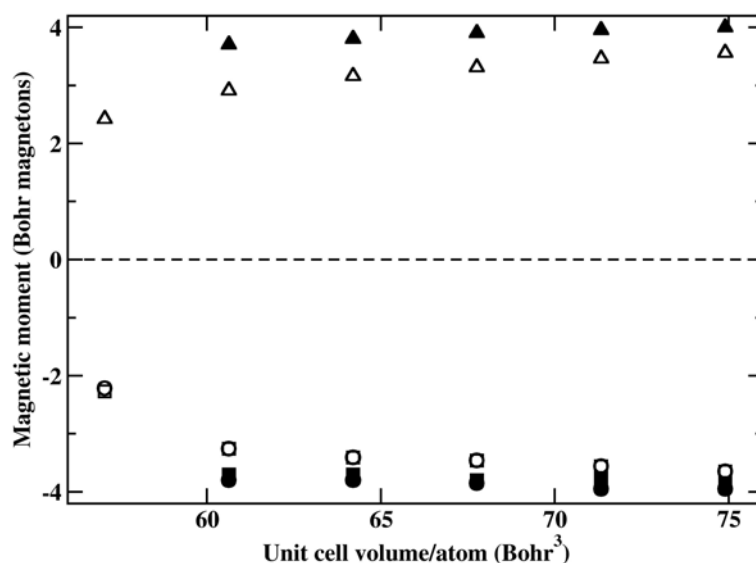


Fig. 3.4-9: Magnetic moments as a function of compression (volume/atom). Open symbols are for GGA computations, filled symbols for the GGA+U ($U=4.6$ eV) computations. The triangles show magnetic moments on the A site, and squares and circles the values for the two B sites.

g. *MnO high-pressure phase diagram: Magnetic ordering and lattice distortion (I.Yu. Kantor and L.S. Dubrovinsky, in collaboration with I.N. Goncharenko/Saclay)*

Our recent Mössbauer, neutron and X-ray diffraction study of non-stoichiometric FeO revealed that the magnetic ordering (Néel) transition and rhombohedral lattice distortion are decoupled over the entire P - T range. We performed a high-pressure and low-temperature neutron diffraction study of MnO, which belongs to the same group of highly correlated transition metal oxides.

Powder neutron diffraction studies were performed on the G6-1 cold neutron two-axis diffractometer in Laboratoire Léon Brillouin, Saclay, France. A monochromatic neutron beam was selected by a graphite monochromator with initial wavelength of 4.741 Å. The

diffractometer was equipped with a linear 400-cell BF_3 multidetector with a 0.1° step. Synthetic MnO powder was loaded in a sapphire-anvil high-pressure cell that was placed in a liquid-He cryostat for low-temperature measurements. Diffraction peak characteristics (position, FWHM and integrated intensity) were extracted for each peak individually using a PeakFit software package assuming a linear local background.

We collected diffraction patterns in a 1.5-250 K temperature range at 5 different pressures up to 9 GPa. In the available 2θ range only the 111 structural reflection of the cubic (high-temperature) phase was observed. Upon the cubic-to-rhombohedral transition it should split into two reflections, 111 and $\bar{1}\bar{1}\bar{1}$, which indicates the temperature of lattice distortion. Due to the nearly 100 % preferred orientation of crystallites in the $\langle 111 \rangle$ direction perpendicular to the diffraction plane (that is the loading direction of the high-pressure cell), only the $\bar{1}\bar{1}\bar{1}$ reflection of a low-symmetry unit cell was observed, but this is sufficient to determine the transition temperature (Fig. 3.4-10a). Magnetization (M/M_0) was determined from the $3/2\ 1/2\ 1/2$ magnetic reflection integrated area, and its temperature dependence provides the Néel temperature (Fig. 3.4-10b).

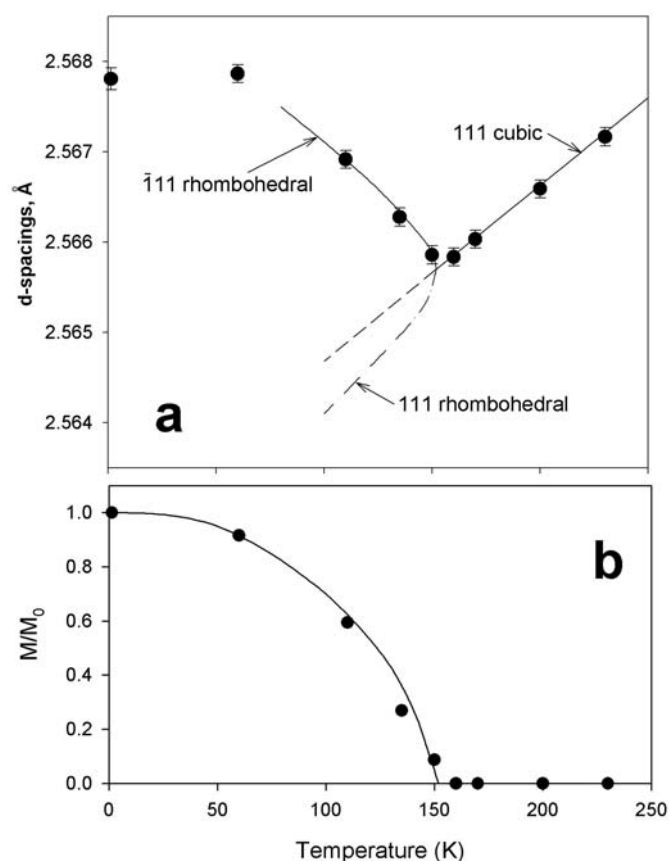


Fig. 3.4-10: a) Temperature dependence of the 111 reflection d -spacing of MnO at 1.9 GPa. The single cubic reflection splits into two below ~ 150 K. The $\bar{1}\bar{1}\bar{1}$ branch is shown, while the 111 branch is “invisible” due to a preferred orientation effect (dashed-dotted line). b) Magnetization curve of MnO at 1.9 GPa.

The phase diagram of MnO up to 9 GPa is shown in Fig. 3.4-11. Below 3.5 GPa the magnetic and structural transitions coincide, indicating strong magnetoelastic coupling. Above a critical pressure of 3.5 GPa the two transitions are decoupled and diverge with increasing pressure. Extrapolation of the structural transition boundary agrees well with the transition pressure of ~ 30 GPa at room temperature reported in the literature. The negative pressure slope of magnetic ordering temperature is unusual and was not reported so far for MnO.

The critical pressure of 3.5 GPa agrees well with previously reported changes from first-order to a tricritical type of magnetic ordering transition. At the same pressure the C_{44} elastic constant derivative changes sign from positive to negative. All these features point to a change in the fundamental physical interactions in MnO that occur at these pressures.

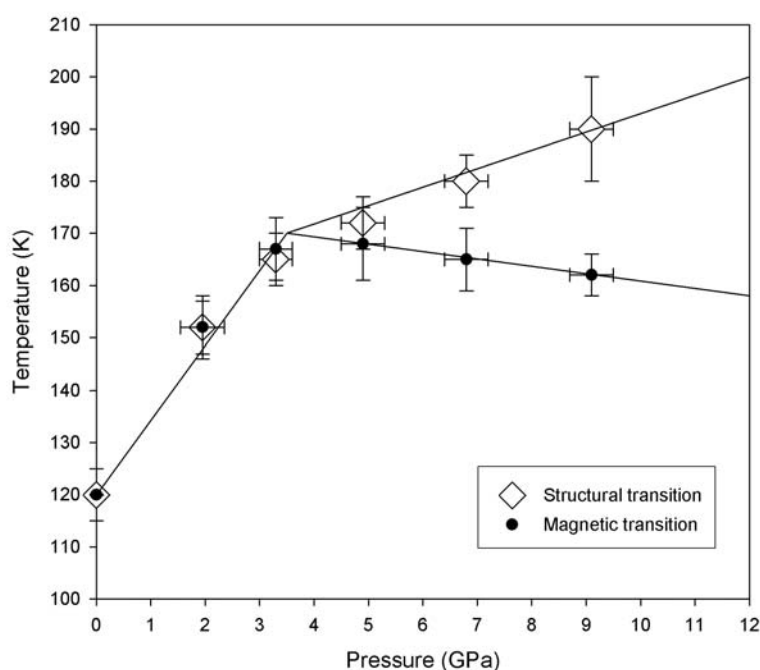


Fig. 3.4-11: MnO phase diagram. Circles indicate the Néel transition; diamonds indicate structural lattice distortion.

h. *Preliminary study of iron behaviour during the breakdown reaction of $(Mg,Fe)_2SiO_4$ to $(Mg,Fe)SiO_3$ perovskite + $(Mg,Fe)O$ (J. Rouquette, D.J. Frost, C.A. McCammon, I.Yu. Kantor and L.S. Dubrovinsky)*

The strong seismic discontinuity at 660 km has long been identified with the breakdown of ringwoodite to $(Mg,Fe)SiO_3$ -perovskite and $(Mg,Fe)O$ based on high-pressure experiments in the system $MgO-FeO-SiO_2$. Iron is present almost exclusively as Fe^{2+} in the olivine starting material, but becomes partly oxidised during the breakdown reaction to satisfy the crystal chemistry of the perovskite phase. Since iron oxidation state can have a significant effect on physical properties, and phases such as Fe metal may be produced during the breakdown

reaction to balance charge, an understanding of iron behaviour is critical to assessing the likely implications for mantle behaviour. We therefore undertook a systematic study of the breakdown reaction in laser-heated diamond anvil cells and multianvil press experiments, and report preliminary results that focus on Raman spectra collected on the high-pressure assemblages.

We used both synthetic ^{57}Fe -enriched olivine and natural San Carlos olivine as starting materials. Diamond anvil cell (DAC) experiments used a Re gasket with NaCl as a pressure transmitting medium, and samples were loaded under argon to avoid oxidising conditions. Samples were heated at high pressure using a YAG laser. In multianvil press (MAP) experiments the starting olivine sample was mixed with metallic iron and an iron capsule was used to maintain reducing conditions. Samples were run at 25-26 GPa for one hour at 1800-2000 °C. Raman spectra were collected using an argon-krypton laser (488, 514.5 and 647.1 nm), a He-Ne radiation source (632 nm), and a 1064 nm FTIR excitation line.

The Raman spectra of DAC run products show no peaks from $(\text{Mg,Fe})\text{SiO}_3$ perovskite, and are dominated by a strong fluorescence possibly related to an electronic transition of iron-bearing clusters in $(\text{Mg,Fe})\text{O}$. In contrast the Raman spectra from MAP experiments showed clear peaks from ringwoodite and $(\text{Mg,Fe})\text{SiO}_3$ perovskite, with much weaker fluorescence possibly arising from contamination of $(\text{Mg,Fe})\text{O}$ by Cr^{3+} from the LaCrO_3 furnace. The complete decomposition of ringwoodite was observed in MAP run products only at the maximum P - T conditions, but even at those conditions different types of Raman spectra were observed that may correspond to different crystallisation steps of the perovskite phase. Experiments using San Carlos olivine as a starting material and run at the highest P - T conditions showed evidence for $\alpha\text{-Fe}_2\text{O}_3$, despite the presence of iron metal. Further experiments, including the collection of Mössbauer spectra at high pressure, are planned to help in further characterising the nature of iron behaviour during the breakdown reaction of $(\text{Mg,Fe})_2\text{SiO}_4$.

3.5 Fluids and their Interaction with Melts and Minerals

Although aqueous and CO₂-rich fluids only occur in small quantities in the Earth's interior, they are very important agents of chemical transport. Many metals that are used in our daily lives are only commercially available because they are greatly enriched in some ore deposits due to fluid transport. It has often been noted that some types of deposits, particularly of tin, are often related to fluorine enrichments. However, both the speciation of fluorine in hydrothermal fluids and the effect of fluorine on the transport of major and trace elements are very poorly known. In the last year, the effect of fluorine on the solubility of silica and of cassiterite SnO₂ was experimentally studied. In order to study cassiterite solubility, a new technology was developed to generate synthetic inclusions of fluids saturated with cassiterite. Fluorine greatly enhances the solubility of both silica and cassiterite. A thermodynamic analysis of the data suggests that Si(OH)₂F₂ is a major species in the fluid. The experimental data also show that in the presence of fluorine, tin may be enriched in the fluid to exceedingly high concentrations.

While the solubility of water in nominally anhydrous mantle minerals is by now a well-established field of research with important implications both for geodynamics and for the global water cycle, the solubility of carbon in most mantle minerals was virtually unknown until a few years ago. This has changed by the development of new experimental and analytical methods at the Geoinstitut, which allow carbon to be detected in minerals even at concentrations below the ppm level. In the recent years, these methods were used to study carbon solubility in all major mantle minerals, including the high-pressure phases of the transition zone and the lower mantle. Carbon solubility in all of these phases was found to be exceptionally low, suggesting that most of the carbon in the interior of the Earth is hosted by carbonates.

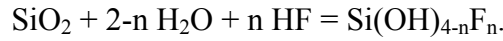
a. *Quartz solubility in fluorine-bearing aqueous fluids (D. Dolejš)*

Findings of colloidal silica in seafloor hydrothermal systems and solute-rich, gel-like inclusions in granite and greisen environments suggest that aqueous fluids may under some circumstances dissolve very high concentrations of silica. Therefore, the effect of fluorine on the solubility and speciation of silica in hydrothermal fluids was studied.

Quartz solubility in HF-H₂O fluids was measured at 400-800 °C and 100-200 MPa. Experiments were performed in rapid-quench cold-seal pressure vessels. SiO₂ solubilities were measured by the weight-loss method using quartz spheres (3-7 mg) and fluid (20-40 mg) in single gold capsules. At all conditions investigated, quartz solubility significantly increases in the presence of hydrogen fluoride (Fig. 3.5-1). At 400 °C and 100 MPa, the SiO₂ solubility ranges from 0.18 wt.% (pure H₂O) to 12.2 wt.% (with 8.3 wt.% F). Similarly, the SiO₂ solubility increases from 1.51 wt.% (pure H₂O) to 15.3 wt.% (with 8.0 wt.% F) at 800 °C and

200 MPa. The highest measured solubilities approach silicothermal gels and silica-rich fluid inclusions, found in natural granitic environments. In addition, the rapid increase in silica solubility in hydrothermal fluids implies approach to supercritical closure of the melt-vapor miscibility gap at low pressures.

The observed increase in quartz solubilities in the presence of fluorine is attributed to the formation of silicohydroxy-fluoride aqueous complexes:



The stoichiometry of the predominant species was determined from the Si/F ratio of the solute. At all conditions studied, experimental solubilities approach $dm(\text{SiO}_2)/dm(\text{F}) = 1/2$, indicating that $\text{Si(OH)}_2\text{F}_2$ is the major dissolved species.

The solubility behaviour of silica is interpreted using a density model (Fig. 3.5-2). The density of aqueous solvent was approximated by the equation of state for pure H_2O . Solubility isotherms have similar $d\log m(\text{SiO}_2)/d\log \rho$ slopes over the entire range of fluorine concentrations. From 800 to 400 °C, the silica solubility decreases regularly by ~ 0.07 log units $m(\text{SiO}_2)$ per 100 °C. On the other hand, isobaric solubilities of SiO_2 appear to be temperature-independent. This implies that effects of temperature versus fluid density on the solubility roughly cancel out and the enthalpy of dissolution is negligibly small. We have fitted the experimental data to the following relationship:

$$\log m(\text{SiO}_2) = a + b.\log \rho + c.\log m(\text{F}) + d.T,$$

where $a = -1.049$ mol/kg, $b = 0.816$ mol.cm³, $c = 0.802$ and $d = 1.256.10^{-3}$ mol/(kg.K).

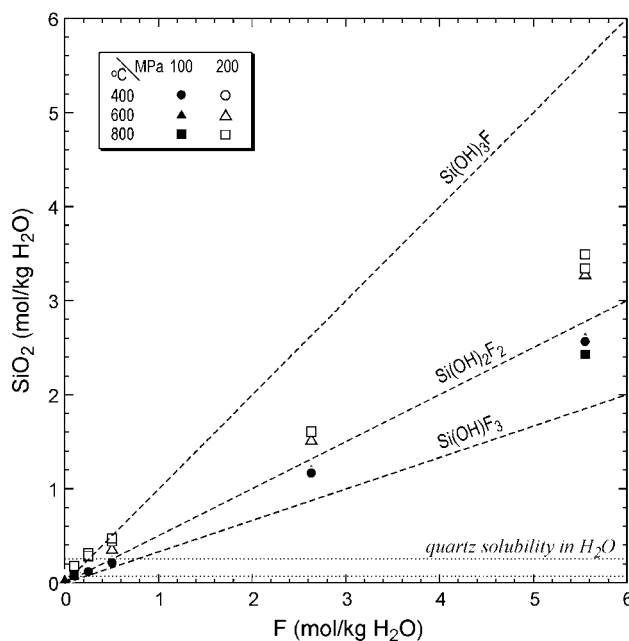


Fig. 3.5-1: SiO_2 solubility in aqueous fluids as a function of fluorine concentration. Symbols indicate experimental temperature and pressure (see insert). Dashed lines indicate solubilities controlled by various silicohydroxy-fluoride complexes $\text{Si(OH)}_{4-n}\text{F}_n$. Quartz solubility in H_2O represents maximum limits at 800 °C and 100 or 200 MPa. Errors in solubility determinations are 0.03 mol/kg based on repeated experiments.

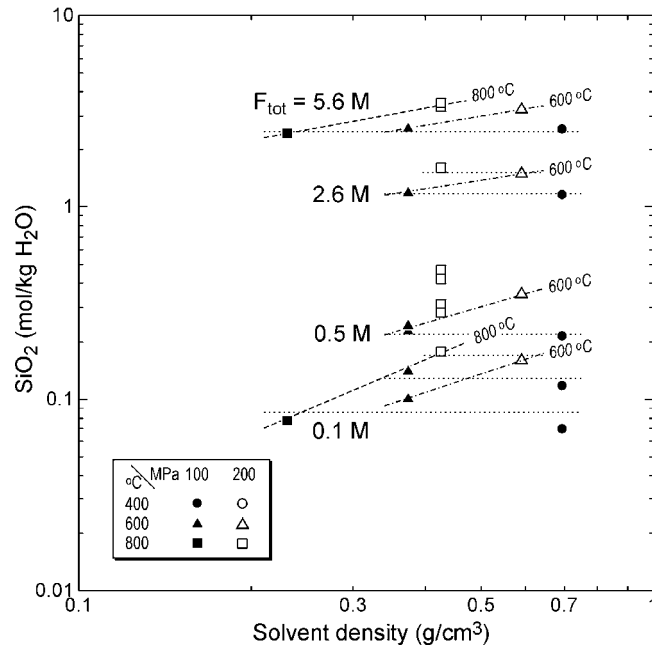
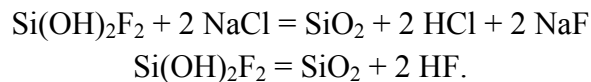


Fig. 3.5-2: Relationships between silica solubility, fluid density, temperature and molal fluorine concentration. Line patterns: dashed lines – solubility isotherms at 800 °C, dot-dashed lines – solubility isotherms at 600 °C, dotted lines – solubility isobars (see text for details).

These experimental results have implications for silica transport and precipitation in fluorine-bearing magmatic and hydrothermal settings. The measured quartz solubility is temperature and density dependent; therefore both factors favor and promote precipitation of quartz during fluid ascent and cooling. In addition, neutralization and increase in the Na/H ratio of chloride brines during alteration reactions or removal of hydrogen halides by fluid boiling will promote breakdown of silicohydroxy-fluoride complexes and precipitation of silica:



Contrary to previous suggestions, the formation of silica-rich fluids and gels does not require alkaline or carbonic fluids and the crystallized, silica-rich inclusions do not have to represent trapped silicate melts.

b. Solubility of tin in magmatic-hydrothermal fluids (*Q. Duc-Tin/Tübingen, A. Audétat and H. Keppler*)

Throughout the world, tin deposits are spatially and temporally associated with evolved, fluorine-rich granites. Although this relationship has been known for a long time, it is still unclear what role fluorine plays in the metal enrichment process. Experiments on tin

solubility in silicate melts and aqueous fluids have not been able to resolve this question, as they provided contradictory results with respect to both quantitative and qualitative solubility behaviour. Part of these inconsistencies may arise from the fact that tin shows a strong tendency to alloy with the noble metals commonly used as sample containers, which can lead to disequilibria in the experimental charge. To circumvent this problem we developed a new method that allows cassiterite-saturated fluid to be trapped that is not in contact with the noble metal capsule. This was done by producing synthetic fluid inclusions in quartz, which subsequently were analyzed by laser ablation inductively coupled plasma mass spectrometry (LA-ICP-MS).

Etched quartz cores were filled together with fine cassiterite sand (10-60 μm grain size), SiO_2 -glass and aqueous solutions into gold capsules, and then equilibrated for 4-7 days at 700°C / 0.14 GPa in cold-seal pressure vessels. Experiments were performed with aqueous solutions containing variable amounts of Cl and F added as HCl, NaCl, HF or NaF, plus 1000 ppm each of Rb, Cs and Ba for internal standardization. Oxygen fugacity was buffered close to the Ni-NiO buffer by the material of the pressure vessel and the use of a nickel filler rod. During the experiment, precipitation of dissolved SiO_2 onto the quartz cores lead to the entrapment of fluid and cassiterite grains in grooves along the quartz surface (Fig. 3.5-3). Runs of variable durations demonstrate that the fluid (\pm cassiterite) initially is trapped in the form of large, irregular inclusions, which subsequently split into several smaller inclusions. Hence, any inclusion that evolves from a larger, cassiterite-bearing inclusion contains fluid that was in equilibrium with cassiterite, but not in contact with the capsule wall (gold in this case), before final isolation. These “equilibrium type” inclusions were the main targets of our analysis. However, in order to check whether the uptake of Sn by the gold capsule caused any disequilibrium effects in the fluid we also analyzed “standard” inclusions that did not split off larger, cassiterite-bearing inclusions.

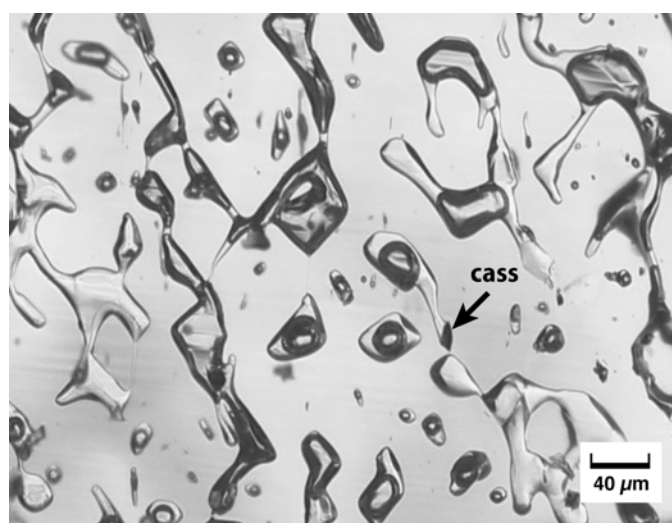


Fig. 3.5-3: Synthetic fluid inclusions and cassiterite grains trapped along a former surface in quartz. The experiment was conducted with 15 wt.% NaCl solution at 700°C / 1.4 kbar (transmitted light photomicrograph).

Computed Sn-contents of individual fluid inclusions from a single experiment typically are reproducible within $\pm 10\text{-}20\%$ relative. As the inclusions did not form all at the same time, this implies that inclusion formation occurred after a constant Sn concentration was attained in the fluid. No compositional difference between “equilibrium type” and other fluid inclusions could be observed, suggesting that equilibrium was reached also in the fluid portions that had access to the capsule wall.

Measured Sn-concentrations in NaCl- and HCl-bearing fluids increase linearly with the Cl content of the fluid (Fig. 3.5-4). This, together with the slope of unity in the log-log diagram implies that Sn was transported as a complex that contained one Cl atom per Sn atom. Our results are therefore compatible with earlier studies that concluded that SnCl^+ is the dominating complex over a wide range of P-T-fO₂ conditions. However, Sn-solubility in Cl-bearing solutions strongly depends on the way in which Cl is added: a fluid containing 4 moles NaCl / kg solution dissolves about 500 ppm Sn; whereas a fluid containing 4 moles HCl / kg contains about 2.6-4.2 wt.% (!) Sn.

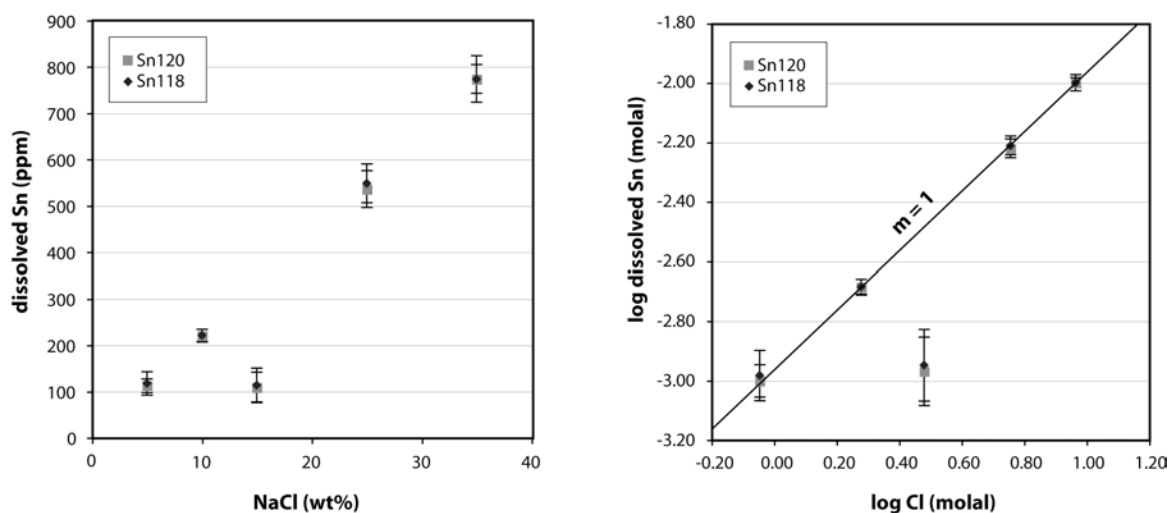


Fig. 3.5-4: Sn-solubility as a function of the NaCl-content of the fluid. The data point at 15 wt.% NaCl either failed to reach equilibrium or was buffered at a different oxygen fugacity and therefore is not considered further. The slope of 1 in the log-log diagram implies that Sn dissolved in the form of a complex that contained one Cl atom per one Sn atom.

Sn-solubility is enhanced also in HF-bearing solutions (reaching 400 ppm Sn at 3 molal HF), in which it increases as a function of the HF-content in a manner that is compatible with the formation of SnF_2 -complexes. Experiments in which fluorine was added as NaF were saturated in an additional melt phase, as is demonstrated by the occurrence of coexisting melt and fluid inclusions. Microprobe analyses of the melt inclusions reveal high concentrations of fluorine (2-5 wt.% F) and extraordinarily high concentrations of Sn (5-8 wt.% Sn). This unexpected result has important consequences for the formation of Sn deposits because it suggests that fluorine and Sn-rich residual melts may be an important transport medium for

Sn during the final crystallization stages of F-rich granites. Such unusual melts may therefore represent the “missing link” between fluorine enrichment and Sn mineralization. This conclusion is supported by reports of highly fractionated melt inclusions in the Ehrenfriedersdorf Sn-W deposit (Western Erzgebirge, Germany) that contains up to 2000 ppm Sn and 6 wt.% F.

c. Thermodynamic modeling of granite-fluid interaction: Gibbs free energy minimization by convex programming (D. Dolejš and T. Wagner/Tübingen)

Chemical interactions between minerals, rocks, melts, aqueous electrolytes and gases underlie numerous geodynamic phenomena, including the exsolution of magmatic brines, volcanic devolatilization, ore-forming processes, hydrothermal and geothermal alteration, and ground-water reactive flow. The increasing availability, coverage and consistency of thermodynamic datasets provide a starting point for modelling mass-transfer processes in complex magmatic-hydrothermal systems. This study is a first attempt to evaluate the performance of Gibbs free energy minimization programs in non-ideal multicomponent systems.

Thermodynamic properties of aqueous species are described by the Helgeson-Kirkham-Flowers model and their activity coefficients are calculated using the Debye-Hückel equation with constant extended term (0.03). Data for mineral end-members are based on the Holland-Powell database. Equations of state for solid solutions include ideal, symmetric and asymmetric van Laar models for main rock-forming minerals (feldspars, micas, amphiboles, pyroxene, oxides, etc.). This database was incorporated into the comprehensive Gibbs-free energy minimization code GEMS (Paul Scherrer Institute, Switzerland) utilizing convex programming and the interior point method to solve chemical equilibrium under mass-balance constraints.

We present results of granite-fluid interaction over a wide range of conditions (200-600 °C, 100 MPa, 0-5 molal NaCl, fluid/rock ratio of 10^{-2} to 10^2) in the system Si-Al-Mg-Fe-Ca-Na-K-Cl-O-H. At low fluid/rock ratio, the system is rock-buffered and the fluid composition is close to invariant. Increasing salinity at 600 °C and 100 MPa leads to successive replacements of mafic minerals: cordierite (at 0-9 wt.% NaCl eq.), andalusite (9-12 wt.% NaCl eq.), biotite (> 12 wt.% NaCl eq.). The pH decreases from the neutral value (6.7) and levels off (~ 6.0) at more than 10 wt.% NaCl eq. Magmatic brines correspond to Na>K>Fe-dominated chloride solutions. Increasing salinity is responsible for partial removal of cations, thus slightly increasing the whole-rock alumina saturation index.

The temperature of magmatic devolatilization strongly affects mineral assemblage and chemistry, pH and ionic strength of the exsolving fluid (Fig. 3.5-5). A temperature decrease from 600 to 200 °C at 100 MPa results in the replacement of cordierite by white mica (565 °C), biotite by chlorite (345 °C), and magnetite by hematite (325 °C). The pH of the fluid remains weakly acidic ($\Delta_{neutral} = -0.5$) in the high-temperature range but it becomes neutral or weakly alkaline ($\Delta_{neutral} = +0.6$) with progressive muscovitization and chloritization, as a

consequence of H^+ removal from the fluid. Ionic strength of the fluid steadily increases from 5 to ~ 90 % dissociation, reflecting an increase in the dielectric constant of the aqueous solvent at low temperatures. During cooling, the Si and Al solute contents steadily decrease, Fe concentration sharply drops whereas Ca contents markedly increase (Fig. 3.5-5). The Ca/Fe ratio of hydrothermal fluids may therefore be utilized as a geothermometer.

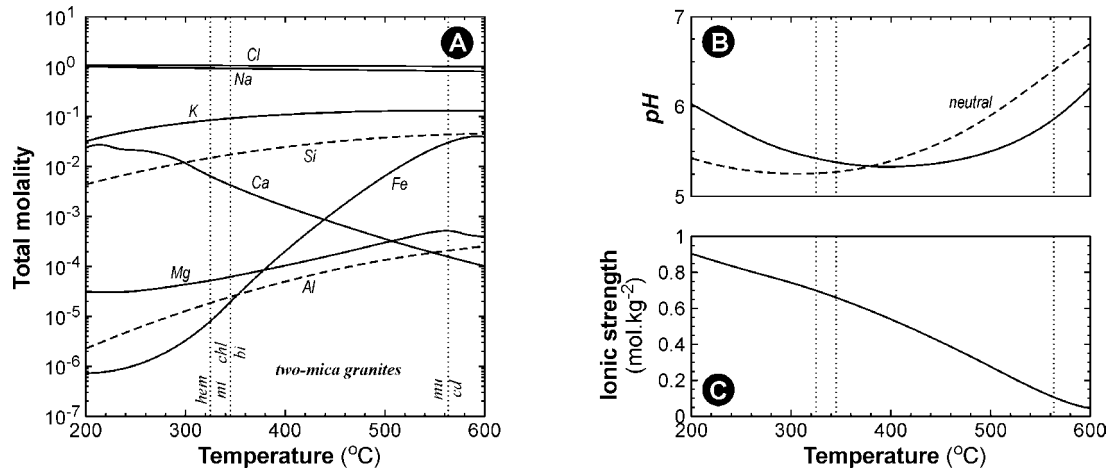


Fig. 3.5-5: Chemical composition of aqueous fluids exsolved from peraluminous granite at 200 - 600 °C, 100 MPa, 1 molal NaCl, water/rock ratio = 0.1. Whole-rock composition (in wt.%): SiO_2 73.91, Al_2O_3 14.59, Fe_2O_3 0.17, FeO 0.72, MgO 0.29, CaO 0.20, Na_2O 4.93, K_2O 5.19. (A) total molalities of individual elements. Note that the two-mica assemblage is stable at subsolidus temperatures only; (B) increase in pH with decreasing temperature due to the formation of muscovite and chlorite; (C) increase in effective ionic strength with decreasing temperature reflecting progressive breakdown of neutral species during cooling.

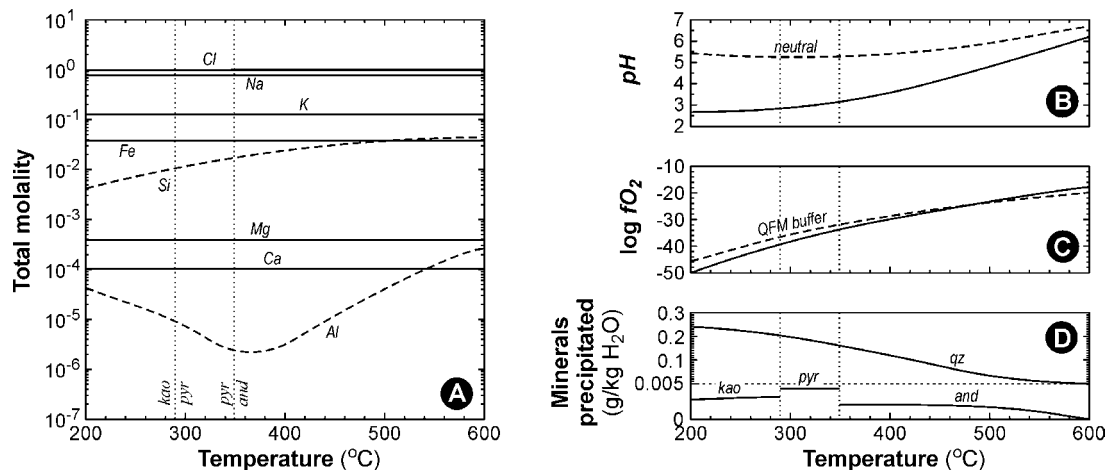


Fig. 3.5-6: Chemical parameters and mineral proportions in aqueous fluid during isobaric irreversible cooling from 600 to 200 °C at 100 MPa. (A) total molalities of individual elements. Note retrograde aluminium solubility; (B) decrease in pH due to the HCl dissociation upon cooling; (C) decrease in oxygen fugacity; (D) absolute amounts of minerals precipitated. Note the distinct stabilities and solubilities of aluminosilicates (andalusite, pyrophyllite, kaolinite).

Variations in the fluid/rock ratio represent a change from the rock-buffered to the fluid-buffered regime and provide a model for sequence of alteration zones due to the incongruent rock dissolution. Mineral assemblage and fluid composition remain invariant up to a fluid/rock ratio ~ 10 by mass. Exsolved fluids are close to neutral ($\Delta_{neutral} = -0.1$), but relatively oxidized (QFM $\sim +3.5$). Progressive infiltration of low-salinity fluids results in K-feldspar dissolution, albitization, chloritization and subsequent dissolution of white mica. The resulting mineral assemblage (albite, chlorite, magnetite) corresponds to “episyenites” and these may be interpreted as low-temperature fluid pathways in the cooling intrusions.

Irreversible processes are modelled by the incremental calculations, using decrements in temperature (5 °C) and adjustments in bulk composition due to the mineral precipitation (Fig. 3.5-6). Cooling and irreversible precipitation of a magmatic fluid exsolved at 600 °C and 100 MPa results in: (1) a steady decrease in pH, leading to strongly acidic low-temperature fluids (pH = 2.7 at 200 °C); (2) progressive reduction, QFM = +2 to -4 (600 to 200 °C); (3) precipitation of quartz-andalusite, quartz-pyrophyllite and quartz-kaolinite vein assemblages; (4) SiO₂ solute contents decrease gently whereas aluminium exhibits a retrograde solubility, marked by a minimum near the andalusite-pyrophyllite transformation temperature (350 °C; Fig. 3.5-6). Irreversible, fluid-buffered cooling provides an alternative explanation for the origin of quartz-aluminosilicate veins in high-grade metamorphic and magmatic settings.

In summary, the Gibbs-free energy minimization by convex programming has been successfully applied to highly non-ideal multicomponent systems. Results of numerical simulations can be used to interpret temperature, salinity and the fluid/rock ratio during formation of natural alteration assemblages. This is the first comprehensive attempt to combine aqueous speciation with several multi-component non-ideal mineral solid solutions and our approach will serve for advanced modelling of reactive flow processes in the Earth’s crust.

d. Carbon solubility and speciation in mantle minerals (S.S. Shcheka, H. Keppler, M. Wiedenbeck/Potsdam and D.J. Frost)

Geochemical data suggest that most of the terrestrial carbon is stored in the Earth’s mantle. Although carbon may exist in the mantle in separate C-rich phases, ordinary mantle silicates and oxides could be a potential host of mantle carbon. Data on carbon solubility in mantle minerals are of extraordinary importance for understanding the geochemical behaviour of carbon in the deep Earth. Recently, silicates and MgAl₂O₄ spinel were shown to incorporate only traces of carbon at uppermost mantle conditions. However, there were no reliable systematic data on carbon solubility in the nominally volatile-free minerals throughout the pressure-temperature range of the entire mantle.

Carbon-saturated crystals of forsterite, enstatite, diopside, pyrope, MgAl₂O₄ spinel, wadsleyite, ringwoodite, MgSiO₃-ilmenite, and MgSiO₃-perovskite were synthesized by growth from carbonatite melts enriched to contain more than 99 % of carbon as the rare ¹³C

isotope. Experiments were performed in a piston-cylinder apparatus ($T = 900 - 1100\text{ }^{\circ}\text{C}$; $P = 1.5\text{ GPa}$) and a multianvil press ($T = 900 - 1400\text{ }^{\circ}\text{C}$; $P = 6 - 11\text{ GPa}$). Carbon contents of the samples were measured with a Cameca ims 6f ion probe modified from its original design to suppress external carbon contamination. Carbon solubilities were calculated from the observed excess of ^{13}C over ^{12}C assuming that any contamination had “normal” isotopic composition. For upper mantle phases synthetic carbon-free minerals, ion-implanted with a known dose of the ^{13}C , were used as standards. For wadsleyite, ringwoodite, MgSiO_3 -ilmenite and MgSiO_3 -perovskite, synthetic tholeiite glasses doped with ^{13}C were used as reference samples.

In upper mantle silicates, carbon solubility is on the order of a few hundred ppb by weight at $T = 900\text{-}1100\text{ }^{\circ}\text{C}$ and $P = 1.5\text{ GPa}$ and increases with pressure to a maximum of $\sim 12\text{ ppm}$ by weight in forsterite at 11 GPa (Fig. 3.5-7). No clear dependence of carbon solubility on temperature, oxygen fugacity and iron content was observed. We failed to determine any discernible amount of carbon in MgAl_2O_4 spinel above the limit of detection of 30 ppb by weight.

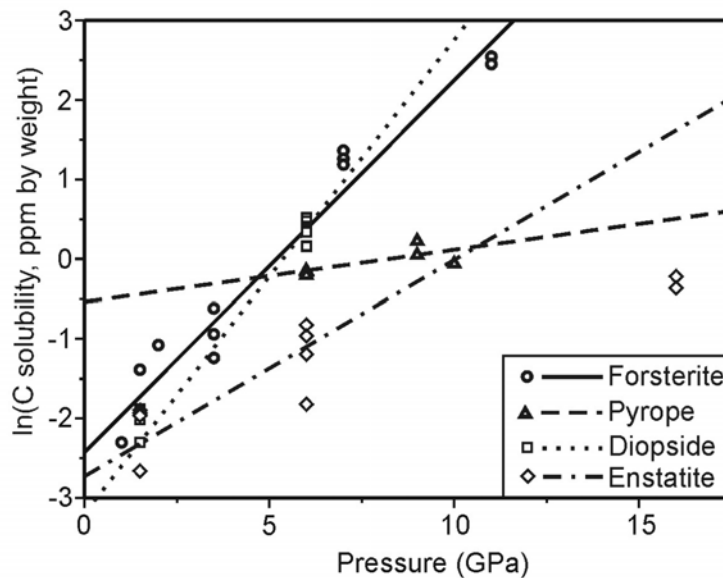


Fig. 3.5-7: Plot of the logarithm of carbon solubility in upper mantle silicates versus pressure for $T=900\text{-}1200\text{ }^{\circ}\text{C}$. The slopes of the lines are related to the volume change ΔV of the dissolution reaction. Estimated values of ΔV are $-5.47\text{ cm}^3/\text{mol}$ for forsterite, $-3.0\text{ cm}^3/\text{mol}$ for enstatite, $-6.4\text{ cm}^3/\text{mol}$ for diopside and $-0.9\text{ cm}^3/\text{mol}$ for pyrope. Except for forsterite, these data are, however, only constrained by a few measurements and they may therefore be subject to substantial errors.

Measurements of carbon-saturated wadsleyite, ringwoodite, MgSiO_3 -ilmenite and MgSiO_3 -perovskite showed no excess of ^{13}C relative to the natural ratio of $^{13}\text{C}/^{12}\text{C}$. Therefore, carbon solubility in transition zone and lower mantle silicates is below the limit of detection of $40 - 110\text{ ppb}$ by weight. Since these numbers were obtained using a non matrix-matched tholeiite glass standard, a systematic error by a factor of 2-3 is possible.

The observation that carbon solubility in olivine is independent of oxygen fugacity implies that the oxidation state of carbon in olivine and in the carbonatite melt is the same. Therefore, carbon in olivine is dissolved as C^{4+} . The systematic variations in carbon solubility observed for different minerals suggest a direct substitution of C^{4+} for Si^{4+} , because there is a clear correlation of carbon solubility with the volume of the Si^{4+} site in the respective mineral (Fig. 3.5-8).

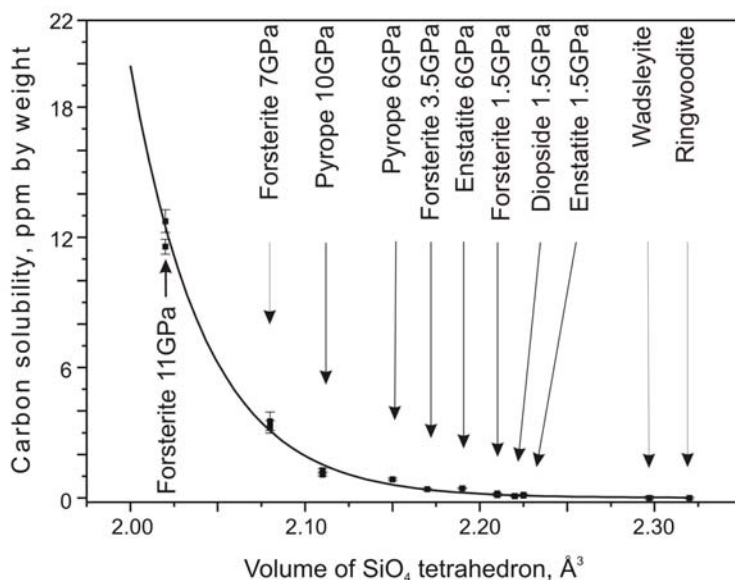


Fig. 3.5-8: Carbon solubility in silicates as a function of the volume of the SiO_4 tetrahedron. The curve shown is a guide for the eye only.

Silicon in $MgSiO_3$ -ilmenite and $MgSiO_3$ -perovskite is in octahedral coordination. This site, still being the smallest in their structures, has a much longer Si-O bond and larger polyhedral volume (e.g., 7.68 \AA^3 in perovskite compared to $2.10\text{-}2.24 \text{ \AA}^3$ in upper mantle minerals). The smallest polyhedra in $MgAl_2O_4$ spinel are MgO_4 tetrahedra with a volume in the range of $3.653\text{-}3.827 \text{ \AA}^3$. It is therefore not surprising that no carbon was detected in $MgAl_2O_4$ spinel and minerals of the transition zone and lower mantle.

The exceedingly low solubility of carbon in major nominally volatile-free mantle minerals implies that the carbon budget of the bulk mantle is probably dominated by carbonates. The low melting point of these carbonates and the high mobility of carbonatite melts may allow massive carbon enrichments in the shallow subcontinental mantle.

e. The hydration of olivine at 12 GPa (J.R. Smyth/Boulder, D.J. Frost, F. Nestola, C.M. Holl/Boulder and G.D. Bromiley/Cambridge)

We have synthesized water-saturated purely magnesian and Fo_{90} forsterites at 12 GPa and temperatures ranging from $1100 \text{ }^\circ\text{C}$ to $1600 \text{ }^\circ\text{C}$ and at silica activities buffered by either

hydroxylinothumite or clinostatite. Hydrogen contents were measured by FTIR spectroscopy on X-ray-oriented, faceted grains using recently published extinction coefficients for water in olivine. We observe an increase in H contents from approximately 5000 ppm by weight H₂O (ppmw) at 1100 °C to about 8800 ppmw at 1250 °C and a decrease above 1250 °C with the onset of melting to approximately 2000 ppm at 1600 °C. Silica activity appears to have a minor effect if any on water contents. The maximum water contents are approximately a factor of two larger than previously observed at 1100°C, which is mostly due to the use of a new infrared calibration.

The substitution mechanism has been deduced from X-ray single crystal structure refinements and polarized FTIR spectra. The absorbance features in the FTIR spectra most likely correspond to protonation of octahedral edges, and polarizations are more consistent with protonation of M1 octahedral edges than of M2 edges. This means that the dominant substitution mechanism for olivine hydration is 2H⁺ for Mg²⁺. We observe an expansion of the M1 polyhedral volume together with a systematic expansion of the unit cell volume with hydration. A linear regression fit to the observed data gives

$$V = 290.107 + 5.5 \times 10^{-5} * (\text{H}_2\text{O})$$

with a correlation coefficient of 0.83, where V is cell volume in Å³ and H₂O is the ppm by weight H₂O as determined from FTIR spectroscopy.

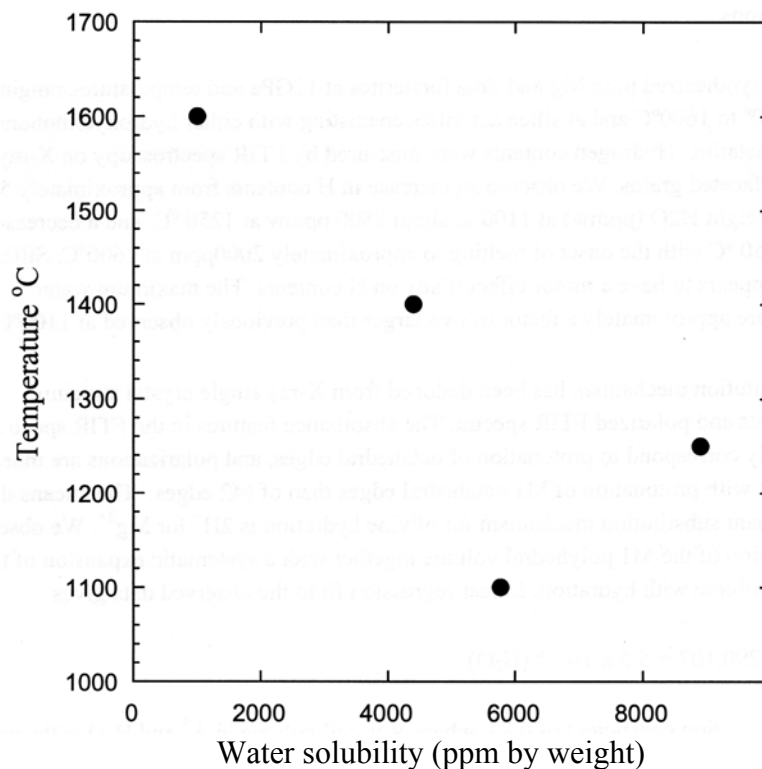


Fig. 3.5-9: Water solubility in forsterite as a function of temperature at 12 GPa. Water contents were determined using polarised FTIR on oriented single crystals of forsterite.

The major geochemical result of this work is that olivine with up to 8900 ppmw H₂O can coexist with a fluid phase at 1250 °C. This means that the geochemical compatibility of H is strongly a function of pressure and temperature, increasing much more rapidly than that of other elements. Dehydration of solid phases by melt extraction will therefore be much less efficient at pressures above 5 GPa, so that geochemical studies based on the incompatibility of H being close to that of Ce or K may need to be revised. It further implies that the efficiency of dehydration by melt extraction on subduction will likely be less than previously assumed. Significant amounts of water entrained in olivine imply the possibility of a deep Earth water cycle whereby the oceans are in dynamic equilibrium with a larger reservoir in the interior incorporated as hydroxyl into solid silicates.

f. Hydration of stishovite and the fate of subducting slabs (G.D. Bromiley and F.A. Bromiley/Cambridge, D.W. Bromiley/Bristol)

The high-pressure silica polymorph stishovite accounts for 10 to 20 % by volume of material in basaltic compositions under conditions of the Earth's transition zone and lower mantle. It has been shown that stishovite can contain trace amounts of water (as structurally incorporated H), charge balanced by substitution of Al³⁺ for Si⁴⁺, although the exact location of H in stishovite remains uncertain. Mechanisms for Al³⁺ substitution into stishovite also remain unclear despite the important effect that Al³⁺ could have on compressibility. In this study we have systematically investigated the mechanisms for H⁺ and Al³⁺ incorporation in stishovite under conditions of the transition zone.

Stishovite samples with varying compositions were synthesized under hydrous and nominally anhydrous conditions at 15 GPa, 1500 °C using a multianvil type apparatus. Phases were identified optically and by micro-Raman spectroscopy, compositions by electron microprobe and water incorporation was investigated using FTIR spectroscopy. Polarised IR spectra from Al-free stishovite (Fig. 3.5-10) contain an OH stretching absorption band at 3111 cm⁻¹ as well as two additional bands at higher wavenumbers. Spectra from Al-stishovite are dominated by a large asymmetrical OH absorption band centered around 3111 to 3116 cm⁻¹, equivalent to the main OH band in Al-free spectra. Peak fitting demonstrates that the asymmetry of this band in spectra from Al-bearing samples is due to the presence of an additional band at 3155 - 3166 cm⁻¹. All OH bands exhibit a degree of anisotropy, and band positions and intensities vary as a function of Al content. Based on these trends, we can conclude the following:

1. The main mechanism for H incorporation in stishovite involves H docking close to the short, shared O-O edge, and not at an interchannel site as recently proposed.
2. Most interstitial H in stishovite is uncoupled from other defects (*i.e.*, from Al_{Si}¹), giving rise to the OH stretching band at 3111 to 3116 cm⁻¹.
3. In Al-bearing samples, some interstitial H docks close to the O-O edge of an octahedral site occupied by Al. NNN effects result in a shift in OH stretching frequency, giving rise to the OH band at 3155 to 3166 cm⁻¹.

4. The amount of H coupled to Al (*i.e.*, $H_i - Al_{Si}$) is not controlled by statistical distribution, but instead appears to be due to the intrinsic nature of the stishovite structure, relative stabilities of different defect types and crystal chemistry.

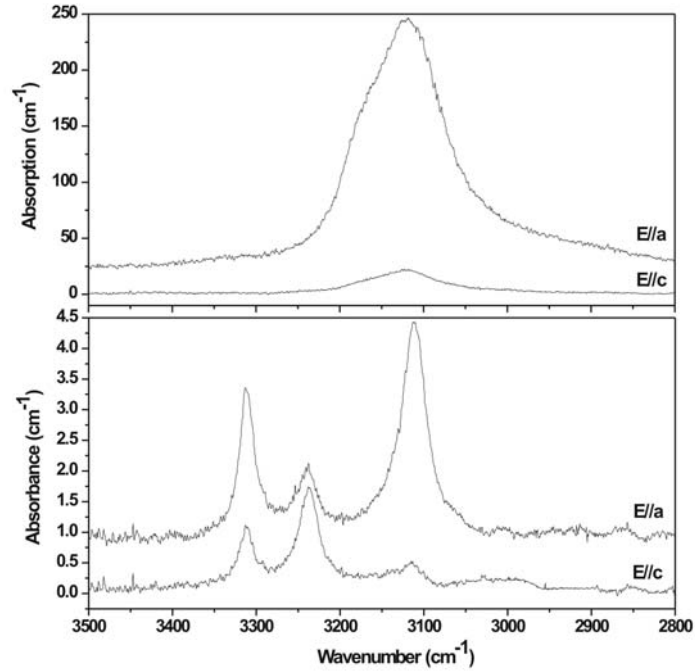


Fig. 3.5-10: Polarized IR spectra of Al-free (below) and Al-bearing (above) stishovite

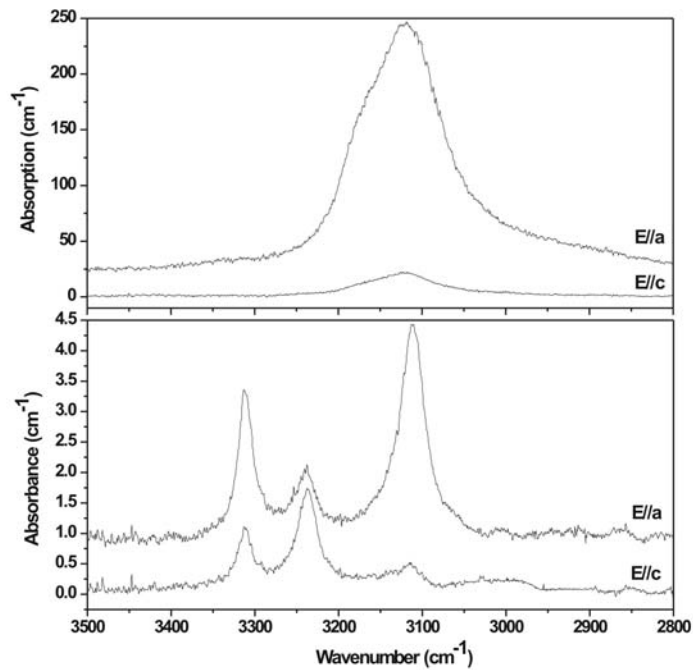


Fig. 3.5-11: Averaged unpolarised spectra from stishovite as a function of composition. Al_2O_3 contents of stishovite samples are given in wt.%, and spectra are offset vertically for clarity.

Both of the main OH bands show interesting trends in O-H stretching frequency as a function of composition, most likely due to a change in the mechanism for Al incorporation in stishovite with increasing Al₂O₃ content. In all samples, Al contents are at least one order of magnitude higher than H contents, implying that the main mechanism for Al³⁺ incorporation in stishovite is unrelated to H. Instead, Al³⁺ could substitute onto Si⁴⁺ sites, charge balanced by oxygen vacancies, or by coupled substitution on Al³⁺ onto the large interstitial octahedral site in the stishovite structure. Shifts in OH stretching frequencies with increasing Al₂O₃ content up to 2.0 wt.% Al₂O₃ are consistent with Al³⁺ substitution onto the main (Si) octahedral site and an increase in unit cell parameters (Fig. 3.5-11). Concurrent changes in intensity and frequency of the stishovite Raman active E_g and A_{1g} modes are most likely the result of an increase in the number of oxygen vacancies. However, above 2.0 wt.% there is a reversal in the direction in which OH bands shift, implying a change in the Al incorporation mechanism. We interpret this as evidence for coupled substitution of Al³⁺ onto both octahedral (Si) and interstitial sites at high Al₂O₃ contents, resulting in a decrease in unit cell parameters and a decrease in H solubility in stishovite.

The Al content of stishovite controls the amount of H that can be accommodated, and also has been shown to have a considerable influence on compressibility. This implies that compositions and phase relations in downgoing slabs could have an influence on how much water can be stored and transported under transition zone and lower mantle conditions, as well as having an impact on slab density and buoyancy relative to the surrounding mantle.

3.6 Physics and Chemistry of Melts and Magmas

The Earth and other planets of the solar system have differentiated and evolved chemically over the past 4.5 billion years largely through the generation of magma (molten or partially-molten rock) through melting or partial melting at depth, the transport of magma and its subsequent crystallisation. For example, it is likely that the Earth was largely molten at a very early stage of its history due to the high energy of large impacts that inevitably occurred during planetary accretion. The formation of a “magma ocean”, possibly more than 1000 km deep, by large scale melting likely facilitated the separation of iron-rich metal from silicate magma to form the core and mantle. The subsequent crystallisation of a deep magma ocean determined the early structure of the planet and may have resulted in differentiation and chemical layering. In addition, igneous activity and volcanism over the past 4.5 billion years may have been responsible for the origin and evolution of the oceanic crust and the continents. Volcanism also causes volatiles to be transported from the interior of a planet into the atmosphere and is therefore a major factor that contributes to atmospheric evolution and climate change.

In order to understand and quantify the role of magmatic activity and volcanism in the chemical differentiation of terrestrial planets such as the Earth, the physical and chemical properties of magmas and melts must be understood. The contributions in this section cover a broad range of such properties. The first contribution presents results of a study of the viscosity of silicate liquid at pressures up to 25 GPa that are directly applicable to understanding the convective behaviour and rate of cooling of a magma ocean. The effects of pressure on viscosity are complex and are likely influenced strongly by changes in the atomic structure of the liquid, which is a topic addressed by the second contribution. Here the structures of glasses, quenched from melts at high pressure, have been studied using nuclear magnetic resonance spectroscopy. Volatiles that are dissolved in magma are of great importance in determining the nature of volcanic eruptions through their effects on physical properties. In order to better understand how volatiles influence physical properties, the effects of dissolved CO₂ on melt structure are being studied using spectroscopic techniques, as reported here in the third contribution. Continuing on the topic of volcanism, results are presented on the absorption of sulphur dioxide by volcanic ash – without a quantification of this effect, predictions of changes in atmospheric chemistry and climate, as a consequence of volcanic eruptions, cannot be made. The final contribution in this section is concerned with the structure and evolution of Titan, the largest of Saturn’s moons, through melting studies of methane clathrate hydrates at high pressures. The results explain volcanic activity on the surface of Titan and the persistence of high levels of methane in the atmosphere.

a. *Viscosity of peridotite liquid up to 24 GPa predicted from self-diffusion coefficients (B. Schmickler and D.C. Rubie, in collaboration with C. Liebske/Zurich, C. Holzappel/Saarbrücken and B.T. Poe/Rome)*

As discussed in previous contributions, knowledge of the pressure effect on the transport properties of peridotite liquid is crucial for understanding the dynamics and evolution of a

Hadean magma ocean and thus the initial differentiation mechanisms of the early Earth. The viscosity of peridotite liquid has been measured up to 13 GPa by *in situ* falling sphere viscometry (see 2004 Annual Report). The determination of self-diffusion coefficients is also a powerful tool for predicting viscosities at higher pressures using the Eyring relationship. To test the Eyring relation for peridotite liquid and to extend measurements to higher pressures, the self-diffusion coefficients of O, Si, Mg and Ca and chemical diffusivities of Co and Ni have been determined simultaneously up to 24 GPa using multianvil presses at BGI. One half of each peridotite diffusion couple contained natural isotopic abundances and 1 wt.% CoO. The other half was enriched in ^{18}O , ^{30}Si , ^{25}Mg , ^{44}Ca and contained 1 wt.% NiO. An automated heating routine ($> 45\text{ }^\circ\text{C}/\text{sec}$) was used. Run durations ranged from 3 to 30 seconds. Profiles of isotopic concentrations of the recovered capsules were analysed by SIMS at the University of Edinburgh, UK. CoO and NiO concentrations were measured by EPMA at BGI. The diffusion coefficients were calculated by fitting a mathematical solution of the diffusion equation to the concentration profiles. The self-diffusivities and chemical diffusivities decrease with pressure up to ~ 9 GPa, and increase again from 9 to 16 GPa. This result is consistent with the viscosities determined up to 13 GPa, which show an inverse trend and pass through a maximum at ~ 9 GPa. The diffusion coefficients determined in the range 20 to 24 GPa are lower than extrapolations of the lower pressure (9-16 GPa) data, which implies a further change in pressure dependence above 16 GPa. The positive pressure dependence of the transport properties up to 9 GPa is consistent with the behaviour of a liquid upon compression, resulting in a decrease of free volume. The negative pressure dependence between 9 and 16 GPa is likely to be the consequence of structural reorganisation in the melt. Above 16 GPa, the pressure dependence becomes again positive, apparently as a result of further melt compaction when the coordination changes are complete. The application of the Eyring relation, which relates diffusivity to viscosity, suggests an average diffusion jump distance of ~ 0.45 nm. The data can be used to explore the dynamics of terrestrial magma oceans at depths to at least 720 km.

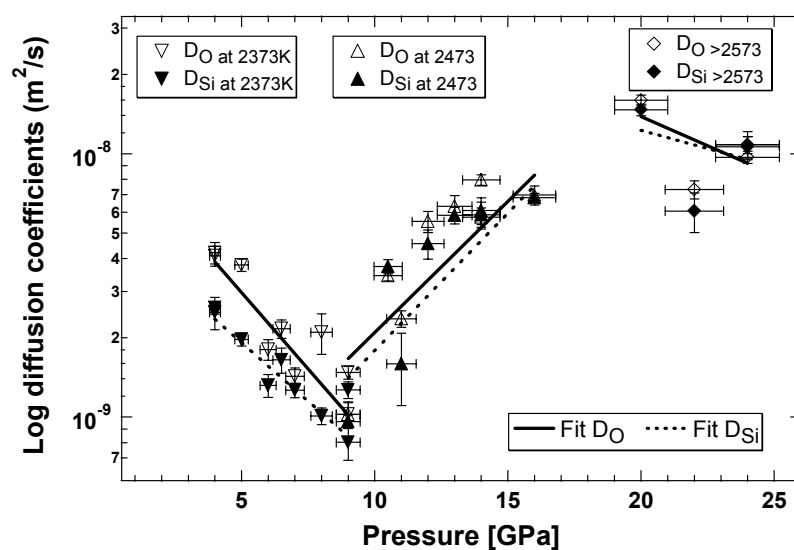


Fig. 3.6-1: Oxygen and silicon self-diffusion coefficients in peridotite liquid decrease with pressure up to 9 GPa, increase again up to 16 GPa, but appear to decrease again when pressure is increased further.

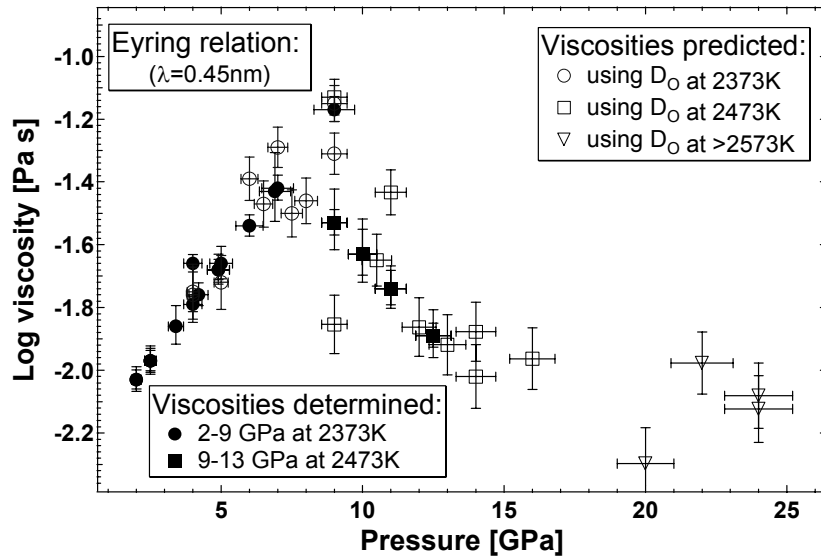


Fig. 3.6-2: Viscosities predicted from oxygen self-diffusion coefficients using the Eyring equation (with a jump distance of 0.45 nm) correspond closely with viscosities measured directly by falling sphere viscometry. This analogy allows viscosities of peridotite liquid to be determined up to 24 GPa.

b. Aluminium coordination and density of 4 and 5 component high-pressure aluminosilicate glasses (J.R. Allwardt, J.F. Stebbins and L.-S. Du/Stanford, D.J. Frost, in collaboration with M.M. Hirschmann and A.C. Withers/Minnesota)

The density of silicate melts has repeatedly been shown to increase with pressure and the magnitude of this change has been shown to be compositionally dependent. Glasses are frequently used as a first approximation for understanding the structure of melts because they have the structure of the liquid at the glass transition temperature. In an attempt to further understand pressure-induced structural changes and how they affect the density of high-pressure melts, we have synthesized aluminosilicate glasses at 2-8 GPa and have measured the density and aluminium speciation. Previous MAS NMR studies have shown that Al is much more susceptible to coordination changes than Si in high-pressure aluminosilicate glasses. One of our previous studies has shown that the Al speciation and densification of the compositionally similar $\text{Ca}_3\text{Al}_2\text{Si}_6\text{O}_{18}$ (CAS) and $\text{K}_6\text{Al}_2\text{Si}_6\text{O}_{18}$ (KAS) glasses are drastically different. For example, the average Al coordinations of the two glasses at 5 GPa are 4.75 and 4.12, respectively. Additionally, these glasses are 10 % and 5 % denser, respectively, than the corresponding ambient-pressure glasses.

Because there is such a large difference in structure and properties between these compositionally similar glasses (*i.e.*, similar NBO/T, Al:Si ratio, etc.), the goal of the present study is to investigate how mixing of modifier cations (Ca, K, and Mg) affects the Al-coordination and density of high-pressure glasses. The ^{27}Al MAS NMR spectra of the $\text{Ca}_2\text{K}_2\text{Al}_2\text{Si}_6\text{O}_{18}$ (C2KAS) and $\text{CaK}_4\text{Al}_2\text{Si}_6\text{O}_{18}$ (CK2AS) glasses quenched from melts at 5 GPa (Fig. 3.6-3) reveal that the average Al-coordination increases with increasing CaO:K₂O

ratio. However, a more detailed quantification shows that the values predicted from the end-members overestimate the abundance of high-coordinated Al in mixed modifier cation glasses. This is also observed in the case of the 3 and 8 GPa glasses.

The densities of the CKAS glasses were measured and compared with the average Al-coordination values to investigate the structural changes that occur in high-pressure melts (Fig. 3.6-4). There is a very obvious bend in the slope of the density- $^{[x]}Al$ curve for all four compositions. This would likely suggest that there are two distinct compression regimes in these glasses, depending on pressure: the lower pressure mechanism(s) involves densification with little change in the Al-coordination; whereas the higher pressure mechanism(s) involves an increase in the Al coordination with a corresponding larger increase in the density of the glass. The pressure where this change occurs also appears to be compositionally dependent because the CAS curve changes slope at a pressure below 2 GPa, while this change occurs between 3 and 5 GPa in the C2KAS glasses. Finally, the slope for the higher pressure mechanism is also compositionally dependent because the CAS curve has the steepest slope, which is likely a result of the differences between the compressibility of CaO_x and KO_x polyhedra.

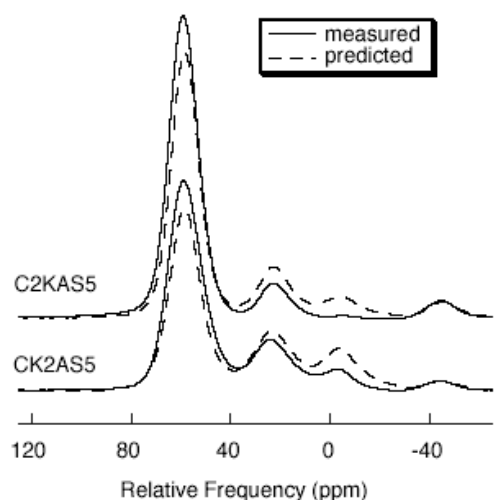


Fig. 3.6-3: The solid lines represent the ^{27}Al MAS NMR spectra (18.8 Tesla) measured for the 5-GPa CKAS glasses. The predicted spectra (dashed) are the result of adding spectra of the CAS and KAS glasses in appropriate ratios. For example, for the C2KAS5-predicted spectra, the intensity of the CAS5 glass is multiplied by 2 and added to the intensity for the KAS5 glass.

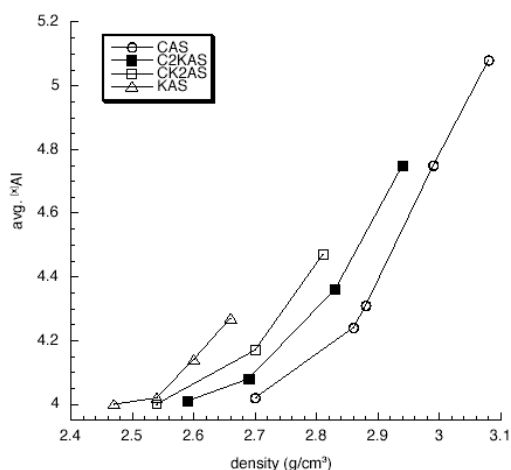


Fig. 3.6-4: The measured density vs. average $[x]Al$ (aluminium coordination) for the CKAS glasses quenched from liquids at 3, 5, and 8 GPa.

c. CO_2 speciation in silicate melts (A. Korschak and H. Keppler)

CO_2 is, after H_2O , the most abundant volatile in terrestrial magmatic systems. Therefore it is important to understand the behaviour of CO_2 in silicate melts, its solubility mechanisms and its influence on the structure and properties of melts. In this study, glasses along the join albite-diopside were synthesized at high pressure in a piston-cylinder apparatus in order to investigate the speciation of CO_2 and its effect on the structure of simplified basaltic melts.

Raman, infrared and NMR spectroscopy on quenched CO_2 -bearing silicate glasses in the past have shown that CO_2 dissolves in molecular form and as $(\text{CO}_3)^{2-}$ groups linked to the silicate network, to non-bridging oxygen atoms (NBO) and to network modifying cations such as Ca^{2+} . The portion of those CO_2 species within a CO_2 bearing silicate glass depends strongly on the bulk composition, on the network modifying cations and on the polymerization degree or corresponding structure of the glass. The structure of the silicate network in a glass is mainly determined by the degree of polymerization of the silicate tetrahedra and described by the abundance of different Q_n species, where Q_n denotes a tetrahedron linked by bridging O atoms to n adjacent tetrahedra. The range of n is 0 (isolated tetrahedra) to 4 (fully polymerized three dimensional network). In strongly polymerized glasses of albitic composition ($\text{NBO}/\text{T} \sim 0$) CO_2 is incorporated in molecular form. In more depolymerized glasses of diopsidic ($\text{CaMgSi}_2\text{O}_6$) composition ($\text{NBO}/\text{T}=2$) CO_2 is fixed in $(\text{CO}_3)^{2-}$ groups. On the other hand, diffusion of bulk CO_2 (in molecular and anionic form) was determined to be independent of melt composition. Therefore, different glasses along the join albite-diopside (as analogues for basaltic melt) were synthesized at 20 kbar and 1600 °C with different amounts of bulk CO_2 in order to investigate the effect on the silicate structure. Raman spectra were fitted with Gaussian forms in order to distinguish the different averaged Q_n species within the glass structure and possible changes with increasing CO_2 content. As an example, Figure 3.6-5 shows the Raman spectra of a CO_2 -bearing glass and its deconvolution into Gaussian components. According to common band assignments the peak near 950 cm^{-1} is linked to Si-O stretching vibrations in Q_2 units, the peak around 1050 to 1100 cm^{-1} to the Si-O stretching vibrations of Q_3 units and that at 1160 cm^{-1} originates from Si-O stretching vibrations in Q_4 species. Only a slight decrease of Q_2 and a moderate increase of Q_3 units with increasing bulk CO_2 contents up to 3.0 wt.% indicate a weak polymerization of the silicate network.

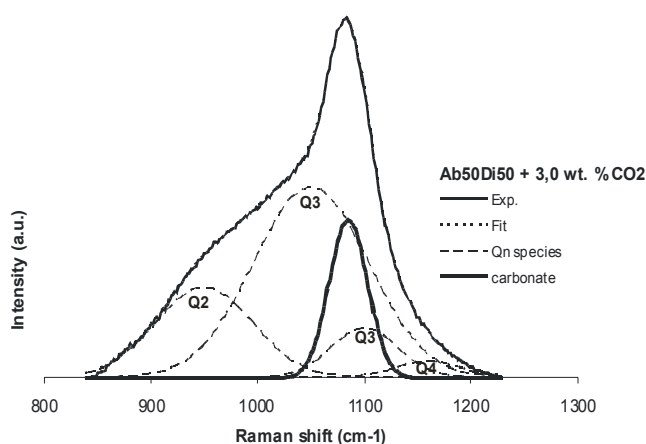


Fig 3.6-5: Example of a Raman spectrum of Albite₅₀Diopside₅₀ + 3.0 wt.% CO_2 glass in the Si-O stretching region (800-1300 cm^{-1}). Experimental data: solid line, fit: dotted line, assigned Si-O stretching vibrations in Q_n units: dash-dotted lines, and carbonate: thick full line.

One major objective of this study is to cross calibrate different spectroscopic techniques, such as Raman spectroscopy, infrared spectroscopy and ^{29}Si NMR. Ongoing research focuses on investigating the effect of pressure on the dissolution mechanisms of CO_2 based on studies of quenched glasses and on the development of *in situ* spectroscopic techniques for studying CO_2 speciation at high temperature.

d. Adsorption of SO_2 onto volcanic ashes (D. Schmauß-Schreiner and H. Keppler)

Volcanic eruptions are the major source of large quantities of ash and magmatic gases that are injected into the atmosphere. The major gaseous species are water vapour and CO_2 , with smaller quantities of SO_2 , H_2S and other species. In explosive eruptions, significant amounts of SO_2 are injected into the stratosphere, where it becomes oxidized to SO_3 through photochemical reactions. By combining with water vapour, SO_3 forms aerosols of sulphuric acid. These aerosols can efficiently backscatter and absorb incident solar radiation, resulting in atmospheric cooling. In 1992, the Mt. Pinatubo eruption injected an estimated 17 megatons of SO_2 into the stratosphere. The resulting global cooling by about $0.5\text{ }^\circ\text{C}$ has compensated anthropogenic warming for a few years. In addition, sulphur-bearing aerosols promote chemical reactions that result in ozone depletion.

The effect of volcanic activity on climate is controlled mainly by the amount of SO_2 that is transferred to the stratosphere. Field observations suggest that a significant fraction of SO_2 may be removed from the eruption column through adsorption onto volcanic ash. However, no experimental data are available that would allow a quantitative prediction of this effect. We have carried out the first experimental study on SO_2 adsorption onto volcanic glasses with rhyolitic, dacitic and andesitic compositions.

Our preliminary results at temperatures of $0\text{ }^\circ\text{C}$ and $25\text{ }^\circ\text{C}$ show that SO_2 is adsorbed readily (Fig. 3.6-6).

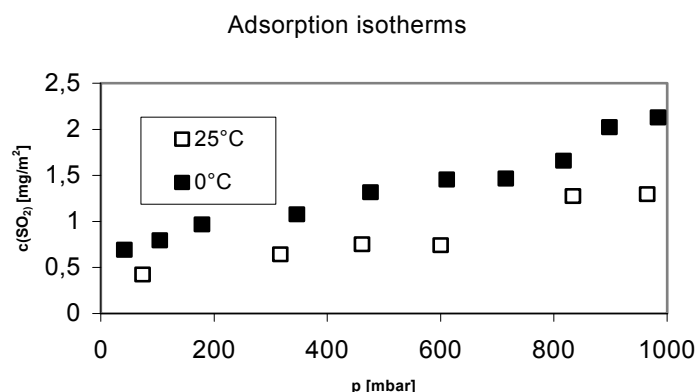


Fig. 3.6-6: Plot of the amount of adsorbed SO_2 per surface area versus pressure at temperatures of $25\text{ }^\circ\text{C}$ and $0\text{ }^\circ\text{C}$. Adsorption is strongly temperature-dependant, with more SO_2 being adsorbed at lower temperatures: here the amount of absorbed gas is proportional to $e^{1/T}$.

Adsorption is partially irreversible (Fig. 3.6-7). Our experiments suggest that about 40 % of the originally adsorbed gas remains on the surface, a value that is confirmed by XRF measurements.

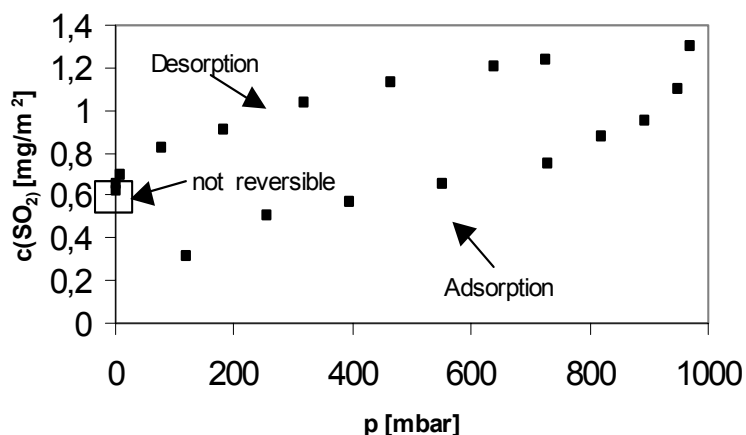


Fig 3.6-7: Adsorption-desorption isotherm at 25 °C. Adsorption is not completely reversible. Experiments suggest that about 40 wt.% of the SO₂ that was originally adsorbed remains on the surface after desorption.

The irreversibly bound SO₂ is of special interest for understanding the effects of the adsorption process on climate. Extrapolations of the experimental data to pressure-temperature conditions found in volcanic plumes (*e.g.*, P(SO₂) = 0.5 mbar; T = -50 °C) show that a significant fraction of the SO₂ could be removed permanently from the eruption column by adsorption. For a plume model (initial values: gas/ash-fraction = 0.03; entrainment coefficient = 0.09; content of volcanic gas = 1.15 wt.%), rhyolitic glass is predicted to remove 30 wt.% and andesitic glass 10 wt.% of the original SO₂.

e. High-pressure melting curve of methane hydrates: Implications for Titan's interior (A.V. Kurnosov and L.S. Dubrovinsky)

Saturn's largest moon, Titan, is the only moon in the solar system known to have a significant atmosphere, which is composed largely of nitrogen with some methane (at 1.5 atm. and -178 °C). Titan's atmosphere is of considerable interest because it may mimic that of the early Earth and even provide insights into the origins of life. The origin of atmospheric methane is still uncertain. The sun's ultraviolet light should have destroyed atmospheric methane within approximately the first ten million years of Titan's history. Currently, the main hypothesis for the presence of methane in Titan's atmosphere involves continuous replenishing from a significant reservoir somewhere in Titan's interior. Thus, in order to explain the composition of Titan's current atmosphere, models of Titan's interior are required. Important constraints on such models include the composition and structure of Titan's interior and relevant phase equilibria data. The evolutionary turbulent model of Saturn's sub-nebula provides information

on Titan's composition and suggests that all volatile compounds were accreted as methane clathrate hydrate and ammonia monohydrate together with small amounts of other clathrate hydrates. The data on Titan's orbital eccentricity, obtained by the spacecrafts Voyager and Cassini-Huygens, together with Earth observations, lead to the conclusion that a liquid layer must have existed beneath Titan's surface during the entire history of Titan. Previous models of this layer as a source of atmospheric methane take into account only the data on ammonia-water phase equilibria and conclude that a liquid layer a few hundreds of kilometers thick is present near the surface based on the low freezing temperature of ammonia solutions. The existence of atmospheric methane has been explained by volcanic activity originating from this water-ammonia magma layer, which melts surface clathrates when reaching an upper ice-clathrate layer. A pressure-temperature phase diagram is required to test this hypothesis, but was previously available only up to 1.5 GPa and 320 K for the methane - water system, and there are no data on phase relations in the three-component methane-ammonia-water system.

We have studied decomposition curves of methane clathrate hydrates at pressures up to 5 GPa (close to the estimated pressure of Titan's core) and temperatures up to 600 K. We have also studied the effects of adding ~ 20 wt.% ammonia (the likely concentration of ammonia on Titan) on the formation and stability of clathrate hydrates up to 2.5 GPa.

Equilibrium phase boundaries were determined in an externally-heated diamond anvil cell (DAC) using Raman spectroscopy and optical microscopy for phase identification. *In situ* X-ray powder diffraction at room temperature has also been performed for phase analysis. Our data on clathrate hydrate melting in the methane-water and methane-ammonia water systems are summarized in Fig. 3.6-8. The addition of ~ 20 wt.% ammonia does not affect the melting temperature of clathrate hydrates within experimental error (± 5 °C), but significantly decreases the melting temperature of ice. We find that the slope of the melting curve of methane clathrate dihydrate (which forms at ~ 1.8 GPa) is significantly steeper than that of the two hydrates at lower pressures.

Based on our data on clathrate hydrate stability we propose a new thermal profile of Titan's interior, which can explain the existence of a liquid layer during the entire history of Titan. Assuming a smooth temperature decrease from the core to the surface and taking into account that silicates and rock can still be mixed with "ice" components, Titan's isentrope can intersect the melting curve of clathrate hydrates twice (see Fig. 3.6-8). This result predicts both the presence of the liquid layer and methane release. Liquid methane, which is immiscible with a homogeneous water-ammonia solution and has a lower density, forms an upper liquid layer. This methane-rich magma can reach the surface without clathrate formation or freezing and injects methane directly into the atmosphere. Indications of cryovolcanic processes on Titan's surface observed by the Huygens probe in January 2005 provide additional support to this idea. We consider that the liquid layer is located slightly deeper and has a different structure compared with previous models. The mechanism of atmospheric methane replenishment according to our new model is simpler and the temperature of the interior is higher than previously assumed.

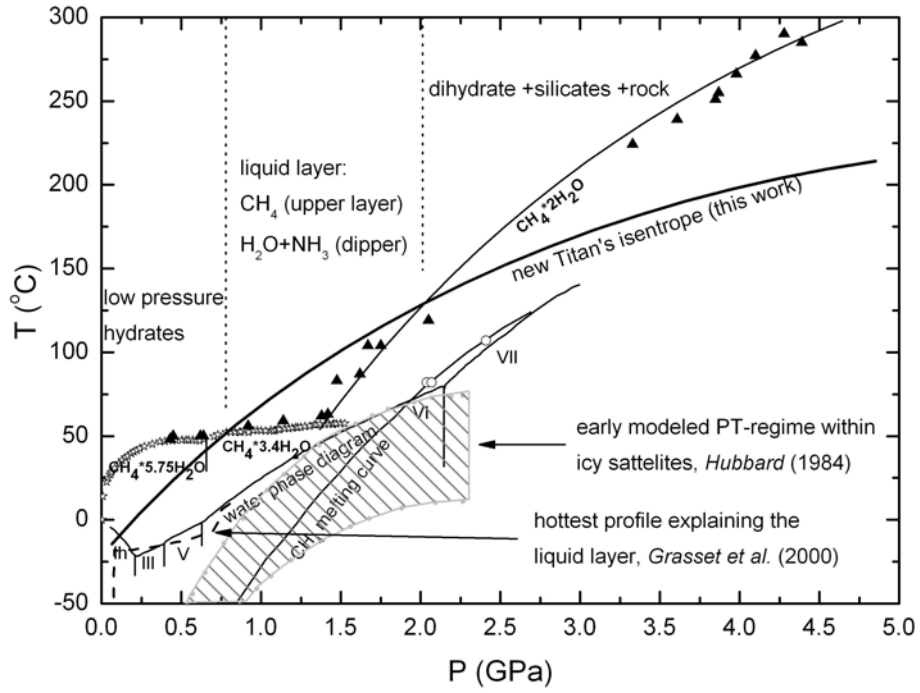


Fig. 3.6-8: Melting curves of methane clathrate hydrates (triangles – this work, stars – Dyadin *et al.*, Mendelev Comm., 1997 (1), 34)

3.7 Rheology

The Earth is a dynamic planet and its interior is characterized by deformational processes on a large range of time scales. The rheological behaviour of rocks is typically brittle at high stresses and fast strain rates (*e.g.*, earthquakes) and ductile at low stresses and slow strain rates (*e.g.*, the movement of lithospheric plates). Flow laws of rocks can be determined in mechanical tests in the laboratory, but the number of variables is rather large. Besides external parameters such as temperature, pressure, and fugacity/activity of various chemical components, also intrinsic material properties such as crystalline defects and crystallographic preferred orientations (texture) have to be taken into account. In addition, plastic deformation of a material will also change its intrinsic properties. In the geosciences the microstructures of deformed rocks are therefore often used to reconstruct their deformation history. Whereas the reconstruction of the deformation path itself can be quite successful in natural rocks, the determination of the stresses that caused the deformation still remains extremely difficult. Here the measurement and extrapolation of data from mechanical tests offer in most cases the only possibility to achieve quantitative results.

The rheology of olivine and its high-pressure polymorphs (wadsleyite, ringwoodite) is of crucial importance for the understanding of the occurrence of earthquakes at depths where normally brittle processes are inhibited by high temperatures and pressures. The phase transition process itself as well as the strength difference between the phases may trigger or inhibit brittle behaviour. Directed stresses on a prescribed fault plane may enhance the phase transition. The influence of added melt on olivine deformation is rather important since the uppermost mantle beneath mid ocean ridges and above subducting slabs most likely contains up to 10 % melt. It appears that the addition of melt leads to a very different texture and consequently to a very different pattern of physical anisotropy. In turn, deformation of a melt-containing rock has strong consequences for the melt distribution inside the rock and its permeability. Whether a melt is trapped in a solid or if it forms an interconnected network that allows it to move through the solid body is largely governed by the deformation that the rock-melt aggregate is undergoing. Experimental approaches that try to shed light onto dynamical microstructural processes such as changing melt distributions in a solid body are seriously limited if the samples are not accessible *in situ*, *i.e.*, at pressure and temperature. Experiments in a moissanite anvil cell overcome this problem since they allow direct observation and are in addition stable to very high temperatures.

The rheology of subducting slabs relative to that of the surrounding mantle is crucial for the understanding of the formation of high-pressure terranes which are found in mountain belts around the world. Whereas the absolute strength of natural rocks at high pressure and temperature can often only be estimated with large errors, field relationships may allow the establishment of relative strengths (*e.g.*, between eclogite and peridotite) in such high-

pressure terranes. The reconstruction of the deformation behaviour of a rock at a certain temperature and pressure is often complicated by subsequent overprinting and change in mineral composition (*e.g.*, symplectites).

Natural examples of ductile deformation in garnet have been reported much more often recently since electron backscattering diffraction in the SEM and the measurement of garnet crystal orientations has become more widespread. An important aspect in these studies is the fact that deformation has an influence on interdiffusion processes and chemical equilibria which are used in garnets to determine P,T paths of metamorphic rocks. Quartz is one of the most important minerals in crustal rocks when we try to understand the deformation behaviour as well as the P,T conditions of deformation. Its detailed textural analysis allows the separation of the kinematics of different deformation phases as well as their temperature of deformation.

a. *Remobilisation of old faults by transformation from olivine to wadsleyite (D.P. Dobson, A. DeRonde and P. Meredith/London, F. Heidelbach)*

Analysis of the orientations of slip planes associated with some deep-focus earthquakes suggests that they might have occurred on pre-existing planes of weakness. The prevailing explanation for the seismic remobilisation of old faults within the transition zone relies on shear localisation related to grain-size reduction during the olivine-wadsleyite transition. We tested this theory by annealing faulted synthetic dunite samples at pressures between 6 and 14 GPa and temperatures up to 1273K. A 7-transducer acoustic emission (AE) detection system allowed us to determine the precise location and sense of displacement of brittle events within the sample and hard buffer-rods ensured that a differential stress was maintained on the sample throughout the experiment. Analysis of recovered samples by electron back-scattered diffraction helped to elucidate the deformation mechanisms.

Figure 3.7-1 (top) shows an orientation contrast SEM image of a faulted dunite sample compressed isothermally from 6 to 7 GPa at 1173 K over one hour. The bright horizontal lines towards the top left and bottom right of the image are a gold strain-marker within the sample, showing a total displacement of $\sim 500 \mu\text{m}$ in a dextral sense: most of this strain would have occurred prior to the hot compression phase. The fault is filled with fine-grained olivine (modal grain-size $\sim 0.3 \mu\text{m}$, but with occasional large, $\sim 5 \mu\text{m}$ grains).

The contoured pole figure plot (Fig. 3.7-1, bottom) shows randomly oriented maxima associated with the large grains in the fault zone. The fine-grained material gave only poor diffraction patterns, but appeared to be randomly oriented as well. AE signals from the fault plane observed during hot compression were indistinguishable from those observed during cold compression and appeared to exhibit stick-slip behaviour.

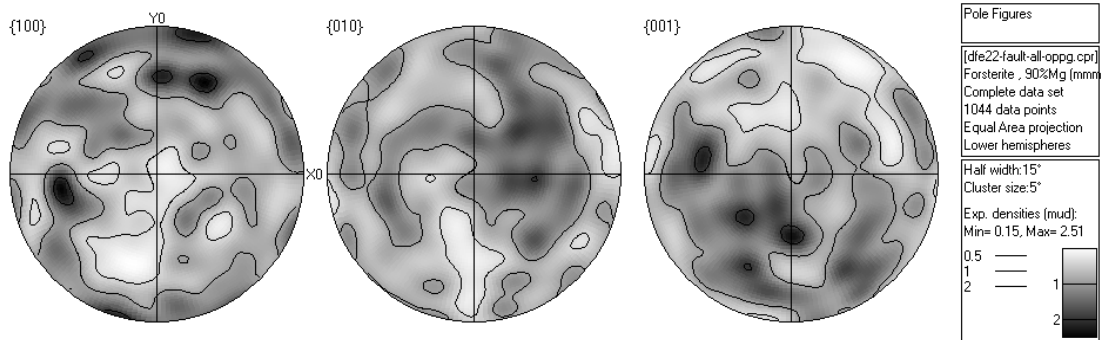
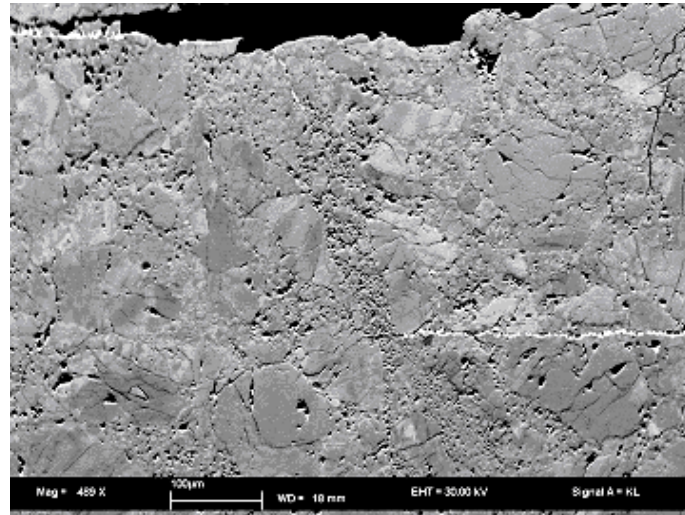


Fig. 3.7-1: SEM orientation contrast image (top) and pole figure plot (bottom) of a fault zone in synthetic dunite sample deformed at 6-7 GPa and 1173 K. The pole figures come from the fine-grained region within the shear zone.

A pole figure plot from a fault-plane deformed at 14 GPa and 1173-1273 K for 20 minutes is presented in Fig. 3.7-2 (top). The plot has been rotated and reflected such that the fault orientation and sense of shear are the same as in Fig. 3.7-1 (top). The wadsleyite filling the fault has a uniform grain-size of ~ 0.8 to $1.0 \mu\text{m}$ and shows a lattice preferred orientation with a-axes oriented in the direction of shear, and b-axes oriented in the fault-plane perpendicular to the shear direction. This lattice preferred orientation is not a relic inherited from the olivine since it shows random orientations in fault zones. In addition, wadsleyite produced outside fault-zones, but in the same cell design, do not show lattice preferred orientation (Fig. 3.7-2, bottom).

We conclude that wadsleyite is significantly weaker than olivine under these conditions. Dislocation creep is the dominant deformation mechanism in wadsleyite, even at grain-sizes as small as 1 micron. Pre-existing faults rapidly fill with wadsleyite due to the small olivine grain-size and wadsleyite nucleation at olivine grain boundaries. Within the Earth, pre-existing faults will be weakened by the transformation to wadsleyite and a plastic shear localisation process might result in seismogenic slip.

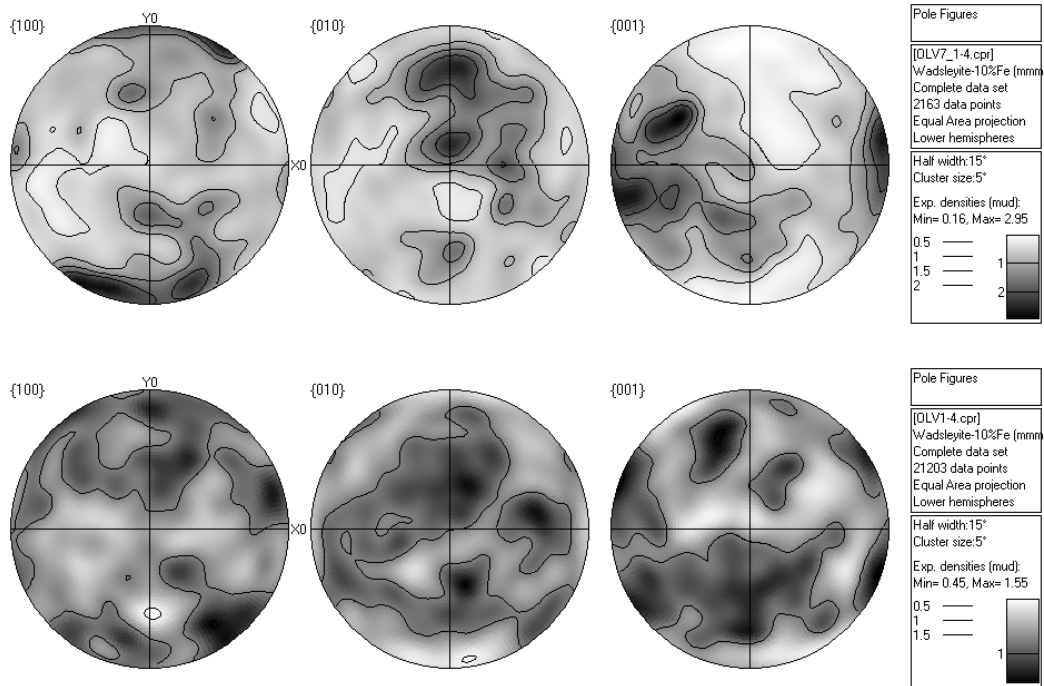


Fig. 3.7-2: Pole figure plots of wadsleyite transformed from olivine at 14 GPa and 1173-1273 K within (top) and outside a fault zone (bottom). The pole figures on top have been reflected such that the orientation and sense of shear is the same as in Fig. 3.7-1 (top).

b. Lattice preferred orientation of olivine in the presence of metallic melt (J. Hustoft and D. Kohlstedt/Minneapolis, F. Heidelberg)

We investigated the effect of simple shear deformation on the distribution of an iron sulfide melt in olivine. Metallic melts in contact with silicate grains have high dihedral angles $\theta = 90^\circ$, and thus are non-wetting melts ($\theta > 60^\circ$) that do not form interconnected networks. We have found that metallic melts of core composition (Fe and FeS, hereafter denoted Fe-S) will segregate into melt-rich bands when the melt fraction present is 0.05 or greater (Fig. 3.7-3).

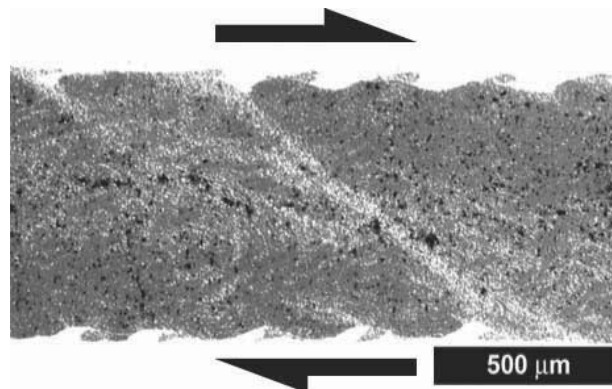


Fig. 3.7-3: Reflected light micrograph of olivine + 9 vol.% Fe-S, sheared dextrally to $\gamma = 2.5$. The metallic melt is segregated into melt-rich bands.

Samples of olivine + Fe-S were mechanically ground together to ensure homogeneous distribution of the metal phase within the silicate phase before hot-pressing in a Paterson vessel at 1523 K and 300 MPa for 4 h. Elliptical slices of the hot-pressed material with major axes of 8 mm and minor axes of 6 mm and 0.5 - 1.0 mm thick were deformed in simple shear utilizing thoriated tungsten pistons cut 45° to the long axis. Samples were deformed to shear strains of 1.3 - 4.5. Electron backscatter diffraction (EBSD) patterns were collected on all samples over areas of ~ 5 mm by ~ 500 μm. The LPO was measured for grains near the center of the samples and away from all edges of the samples. Beam step sizes of 10 μm were on the same order as the grain size (~ 10 μm).

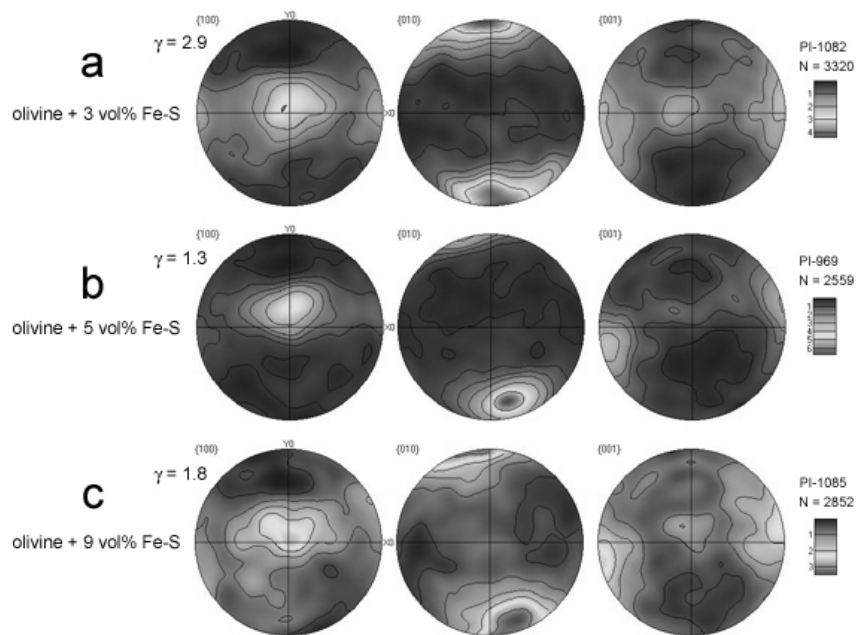


Fig. 3.7-4: Olivine pole figures for samples with 3, 5, and 9 vol.% Fe-S deformed in simple shear (top-to-the-right).

The LPOs of olivine containing 3, 5, or 9 vol.% Fe-S deformed in simple-shear are presented in Fig. 3.7-4. The sense of shear is dextral. The metallic melt in the samples of Fig. 3.7-4b,c was redistributed into melt-rich bands, while the metallic melt of 3.7-4a was not redistributed. In Figure 3.7-4a, the LPO of olivine + 3 vol.% Fe-S deformed to $\gamma = 2.9$ displays girdles of olivine a- and c-axes in the shear plane and b-axes aligned perpendicular to the shear plane. In contrast, the samples of olivine + 5 vol.% Fe-S (Fig. 3.7-4b) and 9 vol.% Fe-S (Fig. 3.7-4c) deformed to $\gamma = 1.3$ and 1.8, respectively, have olivine a-axes aligned in the shear plane perpendicular to the shear direction. The b-axes are back rotated relative to the shear direction.

The LPOs of olivine + 9 vol.% Fe-S are shown in Fig. 3.7-5 with progressively increasing shear strain. The sense of shear is again dextral, and all samples are from the same hot-

pressed material. Figure 3.7-5a is the LPO of the original hot-pressed material, where a weak lattice preferred orientation exists. With increasing shear strain (Fig. 3.7-5b and c), up to $\gamma = 2.5$, the metallic melt has redistributed into metallic melt-rich bands, and the olivine a-axes are aligned in the shear plane perpendicular to the shear direction, with the b-axes back-rotated. At $\gamma = 4$, (Fig. 3.7-5d) the a- and c-axes of olivine are no longer aligned but are now girdled in the shear plane, but the b-axes are still back rotated. At $\gamma = 4.5$, the a- and c-axes are girdled and the b-axes are aligned perpendicular to the shear plane again, as in the aligned melt samples LPOs.

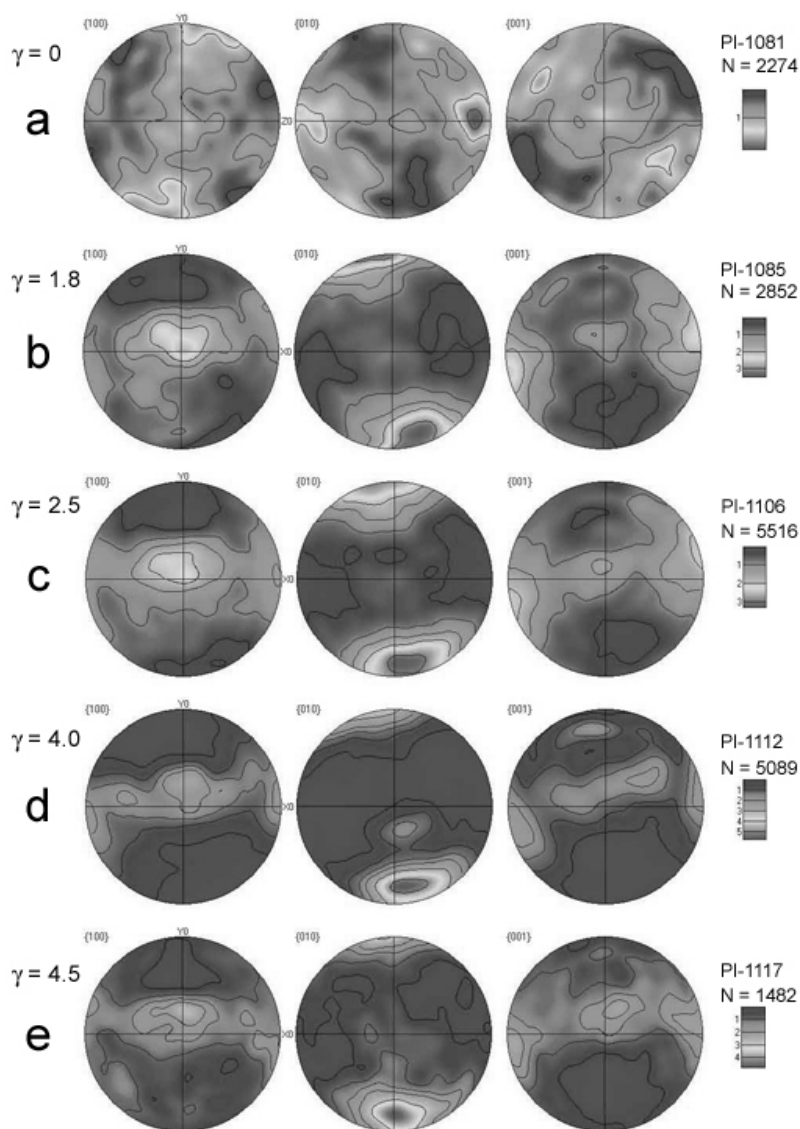


Fig. 3.7-5: Olivine pole figures for samples with 9 vol.% Fe-S deformed in simple shear (top-to-the-right) with increasing shear strain.

In the presence of segregated metallic melt olivine possesses the same LPO as olivine in the presence of silicate melts segregated into melt-rich bands. When the metallic melt fraction is

too low to allow for an interconnected network to form (when the metallic melt fraction is less than 0.05), the olivine in the aligned but unsegregated metallic melt samples has the same LPO as that of olivine with aligned silicate melts. We conclude that the same olivine LPO develops when MORB melt and metallic melt segregate. However, in the case of metallic melt, after the melt-rich bands have developed, the remainder and majority of the sample has isolated metallic melt pockets, and the LPO of the olivine in the melt-poor lenses switches from a- and c-axes aligned in the shear plane to a- and c-axes girdles in the shear plane.

c. Olivine-FeS melt deformation experiments with the D-DIA (N.P. Walte, D.J. Frost and D.C. Rubie)

Many models for the formation of the Earth are based on an early accretional stage from a more or less homogenous starting material, followed by heating and differentiation to form the metallic core. While the density difference between Fe-S-O melt and silicates principally favours gravitational segregation, a generally high solid-liquid dihedral angle $> 60^\circ$ of the system at pressures ≥ 3 GPa hinders complete segregation from a static solid silicate matrix at “textural equilibrium”. Thus, the existence of an early magma ocean of varying depth is commonly assumed to allow for an efficient core formation by gravitational settling of metallic melt. Alternatively, previous studies have suggested that deformation might lead to the formation of interconnected melt pathways, along which the melt could percolate and segregate. However, geochemical constraints indicate that segregation must have been very efficient and the melt pathways of previous experiments have only been observed at melt fractions > 3 vol.%.

Olivine-FeS melt deformation experiments were performed to explore melt distribution and the formation of connectivity as a function of varying the strain rate (ca. 10^{-3} s $^{-1}$ to 10^{-6} s $^{-1}$), the finite strain, and the melt fraction (1.5-8 vol.%). All experiments were done at 1400 °C and at a surrounding pressure of 3 GPa with the Deformation-DIA. Samples were prepared by mixing of synthetic olivine powder (Fo₉₀) with FeS powder and enclosing the mixture into rhenium capsules. Before deformation the samples were statically annealed for 4 hours. The deformation was done by bulk pure shear with a bulk shortening of 5 to 40 %. The samples were quenched rapidly during ongoing deformation to preserve the dynamic melt geometry as accurately as possible. Figure 3.7-6 shows an overview of a static experiment after 4 hours annealing and an experiment after deformation.

Our experiments show that the melt distribution is determined by a complex interplay between the melt fraction, the solid-melt dihedral angle, and deformation. At a very high strain rate of 10^{-2} s $^{-1}$ (e.g., impact deformation), melt occupies elongated intercrystalline and intracrystalline cracks that are oriented approximately parallel to σ_1 . At a high to “moderate” strain rate (10^{-3} to 10^{-4} s $^{-1}$) elongated melt pockets are observed that locally wet grain boundaries and probably induce localized grain boundary sliding. At lower strain rates (10^{-5} to

10^{-6} s^{-1}) the melt pockets are often passively dragged by migrating grain boundaries or form melt inclusions (Fig. 3.7-7).

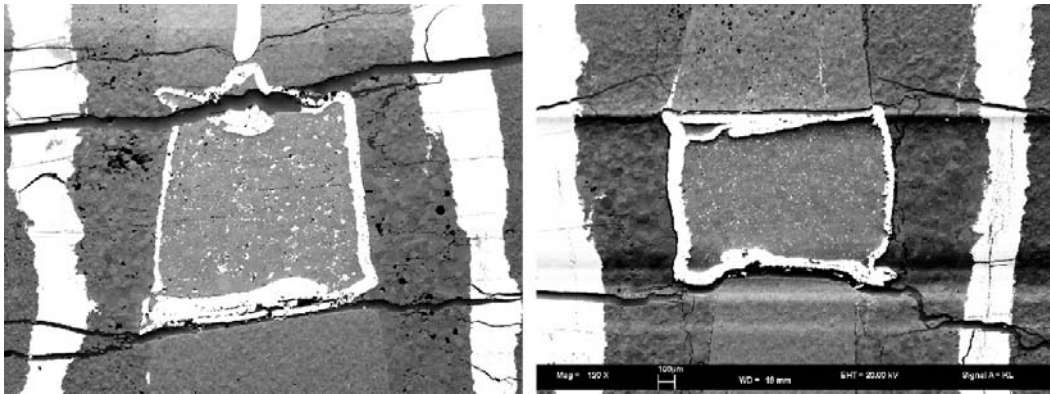


Fig. 3.7-6: Orientation contrast overview image of an undeformed capsule after 4 hours of annealing (left) and of a deformed sample (right).

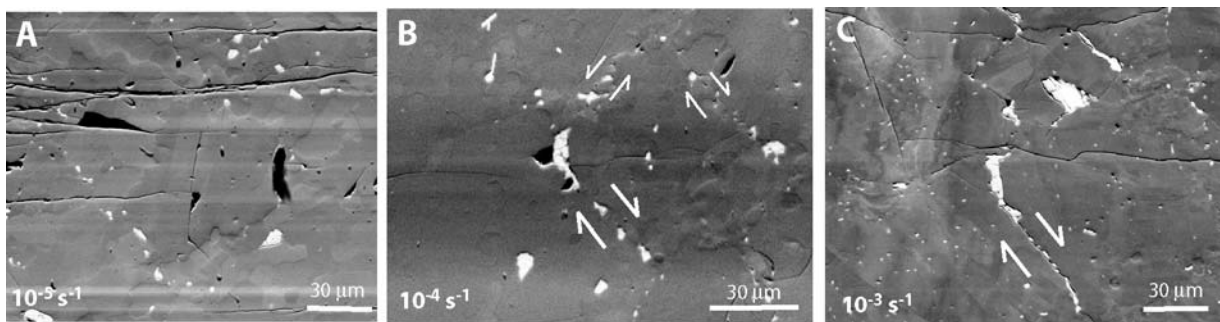


Fig. 3.7-7: SEM orientation contrast images of samples for melt distribution at different strain rates (numbers at lower left) and a low melt fraction (2.5 wt.%). Vertical shortening. **(a)** Melt pockets locally align, but shapes are hardly affected by the deformation. **(b)** Strain localizes along melt pocket arrays and influences their shape. **(c)** Further strain or higher strain rate can lead to a locally interconnected melt film that results in grain boundary sliding.

Despite local wetting of grain boundaries during deformation, we did not observe an interconnected melt network or melt pathways in experiments with a melt fraction ≤ 8 vol.%, so that continuous melt migration should be inhibited. However, at the same time the bulk melt fraction decreases in all deformation experiments with an initial melt-fraction higher than ca. 2 vol.% (Fig. 3.7-8). Higher initial melt fractions drop to an apparently stable level of ca. 1.5-2 vol.%, which is well below the theoretical static connectivity threshold of 3-5 vol.%. Segregated melt either collects along the side of the capsule or migrates through cracks of the capsule into the surrounding MgO mantle. Additionally, the distribution of melt in statically annealed samples is different than the distribution in deformed samples, even at low melt fractions. During deformation, the relative amount of melt in large melt pockets decreases,

while the amount of melt in smaller pockets strongly increases. This could even be observed in samples that were only shortened by a few percent.

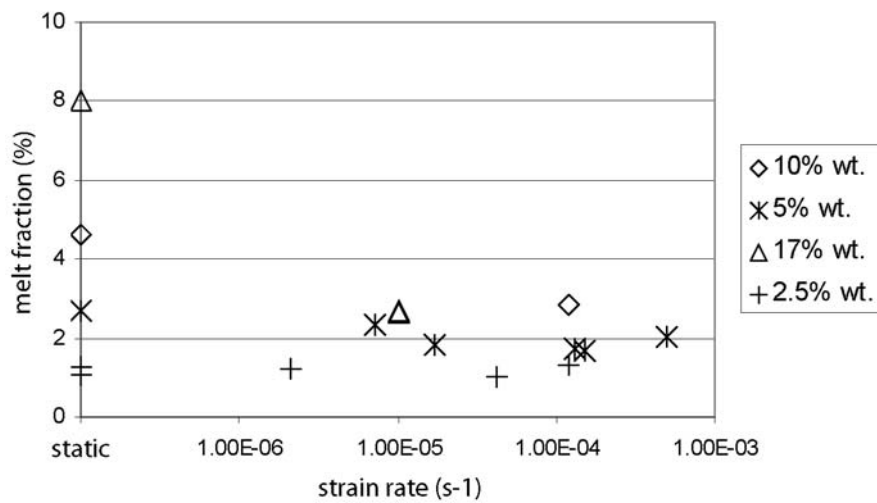


Fig. 3.7-8: Evolution of the bulk melt fraction as a function of the strain rate. The final melt fraction of all samples is below 3 vol.%.

Deformation therefore effectively distributes the melt more evenly throughout the grain matrix. Because of the lack of an interconnected melt network the observed melt mobility requires a non-continuous migration mechanism. Possible mechanisms that might establish a transient short-range permeability are a collapse of larger melt pools and injection of the melt into the surrounding matrix and the local wetting of grain boundaries along short shear zones. The combined effect of such processes might be responsible for the observed non-continuous melt distribution and segregation over short distances. Our experiments show that deformation might help to segregate metallic melts with a high dihedral angle significantly below the interconnection threshold. However, segregation below ca. 1.5 vol.% was not observed even at a very high strain rate so that efficient core formation can probably not be achieved by deformation alone.

d. *In situ* observation of high-temperature textural processes with the Moissanite cell (N.P. Walte and H. Keppler)

A drawback of many experimental techniques in Earth and material sciences is the inability to observe time-dependent high-temperature processes during an experiment. Examples for such ongoing processes are the textural development of rocks during melting and solidification, microstructural changes during solid-state and fluid-present metamorphic reactions and processes of grain-growth and Ostwald ripening. These processes are also important for solid and liquid state sintering in the material sciences, since the microstructural evolution of a sample during sintering determines its strength and other physical properties. However, the

conventional investigation of microstructural changes by post-mortem analysis of quenched samples is often unsatisfactory to fully understand ongoing processes. The moissanite cell was therefore developed as a new tool for investigating high-temperature processes with an emphasis on the development of the microstructure. It allows optical *in situ* observation of long-term experiments at high temperatures exceeding 1200 °C. Moissanite is a transparent gem-quality type of SiC that is characterized by its hardness and superior chemical and thermal resistance. Samples are placed directly between two moissanite windows and the cell is assembled similarly to a large diamond anvil cell. The assembled cell is positioned under a microscope and real-time or time-lapse movies can be recorded with an attached digital camera during an experiment to reveal slow microstructural changes.

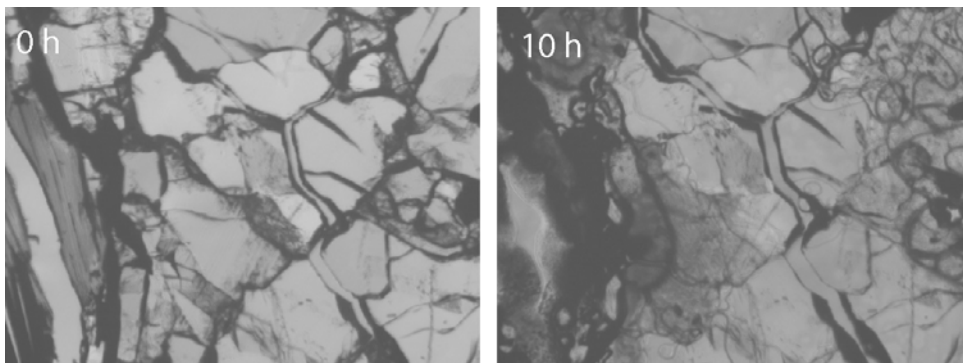


Fig. 3.7-9: *In situ* melting of a mica schist at 1200 °C. Muscovite first transforms to an OH-free sheet silicate before a melt is formed at the contact to plagioclase. Image width is 1 mm.

First tests and studies of the moissanite cell were performed at ambient pressure. Figure 3.7-9 shows *in situ* melting of a thin section from a mica schist. At ambient-pressure muscovite and biotite (on the left) transforms into an OH-free layer silicate before breakdown. At a temperature above 1000 °C a melt forms at the contact between the dehydrated micas and plagioclase. Bubble nucleation and growth can be observed in Fig. 3.7-10. A $K_2O-Na_2O-SiO_2$ glass is heated and starts to nucleate and grow bubbles, probably due to degassing of dissolved carbonate and H_2O . Such experiments can give new clues for the degassing behaviour of lavas during decompression, since bubble nucleation and growth can be directly measured.

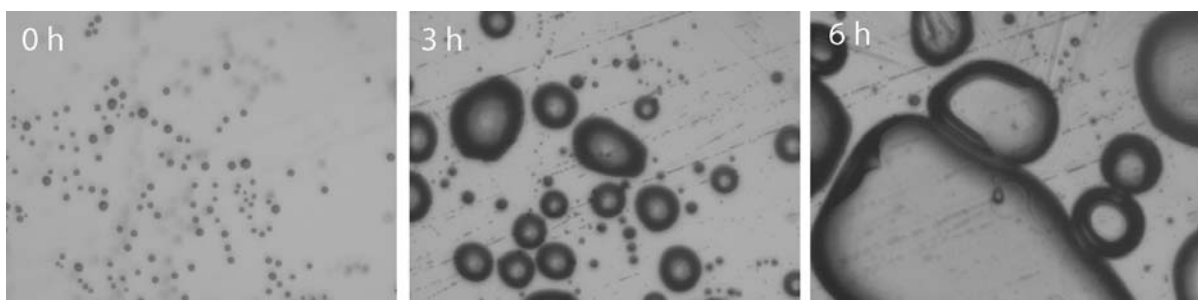


Fig. 3.7-10: Degassing of a $Na_2O-K_2O-SiO_2$ glass at 650 °C. Image width is 0.5 mm.

The main advantage of the new moissanite cell compared to conventional devices for *in situ* heating tests such as hot stages is that the sample is directly confined between the moissanite windows, which allows for a very good shape and temperature control of a sample *e.g.*, as a thin film even during melting, degassing, or crystallizing. This makes the moissanite cell ideal for studies involving a melt phase, such as liquid phase sintering and magmatic processes at the grain scale.

e. Stress induced changes in slip systems in natural olivine from the Kvalvika peridotite lens, Western Norway (M.P. Terry and F. Heidelbach)

The Kvalvika peridotite lens occurs in eclogitized Ulla (diorite) gneiss in the Western Gneiss Region (WGR) of Norway (Fig. 3.7-11) and contains the mineral assemblage Grt + Olv + Opx + Spl ± Cpx. Petrological data indicate that both units underwent Scandian continental subduction 410 Ma ago. Modeling of the changes Fe/Fe+Mg (FM) ratio and Al content in Opx yield a clockwise P-T path indicating metamorphic conditions were at ~ 740 to 850 °C and ~ 3.0 to 4.0 GPa. Both units exhibit the same foliation and lineation which was produced during Scandian metamorphism. The lens itself displays increasing strain from the center to the rim which is reflected in the decreasing grain size and increasing grain shape alignment.

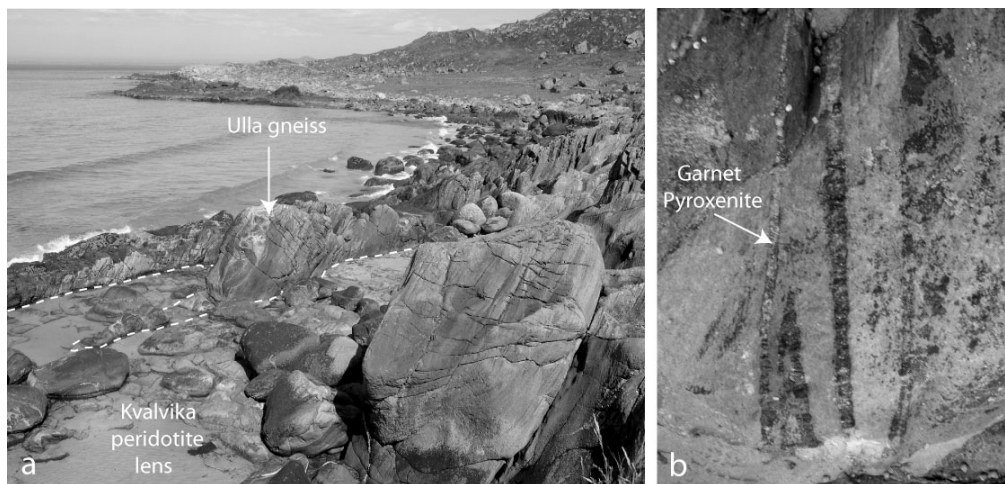


Fig. 3.7-11: (a) Photograph of the Kvalvika peridotite lens viewed from the WSW. The Ulla gneiss (gray) encloses the peridotite (dark grey). (b) Close-up view of the peridotite lens showing pyroxenite layers that define tight to isoclinal folds.

The crystallographic preferred orientations (CPO) of olivine were analyzed in a low (center) and a high strain sample (rim) from the peridotite lens. Results indicate that olivine deformed by c-slip in both cases with intracrystalline with dominant glide on the (100)[001] slip system in the low strain sample and by glide on the (010)[001] slip system in the high strain sample (Fig. 3.7-12). The strength of the CPO increases with increasing deformation at the rim. The c-slip is interpreted to be the result of high stresses in the peridotite lens imposed by the

surrounding eclogitic gneiss which was presumably significantly stronger at the P,T conditions of deformation. According to experimental data from the literature the change in the dominant slip plane, from (100) to (010), is most likely produced by increased stress at the rim of the peridotite lens.

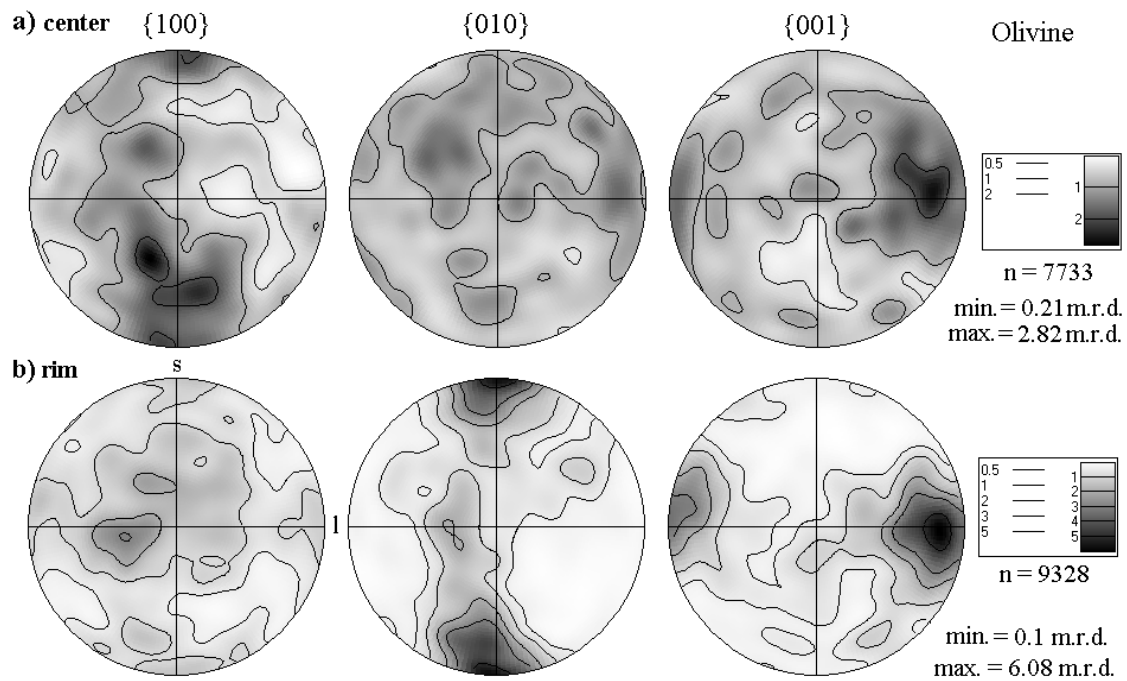


Fig. 3.7-12: Pole figures of olivine from the center and the rim of the Kvalvika peridotite lens.

f. Inherited fabric in a symplectite: A key to deformation history (F. Heidelbach and M.P. Terry)

We studied the deformation structures in the eclogitic Ulla Gneiss from the Western Gneiss Region in Norway which was subducted as part of Baltica lithosphere beneath Laurentia during the Scandian orogeny (see previous contribution, Fig. 3.7-11). Petrologic data indicate that deformation took place at ~ 3 to 4 GPa and ~ 740 to 850 °C and produced a foliation and lineation in garnet and omphacite. Whereas the garnet fabric remained rather unchanged during exhumation, omphacite was transformed into a symplectite consisting of diopside, hornblende and plagioclase (Fig. 3.7-13). Although the original grain structure of the omphacite is still recognizable, the actual grains themselves were completely replaced by the lamellar symplectite.

Measurements of the crystallographic preferred orientation (CPO) with electron backscattering diffraction (EBSD) show that diopside and hornblende of the symplectite have a systematic orientation relationship with the macroscopic fabric as well as the (presumed) orientation of the host omphacite.

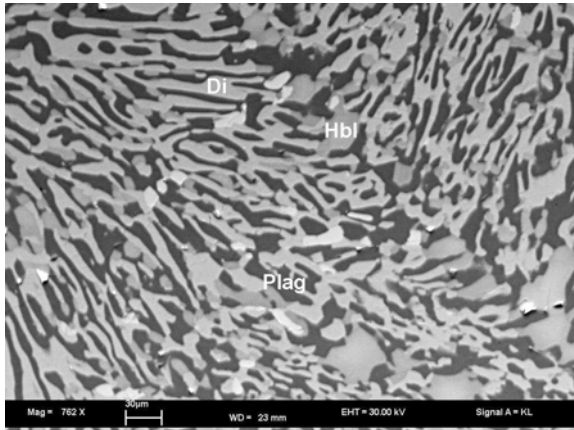


Fig. 3.7-13: SEM-BSE image of microstructure of symplectite; Di – diopside, Hbl – hornblende, Plag – plagioclase.

The orientation relationship between the two chain silicates is very sharp with the crystallographic forms $\{100\}$, $\{010\}$ and $\langle 001 \rangle$ being parallel. Their bulk texture shows a maximum of $\langle 001 \rangle$ parallel to the lineation and girdles of $\{010\}$ and $\{110\}$ perpendicular to the lineation with maxima subparallel to the foliation (Fig. 3.7-14).

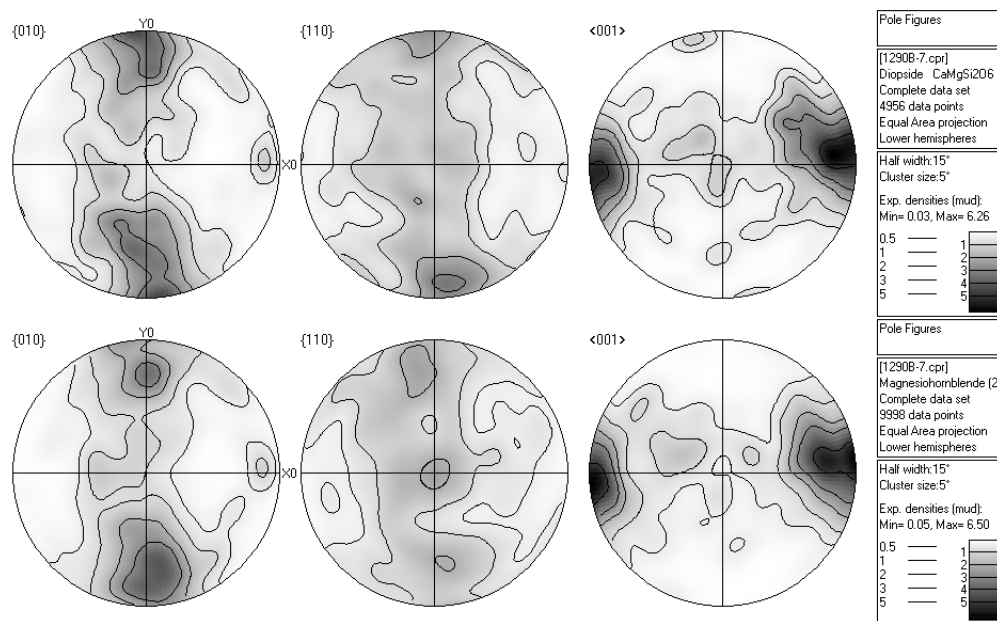


Fig. 3.7-14: Pole figures of diopside (top) and hornblende (bottom) in the symplectite.

This corresponds to an L-type texture of the original omphacite and indicates constrictional strain with an additional component of simple shear. For feldspar the orientation relationship to the presumed host orientation is apparently lost. Thus the deformation texture of the original omphacite is only inherited and preserved by the structurally similar phases such as diopside and hornblende that formed during retrograde amphibolite facies metamorphism. It should be noted that the topotaxial relationship seems to hold although the grain structure has

been completely changed. Therefore the completely static grain fabric of the symplectite still yields information about the strain along the P-T path at much higher metamorphic conditions.

g. Intra- and intergranular dynamic recrystallisation and accompanied geochemical diffusion processes in deformed garnets (M. Bestmann, G. Habler and M. Thoeni/Vienna, F. Heidelberg)

Garnet is stable at a wide range of P-T conditions and bulk compositions and thus is ubiquitous in several rock types of the Earth's crust and mantle. It is therefore of particular interest to obtain knowledge of its deformation mechanisms. Descriptions of plastic deformation and recrystallization features are still rare. Here we present EBSD and geochemical data of deformed magmatic pegmatite-garnet from the Austroalpine Koralpe crystalline basement (Austria).

A garnet-, aluminosilicate bearing pegmatite with a Permian emplacement age has been deformed together with its metapelitic host rock during the Cretaceous HP metamorphic event (~ 650-700 °C/1.8-2 GPa). Magmatic almandine-spessartine garnet grains with ca. 10 mm grain size show distinct intra- and intergranular deformation zones with a well-developed grain and subgrain microstructure. EBSD maps (Fig. 3.7-15a) reveal continuous lattice distortion patterns (up to 35° lattice rotation from the less distorted area towards the distinct deformation zones). Smaller grains (20-30 micrometer sized) within the initial intragranular deformation zones have a similar crystal orientation as the host grain. New grains (30-50 micrometer sized) from more progressed deformation zones show more or less random distribution.

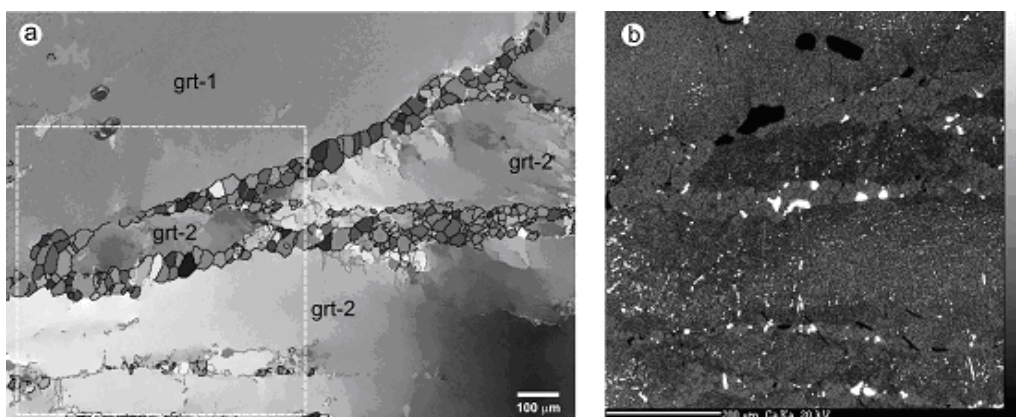


Fig 3.7-15: (a) EBSD orientation map of deformed garnet grains (grt-1, grt-2). Grayscale represents orientation differences. Intra- and intergranular recrystallization zones are developed. (b) X-ray Ca-map of the marked area in (a). Grey shades show the distribution of the grossular content in Grt (brighter domains indicate higher Ca-content). White spots represent apatite grains; black acicular grains in the lower part of the image are kyanite.

Transitions between the two end member deformation zones also exist. Along initial deformation zones needles of kyanite were observed. The deformation zones show a slight but distinct Ca enrichment of new (sub)grains and a Ca depletion of immediately adjacent host domains. Ca variations are below the extent of magmatic continuous zoning (< 1 mol.%) and indicate the lack of significant material exchange with the matrix. Crystallization of 20-50 micrometer sized apatite- and xenotime grains also occurred within the deformation zones; whereas these inclusions have < 1 micrometer grain sizes in the magmatic host garnet (Fig. 3.7-15b).

The individual garnet porphyroclasts record an evolution of progressive strain accommodation by initial dislocation creep and recovery processes, followed by subgrain rotation recrystallization. We suggest that recrystallized grains, once formed, are able to deform partly by diffusion accommodated grain boundary sliding. Diffusion processes resulting in enhanced Ca content and the crystallization of apatite and xenotime accompanied the process of dynamic recrystallization. Whereas magmatic Grt growth had taken place at LP conditions in equilibrium with andalusite, the appearance of kyanite, possibly triggered by the localized crystal plasticity, gives evidence that the deformation occurred during Cretaceous HP metamorphism.

h. *New constraints on the evolution of the Bayerischer Pfahl shear zone (E. Galadi-Enriquez and G. Zulauf/Frankfurt, F. Heidelberg)*

Our study area is located in the southern Bavarian Forest, which is geologically situated in the Moldanubian Zone of the Central European Variscides, between the NW—SE trending Bayerischer Pfahl (BPSZ) and Danube shear zones. The most common rocks in the study area are gneisses affected by anatexis and intruded by igneous rocks. The gneisses show a foliation which parallels the steeply dipping NW—SE striking mylonitic foliation of the BPSZ. The latter results from dextral shearing.

The gneisses are often cut by granite dykes with different orientations. Our study is focussing on WNW—ESE to ENE—WSW trending granite dykes which were sinistrally sheared under ductile conditions. The aim of our investigation is to constrain the relationship between the deformation of the granite dykes and the deformation along nearby major shear zones, that is mainly the BPSZ.

Several authors have studied the deformation of the BPSZ and the conjugated, NE—SW trending shear zones (constituting what we will call BPSZ-system), which presumably formed under compression in a N—S direction. This deformation started at very early Variscan times under amphibolite facies conditions and continued at least until the Permian or even the Miocene. The main deformation observed under ductile conditions resulted from dextral

strike slip. The quartz textures reported by former authors include *c*-axes displaying crossed girdles, point maxima around the *Y*-axis of strain and point maxima around the stretching lineation. That means that the BPSZ-system was active under a large variety of temperature conditions.

The above mentioned granite dykes were sinistrally sheared after intrusion. The major recrystallization mechanisms were grain boundary migration and subgrain rotation. This deformation is geometrically difficult to reconcile with a compression in the N—S direction. Therefore change of the bulk stress field is necessary. Thus, the compression direction during the sinistral shearing of the dykes was most probably rather NE—SW trending. In order to better estimate the relative age of this deformation phase, as well as the stress state and metamorphic conditions governing it, we performed a detailed microtectonic and textural study of the rocks belonging to the BPSZ-system and the deformed granitic dykes.

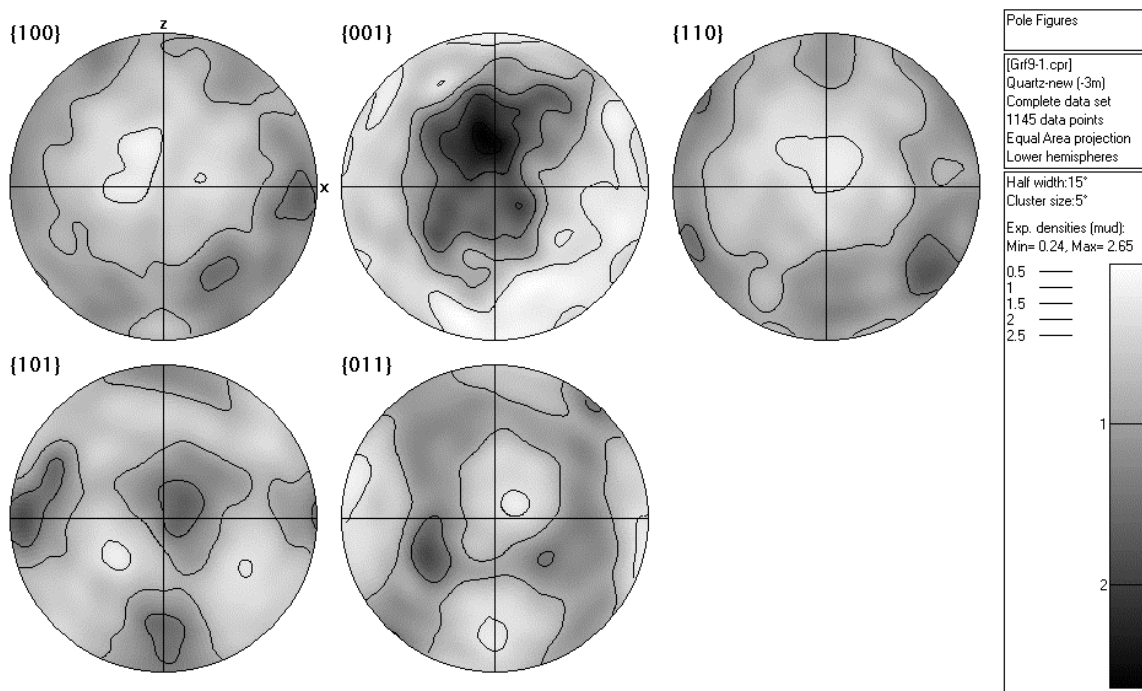


Fig. 3.7-16: Quartz texture at the BPSZ.

We analysed the quartz texture of several samples from the BPSZ and from different sheared dykes by means of electron backscattering diffraction (EBSD) in the SEM. The samples taken at the BPSZ show almost always a point maximum of *c*-axes around or near the *Y*-axis of the finite strain ellipsoid (Fig. 3.7-16). The texture of the sinistrally sheared dykes consists without exception of a point maximum of *c*-axes around the *Y*-axis of the finite strain ellipsoid (Fig. 3.7-17). Quartz *a* and *c*-axes patterns obtained from the dykes indicate that during sinistral shear, intracrystalline slip in quartz took place predominantly along prism planes in the $\langle a \rangle$ direction.

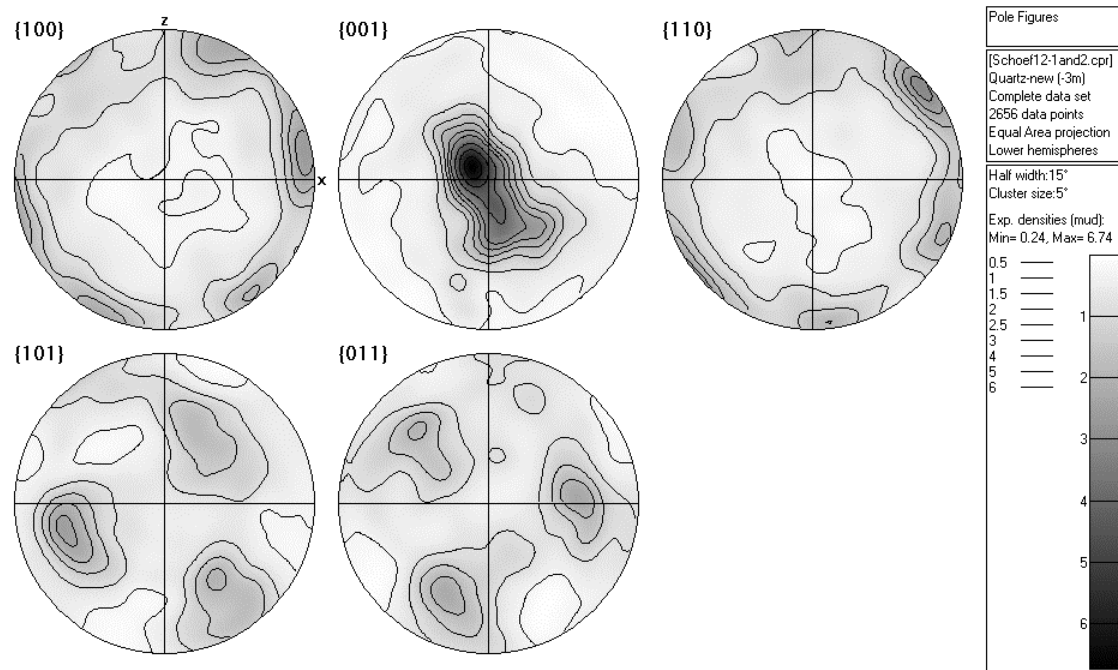


Fig. 3.7-17: Quartz texture in sinistrally sheared granite dykes.

From our results, there are no major textural differences between the mylonites of the BPSZ and the deformed granite dykes. Nevertheless, taking into account the previous results from other authors, we must conclude that the deformation at the BPSZ-system took place during a broad time span and under a large temperature range; whereas the deformation in the dykes seems to have taken place under very discrete temperature conditions (around the boundary between greenschist and amphibolite facies) and hence at a short time span of the tectonic evolution of the Bavarian Forest. Consequently, we propose that an episode of NE—SW compression interrupted for a short period of time the “normal” N—S compression, producing the sinistral deformation in granitic dykes.

3.8 Metamorphism

Metamorphic rocks make up about 85 % of the Earth by volume, and almost all of these are formed in the lower part of the crust and mantle as a result of tectonic processes like subduction at plate boundaries, crustal thickening in continental and mountain belts, rifting during creation of plate boundaries, and by mantle circulation in the Earth's interior. Metamorphic rocks are formed from preexisting rocks that are subjected to a new set of conditions imposed in these tectonic environments. Their formation involves physical and chemical changes in the solid state. Physical changes are produced by deformation and the formation of new minerals and chemical changes result from continuous and discontinuous metamorphic reactions that create new stable minerals or modify compositions of minerals.

Experimental study of the conditions at which different metamorphic minerals are stable and how their composition varies as a function of P and T provide crucial information such as pressure and temperature in a particular tectonic environment. Information about the conditions of metamorphism can be extracted by careful study of the stable minerals and their composition in a metamorphic rock. Experimental studies also give insights into how and under what conditions (*e.g.*, pressure, temperature, stress, and fluid activity) metamorphic minerals deform by certain mechanisms. The experimental observations in these two areas when coupled with observations from natural rocks give crucial insights into the thermal-mechanical processes and evolution that take place in a variety of tectonic settings.

The contributions in this section explore both tectonic evolution and thermal-mechanical processes that involve metamorphism which have taken place in ancient and modern mountain ranges at depths ranging from several kilometers below the surface to 125 km. Studies from west Norway offer insights into the tectonic evolution of the microdiamond-bearing garnet-kyanite gneiss that have a rather unusual occurrence of fibrous pumpellyite associated with a late stage of metamorphism, and into how the crust and mantle interact at depths greater than 100 km by study of the Kvalvika peridotite lens where changes in composition are used to determine conditions of metamorphism. Studies of how minerals deform through their orientation acquired during mountain building help constrain how dense eclogites composed of garnet and omphacite at high-pressure conditions are brought back to the surface in the Austrian Alps, and the conditions of metamorphism for plate scale crustal faults in Pan-African belt of central Africa. Together, these contributions provide examples of how the physical and chemical changes that take place during metamorphism can be used to help to understand tectonic processes and the evolution of mountain belts.

a. *Coarse-grained graphite calc-silicate rock enclosed in microdiamond-bearing garnet gneiss, Fjørtoft, Norway (P. Robinson and M.P. Terry)*

The first discovery of microdiamonds in the UHP terrane of west Norway was by chemical digestion of a kyanite-garnet-graphite gneiss. The gneiss was extensively studied, though without yet locating microdiamonds in other minerals, but other bulk compositions in the

same outcrop have not been studied. Here we examined relationships in a 10-15 cm thick graphite-rich calc-silicate bed to gain more insight into the metamorphic-tectonic evolution of this unit.

The primary metamorphic minerals in the calc-silicate rock are pale brownish pink garnet, colorless zoisite, calcite, graphite, minor quartz and sphene, and rare anorthite (An₁₀₀) and diopside. The graphite occurs in plates up to 2 mm in diameter in close association with garnet, as well as in finer-grained clusters and coatings associated with all other minerals. Most of the garnet is grossular with a major almandine component and minor andradite, pyrope and spessartine. Representative EMP analyses gave the following compositions:

(1)	Gro 63.5	Alm 24.5	And 5.9	Pyr 1.5 Spe 3.5	Other 1.0
(2)	Gro 79.5	Alm 11.0	And 3.3	Pyr 4.0 Spe 1.1	Other 0.8
(3)	Gro 74.5	Alm 16.8	And 2.0	Pyr 4.0 Spe 1.4	Other 0.8
(4)	Gro 78.1	Alm 8.3	And 6.6	Pyr 4.8 Spe 0.8	Other 1.2
(5)	Gro 69.4	Alm 19.4	And 4.7	Pyr 3.6 Spe 1.7	Other 1.2

The most almandine and spessartine-rich grain (1) occurred in a small relict core surrounded by more typical grossular-rich garnet (2) with local mottling to slightly higher Fe content (3). In another thin section, cores were more magnesian and Mn-poor (4), with Fe- and Mn-rich rims (5), possibly related to retrograde reaction with adjacent diopside. Massive garnet-rich volumes are commonly cross cut by metamorphic veins richer in quartz, calcite, and zoisite.

The zoisite consists of optically zoned crystals 5-10 mm long that are dominated by Fe-poor zoisite (gray interference colors) ($\text{Fe}^{3+}/(\text{Fe}^{3+}+\text{Al}) = 0-0.03$) consistent with the occurrence of graphite, but there are extensive patches and also small grains of ferrian zoisite with abnormal blue interference colors ($\text{Fe}^{3+}/(\text{Fe}^{3+}+\text{Al}) = 0.09-0.12$), confirmed by EMP analyses. A discrepancy between a Fe element map and electron backscatter images of zoisite led to preparation of a Sr element map which showed substantial delicate growth zoning that is being investigated. Locally, the zoisite appears to have grown on seed crystals of allanite.

Calcite occurs in large primary grains and smaller patches with secondary minerals. A peculiar feature of the small grains is that they commonly have narrow rims of graphite, suggesting a complex late fluid reaction. Pure anorthite occurs rarely, in a moderate-sized twinned grain sieved with calcite and rounded blebs of garnet, suggesting garnet-growth at the expense of anorthite. Nearby ferroan diopside shows a very limited composition range:

Ca_{0.92-0.99} Na_{0.01} Mn_{0.01} Fe²⁺_{0.31-0.40} Mg_{0.55-0.58} Fe³⁺_{0.04-0.10} Al^{VI}_{0.06-0.02} Al^{IV}_{0.04-0.11} Si_{1.89-1.96}
O₆

The dominant secondary mineral is an unusual fibrous variety of pumpellyite occurring in abundance in the sections associated with all the other minerals including graphite. Locally it occurs as rosettes within garnet, where it may have formed by reaction between former included diopside and zoisite. Some analyses are from a pumpellyite-calcite vein cutting

across a large zoned zoisite crystal with inclusions of garnet, calcite and sphene. There is also minor Mg-rich chlorite with a peculiar brownish appearance in thin section. The pumpellyite appears as dense colorless, wedge-shaped and varied sprays of gently bent fibers commonly with inclined extinction, having a resemblance to networks of fine-grained clinoamphibole. The indices of refraction are close to the adjacent zoisite. The maximum interference color is yellow in standard sections. A typical interference color is gray or bluish gray, with very little of the component of abnormal blue that is striking in adjacent ferrian zoisite. Because of fiber bending, extinction is wavy and irregular. In larger patches showing a yellow interference color, the sign of optical elongation is negative, but some patches with a yellow color showed positive elongation, and in messy areas of gray colors, the signs of elongation are chaotic.

Pumpellyite in metamorphic rocks commonly occurs as concentrations of high-relief granules and fine stubby prisms with a pale greenish color, making EMP analyses difficult. This fibrous pumpellyite is in dense masses and excellent analyses were obtained which allowed mineral recognition. From the lack of color and presence of graphite there was no need to assume Fe^{3+} and, with likely variable O, OH, no easy way to calculate it. Assumption of all Fe as Fe^{2+} gave formulae close to the ideal $\text{Ca}_2 \text{Al}_{0.5} (\text{Fe}^{2+}, \text{Mg})_{0.5} \text{Al}_2 \text{Si}_3 \text{O}_{10} (\text{O}, \text{OH})_4$ with a range of $\text{Fe}^{2+}/(\text{Fe}^{2+} + \text{Mg})$ from 0.189 to 0.509 and average like that of diopside and far from garnet.

Exploration of petrography and chemography suggests the following history: A pre-Scandian high-T metamorphism of an organic-rich calcite, quartz, ankerite, kaolinite-rich sediment bed, within an organic-rich aluminous shale, produced a quartz-calcite-graphite-anorthite-magnesian hedenbergite assemblage. During Scandian (Early Devonian) high P to UHP metamorphism, anorthite reacted with calcite to produce zoisite, and calcite-anorthite-magnesian hedenbergite reacted to produce abundant grossular-rich garnet, leaving scarce residual ferroan diopside. In a post-Scandian retrograde hydration, either Late Devonian, or even Jurassic, pumpellyite formed with composition partly dependent on local environment, but, based on chemography, largely in reaction between zoisite and residual diopside, and only marginally involving more refractory garnet. Minor magnesian chlorite grew, locally at expense of diopside. Future research on this carbon-rich rock will include appropriate tests for micro-diamonds, XRD confirmation of the peculiar pumpellyite, and exploration of fluid inclusions.

b. *Metamorphic conditions of olivine c-slip in the Kvalvika peridotite, Norway (M.P. Terry, F. Heidelbach, H. Couvy/Stony Brook, G.D. Bromiley/Cambridge, T. Krogh/Toronto)*

Olivine in the upper mantle is thought to deform mainly by slip parallel to the **a**-axis which provides the basis for understanding deformation in the upper mantle through studies of seismic anisotropy. However, relatively recent studies have shown that olivine c-slip occurs in natural samples and it is crucial to understand the conditions and the tectonic environment in which this slip system is active if we want to understand deformation in the upper mantle and interactions between the crust and mantle. Olivine c-slip is observed in the Kvalvika

peridotite that occurs in locally eclogitized diorite gneiss and both contain the same foliation and lineation formed during HP metamorphism. Metamorphic zircon in nearby (500 m) eclogitized gabbro with the same fabric yield Scandian (425-375 Ma) ages of 410 ± 1 and 408 ± 1 Ma. Olivine in samples 1632 and 1632a show alignment of foliation and lineation indicating dislocation glide on the (010)[001] and the (010)[001] slip systems, respectively. Metamorphic conditions and the P-T path during UHPM were determined by geothermobarometry and differential thermodynamic modeling in the NCFMAS system using the program Gibbs. The temperatures and pressures were determined using rim or near rim mineral compositions for Scandian mineral assemblage of Grt + Cpx + Opx + Olv + Spl (Fig. 3.8.1).

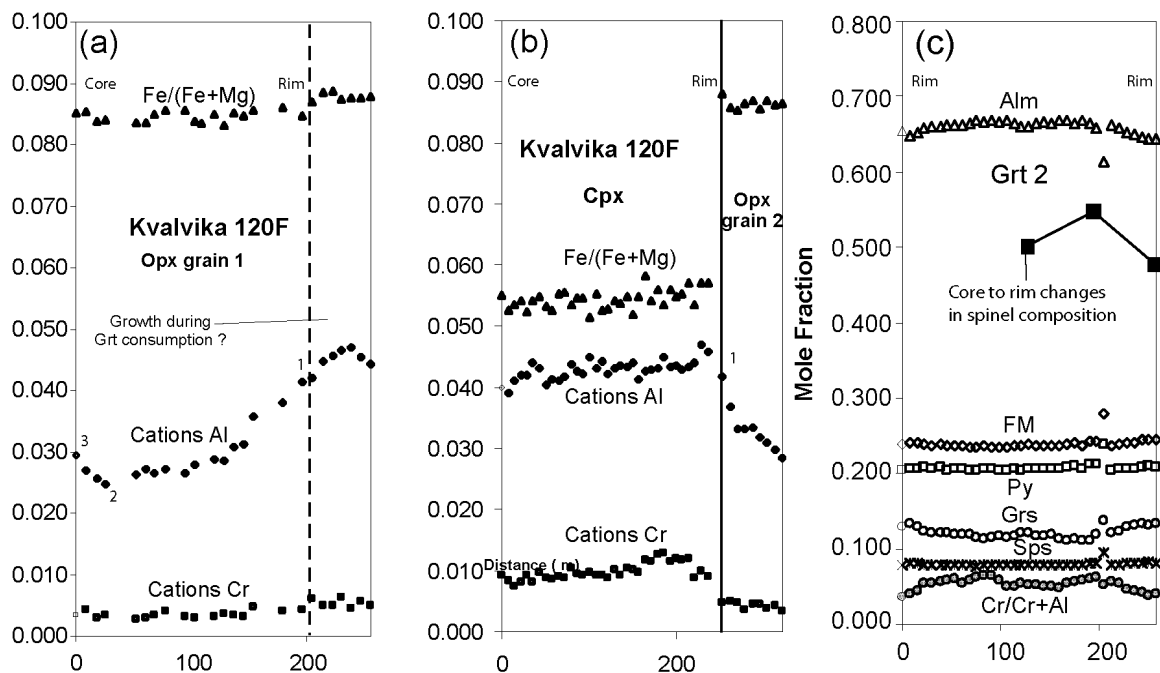


Fig. 3.8-1: Chemical zoning in the Scandian pyroxene and garnet. Numbers 1, 2 and 3 refer to compositions used in geothermobarometry calculations and thermodynamic modeling.

Temperatures were estimated using the Fe-Mg exchange between Grt and Cpx, the two pyroxene thermometer, and the Ca content in Opx. Pressures were determined using three different calibrations of the Al-Opx barometer which has moderate temperature dependence. The results indicate pressures and temperatures that range from 2.9-3.1 GPa and 810-830 °C. These estimates agree well with the revised estimate for a nearby UHP kyanite eclogite. The combined results indicate pressures and temperatures that range from 2.9-3.4 GPa and 810 to 860 °C (Fig. 3.8.2). The P-T path was determined using changes in mineral compositions to calculate changes in P and T and new compositions in other minerals present in the assemblage from known P-T conditions (820 °C, 3.2 GPa). Changes in the Fe/(Fe+Mg) ratio and the Al content at the three different points (labeled 1, 2 and 3 in Fig. 3.8-1) along the zoning in Opx were used to determine the P-T path. The observed changes of the grossular

content in garnet, which serves as an independent monitor, agree with those predicted by the model. The observed changes in Cr/ (Cr+Al) in garnet and spinel included in garnet agree with those inferred from experimental studies for this path. Results indicate a short clockwise path at UHP conditions that from core to rim shows an increase in P and T of 750 °C and 3.3 GPa to 770 °C and 3.7 GPa, followed by decompression and heating to 820 °C and 3.2 GPa.

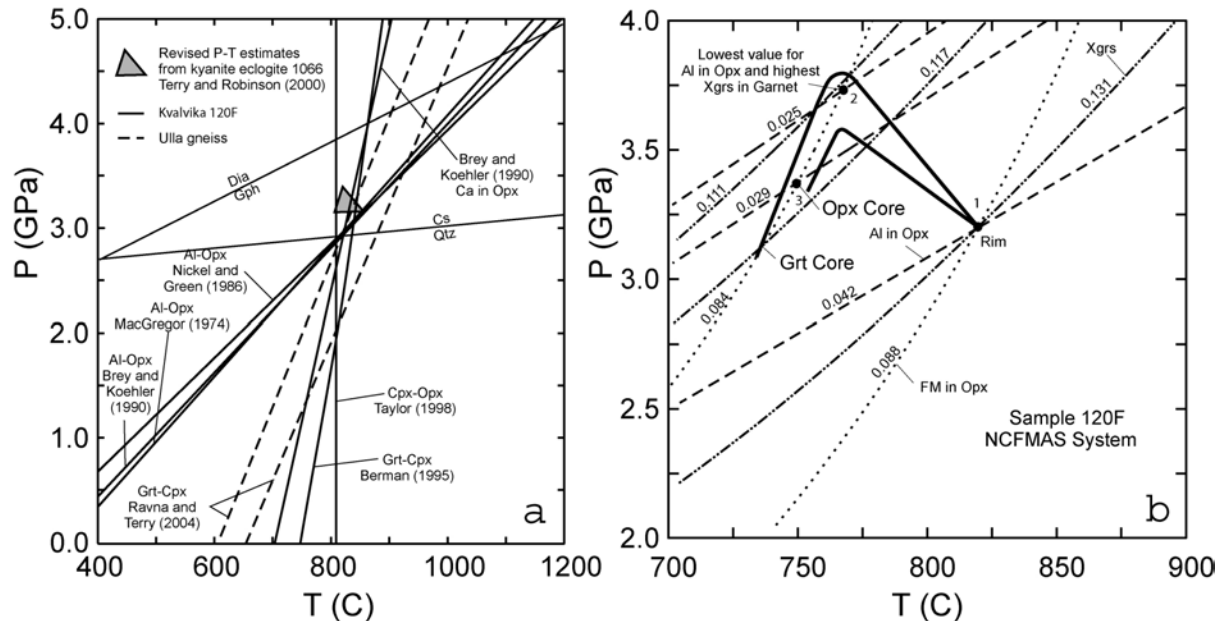


Fig. 3.8.2: Results of geothermobarometry calculations (a) and thermodynamic modeling (b).

The modeled P-T path records a transition from subduction to exhumation and indicates that olivine c-slip was active over a range of conditions during UHP metamorphism. The increasing P and T in the early part of the path indicate that the peridotite lens was incorporated into the crust prior to metamorphism or was part of the subducted mantle lithosphere and emplaced during metamorphism.

c. Omphacite textures in eclogites of the Tauern Window: Implications for the exhumation of the Eclogite Zone (Austrian Alps) (K. Neufeld and A. Kühn/Mainz, U. Ring/Christchurch, F. Heidelberg)

The question as to how extremely dense eclogites are exhumed in orogens remains a lively debated controversy in tectonics. A widely held opinion is that buoyancy is the main driving mechanism and that buoyancy forces lead to the formation of an extrusion wedge that is bounded by a lower thrust and an upper normal fault. We are testing this hypothesis by studying the deeply exhumed Eclogite Zone in the Tauern Window of the Austrian Alps. The Eclogite Zone is part of the Pennine nappe edifice of the Tauern Window and sandwiched

between metasedimentary rocks of the Venediger Nappe as the footwall and ophiolitic rocks of the Glockner Nappe as the hanging wall. While maximum pressures of the surrounding rocks were 10-12 kbar, the eclogites were subjected to pressures of 20-25 kbar. The Eclogite Zone is surrounded by lower pressure rock which supports extrusion of a high-pressure wedge of rock that is bounded by a top-N thrust fault below and a top-S normal fault above. P-T calculations in combination with Rb/Sr multi-mineral analysis indicate a minimum exhumation rate of 40 mm/yr for the Eclogite Zone. This is assumed to be fast enough for eclogite exhumation driven by buoyancy forces.

The validity of the wedge-extrusion model can be tested by Electron Backscattered Diffraction (EBSD) measurements of the crystallographic preferred orientations (CPO) in omphacite from oriented samples along N-S profiles across the Eclogite Zone in order to resolve differences and changes in microstructures and CPO. If the extrusion wedge assumption is valid, the high-pressure textures should show clearly different asymmetries in profiles across the Eclogite Zone, since the shear kinematics are of opposite sense at the thrust and the normal fault.

Inside the Eclogite Zone the eclogitic rocks occur in layers embedded in mainly garnet mica schists. These layers occur in lenses approx 1000 m by 700 m as the maximum size. The rocks can be divided in two different eclogite types (E1 & E2). E1 is characterized by fine-grained garnet layers in an omphacite groundmass. This variation of eclogite is much more common in the Eclogite Zone in comparison to E2, which occurs as the coarse grained eclogite variation with garnets of sizes up to 5 mm in an omphacite groundmass and without any lineation. All samples were prepared perpendicular to the foliation.

The CPO patterns do not show significant changes in omphacite fabrics across the entire Eclogite Zone. A typical pattern is shown in Fig. 3.8-3. The fabrics show either a strong symmetry or only a slight asymmetry that is homogeneous in the whole study area. Omphacite textures are characterized by an alignment of {010} and {110} with the foliation plane and a maximum of <001> close to the lineation that is marked by X0 (Fig. 3.8-3). This pattern is indicative of deformation by intercrystalline glide on the (010) [001] and (110) [001] slip systems.

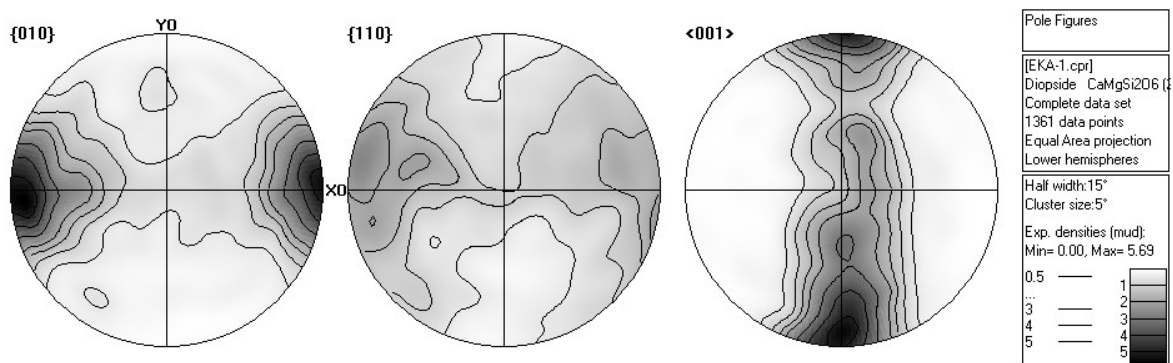


Fig. 3.8-3: Representative pole figures of omphacite in the eclogite zone.

Our conclusion is that the overall symmetry in the omphacite CPO patterns indicates a type of exhumation that enables the eclogite rocks to keep a symmetric texture. This is consistent with the suggestion of an exhumation driven by buoyancy forces when the observed CPO patterns represent a prograde texture that has been preserved during the exhumation process. In such a model for the exhumation process, the extremely dense eclogite lenses were embedded in lower dense mica schists that were exhumed fast enough (around 40 mm/yr) by buoyancy to transport the included eclogite bodies upwards. A change in the CPO asymmetries which is required for a common extrusion wedge model because of different contacts with the surrounding rock units (a thrust fault on one and a normal fault on the other side) is not observed in the study area, *i.e.*, the distribution of omphacite CPOs in the Eclogite Zone does not support the extrusion wedge suggestion.

d. *Assessing the tectonothermal evolution of a large-scale shear zone in the western Pan-African belt of central Africa (G. Njiekak and G. Zulauf/Frankfurt, F. Heidelbach)*

This study is part of a project that aims at constraining the tectonothermal evolution of subvertical crustal-scale shear zones that cut the Neoproterozoic fold belt of west Cameroon (NFBC) (Fig. 3.8-4). The study area consists of three main complexes: The Batié granitic pluton (BP), the metagranodioritic complex of Bangwa (MCB) and the migmatitic complex of Foubot (MCF). The MCF was intruded by the MCB, while the BP cuts through both the MCF and the MCB. A large scale shear zone (width > 30 km), mostly dextral, cuts across the study area and shows two branches: the N30-trending branch in the south cuts the MCB and the BP and the N65-trending branch in the north cuts MCF and the northern termination of MCB. There is no apparent cross-cutting relationship between the two shear zone branches. The MCB consists of meter-scale bodies of metagranitoids while the MCF is formed by diatexites and metatexites of granitic to syenogranitic bulk composition. Evidence for shear zone control on the internal magmatic fabric of the BP as well as the structural continuity of the deformation across its contacts with the country rocks demonstrates the synkinematic emplacement of the BP with respect to both shear zone branches.

Microstructures and textures in samples from the MCB and the MCF were investigated to constrain the conditions and timing of deformation within the two shear zone branches. The rocks within the MCB show variable degrees of deformation, increasing towards its contacts with the adjacent BP and MCF. In the weakly deformed granitoids, quartz appears mostly as statically recrystallized grains that often merge into discontinuous layers. Evidence for intracrystalline deformation (*e.g.*, numerous deformation bands), chessboard patterns, stepped grain boundaries, and sometimes indenting grain sutures characterize the quartz grains. Dynamically recrystallized quartz grains predominate in the strongly deformed granitoids (mylonites) of the MCB. Subgrain rotation and grain boundary migration in quartz are significant in the mylonites.

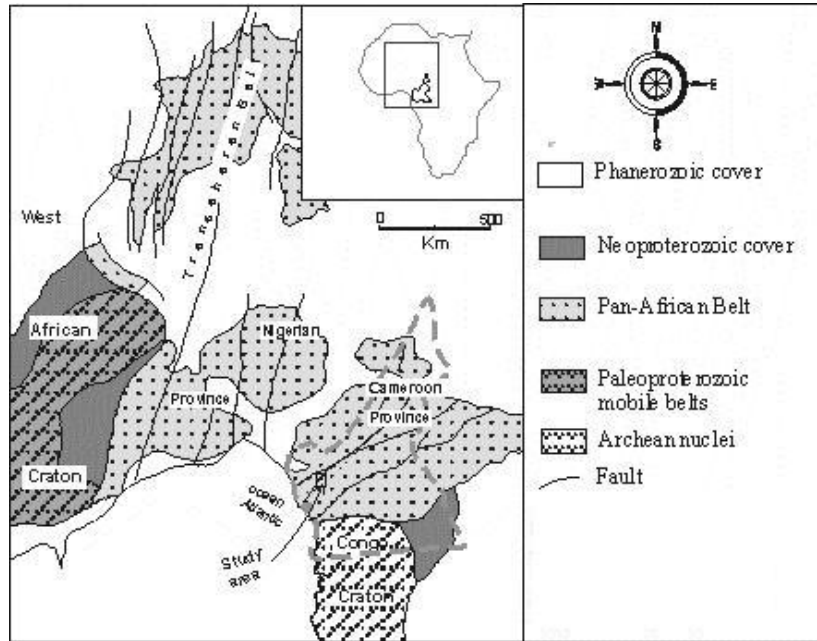


Fig. 3.8-4: Generalized geologic map of west-central Africa modified from previous workers.

The deformation in the migmatites of the MCF is stronger than in the MCB. The diatexites show a strongly deformed microstructure, which is underlined by the shape-preferred orientation of feldspars megacrysts and equigranular polycrystalline quartz ribbons in a very fine grained matrix of biotite and feldspar. Progressive subgrain rotation and bulging recrystallization appear to have been the dominant recrystallization mechanisms of quartz. Quartz grains displaying two sets of subgrains (chessboard extinction) as well as grains with more regular shapes and almost no intracrystalline deformation are sometimes visible.

Quartz texture analyses using EBSD were carried out on samples with different strain intensities from MCB and MCF (Fig. 3.8-5), since the the crystallographic preferred orientation (CPO) of quartz can be used to estimate the temperature conditions of deformation. The axes of the sample reference frame are defined by X parallel to the mineral lineation, Z normal to the shear zone boundary, and Y perpendicular to both. In rocks displaying relatively weak fabric intensity within the N30-trending shear zone branch, the $[c]$ -axes cluster in single or crossed girdles subparallel to the Z -axis of the finite strain ellipsoid. The $[m]$ and $\langle a \rangle$ -axis patterns cluster generally in small circles around X . These CPO patterns suggest dominant basal $\langle a \rangle$ slip, with some contributions from rhombohedral slip. With increasing deformation towards the contacts MCB-BP and MCB-MCF, near the junction zone between the N30-trending shear branch and the N65-trending shear branch, the maximum concentration of quartz c -axes moves progressively towards the intermediate Y -axis of the finite strain ellipsoid, reflecting dominant prism $\langle a \rangle$ slip in quartz (Fig. 3.8-5a). As a whole, textures in the N30-trending shear branch suggest deformation at high- to low-temperature conditions, that is, at amphibolite to greenschist facies.

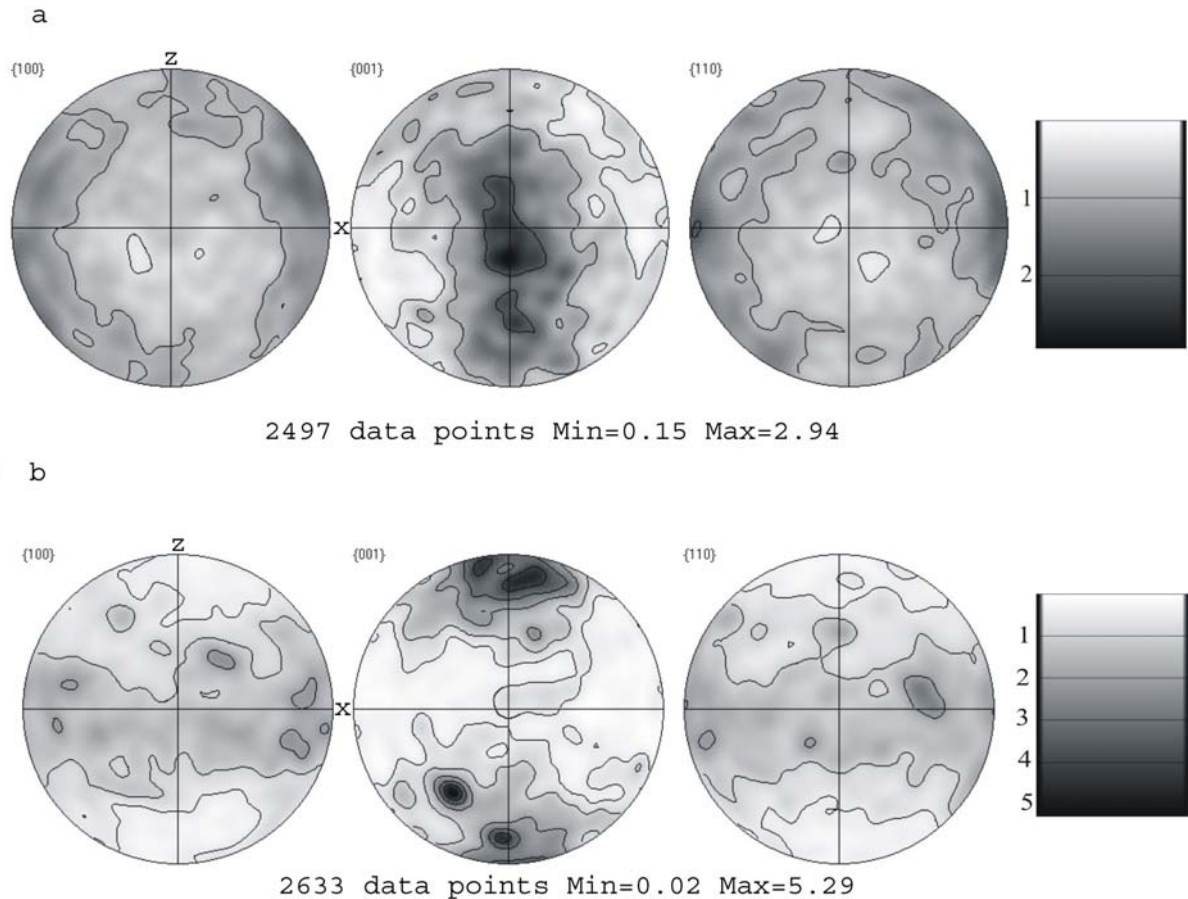


Fig. 3.8-5: Pole figures of quartz from the MCB (a) and MCF (b).

In the N65-trending shear branch, quartz textural analyses on diatexites with strong fabric intensity show a maximum near the periphery in the $[c]$ -axis patterns and maxima subparallel to the XY plane for the $[m]$ and $\langle a \rangle$ -axis patterns. The $[c]$ -axes can be found forming small circle orientations around Z (Fig. 3.8-5b). These textures are interpreted to indicate dominant basal $\langle a \rangle$ slip, which is known to be mostly active at low temperatures. This correlates largely with the dominant recrystallization mechanisms of quartz deduced from microstructural observations.

In summary, the EBSD and microfabric analyses suggest that deformation in the N30-trending shear branch started at much higher temperature, but ceased earlier than in the N65-trending branch. In the latter, the deformation continued extensively under greenschist facies conditions. Moreover, the CPO of quartz in both shear zone branches suggests a significant coaxial component during the deformation process.

3.9 Materials Science

The last decades brought great progress in the design of the apparatus for the generation of high pressures and high temperatures. As a result, high pressure has become a common and relatively inexpensive method for tuning volume, structure, electronic, magnetic, etc. properties of solids in fundamental physical experiments, as well as a promising synthesis route for new prospective applied materials. Bayerisches Geoinstitut, as a place holding and developing unique high-pressure equipment and methods, is involved in sophisticated and challenging material research at extreme conditions. This year we present results of the studies of various classes of solids – carbon and carbon-based materials, metals and alloys, bulk and nanocrystalline oxides, and nitride-based ceramics.

Due to a combination of unique physical and chemical properties such as hardness, high thermal conductivity, wide band gap, high electron and hole mobility, chemical inertness, diamond has found wide applications in modern science and technology. There is a growing demand for diamond-like materials in electronic applications. Although there are few prospects of diamond-based microelectronics ousting silicon totally, diamond devices could function in situations when silicon electronics fail. For example, diamond chips potentially could still work at temperatures of several hundred degrees; whereas silicon devices generally fail above 450 K. Electrochemical applications of diamond-based films have been developed significantly in the last few years and are considered as a promising research area. Pure diamond is a perfect insulator and conducts electricity very poorly. But, like silicon, it can be turned into a semiconductor by traces of boron or nitrogen impurities. Studies conducted in Bayerisches Geoinstitut on B-C system at elevated pressures and temperatures open a new perspective in synthesis of heavily boron-doped diamonds and demonstrate a material combines extremely high hardness with unique electronic (particularly, superconducting) properties.

Nanocrystalline forms of known materials can enhance useful properties of their macrocrystalline counterparts. In recent years nanotubes, nanowires, nanorods and nanowhiskers have become an attractive target for synthesis and study. Although the production of nanorods from various materials is proving very successful, so far nobody has reported experimental observation of diamond nanorods, although several theoretical groups have predicted their possible existence and superior physical properties. This year the synthesis in Bayerisches Geoinstitut of aggregated diamond nanorods (ADNRs) from fullerene C₆₀ using a multianvil apparatus has been reported. Individual diamond nanorods are 5 to 20 nm in diameter and longer than 1 μm. The X-ray and measured density of ADNRs is ~ 0.2- 0.4 % higher than that of usual diamond. The extremely high isothermal bulk modulus $K_T = 491(3)$ GPa (compared to $K_T = 442(4)$ GPa of diamond) was obtained by *in situ* X-ray diffraction study. Thus, ADNRs are the densest among all carbon materials and they have the lowest so far experimentally determined compressibility.

Among the known and potential technological applications of nanocrystalline titania and titania-zirconia solid solutions are pigments, plastics, cosmetics, electronics, and catalysts

industries. Experiments using the entire range of high-pressure devices available in Bayerisches Geoinstitut allowed not only the synthesis of new phases of $(\text{Ti,Zr})\text{O}_2$, but also revealed a number of interesting and enigmatic phenomena, for example the size dependence of pressure-induced amorphization in titania.

One of the significant problems with materials science-oriented high-pressure research is the synthesis of bulk (on the order of several cubic mm) samples. The task becomes even more difficult if there are no low-pressure precursors of the substance of interest. New experiments conducted in Bayerisches Geoinstitut on synthesis of nitrides (particularly nickel nitride) using potassium azide as a nitrogen source give good chances to solve the problem.

a. *Aggregated diamond nanorods, the densest and least compressible form of carbon (N.A. Dubrovinskaia, L.S. Dubrovinsky, W.A. Crichton/Grenoble, F. Langenhorst/Jena and A. Richter/Wildau)*

We report the synthesis of aggregated diamond nanorods (ADNRs) from fullerene C_{60} at 20(1) GPa and 2200 °C using a multianvil apparatus. Individual diamond nanorods are of 5 to 20 nm in diameter and longer than 1 μm . The X-ray and measured density of ADNRs is ~ 0.2 - 0.4 % higher than that of normal diamond. The extremely high isothermal bulk modulus $K_T=491(3)$ GPa (compared to $K_T=442(4)$ GPa of diamond) was obtained by an *in situ* X-ray diffraction study. Thus, ADNRs are the densest among all carbon materials and they have the lowest so far experimentally determined compressibility.

Due to the exciting promise for nanotechnology, nanotubes, nanowires, nanorods and nanowhiskers have become the most attractive target for synthesis and study. Although production of nanowires from various materials is proving very successful, the development of diamond nanowires has been slow. Theory predicts that diamond nanorods would have a brittle fracture force and a zero strain stiffness that exceeds that of carbon nanotubes for radii greater than about 1-3 nm. We conducted a series of experiments in a 5000-tonne multianvil press. The samples obtained at 20 GPa and high temperature (2200 ± 50 °C) came out as solid cylinders (1.8 mm diameter, 3 mm height) of a very compact translucent material (Fig. 3.9-1).

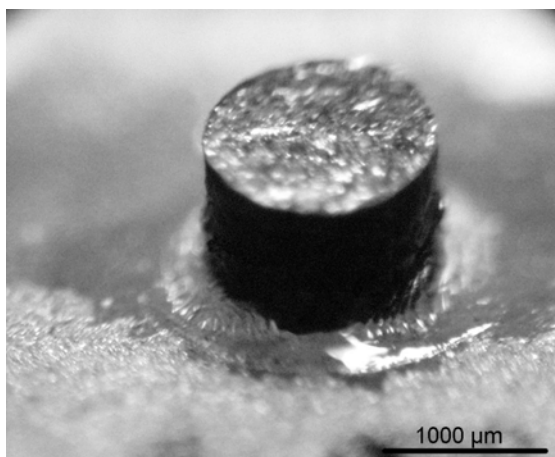


Fig. 3.9-1: Optical micrograph of an ADNRs sample.

The X-ray diffraction pattern contains only the diamond-structure reflections. High-resolution transmission electron microscopy (HRTEM) images from the sample, slowly cooled with a rate of ~ 10 K/min after heating for about 1 hour at 2200 ± 50 °C, show that the bulk samples of diamond consist of elongated crystals that are aggregated diamond nanorods. The orientation of diamond nanorods is not uniform throughout the sample. The high hardness can possibly be attributed to this random intergrowth of diamond nanorods. The X-ray density of diamonds with natural abundance of isotopes is $3.515\text{-}3.519$ g/cm³. The lattice parameter of ADNRs obtained from X-ray powder diffraction is $3.5617(3)$ Å, and consequently, the X-ray density of the material is $3.528(1)$ g/cm³, $\sim 0.2\text{-}0.4$ % higher than that of normal diamond. In order to study the equation of state of ADNRs, isometric pieces (of about 20 μm in diameter) of natural diamond and ADNRs were placed into a 150 μm diameter hole drilled in a steel gasket indented to a thickness of 60 μm . Both diamond and ANDRs were compressed simultaneously in an Ar pressure medium to over 27 GPa, until the samples were bridged between the diamond anvils and further compression was not possible. After high-pressure treatment the X-ray diffraction patterns, and Raman and IR spectra of the recovered material did not change. Pressure was measured using ruby spheres of 2-3 μm in diameter, placed in different parts of the sample. Figure 3.9-2 presents an example of the diffraction patterns collected at 16.7(1) GPa. Positions of the diffraction lines of Ar are the same in the different

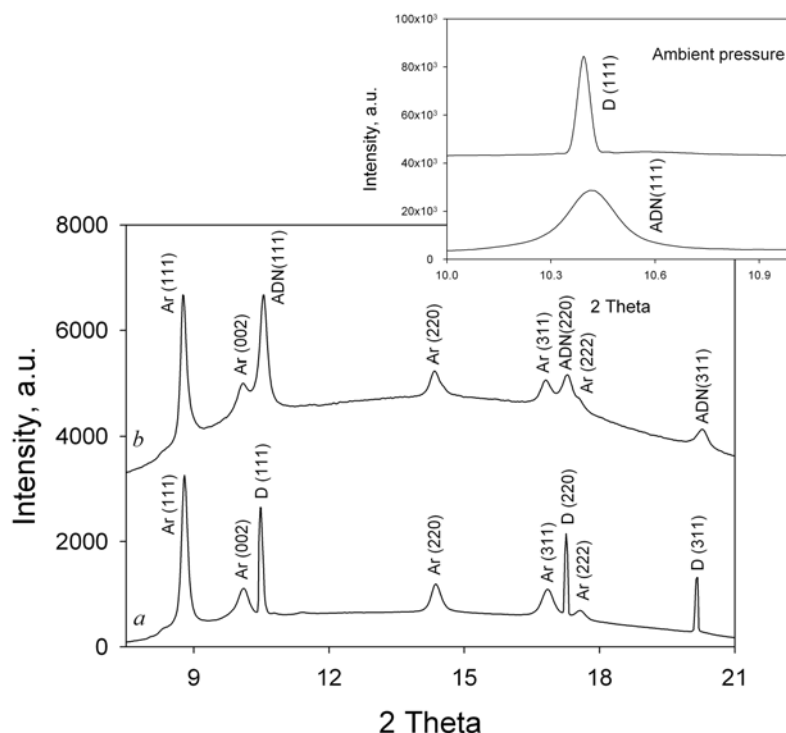


Fig. 3.9-2: Examples of diffraction patterns collected at 16.7(1) GPa from (a) diamond and (b) ADNRs compressed simultaneously in argon quasi-hydrostatic pressure medium. The insert shows (111) diffraction lines of diamond and ADNRs collected at ambient pressure (*i.e.*, before cryogenic loading of Ar into the pressure chamber) (D – diamond, ADN – aggregate diamond nanorods, Ar – argon; the patterns were collected at ID30 beam line at ESRF with constant wavelength 0.3738 Å).

parts of the pressure chamber occupied by diamond and ADNRs, proving that both materials are at the same quasi-hydrostatic pressure. While the diffraction lines of diamond are very narrow, the lines of ADNRs remain broad as in the initial sample. The experimental pressure-volume data were fitted (Fig. 3.9-3) using the third order Birch-Murnaghan equation of state. The fitting procedure for diamond gives $K_T=442(4)$ GPa, $K'=3.2(2)$, $V_0= 3.4157(9)$ cm³/mol, which coincide with the literature data within the uncertainty. For ADNRs we obtained $K_T=491(3)$ GPa, $K'=3.1(2)$, $V_0=3.4014(5)$ cm³/mol. Thus, ADNRs are more than by 11 % less compressible than normal diamond. It has also the lowest experimentally determined compressibility (compared with the highest K_T measured so far: 462 GPa for Os, 420 GPa for WC, 383 GPa for Ir, 380 GPa for cubic BN, 306 GPa for HfN).

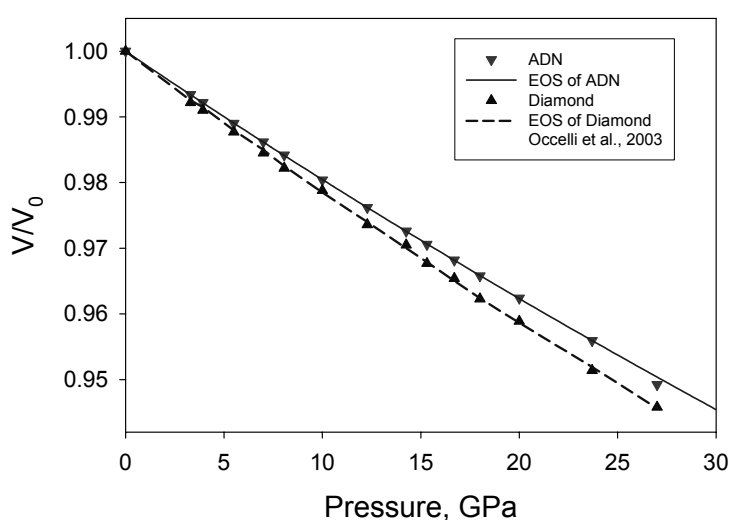


Fig. 3.9-3: Pressure dependence of reduced volume (V/V_0) of diamond (triangles) and aggregate diamond nanorods (inverted triangles). The dashed line shows a third-order Birch-Murnaghan equation of state (EOS) with parameters $K_T=446(3)$ GPa, $K'=3.0$, $V_0=3.4170(5)$ cm³/mol. The continuous line is the fit to our data with $K_T=491(3)$ GPa, $K'=3.1(2)$, $V_0=3.4014(5)$ cm³/mol.

b. Processing and characterization of heat resistant polycrystalline diamond with calcium carbonate as sintering aid (J.E. Westraadt, J.H. Neethling/Port Elizabeth, N.A. Dubrovinskaia and I. Sigalas/Johannesburg)

It is well known that a tough and homogeneous polycrystalline diamond (PCD) with extensive diamond-diamond bonding can be synthesized at high temperatures and pressures using Co metal or Fe-Ni-Co alloy as a sintering agent. Although the material has superior physical properties, a large amount of metallic agent in the PCD causes deterioration such as graphitization and cracking at high temperature. It was found that PCD sintered with CaCO₃ had superior thermal properties, in particular less cracking at high temperatures of 1400 °C. In this study the sintering behaviour of diamond with CaCO₃ was investigated to gain knowledge about heat resistant PCD.

Commercially available synthetic diamond powder with a grain size of 12 μm obtained from Element Six (Pty) Ltd and CaCO_3 with 99.9 % purity from Sigma Aldrich was used as starting materials. The CaCO_3 was dried at 300 $^\circ\text{C}$ overnight. The diamond powder layered with 25 vol.% CaCO_3 was treated at 8 GPa and 2050 $^\circ\text{C}$ for 10 minutes in a multianvil press. Temperature was measured using a W3%Re – W25%Re thermocouple and the pressure was calibrated using known phase transitions. The uncertainty in temperature was 100 $^\circ\text{C}$ and in pressure about 0.5 GPa. The material obtained was analyzed using scanning and transmission electron microscopy (SEM and TEM), energy dispersive spectroscopy (EDS) and X-ray diffractometry (XRD). Wear testing was used to determine the degree of diamond-diamond intergrowth that occurred between the diamond grains. The test consisted of machining a Silica epoxy resin bar with the following parameters: Speed 100 $\text{m}\cdot\text{min}^{-1}$, Depth of cut 0.25 mm, Feed 0.3 $\text{mm}\cdot\text{rev}^{-1}$, time of 5 minutes. The thermal resistance of the material was tested by heating the samples in a vacuum of 5×10^{-3} Pa. A comparative study was performed between diamond sintered with CaCO_3 and a commercial PCD product, Syndite010, which uses Co as a sintering aid.

The cutting test conducted on the diamond sintered with CaCO_3 had a flank wear scar of 95 ± 12 μm compared the Syndite010 which had a flank wear scar of 38 ± 2 μm after the 5 minute test. Heat treatment of the Syndite010 sample to 850 $^\circ\text{C}$ for 30 minutes caused graphitization of the compact as shown by XRD, while the diamond sintered with CaCO_3 showed no signs of graphitization. Figure 3.9-4 is a typical secondary electron SEM image showing the microstructure of the diamond sintered with CaCO_3 . The darker areas consist of diamond grains and the lighter regions around the grains are contamination introduced during polishing of the sample. The microstructure shows that intergrowth of the diamond grains had occurred, which were confirmed by the wear tests. Sintering of diamond in the absence of a sintering aid showed partial intergrowth, and the sample performed poorly on the wear test. This shows that CaCO_3 acted as a sintering aid promoting extensive diamond-diamond bonding. XRD spectra of the CaCO_3 sintered diamond show the presence of diamond and the high-pressure phase of CaCO_3 , aragonite.

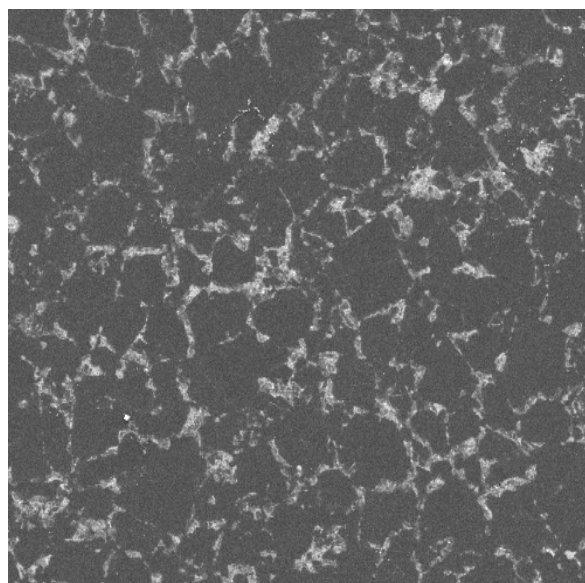


Fig. 3.9-4: A typical secondary electron SEM image showing the microstructure of the diamond compact sintered with CaCO_3 . The size of the area shown is 100x100 μm .

Diamond was successfully sintered using CaCO_3 as a sintering aid. The compact had improved thermal properties compared to a standard commercial PCD product.

c. Synthesis of new fullerene materials by extreme hydrogenation at high-pressure/high-temperature conditions and their characterization (A.V. Talyzin, A. Dzwilewski and B. Sundqvist/Umeå; Y.O. Tsybin, J.M. Purcell and A.G. Marshall/Tallahassee; Y. Shulga/Chernogolovka, C.A. McCammon and L.S. Dubrovinsky)

Hydrogenation at high-pressure/high-temperature conditions (0.6-3 GPa and 870K) aimed at synthesis of C_{60} hydrofullerenes was previously reported. The main products of the performed synthesis were C_{60}H_x with $x=24-36$ due to a relatively small heating time. Hydrofullerenes with higher hydrogen content were never observed in these experiments. Even more extreme conditions of hydrogenation were tested in our experiments. Synthesis of samples using a piston-cylinder apparatus was performed in Bayreuth, while characterization of samples was done in Sweden, USA and Russia. Hydrogenation of C_{60} at 2 GPa and 723-823 K was performed with thermal decomposition of LiAlH_4 as a hydrogen source. Analysis of hydrogenation products was performed using several characterization methods: X-ray diffraction, Raman and IR spectroscopy, advanced mass spectrometric methods (high-resolution atmospheric pressure photoionization Fourier transform ion cyclotron resonance mass spectrometry).

A broad range of hydrogenation products was identified, including $\text{C}_{60}\text{H}_{36}$, highly reduced fullerenes with 40-44 hydrogen atoms and products of hydrofullerene fragmentation (Fig. 3.9-5).

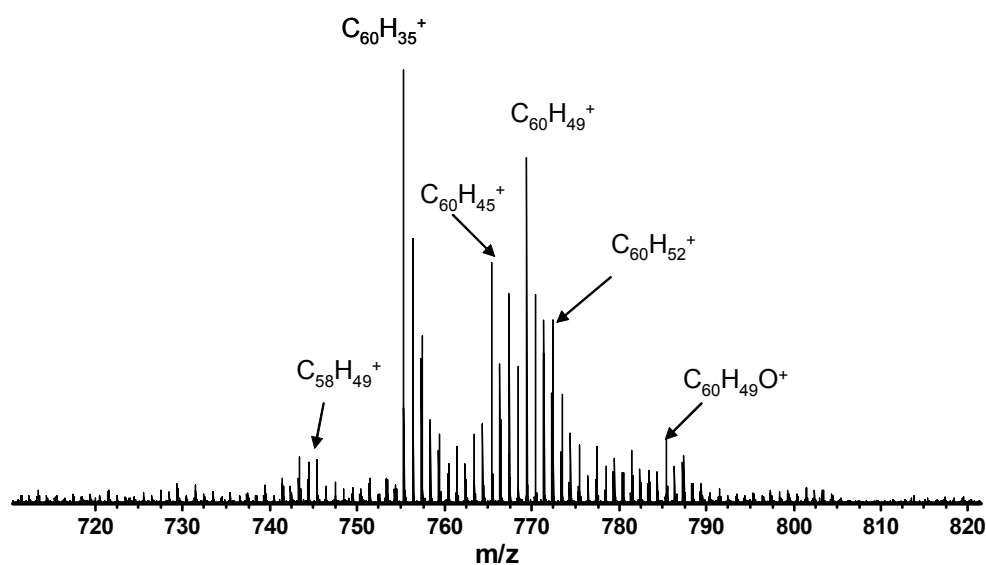


Fig. 3.9-5: Atmospheric pressure photoionization FT-ICR mass spectrum of highly reduced C_{60} .

Unlike other hydrogenation methods in which pristine C_{60} reacts with hydrogen, the high-pressure/high-temperature conditions result first in C_{60} polymerization into a tetragonal phase which later reacts with hydrogen. It is suggested that hydrogen first attacks intermolecular carbon-carbon bonds, resulting in complete depolymerization of C_{60} in the process of hydrogenation. This model suggests the possibility to select starting points for hydrogenation by choosing specific polymeric structures of C_{60} . Hydrogenated polymeric C_{60} was identified as an intermediate reaction product.

d. Reaction of metallic iron with C_{60} : Possible implications for “magnetic carbon” (*A. Talyzin and A. Dzwilewski/Umeå; L.S. Dubrovinsky; A. Setzer and P. Esquinazi/Leipzig*)

There are controversial reports in the literature regarding the possible existence of magnetic carbon. Reports that ferromagnetic C_{60} polymers could be produced near the pressures and temperatures of fullerene cage collapse were not confirmed by our earlier studies. New experiments were performed with the purpose to study some alternative explanations for previously described ferromagnetism in fullerene-based carbon samples. In this study the C_{60} powder was intentionally contaminated by iron powder (3 % and 10 %) with small particle size (about 2 μm). The mixture was subjected to high-pressure/high-temperature treatment at conditions where formation of “magnetic carbon” was reported.

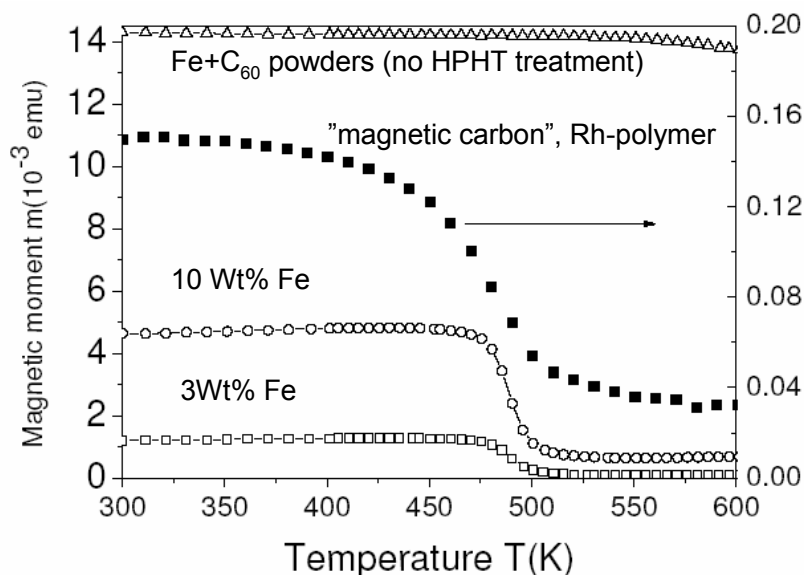


Fig. 3.9-6: Magnetic moment as a function of temperature for the three samples studied in this work at an applied field of 500 Oe.

After treatment at 2.5 GPa and 1040 K all iron was found to transform into the iron carbide phase Fe_3C , wherein C_{60} formed tetragonal polymeric phase which is typical for these conditions. Magnetic properties of these samples were studied using SQUID magnetometer.

The sample showed a Curie temperature of Fe_3C at about 500 K (Fig. 3.9-6), very similar to “magnetic carbon” samples. These results prove that if any iron contamination was accidentally introduced to the initial powder of C_{60} before or in the process of synthesis, all iron had to transform into Fe_3C . The reaction of iron should go more easily with fullerene phases (which results in collapse of C_{60} molecules) compared to the hard carbon phase with a graphite-like structure formed after C_{60} collapse above ~ 1075 K. This could possibly explain why “magnetic carbon” was found previously only at certain temperature conditions near the point of fullerene cage collapse.

e. *High-pressure/high-temperature behaviour of graphite-like B–C phases (V.L. Solozhenko and O.O. Kurakevych/Villetaneuse, N.A. Dubrovinskaia and L.S. Dubrovinsky)*

Recently a number of new graphite-like B–C phases of different stoichiometry have been synthesized by thermal chemical vapour deposition (CVD). Up to now the high-pressure behaviour of these materials has not been studied, even though diamond-like phases containing boron and carbon are highly desirable as they might combine the best properties of the elements. Here we report our recent results on the attempted synthesis of the diamond-like B–C phases.

Graphite-like B–C solid solutions of different stoichiometry (BC , BC_3 and $\text{BC}_{1.5}$) have been used as starting materials. Experiments at pressures from 20 to 25 GPa and temperatures up to 2500 K were conducted using a two-stage 6-8 type large-volume multianvil system with the Zwick 5000-tonne press. The classic 18/11 cell assembly, composed of truncated WC cubes, MgO octahedron and cylindrical LaCrO_3 furnace, was employed. Quenched samples were investigated using SEM at BGI and X-ray powder diffraction (conventional at LPMTM-CNRS and with synchrotron radiation at HASYLAB-DESY).

X-ray diffraction analysis of the quenched sample shows that above 2000 K in the entire pressure range under study all graphite-like B–C phases decompose into boron-doped diamond and boron carbides (B_{13}C_2 and B_{50}C_2). Bulk composite materials obtained at 25 GPa and 2300 K consist of intergrown boron carbides and boron-doped diamond with 1.5-2 at.% B. The materials exhibit semiconducting behaviour and have very high hardness ($H_V=88$ GPa for BC_3 composition) comparable to that of single-crystal diamond. Combination of semiconducting properties and extreme hardness make the synthesized materials potentially important for precision machining, electrochemical and electronic applications.

f. *Turbostratic graphite-like BC_4 under pressure: Raman scattering (V.L. Solozhenko and O.O. Kurakevych/Villetaneuse, A.Yu. Kuznetsov)*

Turbostratic graphite-like BC_x phases have become a subject of investigation because they are potential precursors for high-pressure/high-temperature synthesis of novel superhard

materials. Here we report the Raman scattering studies of t-BC₄, give the band assignment and describe the effect of pressure on the first-order high-frequency $E_{2g}^{(2)}$ Raman mode.

High-pressure Raman experiments were conducted using a DAC technique. The sample was loaded into a Re gasket without pressure-transmitting medium. Sample pressure was determined from the shift of the ruby fluorescence R_1 line. The Raman scattering measurements were performed at 300 K using a Dilor XY system and argon ion laser ($\lambda = 514.5$ nm). Raman scattered light was collected in a backscattering geometry using a CCD detector. The pressure-induced frequency shift for t-BC₄ was monitored on compression to 45 GPa and on decompression down to ambient pressure.

Figure 3.9-7 shows the Raman shift of the $E_{2g}^{(2)}$ mode of t-BC₄ under compression. In contrast to graphite, where the $E_{2g}^{(2)}$ mode disappears at pressures above 14 GPa due to the phase transformation into sp^3 forms of carbon, the G mode of turbostratic graphite-like BC₄ can be seen at least up to 45 GPa. A pronounced nonlinear dependence of the Raman shift of the $E_{2g}^{(2)}$ mode on pressure is observed. Raman line frequencies are reproducible upon decreasing the pressure. The relation

$$\omega_p = \omega_0 \cdot \left(1 + \frac{\delta_0}{\delta'} \cdot p \right)^{\delta'}$$

was used to describe the pressure dependence of the $E_{2g}^{(2)}$ mode. A least-squares fit to the experimental data yields the first-order parameter $\delta_0 = 0.0047 \pm 0.0016$ GPa⁻¹. The obtained value of δ_0 is higher than that of graphite ($\delta_0 = 0.00296$ GPa⁻¹). The corresponding absolute frequency shift is $\delta_0 \omega_0 = 7.3$ cm⁻¹/GPa.

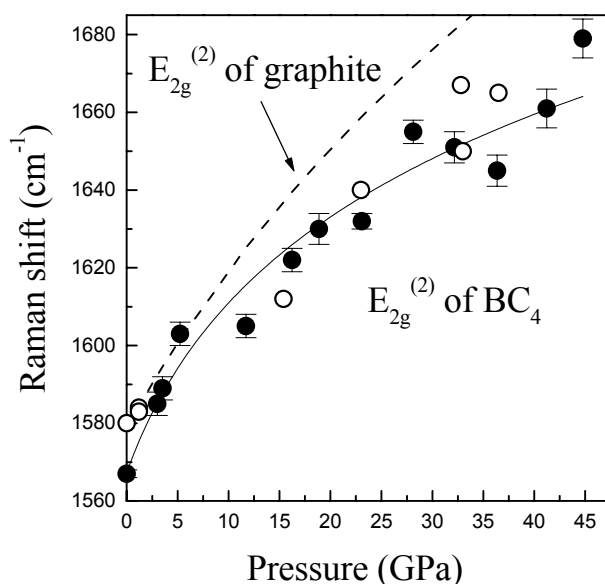


Fig. 3.9-7: Raman shift of the $E_{2g}^{(2)}$ mode of t-BC₄ under compression (solid symbols – compression, open symbols – decompression, continuous line – least-squares fit to the experimental data of t-BC₄, dashed line – dependence of $E_{2g}^{(2)}$ mode of graphite).

g. Synthesis and properties of new materials in the B–C system (N.A. Dubrovinskaia and L.S. Dubrovinsky; G. Eska and H. Braun/Bayreuth; G.A. Sheshin/Kharkov)

Synthesis of a series of bulk samples of B-doped diamonds was realized in a wide spectrum of pressures and temperatures using a 5000 tonne multianvil press. A bulk sample ($\sim 7.5 \text{ mm}^3$) of boron-doped diamond containing 2.6(6) at.% B was synthesized by means of direct reaction between boron carbide and graphite in a multianvil apparatus at 20 GPa and 2700 K. Electrical resistance of the sample was measured in the temperature interval from 10 mK to 300 K and revealed a transition to a superconducting state at 2.4 K to 1.4 K. Ever since the first experimental observation of superconductivity in B-doped polycrystalline diamond was published, the question of whether superconductivity is a universal property of diamond, has arisen.

The purpose of the present study was to synthesize B-doped polycrystalline diamonds using a multianvil apparatus at high pressures to investigate how synthesis conditions influence the temperature of the transition to the superconducting state. As starting materials in different experiments we used pure graphite (99.99 %, Goodfellow Inc.) and B_4C (99.99 %, Goodfellow Inc.). The pure powders ($\text{B}_4\text{C}+\text{C}$ -graphite) were mixed in the proportion C_{13}B (~ 7 at.% B). Quenched samples were studied by X-ray powder diffraction using a high-brilliance FRD RIGAKU diffractometer (MoK_α radiation, 60 mA- 55 kV, APEX CCD area detector). The chemical composition and texture of the samples were studied using a LEO-1530 scanning electron microscope (SEM). For quantitative chemical analysis a Camebax SX50 microprobe analyzer employing a PAP correction procedure was used. Raman spectra were collected using two Raman spectrometers (XY Dilor, operating with 514 nm laser, and LabRam, operating with 632 nm incident laser).

Resistivity measurements were made in a standard four-probe configuration using an LR700 a.c. resistance bridge (Linear Research Inc.) with excitation frequency of 16 Hz and excitation current of 100 μA . The sensitivity of the resistance measurement was on average 10 μOhm . Measurements in the temperature interval 10 mK to 300 K were performed in a dilution cryostat with a nuclear demagnetisation stage at the Physics Department in the University of Bayreuth. Measurements in the range 10 mK - 2 K in magnetic fields to 2 Tesla were performed in the same cryostat. Thermometry was performed to an accuracy of about 1 % using calibrated Pt-, Ge-, and carbon resistors. Silver glue was used to attach 0.25-micron Pt wires to the sample of ~ 0.5 mm thickness.

Figure 3.9-8 shows the diffraction pattern of the sample recovered after the experiment at 20 GPa and 2700 K. Only diamond lines are present in the diffraction pattern. If some boron carbide B_4C remained in the sample, its amount was below the detection limit (< 1 %) of the diffractometer. Graphite after treatment completely transformed into cubic diamond with a lattice parameter from 3.5724(4) Å to 3.5739(2) Å in different samples, which is higher than that of pure diamond (3.5667 Å, JCPDS No. 6-0675) and, thus, in agreement with literature data showing the increase of the lattice parameter of boron-doped diamonds with increase of

B content. The presence of boron in the diamond lattice was confirmed by Raman spectra in agreement with literature data for B concentrations higher than $\sim 3 \times 10^{20} \text{ cm}^{-3}$ (0.17 at.%).

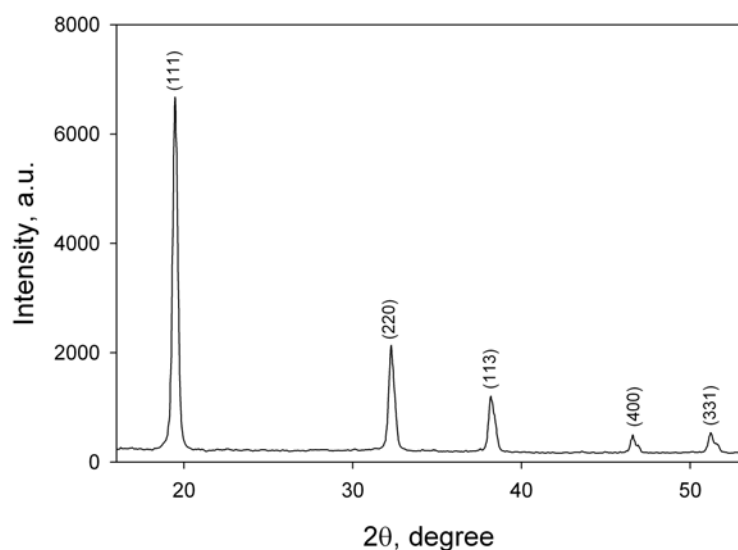


Fig. 3.9-8: The diffraction pattern of the sample recovered after the experiment at 20 GPa and 2700 K.

Figure 3.9-9 shows the temperature dependence of the electrical resistance of the sample measured on cooling and warming in the temperature interval 100 mK to 300 K. The resistance slowly decreases at temperatures between 300 K and 230 K, then starts to increase gradually, and at ~ 6 K reaches a plateau (where the resistance is $\sim 13\%$ higher than the initial one). From ~ 6 K down to ~ 2.4 K the resistance remains essentially constant and then

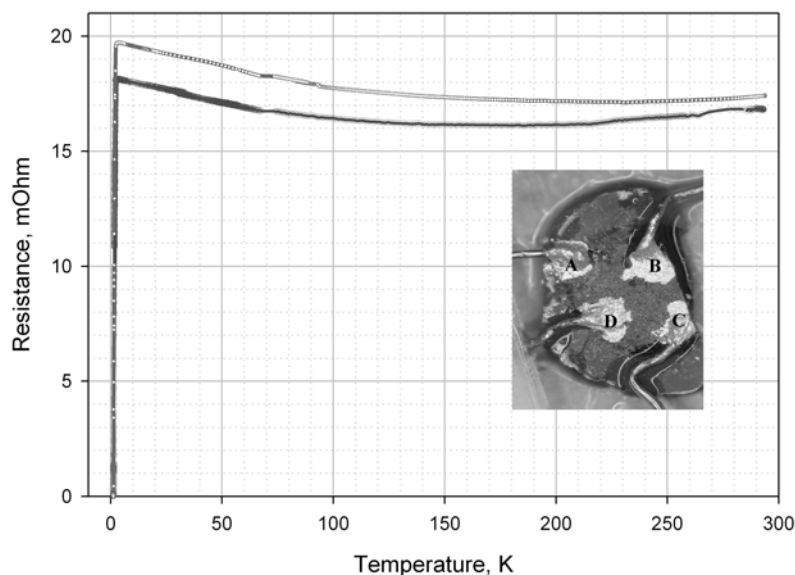


Fig. 3.9-9: The temperature dependence of the resistance of the boron doped diamond sample measured on cooling (upper curve) and warming (lower curve) at the temperature interval 100 mK to 300 K ($B=0$ T). The difference in absolute values of the resistance in the two passes is due to different pairs of contacts used on cooling and warming. Contacts A and D were used for

current and B and C for voltage measurements on cooling, while A and B for current and D and C for voltage on warming. The transition temperature was not influenced due to the use of different pairs of contacts. The inset shows the sample of B-doped diamond in a c-BN capsule with attached electrical contacts. The diameter of the sample without capsule is about 2 mm.

starts to decrease rapidly until it drops to 0 within an accuracy of 10 μOhm at 1.4 K. Applying a magnetic field shifts the transition to lower temperatures, but it does not broaden the transition as would be expected for inhomogeneous superconductors. In contrast, the transition narrows to 0.24 K at 1.2 T (versus 1 K at 0 T). Our results imply that increase of synthesis pressure from 8-9 GPa to 20 GPa does not significantly affect boron content in diamond, but decreases the temperature of the transition to the superconducting state. Narrowing of the temperature interval of the transition to the superconducting state in a magnetic field suggests that superconductivity in our samples may arise from filaments of zero-resistant material.

h. *Stacking faults and internal strains in dhcp phase of La (A.Yu. Kuznetsov, F. Langenhorst/Jena and L.S. Dubrovinsky, in collaboration with E. Estevez-Rams/Habana, V.P. Dmitriev/Grenoble and H.-P. Weber/Lausanne)*

Within our studies on mechanisms of phase transformations between close-packed structures, we analyzed *quantitatively* the microstructural properties of La metal at ambient pressure as a function of temperature. This work revealed an *equilibrium* nature of the observed lattice imperfection which can be explained in the framework of existing theories of polytypism.

High-resolution X-ray diffraction measurements of La have been carried out in the range of temperatures from 80 K to 800 K at ambient pressure at the Swiss-Norwegian Beam Lines of the European Synchrotron Radiation Facility. X-ray diffraction patterns were collected in angle-dispersive geometry with a monochromatic beam at wavelength $\lambda=0.799 \text{ \AA}$ on a high-resolution powder diffractometer. The sample consisted of filings of polycrystalline La metal (99.99 % purity). All manipulations with the sample were performed in an inert atmosphere. The filings were loaded in capillaries, furnished with ultrahigh-purity He gas, and pumped out to high vacuum and sealed.

X-ray diffraction patterns were fitted using TOPAS-Academic software. Instrumental and other sources of peaks broadening were convoluted with the peaks of the *dhcp* phase affected by stacking faults. A direct method for the solution of the diffraction pattern from a faulted layer crystal was used for quantitative characterization of planar faulting in the *dhcp* structure of La.

Figure 3.9-10 shows the average lattice strain and the probability to find “hexagonal” (nearest neighbor planes are identically stacked) or “cubic” (nearest neighbor planes differ in stacking) close-packed planes of atoms in the *dhcp* phase of the La structure. The ideal *dhcp* structure consists of a sequence of alternating “hexagonal” and “cubic” planes, or simply “hchc...”. At ambient conditions, the *dhcp* structure of La is dominated by “c”-type planes, inserted as stacking faults in the ideal *dhcp* lattice (Fig. 3.9-10). On heating of the sample from room temperature, non-equilibrium stacking faults are annealed. This result is confirmed by the approaching of the relative rate of occurrence of “c” and “h” planes, and also by the reduction

of the average lattice strain with increasing temperature (Fig. 3.9-10). At the *dhcp-fcc* phase transition (above 450 K), however, an increase of stacking fault concentration in the *dhcp* phase is not accompanied by an increase of lattice strain in this phase. On cooling of the completely transformed *fcc* phase La, a progressive decrease of the stacking faults concentration in *dhcp* phase is observed after the *fcc-to-dhcp* phase transition (below 450 K). At the same time, an increasing lattice strain characterizes the *dhcp* phase of La on cooling. The above result contradicts the temperature behaviour of non-equilibrium imperfections in a structure of a material, which should exhibit smaller lattice deformations at lower defect concentrations.

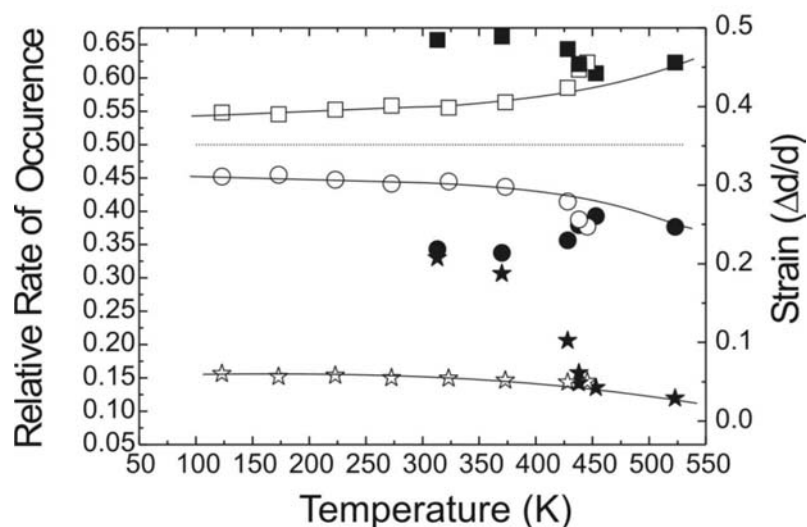


Fig. 3.9-10: Relative rate of occurrence of “c”-type planes (squares) and “h”-type planes (circles), and an average strain (stars) in the *dhcp* phase of La as a function of temperature. Solid lines are guides for the eye. Solid and open symbols correspond to the experimental data obtained on heating and cooling, respectively.

The temperature variation of the structural parameters of La provided strong support to our results on microstructural analysis. Figure 3.9-11 shows the variation of the atomic volume and the spacing between close-packed planes as a function of temperature. The remarkable result is an upward jump of the interplanar spacing accompanied by a downward jump of the atomic volume at the *dhcp-fcc* phase transition.

Bruinsma and Zangwill’s theory of polytypism in close-packed metals reconciles all experimental results obtained on heating of La metal. Crystalline polytype can be regarded as a periodic array of stacking faults. Such an array can be energetically favorable in the case of an attractive interaction between nearest planar defects. From this point of view, the ideal *dhcp* structure contains either 50 % of “c”-type defect planes in an originally non-faulted *hcp* structure or 50 % of “h”-type defect planes in an originally defect-free *fcc* structure. Explicit calculations show that an interaction energy $V(d)$ between two stacking faults is a damped oscillatory function of defect separation and valence (Fig. 3.9-12). Two defect planes can gain

electronic energy if they move closer to bring their separation to a minimum in $V(d)$. An elastic distortive energy opposes this displacement.

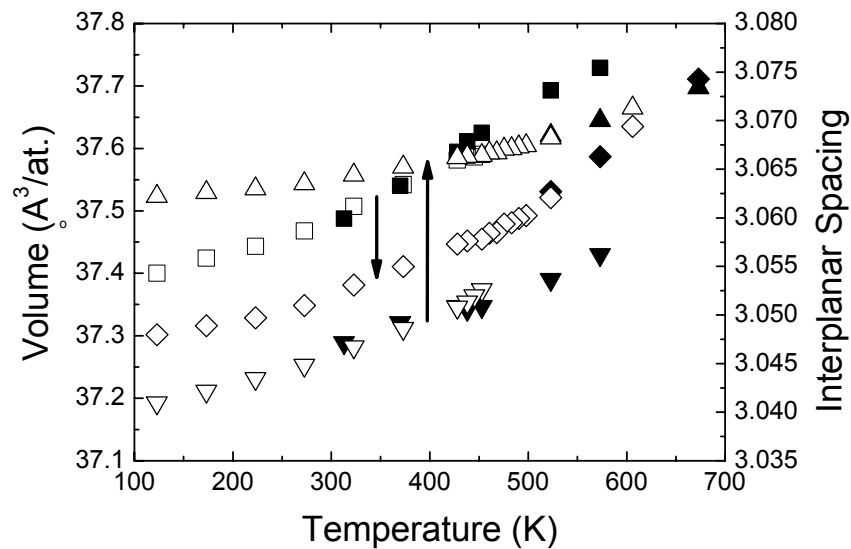


Fig. 3.9-11: Temperature-induced variation of the atomic volume and the interplanar spacing of La. Solid and open symbols correspond to the experimental values obtained on heating and cooling, respectively. Squares and diamonds refer to the atomic volumes of the *dhcp* and *fcc* phases, respectively. Triangles and inverted triangles represent the distances between the close-packed planes in *fcc* and *dhcp* phases, respectively.

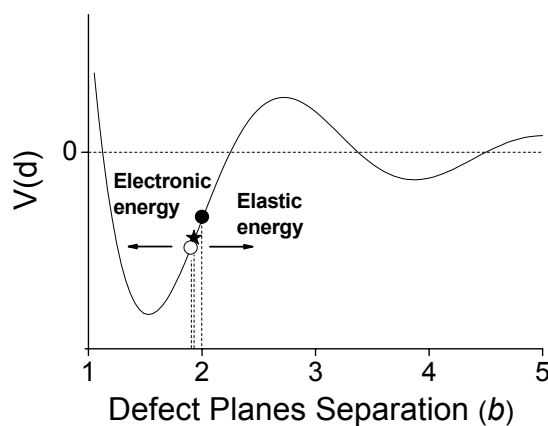


Fig. 3.9-12: Schematic representation of the defect-defect interaction potential as a function of close-packed interplanar spacing b . The solid circle represents the separation of close-packed layers approximating hard-spheres. The open circle represents the separation in the deformed non-faulted *dhcp* structure. The star shows the interplanar spacing in a faulted *dhcp* structure.

Our experimental results indicate that the situation demonstrated in Fig. 3.9-12 is realized in the *dhcp* phase of La. Considerable deformation of the *dhcp* structure along the stacking direction is caused by an attractive interaction between “h”-type planes. A partial relaxation

of the induced stresses proceeds via insertion of stacking faults in the *dhcp* phase, resulting in a slight increase of interplanar spacing. This result demonstrates that a complicated microstructure may define a ground state of a given polytype.

i. *Finite-size and pressure effects on the Raman spectrum of nanocrystalline anatase TiO₂ (V. Swamy and B.C. Muddle/Clayton, A.Yu. Kuznetsov, L.S. Dubrovinsky, R.A. Caruso/Melbourne and D.G. Shchukin/Potsdam)*

Several recent studies focused on the finite-size effects on properties and phase stability of nanocrystalline (*nc*) TiO₂. The interest in *nc*-TiO₂ stems from the large number of technological applications of this material (*e.g.*, photocatalysis, photochemical solar cells, optoelectronic devices, chemical sensors, etc.) as well as from its proven role as a model system in the study of size-dependent structural phase transitions. Evaluation of size-related changes to the vibrational spectra (Raman and infrared) represents an attractive approach to studies of *nc*-TiO₂, for it will not only improve understanding of nanoscale systems, but also assist in practical use of vibrational spectroscopy as a simple and effective tool for the characterization of crystal structure and crystallite size. We carried out a Raman spectroscopic study of the effects of finite size and high pressure on *nc*-anatase TiO₂. Raman spectroscopy is a powerful tool to investigate the effects of finite size and high pressure, including pressure-induced amorphization. Finite-size effects on the phonon spectra of a variety of materials have been well established via Raman scattering experiments on nanocrystals combined with theoretical phonon confinement modelling. The effect of pressure on bulk TiO₂ has been investigated extensively, but there have been relatively few studies of the high-pressure behaviour of *nc*-TiO₂, reporting contrasting high-pressure behaviour of *nc*-anatase and rutile.

Four high-purity (> 99 % TiO₂) *nc*-anatase samples with crystallite sizes 4±1, 8±2, 20±8, and 32±5 nm were investigated in this work. The samples were prepared using different methods in order to minimize compositional influences on the Raman spectrum. Raman data were obtained on a Dilor XY spectrometer with an Ar (514.5 nm) laser as the excitation light. High-pressure Raman spectra were obtained to 40 GPa at ambient temperature using the diamond anvil cell (DAC) technique.

Figure 3.9-13 shows the position (A) and width (B) of the most intense *E_g* Raman mode of anatase against crystallite size obtained from our samples and from the literature. Also shown is the calculated phonon confinement model curve. The agreement between the experimental data and the model is good, given that the model involves some assumptions and that the phonon dispersion used to calibrate the model is that of rutile, not anatase. The good agreement between the experimental Raman data and the phonon confinement model predictions suggests that three-dimensional confinement of phonons in finite-sized anatase nanocrystals is the major factor determining the Raman spectral characteristics of *nc*-anatase. Surface tension and stress effects, suggested as alternative explanations, are not major factors influencing changes in the anatase Raman spectrum. We also rule out oxygen-deficiency as a

factor contributing to the spectral changes because oxygen-deficient samples are blue-colored whereas our samples are opaque white. The deliberate choice of samples prepared by a variety of methods ensures the absence of systematic composition dependence. The possibility of residual reactant species left in the samples after synthesis is also not high, especially for the thermally annealed samples (B-D).

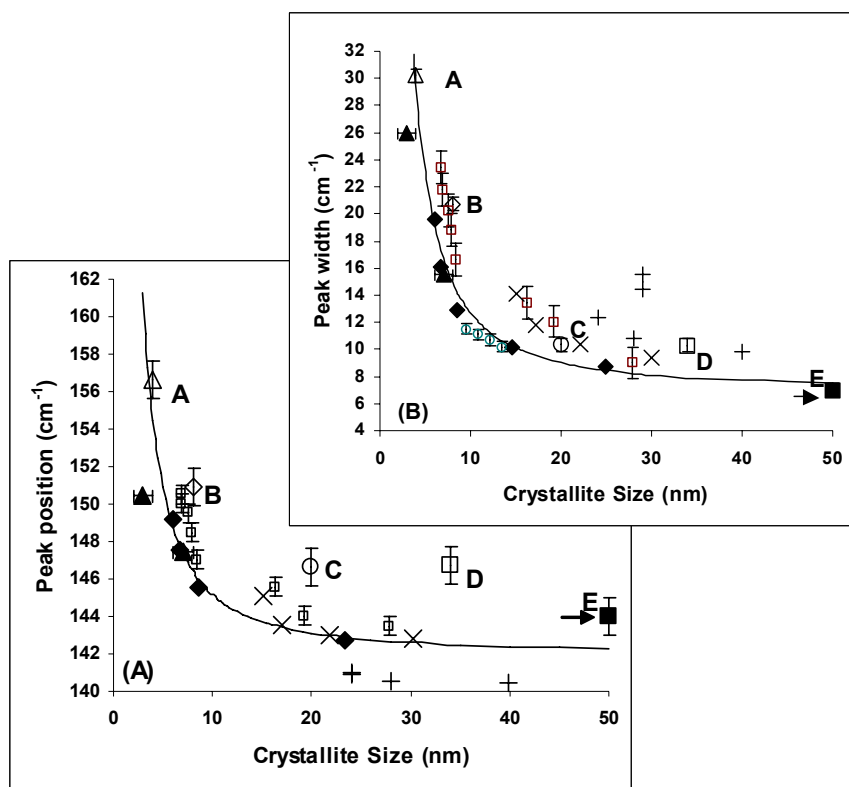


Fig. 3.9-13: Raman frequency (A) and line width (FWHM) (B) of the intense anatase E_g mode versus crystallite size. Samples A-E are from this study, others are from the literature. The curve is according to a phonon confinement model.

In order to evaluate the effect of crystallite size on the structural stability of anatase, we have followed the pressure evolution of the strongest E_g band to pressures of 30-41 GPa. Depending on the crystallite size, two distinct pressure evolution trends were observed: samples with crystallite size < 10 nm showed enhanced metastability versus pressure (stable to 20-25 GPa) and amorphized above this pressure range. An amorphous phase was recovered upon decompression to ambient pressure. Coarser (> 10 nm) nc -anatase transformed directly to the baddeleyite structure at pressures around 18 GPa. Upon decompression to ambient pressure, the samples transformed to the α - PbO_2 structure without any noticeable residual amorphous component. By combining our results with the scant literature data, it is possible to recognize three crystallite size regimes with regard to pressure-induced phase transitions of anatase at room temperature. In the first regime, anatase undergoes amorphization at pressures > 20 -25 GPa. This regime approximately overlaps the crystallite size range where phonon confinement effects are most pronounced. In the second regime, nc -anatase transforms to the

baddeleyite structure at moderate pressures. The third “bulk-like” regime comprises large nanocrystals to single crystals where direct anatase– α -PbO₂ transition is easily achieved in high-pressure experiments around 5 GPa. This size-dependent phase selectivity can be attributed to the dominance of surface energy contributions at small crystallite sizes.

j. *Size effects on the structure and phase transition behaviour of baddeleyite TiO₂ (V. Swamy/Clayton, L.S. Dubrovinsky, N.A. Dubrovinskaia and F. Langenhorst/Jena)*

Structural phase transitions of nanocrystals at high pressures have attracted significant attention in the study of kinetics and microscopic mechanisms of first-order solid-state phase transitions. They also draw attention because of the potential use of dense nanometer-sized phases in shocked Earth’s crustal materials and in meteorites and possibly around presolar stars to constraining formation conditions. Several high-pressure studies on semiconductor nanocrystals (*e.g.*, CdSe, CdS) have shown that these nanocrystals behave as nearly defect-free single structural domains that cycle through the transitions between four-coordinate and six-coordinate structures reproducibly, with simple phase transition kinetics. While considerable understanding of the microscopic mechanisms of pressure-induced first-order solid-solid transitions has been achieved by investigating semiconductor nanocrystals, the size effects on the detailed atomic arrangements in the crystal structures and on other physical properties of the resulting high-pressure phases have not been investigated in detail. In very small nanocrystals (< 50 nm) the proportion of constituent atoms residing at or near the surface increases drastically with decreasing crystallite size, and the coordination environments also are expected to be substantially different from those in the bulk. We investigated nanocrystalline (*nc*) TiO₂ to understand the size effects on the crystal structure, bulk modulus, and crystallite size evolution across the pressure-induced orthorhombic (*Pbcn*) α -PbO₂ – monoclinic (*P2₁/c*) baddeleyite structural phase transition. In bulk TiO₂, the α -PbO₂ phase forms from anatase, rutile, or brookite at 2.5-12 GPa. Above ~ 12 GPa, TiO₂ adopts the baddeleyite structure that upon decompression converts back to α -PbO₂ at ~ 7 GPa.

Phase-pure (> 99.5 %) nearly equiaxial *nc*-anatase with dimensions of 34±5 nm (Scherrer, BET, and TEM determinations) was used as a starting material. Nanocrystalline α -PbO₂ and baddeleyite TiO₂ were synthesized in electric- and laser-heated diamond anvil cells (DACs). In order to synthesize nanocrystalline and bulk baddeleyite, we compressed the appropriate starting material in a DAC to ~ 37 GPa, heated the sample in the DACs to 850-900 K for 4-5 hours, and subsequently cooled to ambient temperature. The pressure-induced changes in the *nc*-structures were mainly monitored with angle-dispersive X-ray diffraction (XRD) at the BM01 and ID22 beamlines of the European Synchrotron Radiation Facility. The XRD images were integrated using the FIT2D program and Rietveld refinements were carried out using the GSAS package. Additional DAC XRD experiments, including those on the bulk phases, were carried out at the Bayerisches Geoinstitut. Possible size effects on the vibrational spectra of the high-pressure TiO₂ polymorphs were examined using *in situ* Raman scattering data. The crystallite sizes were determined with transmission electron microscopy (TEM). The chemical composition of the samples was verified using scanning electron and analytical transmission

electron microscopy. High-pressure and temperature treatment did not result in any chemical reactions.

A comparison of the XRD spectra of *nc*- and bulk baddeleyite reveals distinct differences at mid-to-high 2θ ranges. Additional diffraction peaks are seen for *nc*-baddeleyite. Rietveld refinement in the space group $P2_1/c$ yielded comparable good quality solutions with a and b parameters of *nc*-baddeleyite 1.4 % and 1.7 % larger, c marginally bigger (0.4 %), and β nearly identical relative to the bulk structure. The cell volume of *nc*-baddeleyite at 34(1) GPa, 104.20 \AA^3 , is about 4 % larger than that of the bulk (100.60 \AA^3), clearly demonstrating size-induced lattice expansion. The atomic arrangement also changes significantly at the nanoscale. We observed up to 14 % change in the Ti-O distances in *nc*-baddeleyite relative to the bulk. This represents a severe distortion of the atomic arrangement at the nanoscale in relation to the extended structure. Small modifications to the Raman spectra also reflect these changes at the atomic level. Taken together, our XRD and Raman data suggest that atomic reorganizations in finite crystals are not confined to near surfaces, but extend to crystallite interiors.

The size/shape changes due to structural transformations in the nanocrystals were examined by comparative TEM of the starting anatase and samples quenched to ambient pressure after several compression-decompression cycles. The baddeleyite structure is not quenchable even as nanocrystals and could not be examined under TEM. The starting anatase has fairly equiaxial crystallites. A recovered $\alpha\text{-PbO}_2$ showed mostly elongate crystallites of 25-35 nm (Fig. 3.9-14). The size reduction in the $\alpha\text{-PbO}_2$ is approximately consistent with the density difference between the two phases. Crystallite coarsening as result of sintering could not be observed in

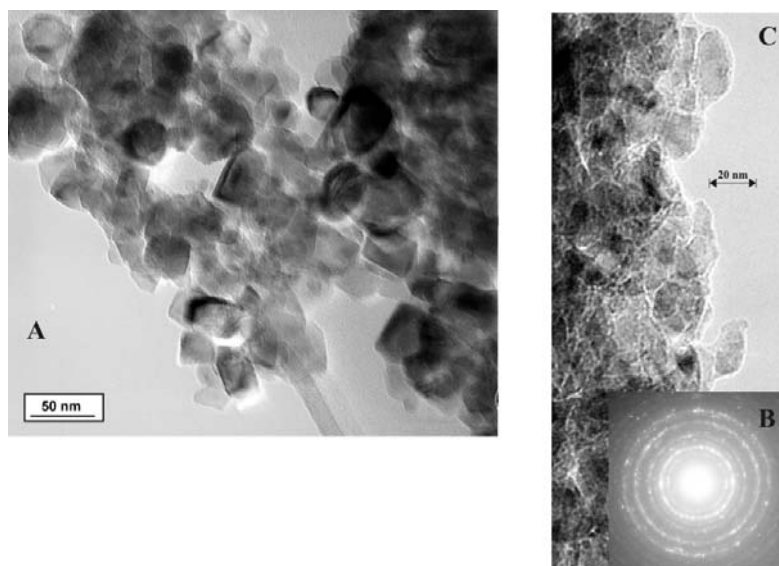


Fig. 3.9-14: A. TEM image of *nc*-anatase showing equiaxial crystallites. B. Electron diffraction of the $\alpha\text{-PbO}_2$ phase recovered after compression-decompression cycles in the pressure range 0-40 GPa. C. TEM image of the recovered $\alpha\text{-PbO}_2$ sample shown in B. The crystallites are elongated and have sizes in the range of 25-35 nm with an average diameter of about 30 nm.

the transformed material, despite laser and electrical heating. This indicates that the majority of the crystallites are preserved as coherent units across multiple transitions involving 6 to 7 Ti-O coordination change among anatase, α -PbO₂, and baddeleyite. This is suggestive of the “single structural domain” behaviour of the nanocrystalline system, as seen for the semiconductors Si and CdSe. The elongate *nc*- α -PbO₂ in contrast to equant *nc*-anatase (Fig. 3.9-14) suggests that low-index equiaxial crystallites are converted to (presumably) high-index high-energy surfaces in the high-pressure phase in consonance with crystallite integrity in the nanocrystals. In view of these results, the use of nanocrystals as models of bulk phase transitions and as geothermobarometers must be done with great caution.

k. *Size-dependence of pressure-induced amorphization in nanoscale TiO₂ (V. Swamy and B.C. Muddle/Clayton, A.Yu. Kuznetsov and L.S. Dubrovinsky, P.F. McMillan/London)*

Pressure-induced amorphization (PIA) has been observed for several types of materials. PIA involves metastable transformation of crystalline materials to amorphous solids by application of pressure at temperature that is sufficiently low to preclude nucleation and growth of stable crystalline phases. It is a kinetically-controlled event correlated with a frustrated attempt by the crystal to reach its stable packing at high density. PIA has been mostly described among tetrahedrally-coordinated solids (*e.g.*, SiO₂, H₂O, and Si). In the cases of H₂O and Si, PIA results in new high-density amorphous (HDA) forms that can either be recovered metastably to ambient pressure or transform to low-density amorphous (LDA) structures upon decompression. The HDA-LDA polyamorphism is usually linked to an underlying density-driven liquid-liquid phase transition, and is of great significance in the physical chemistry of materials. We investigated the high-pressure behaviour of two sub-10 nm sized nanocrystalline (*nc*) anatase using angle-dispersive synchrotron X-ray diffraction (XRD) and Raman spectroscopy in diamond anvil cells.

The *nc*-anatase structure is retained metastably to 20-24 GPa during compression, with PIA occurring beyond this pressure range (Fig. 3.9-15). During a typical compression-decompression cycle, the *nc*-anatase XRD peaks broadened and weakened with increasing pressure to \sim 20 GPa; spectra obtained following decompression from 45 GPa showed very broad features typical of *a*-TiO₂. The broad features in the high-pressure ($>$ 20 GPa) XRD spectra could not be correlated with the diffraction patterns of any known TiO₂ phases stable in this pressure range. The broad bands resemble the diffraction peaks of α -PbO₂ TiO₂ at low pressures. However, TEM and electron diffraction studies do not indicate the presence of any crystalline material. We suggest that the *a*-TiO₂ recovered to ambient pressure is noncrystalline but has a structural relationship to α -PbO₂. The *a*-TiO₂ formed by PIA at high pressure is likely to be structurally related to the baddeleyite structure as suggested by Raman data (see below). In that case, the data indicate a polyamorphic transformation occurring during decompression of *a*-TiO₂ between an HDA form produced by PIA and an LDA polymorph that is recovered at ambient pressure. This is similar behaviour to H₂O and *a*-Si produced by PIA of nanocrystalline porous-Si materials. Interestingly, the high- and low-

pressure XRD spectra of α -TiO₂ are similar to those obtained at similar pressures from a chemically-synthesized sample during a decompression run from similar peak pressure.

In order to characterize the pressure-dependent α -TiO₂ structures, we obtained Raman spectra during compression-decompression cycles. The strong E_g Raman mode of nc -anatase at 144 cm⁻¹ is observable to 20-24 GPa; the band weakens dramatically and essentially disappears above 14-15 GPa. Raman spectra obtained above this pressure exhibit a broad density-of-states function with broad weak maxima near 225-290 cm⁻¹ and 495-540 cm⁻¹. During decompression, new broad features began to emerge at high- (550-650 cm⁻¹) and low-wavenumbers (100-300 cm⁻¹) below pressures of 15-16 GPa for both samples, indicating the presence of an LDA polymorph. The new peaks grew and red-shifted with decreasing pressure, evolving into a distinct LDA spectrum below ~ 10 GPa. The ambient pressure spectra from recovered material are different from those of sol-gel produced α -TiO₂ that is shown to be structurally related to brookite/anatase. Upon re-compression, the LDA-TiO₂ spectrum transformed back into that of the HDA polymorph above ~ 14 GPa, suggesting the possibility of a reversible HDA-LDA polymorphic transition such as that observed for α -H₂O and α -Si.

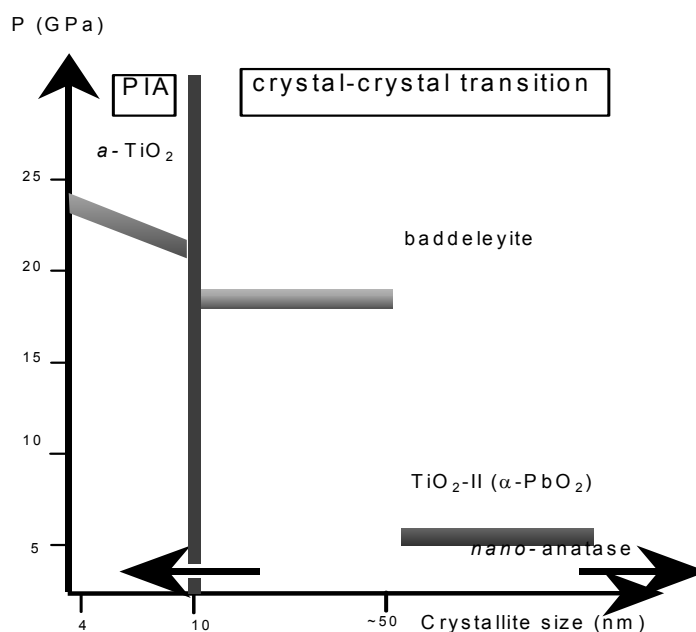


Fig. 3.9-15: Size-dependent pressure stability of nc -anatase. Nanocrystals of size < 10 nm undergo PIA and remain amorphous (α -TiO₂) upon further compression/decompression. The ~ 12-50 nm crystallites transform to baddeleyite structure upon compression, which then transform to α -TiO₂ on decompression. Coarser crystallites transform directly to α -PbO₂-structured TiO₂. The average transition pressures are indicated.

Both the PIA and HDA-LDA transformations observed for nc -anatase are similar to those that occur for ice (H₂O) and Si. For these latter systems, a thermodynamic explanation of PIA

involves interception along the compression/decompression path of the metastable extension of the melting curve (with negative slope or a maximum). We cannot yet test this proposition for TiO_2 because the available high-P,T phase relations do not include melting curve determinations, and stable versus metastable transformations for TiO_2 polymorphs, including melting, are strongly modified by surface energy contributions within nanocrystalline materials. Our results indicate that PIA can occur for nanoparticles among systems that are poor glass-formers, and that this process could yield useful amorphous ceramics and nanocomposites.

I. Sol-gel synthesis of amorphous and nanocrystalline $\text{ZrO}_2\text{-TiO}_2$ (E. Holbig, L.S. Dubrovinsky, T. Boffa Bollaran and N. Miyajima, in collaboration with P. Löbmann and M. Bockmeyer/Würzburg)

High-pressure experiments on the system $\text{TiO}_2\text{-ZrO}_2$ require starting materials with varying relations of Ti:Zr that are homogeneous on a micrometer or (better) nanometer scale. As such powders can hardly be produced from sintering of ceramic powders, we developed a route for synthesis with the sol-gel method. We synthesized $\text{ZrO}_2\text{-TiO}_2$ amorphous material as well as solid solutions with grain sizes in the nanometer range with varying stoichiometry.

Precursor powders were synthesized by adding one mole acetylacetone to one mole zirconium-*n*-propoxide, or titanium-*n*-ethoxide. The yellow solution obtained was stirred at 40 °C for one hour. 3 moles distilled water were added and stirred for 30 minutes at 80 °C. The solution was distilled under rotational evaporation at 80 mbar air pressure and 80 °C. The powder obtained has a concentration of ~ 53 wt.% oxide, obtained from heat loss analysis after heating at 1000 °C.

The precursor powders were weighed and dissolved in either H_2O - or ethanol-based solutions, yielding stoichiometries of $\text{Ti}_x\text{Zr}_{1-x}$ with $x = 0, 10, 25, 33, 50, 67, 75, 90$ and 100 and metal oxide concentrations of 10 wt.% in the sol. The sols were stirred for about one hour until they were clear. Within the sols, the Ti and Zr atoms are homogeneously distributed at an atomic scale, ideal for obtaining homogeneous gels and powders. The sols were distilled under rotational evaporation at 80 mbar air pressure and 80 °C, obtaining gel powders.

The gel powders were heated at 200 °C for one hour, ground in an agate mortar and heated at 200 °C for another 30 minutes. In six portions of ~ 8 g each, the dried powders were then placed in a metal chamber into the furnace and heated at 400 °C or 500 °C for 2 hours, while 400 ml of distilled water were sprayed into the chamber. The samples were then heated at the same temperature in the drying oven for another hour.

X-ray powder diffraction patterns were collected on the Phillips X'Pert diffractometer at BGI. Samples with $25 \leq x \leq 50$ are amorphous, samples with $x \leq 10$ have cubic zirconia present, and at

$x \geq 67$ anatase appears (Fig. 3.9-16). TEM analysis of a sample with $x = 50$ shows amorphous material (Fig. 3.9-17), and Raman spectra indicate that no organics are present. The analysis confirms that our route of sol-gel synthesis was sufficient to produce starting materials that fulfill all requirements, being homogeneous on a nanometer scale and having varying composition.

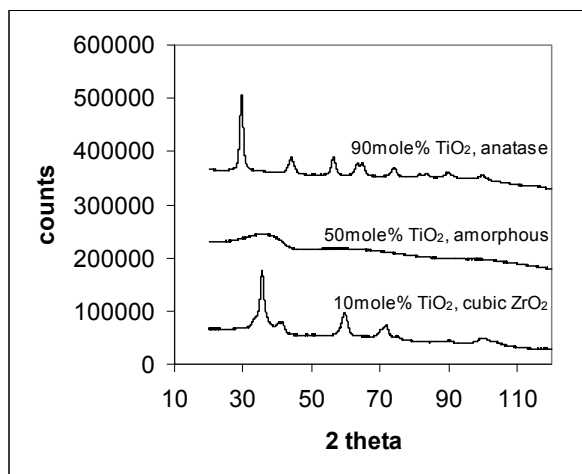


Fig. 3.9-16: Powder X-ray diffraction data of samples with 10, 50 and 90 mol.% TiO₂, collected at the Phillips X'Pert diffractometer at BGI, using Co K α radiation.

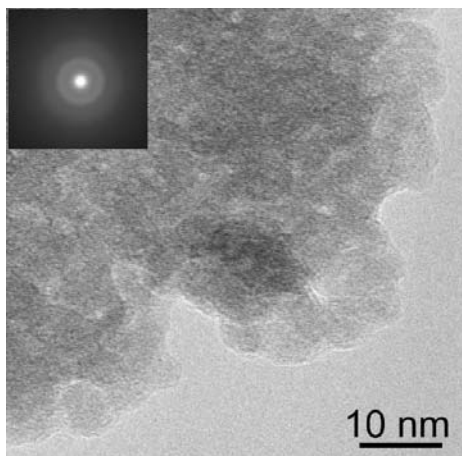


Fig. 3.9-17: HRTEM image and electron diffraction pattern (inset) of a sample with 50 mol.% TiO₂, indicating the amorphous state.

m. *ZrO₂-TiO₂ phase equilibria at high pressures and temperatures (E. Holbig, L.S. Dubrovinsky, C.A. McCammon and D.J. Frost)*

We studied TiO₂-ZrO₂ phase equilibria at high pressures and temperatures experimentally in order to constrain the stability of the srilankite phase. The origin and stability of srilankite are controversial and so far, a hydrothermal origin was proposed for natural samples. However,

experimental studies in flux systems show an ordered low temperature phase $ZrTi_2O_6$ and at temperatures higher than 1100 °C $(Zr,Ti)O_2$ is stable as a disordered phase, which is not consistent with a hydrothermal origin.

High-pressure experiments were carried out in the piston cylinder apparatus at pressures of 2 GPa and 3.5 GPa and temperatures of 1300 °C and 1600 °C, as well as on the multianvil apparatus at pressures of 10 GPa and 20 GPa and temperatures of 1350 °C and 1650 °C.

As a starting material, we used mixtures of TiO_2 (99.999 %) and ZrO_2 (99.99 %) that had TiO_2 contents of 75 and 30 mol.%. In order to get a homogeneous and fine grained mixture, the oxides were ground for 6 hrs using an agate mortar and pestle and heated in a furnace at 1300 °C for 24 hrs, then ground again for 12 hrs.

Figure 3.9-18 shows the phase diagram constructed from our analysis. Between 2 and 3.5 GPa, the Ti content of the Zr-rich phase (baddeleyite and high-pressure polymorphs) and the intermediate phase increase (srilankite and high-pressure polymorphs) with increasing pressure, as expected for the smaller cation in the high-pressure phase. The phase boundary of the Ti-rich phase (rutile and high-pressure polymorphs) does not shift with pressure, indicating that the Zr solubility in TiO_2 phases is limited to ~ 10 mol.%.

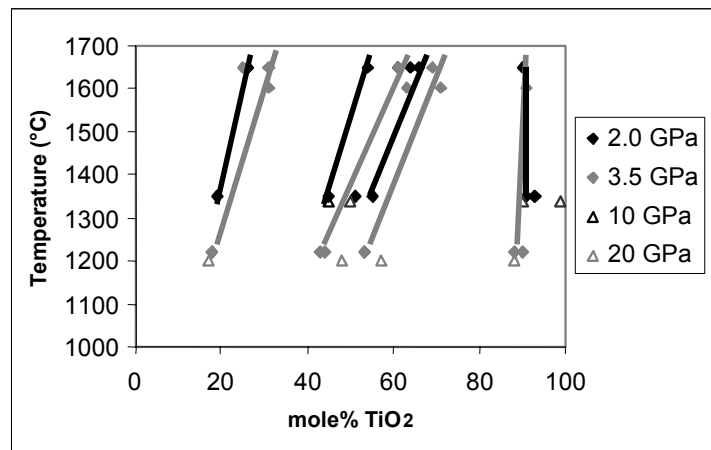


Fig. 3.9-18: Phase diagram of the system TiO_2 - ZrO_2 at high pressures and temperatures, constructed from our data. The Zr-rich phase is baddeleyite and high-pressure polymorphs, the intermediate phase is srilankite and high-pressure polymorphs, and the Ti-rich phase is rutile and high-pressure polymorphs.

Powder X-ray diffraction data show that disordered orthorhombic srilankite is stable up to at least 3.5 GPa and transforms to a high-pressure polymorph between 3.5 and 10 GPa.

From our study we can rule out a hydrothermal origin for srilankite and confirm an igneous origin, consistent with the occurrence in high grade rocks such as eclogites, granulites, lamprophyres and chromatites. We can furthermore give an upper pressure limit for the stability of srilankite.

n. *Semiconductor-metal transition and crystal structure of LaCoO₃ at high pressure probed by Raman spectroscopy and X-ray diffraction (D.P. Kozlenko/Dubna, L.S. Dubrovinsky, Z. Jirák and B.N. Savenko/Prague)*

Among rare-earth – transition metal oxides with perovskite-like structure, lanthanum cobaltite LaCoO₃ exhibits unusual electronic and magnetic properties at ambient pressure. At low temperature LaCoO₃ is a nonmagnetic semiconductor with a ground state of Co³⁺ ions with low-spin (LS) configuration (t^6_{2g} , $S = 0$). As temperature increases, a sharp anomaly in the magnetic susceptibility corresponding to the appearance of the paramagnetic state was observed at $T \sim 100$ K, and a semiconductor-metal (S-M) transition accompanied by another broad anomaly in the magnetic susceptibility occurs at $T_{S-M} \sim 500$ K. These phenomena were explained by thermally activated transitions of Co³⁺ ions from LS to an intermediate spin (IS) state ($t^5_{2g}e^1_g$, $S = 1$) at $T \sim 100$ K, and then from IS to either a modified IS with different electronic configuration or a high spin (HS) state ($t^4_{2g}e^2_g$, $S = 2$) at $T_{S-M} \sim 500$ K. Recently it was shown that surface heating by laser leads to a sharp decrease of some Raman mode intensities of LaCoO₃ and their disappearance at temperatures estimated to be close to T_{S-M} .

In order to establish whether Raman spectral changes are indeed related to the S-M transition and to study the high-pressure effects on T_{S-M} and the crystal structure of LaCoO₃, Raman spectroscopy, X-ray diffraction and resistivity (at $P = 0$) measurements were performed (Fig. 3.9-19).

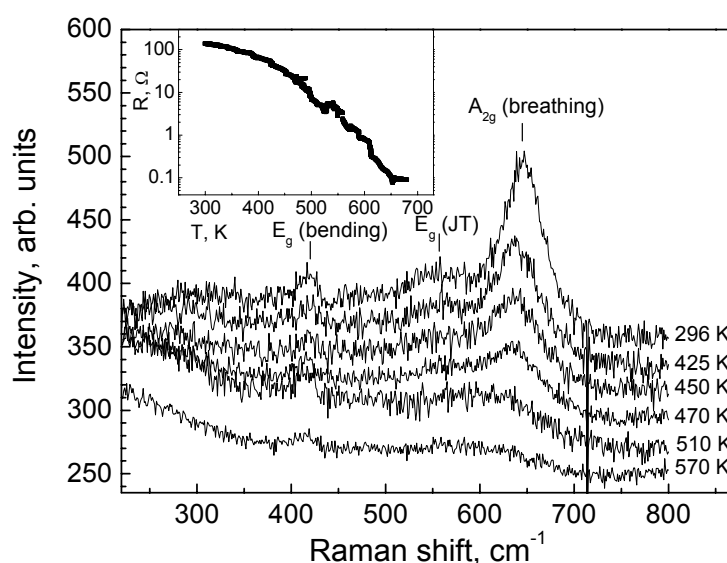


Fig. 3.9-19: Temperature dependence of Raman spectra and resistivity (inset) of LaCoO₃ at ambient pressure. Raman spectra are shifted along the vertical axis by a constant value for clarity.

At ambient pressure and $400 < T < 630$ K the resistivity of LaCoO₃ deviates from the conventional $R \sim \exp(E_a/kT)$ behaviour and decreases drastically by three orders of magnitude. At higher temperatures R remains nearly constant (Fig. 3.9-19, inset). In Raman

spectra of LaCoO_3 at ambient conditions three modes located at ~ 645 , 565 and 420 cm^{-1} were observed (Fig. 3.9-19). They can be assigned to A_{2g} breathing, E_g quadrupole (JT) and E_g bending modes, respectively. A sharp decrease of the A_{2g} breathing and E_g quadrupole (JT) modes intensities was observed at $T > 400 \text{ K}$, which correlates with the resistivity drop (Fig. 3.9-19). At $T = 570 \text{ K}$ both peaks nearly disappear.

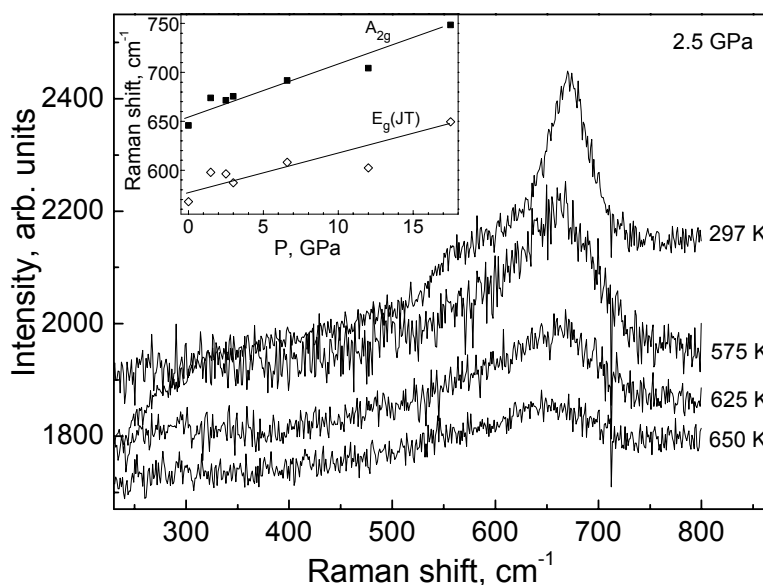


Fig. 3.9-20: Raman spectra of LaCoO_3 measured at elevated temperatures and $P = 2.5 \text{ GPa}$ and pressure dependence of A_{2g} and E_g (JT) mode positions at ambient temperature (inset).

At $P = 2.5 \text{ GPa}$ the decrease of A_{2g} and E_g (JT) mode intensities was observed at $T > 550 \text{ K}$ only (Fig. 3.9-20), indicating that the S-M transition in LaCoO_3 is extremely pressure sensitive and shifts by about 150 K to higher temperatures. Both A_{2g} and E_g (JT) mode frequencies increase nearly linearly with pressure (Fig. 3.9-20, inset). The smallest intensity E_g bending mode could not be detected in the high-pressure experiment.

The X-ray diffraction experiments have shown that the rhombohedrally distorted perovskite-like crystal structure (space group $R\bar{3}c$) is retained in LaCoO_3 at high pressures up to 18.5 GPa and ambient temperature. The values of the bulk modulus $B = 159 \text{ GPa}$ and its pressure derivative $B' = 4$ were obtained from the fit of experimental volume compressibility data using a second order Birch-Murnaghan EOS.

o. *Structural changes and pressure-induced chemical decomposition of boric acid (A.Yu. Kuznetsov, L.S. Dubrovinsky and A. Shiryayev)*

Boric acid (H_3BO_3) was one of the first compounds with a hydrogen bonded crystal structure to be characterized by X-ray diffraction methods. Its triclinic crystal structure, space group

$P\bar{1}$, consists of a layered packing of slightly buckled sheets. Each sheet is formed by H_3BO_3 molecular units with nearly perfect C_{3h} symmetry, linked together by hydrogen bonds $\text{O}-\text{H}\cdots\text{O}$.

In contrast to temperature-induced changes of H_3BO_3 , the influence of pressure on the structure and stability of H_3BO_3 have not yet been comprehensively studied. The available laboratory energy-dispersive X-ray diffraction and Raman spectroscopy studies showed that the layered structure of H_3BO_3 is highly unstable under pressure, even at room temperature. This work showed a transition of H_3BO_3 to a highly disordered, probably amorphous state at pressures about 2 GPa and the appearance at higher pressures of a new phase whose diffraction pattern could be indexed with the cubic polymorph of the metaboric acid ($\gamma\text{-HBO}_2$). The observed transitions were interpreted as a novel pressure-induced chemical decomposition of H_3BO_3 on HBO_2 and H_2O . However, questions remained about a conclusive identification of the decomposition products, their structures and the possible formation of new phases of boric acid induced by pressure.

In order to elucidate the structural aspects of the pressure-induced decomposition of H_3BO_3 and the possible role of hydrogen bonds in the observed transformations, we have performed *in situ* measurements using a focused beam from a 3rd generation synchrotron source along with a complementary study by Raman and IR spectroscopy. The obtained experimental results allowed us to propose a mechanism of pressure-induced dehydration of boric acid which implies proton transfer in the H_3BO_3 compound.

The high-pressure studies of boric acid were carried out on reagent grade H_3BO_3 powder samples with purity 99.9 % loaded in a diamond anvil cell (DAC). Structural data were obtained at the ID30 beam line at the European Synchrotron Radiation Facility (ESRF, Grenoble, France). *In situ* high-pressure measurements employed an angle-dispersive X-ray powder diffraction technique with monochromatic ($\lambda=0.3738$) radiation. Diffraction patterns were collected with an image plate detector (MAR345). The Raman scattering measurements were carried out at Bayerisches Geoinstitut using a Dilor XY system with the 5145 Å Ar-ion laser as the excitation line. Raman spectra were collected in the 100-4000 cm^{-1} range. The high-pressure IR measurements followed the Raman data collection at each pressure step. The IR spectra were obtained in reflection mode on a Bruker IFS 120 HR high-resolution FTIR spectrometer with a Bruker IR microscope. A thin platinum foil was placed in the gasket hole of the DAC assemblage and was covered by the sample, providing thus a reflection surface for the incident IR radiation. The sum of 500 scans defined each high-pressure IR spectrum in the 600-4000 cm^{-1} spectral region.

The increase of pressure to about 2 GPa resulted in a fast decrease of the parameter c of the triclinic lattice of H_3BO_3 compared with the respective changes of a and b lattice parameters (Fig. 3.9-21). Such behaviour of the lattice parameters fits well to theoretical predictions from which one can expect a higher compressibility of the H_3BO_3 structure along the crystallographic c axis than along the a or b axis. The Birch-Murnaghan isothermal equation

of state was fitted to the experimental data. The numerical results of the fitting procedure ($V_0=274.394(70)$, $B_0=5.3(6)$ GPa, $B'=19(3)$) reveal the overall high compressibility of boric acid.

The appearance of new reflections was clearly seen at pressures above 2 GPa. Three new phases were identified: cubic metaboric acid ($\gamma\text{-HBO}_2$, $a=8.8693(3)$ Å), tetragonal ice-VI ($a=6.0871(8)$ Å, $b=5.579(2)$ Å) and cubic ice-VII ($a=3.3552(7)$ Å) revealing thus the pressure-induced decomposition of H_3BO_3 to HBO_2 and H_2O at ambient temperature.

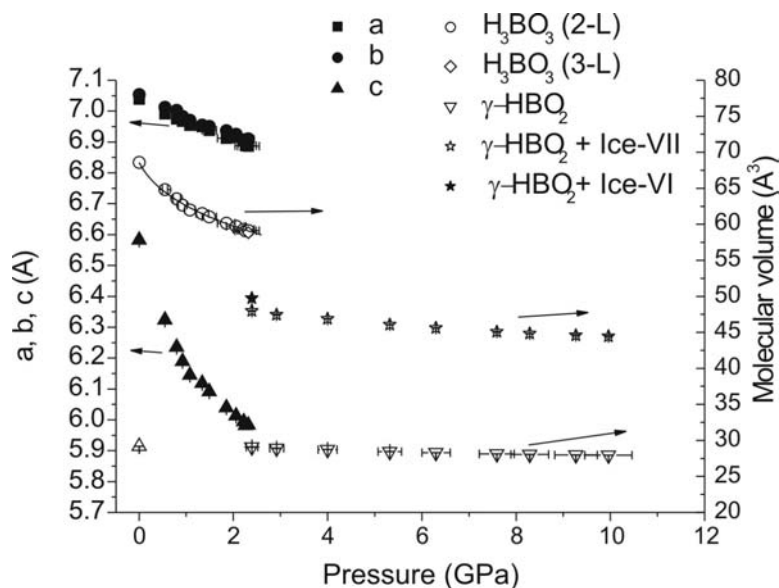


Fig. 3.9-21: Pressure-induced variation of the lattice parameters of boric acid (H_3BO_3) of the molecular volume of H_3BO_3 and its chemical decomposition products, metaboric acid (HBO_2) and ice. Solid squares, circles and triangles are a , b , c lattice parameters of the triclinic H_3BO_3 . Open circles and inverted triangles are the molecular volumes of triclinic H_3BO_3 and cubic HBO_2 phases. Open stars and solid stars refer to the sum of the molecular volumes of HBO_2 and ice-VII phases, and to the sum of HBO_2 and ice-VI molecular volumes, respectively. The open triangle at ambient pressure represents the molecular volume of cubic HBO_2 phases from the literature. The open diamond at 2.3 GPa shows the molecular volume of a 3-layered structure of H_3BO_3 .

One can see that the chemical decomposition of H_3BO_3 to HBO_2 and H_2O results in a large overall volume reduction, suggesting that this pressure-induced reaction is driven by a density effect.

Complementary Raman and IR spectroscopy measurements are consistent with the results of the X-ray diffraction study. The high-pressure Raman and IR spectra suggest that the $\text{B}(\text{OH})_3$ molecular complexes of orthoboric acid preserve their structure up to the pressure of the decomposition (around 1.6 GPa). The molecular H_3BO_3 crystal remains stable at pressures up to 1.6 GPa, despite the large density effect which one can expect at the decomposition of

H₃BO₃ at much lower pressures (Fig. 3.9-21). The reason for this stability can be attributed to the kinetic requirements for the H₃BO₃ → HBO₂ + H₂O chemical reaction. The activation energy of this reaction is too high to be observed at low pressures and ambient temperatures. A large separation between the oxygen atoms situated in adjacent sheets of B(OH)₃ molecular complexes prevents the formation of hydrogen bonds in the direction of the stacking of sheets. One can estimate from the data of Fig. 3.9-21 the interlayer O-O distances. The shortest interlayer O-O distance becomes comparable with the intralayer O-O distances at about 2 GPa. Consequently, the activation barrier for hydrogen bond formation in this direction should be low enough to trigger a decomposition of H₃BO₃ to the more stable hydrogen-bonded components, HBO₂ and H₂O.

p. *Synthesis of hexagonal nickel nitride using high pressures and temperatures (C. Guillaume, G. Serghiou and J.P. Morniroli/Edinburgh; D.J. Frost)*

The investigation of phase relations of nitride compounds at high pressures and temperatures is in its infancy, but already a diversity of behaviour even among elements of the same group of the periodic table seems to be evident. For some elements new dense structural forms have been synthesised at high pressure, *e.g.*, (Si, Ge, Sn, Hf, Zr)-N. There are examples such as TiN, however, where the ambient pressure structure appears to be stable to very high pressures. In other systems the application of pressure does not seem to lead to the synthesis of new compounds, *e.g.*, C-N. One problem with the synthesis of dense nitride structures at high pressures is adding significant nitrogen to the system when suitable low-pressure nitride precursors do not exist. Here we report the investigation of the high pressure and temperature stability of nickel nitride, which belongs to the broader class of interstitial nitrides that includes ambient pressure (Hf, Zr, Ti)-N. In order to provide a high N concentration we have investigated the use of NaN₃ azide as a N source.

Multianvil synthesis experiments were performed at 20 GPa and 2000 K using nickel (Ni) and sodium azide (NaN₃) starting materials packed into rhenium foil capsules. The recovered products were characterized using scanning electron microscopy and transmission electron microscopy. Using energy dispersive X-ray analysis and backscattered electron microscopy images we identified two phases in these experiments: a sodium rhenium nitride phase, which formed via reaction with the capsule, and a nickel nitride phase. Figure 3.9-22 is an SEM image of the nickel nitride phase. Selected area electron diffraction (SAED) and convergent beam electron diffraction (CBED) were used for collecting diffraction patterns from the polycrystalline matrix and individual grains, respectively. A series of zone-axis diffraction patterns collected from several crystals showed a very good fit of the spot patterns to the ordered hexagonal Ni₃N structure with coordinates (S.G. P6₃22, $a = 4.62 \text{ \AA}$, $c = 4.30 \text{ \AA}$, $Z = 2$). The zone axis patterns observed were ones along [001], [00-1] and [-2-13] (Fig. 3.9-23). Powder patterns obtained using SAED matched rings belonging to ordered hexagonal Ni₃N. In addition, the existence in some patterns of diffuse rings and most notably a concomitant

ring, where nitrogen is randomly distributed, provides evidence for the presence of a second disordered hexagonal nickel nitride modification.

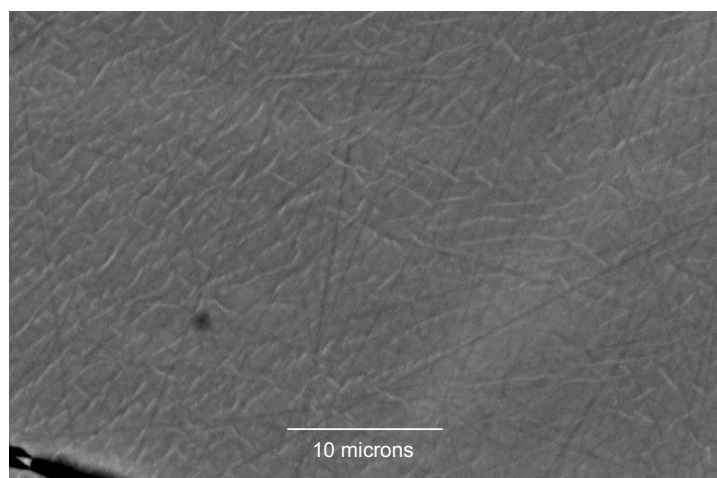


Fig. 3.9-22: Backscattered scanning electron microscopy (BSE) image of nickel nitride recovered after heating nickel and sodium azide at 20 GPa and 2000 K. This temperature is more than three times the dissociation temperature of nickel nitride at ambient pressure and 100 K below the melting point of nickel at 20 GPa.

NaN_3 azide therefore seems to provide an effective source of N in high-pressure experiments. Because the liberated Na is scavenged by a reaction with the Re capsule it does not interfere with the formation of nitride phases. The thermal stability of Ni_3N increases significantly with pressure from 580K at ambient pressure to over 2000K at 20 GPa. The use of NaN_3 is a potentially effective route to the synthesis of new nitride compounds at high pressure and temperature.

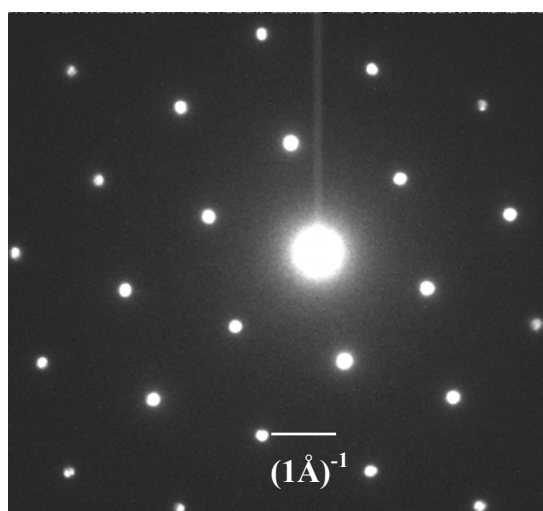


Fig. 3.9-23: Convergent beam electron diffraction (CBED) patterns of zone [001] of the hexagonal (S.G. $P6_322$) nickel nitride (Ni_3N) structure.

q. *Synthesis and properties of new (oxide)-nitride-ceramics: spinel-nitrides and -sialons (T. Gross, T. Locherer, R. Riedel and H. Fuess/Darmstadt; E. Kroke and M. Schwarz/Freiberg, in collaboration with D.J. Frost)*

It has been shown that nitrides such as Si_3N_4 and Ge_3N_4 transform into dense spinel structures at pressures over 10 GPa and temperatures between 1500-2000 °C. $\gamma\text{-Si}_3\text{N}_4$ and $\gamma\text{-Ge}_3\text{N}_4$ are the first members of a new class of hard ceramic nitrides, which are also wide band gap semiconductors. As a result of this renewed interest in high-pressure nitrides work has continued on the synthesis of various other spinel-nitrides and -sialons (SiAlON). We have performed high-pressure/high-temperature syntheses in the systems Zr-O-N, Si-Al-O-N and on ternary nitrides of the system Ge-Ti-N using a multianvil apparatus at pressures between 5 and 20 GPa and temperatures up to 2000 °C.

In comparison with the other systems investigated, the solidsolutions of the spinel-sialons $\text{Si}_{3-x}\text{Al}_x\text{O}_x\text{N}_{4-x}$ have been particularly amenable to synthesis. Several pure samples with the compositions $x = 1.0, 1.1, 2.0$ and 2.1 were synthesized at 13 GPa and 1800 °C using the analogous β -sialons as starting materials. A boron nitride capsule provided a suitably inert and reducing environment for the synthesis experiments. The recovered samples have been used to make the first mechanical property measurements on such spinel solid solutions. The hardness and fracture toughness have been measured with respect to the degree of substitution x across the solid solution. With increasing AlO-substitution ($= x$) the hardness H_V drops from 27 GPa to 18-20 GPa. In comparison β -sialons with the same stoichiometry have values for the Vickers-hardness H_V between 16.7 and 13.2 GPa. Measurements of the band gap dependence on x are currently under investigation.

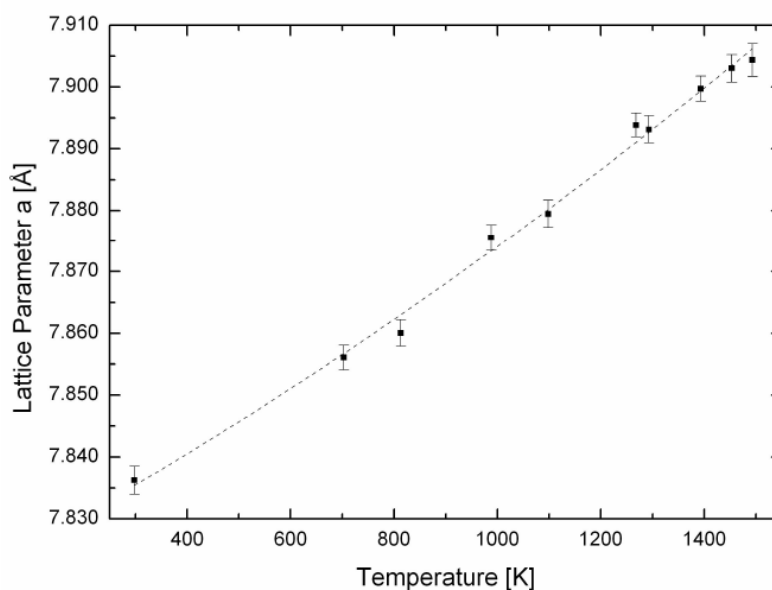


Fig. 3.9-24: The lattice parameter a versus temperature of the β -Sialon $\text{Si}_{3-x}\text{Al}_x\text{O}_x\text{N}_{4-x}$ where $x=1.1$.

The first investigation of the thermal expansion behaviour of spinel-sialons has been carried out using a sample with $x = 1.1$. The X-ray diffraction measurements were performed using a halogen mirror furnace at the B2 line of the Hasylab synchrotron radiation source. As shown in Figure 3.9-24 no evidence for either a phase transformation or decomposition of the spinel-sialon was observed up to 1500 K, thus demonstrating relatively high-temperature metastability of this novel hard material.

r. Mixing and reactivity across the semiconducting to metal transition in group IV alloys (C. Guillaume, G. Serghiou, J.P. Morniroli and A. Thomson/Edinburgh; D.J. Frost)

The formation of new alloys comprised of group IV elements (C-Si-Ge-Sn) may be important in the development of useful semiconductor materials. Here we have investigated the Ge-Sn system, for which there is no solubility regime at ambient pressure. In the first set of experiments up to 24 GPa and 1700 K, equimolar Ge-Sn starting compositions were quenched from the melt. Below 9 GPa, pure germanium is recovered together with pure tin (up to 3.5 GPa), or together with mixture of germanium-rich and tin-rich regions (Fig. 3.9-25). Above 9 GPa only a mixture of these regions is recovered, as depicted in the right section of Fig. 3.9-26. Electron diffraction measurements from some crystallites recovered from higher pressure, whose EDX signals reveal both elements, exhibit patterns that could not be indexed with any of the known endmember phases. The small size and extremely intimate mixture of the recovered crystallites made further assessment of the structure and phase relations in the Ge-Sn system difficult.

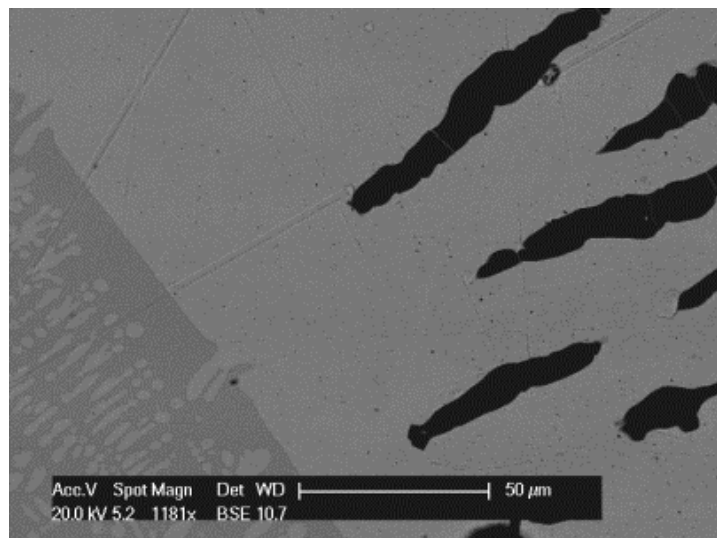


Fig. 3.9-25: Scanning Electron Microscopy image in backscattering mode of a recovered sample after heating an equimolar mixture of Ge and Sn at 8 GPa and 1500 K for 5 minutes and then annealing at about 820 K for one hour. The sharp line demarcates the melt quenched structure from that annealed in the solid state. To the right of the sharp line, the dark regions are pure Ge and the bright regions are pure Sn. To the left of the sharp line, the darker regions contain Ge and Sn and the brighter regions are pure Sn.

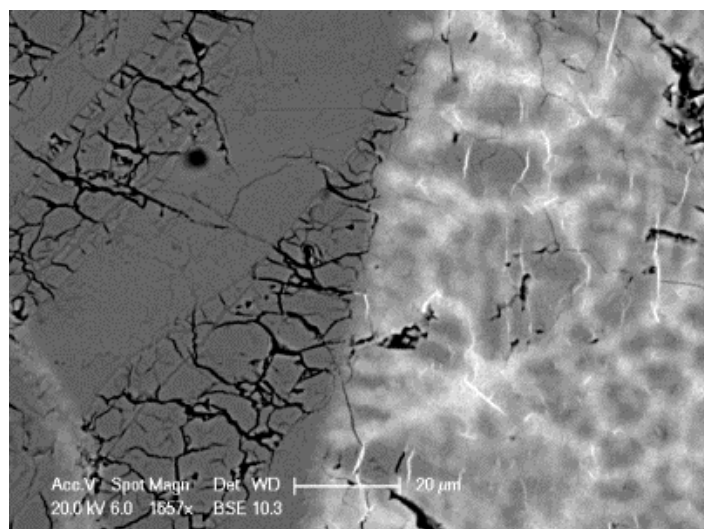


Fig. 3.9-26: Scanning Electron Microscopy image in backscattering mode of a recovered sample after heating an equimolar mixture of Ge and Sn at 10 GPa and 1500 K for 5 minutes and then annealing at about 770 K for one hour. The sharp line demarcates the melt quenched structure from that annealed in the solid state. To the left of the sharp line, the entire dark region contains Ge and Sn. To the right of the line, the dark and bright regions both contain Ge and Sn, with the dark regions containing a greater Ge proportion than in the bright regions.

We are performing a series of annealing and compositional variation experiments to enhance crystal growth, promote separation or reactivity and minimize pinning effects. We are finding a significant difference in the mixing behaviour of Ge with Sn below and above the germanium semiconductor to metal transition ($P \sim 9$ GPa). At 8 GPa, after annealing at about 820 K the system segregates completely into the endmembers (Fig. 3.9-25). The sharp boundary demarcates the quenched melt structure from that annealed in the solid state. A detailed examination of the recovered product reveals that the pure elements have crystallized as two distinct phases. Above 9 GPa after annealing at about 770 K at 10 GPa a single large, apparently homogeneous region containing both Ge and Sn is recovered (Fig. 3.9-26). TEM measurements are underway to investigate this region. Here also, the sharp boundary apparently demarcates the quenched melt structure from that annealed in the solid state, and reveals the significant influence of annealing. These experiments indicate that mixing and reactivity of Ge with Sn is promoted above the semiconductor to metal transition.

Concurrent with our annealing experiments we are employing lower Sn to Ge starting ratios to examine whether larger homogeneous regions can be recovered by reducing pinning effects by having surplus Sn. This may be the case based on an experiment at 24 GPa. There, unlike previous experiments with equimolar starting stoichiometries which gave rise to products as in the right section of Fig. 3.9-26, only a large single region is recovered.

3.10 Methodological Developments

The development of new experimental and analytical techniques is a fundamental prerequisite to compete at a high scientific level and play a leading role in a scientific discipline. This is particularly important for the Bayerisches Geoinstitut, which serves, in part, as a “European Research Infrastructure”. Methodological developments are a time-consuming challenge and require high technical and financial support, both of which are provided at the Bayerisches Geoinstitut. In the past year, we have developed, tested, and improved various methods that fall into two categories: (1) *in situ* techniques for sample characterization at high pressure and high temperature, and (2) *ex situ* techniques for sample characterization at ambient conditions.

An important step towards the understanding of redox conditions in the Earth's mantle has been made by applying the micro-XANES method of $\text{Fe}^{3+}/\Sigma\text{Fe}$ determinations to *in situ* conditions in the diamond anvil cell (DAC) and to calculate the effect of pressure on such measurements. Similarly, the use of ruby fluorescence allows Gigahertz ultrasonic interferometry to be conducted in the DAC with a rigorous control on pressure. The capabilities of our high-brilliance X-ray system have been extended by adding a rotational stage, which is necessary to obtain high-quality diffraction patterns from “poor powders” such as those represented by ice or clathrate samples in the DAC. Further, a method for simultaneous X-ray diffraction and electrical resistivity measurements has been developed. *In situ* Raman spectroscopy is now also applied in laser-heated diamond anvil cell experiments to study phase equilibria and melting at high pressures.

A novel technique has been developed in the multianvil laboratory to synthesize large-volume perovskite samples for equation-of-state measurements through shock-wave experiments. This technique, which uses the 5000 tonne multianvil system, has resulted in the synthesis of what are likely the largest MgSiO_3 perovskite samples ever made. In the field of Mössbauer spectroscopy, progress has been made by developing a goniometer stage for analysis of single-crystals at constant absorber thickness. This setup allows fundamental properties like the electric field gradient and the recoil-free fraction anisotropy to be studied, knowledge of which is required for the correct deconvolution of heavily overlapping Mössbauer spectra. We also present a new technique to produce extremely thin, contamination-free TEM foils for high-resolution TEM and EELS applications. Finally, a natural, crystallographically-homogeneous hemo-ilmenite sample was identified and prepared in a specific orientation to test the theory of lamellar magnetism.

a. *Ferric iron determination at high pressures using micro-XANES analysis (I.Yu. Kantor, L.S. Dubrovinsky and C.A. McCammon)*

Iron is one of the most abundant elements in the Earth, existing either in the Fe^0 , Fe^{2+} or Fe^{3+} state. In many cases, the ratio of ferric to ferrous iron in a mineral is indicative of the redox

conditions during its formation or re-equilibration as a solid. The $\text{Fe}^{3+}/\Sigma\text{Fe}$ -ratio is therefore mostly defined by oxygen fugacity, but effects of crystal chemistry always need to be taken into account as well. Determination of the valence (oxidation) state of iron in solids at elevated pressures and temperatures is of great interest for mineralogy, petrology, geochemistry and solid-state physics.

The most precise technique for ferric iron ratio determination is wet chemical analysis. Unfortunately, this technique works only for samples weighing more than about one milligram. Conventional and synchrotron Mössbauer spectroscopy are two other relatively accurate methods (with an accuracy of $\sim 1\text{-}3\%$), but also these techniques require relatively large samples (*e.g.*, analysis of individual grains in a thin section is impossible). In contrast to these techniques, absorption edge methods EELS and XANES (X-ray absorption near edge structure – spectroscopy) can easily be applied at the micrometer scale. In many high-pressure experimental studies, *in situ* determination of the $\text{Fe}^{3+}/\Sigma\text{Fe}$ ratio at this resolution is desirable.

Application of micro-XANES for high-pressure $\text{Fe}^{3+}/\Sigma\text{Fe}$ ratio determination requires knowledge of potential pressure effects. The goal of this study was to find out whether such pressure-effects exist and, if so, to derive appropriate corrections. For this purpose, four oxide samples with contrasting Fe^{3+} contents (Fe_2O_3 – hematite; Fe_3O_4 – magnetite; FeO – wüstite; $(\text{Mg},\text{Fe})\text{O}$ – ferropicrinite) were synthesized from ^{57}Fe -enriched (70-90 % ^{57}Fe) starting material and studied *in situ* at pressures up to ~ 100 GPa in the diamond anvil cell (DAC) by both micro-XANES and Mössbauer spectroscopy. Results of the latter technique demonstrate that within analytical uncertainty, $\text{Fe}^{3+}/\Sigma\text{Fe}$ ratios remain constant over this pressure interval.

XANES measurements were carried out on the dispersive XAS beamline ID24 at the ESRF. The size of the beam on the sample was approximately $10\ \mu\text{m} \times 10\ \mu\text{m}$ FWHM. The results show that pressure strongly affects the energy position of XANES spectra. We used two features of XANES spectra as indicators of the $\text{Fe}^{3+}/\Sigma\text{Fe}$ ratio: (1) the energy position at which the absorption reaches a value of 1 (E_1 ; Fig. 3.10-1), and (2) the position of the first derivative maximum (E_{der} ; Fig. 3.10-2).

Linear regression of the experimental data results in the following relations for ferric iron ratio determination by micro-XANES:

$$\frac{\text{Fe}^{3+}}{\Sigma\text{Fe}} = \frac{(E_1(\text{eV}) - 7122.448(5) - 0.0531(5) \times P(\text{GPa}))}{4.9835(9)}$$

and

$$\frac{\text{Fe}^{3+}}{\Sigma\text{Fe}} = \frac{(E_{der}(\text{eV}) - 7118.773(6) - 0.021(4) \times P(\text{GPa}))}{3.9617(4)}$$

The accuracy of these equations is within a few percent for octahedrally-coordinated Fe oxides, but their validity for other Fe-compounds (e.g., Fe-silicates) still needs to be confirmed.

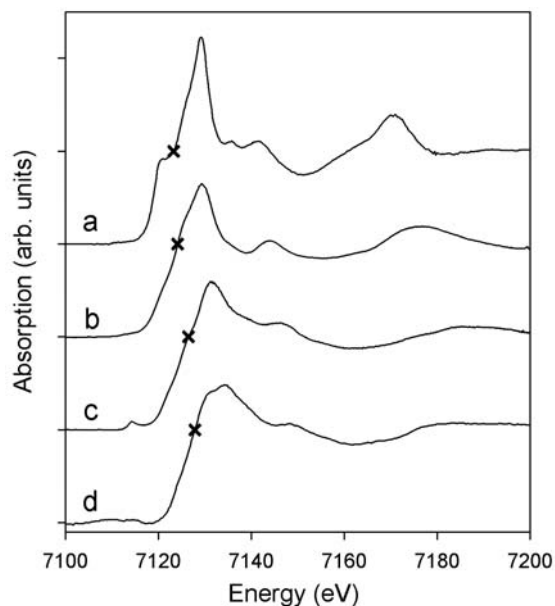


Fig. 3.10-1: XANES spectra of ferropericlase (a), wüstite (b), magnetite (c), and hematite (d) at 13 GPa. Crosses show the E_1 position.

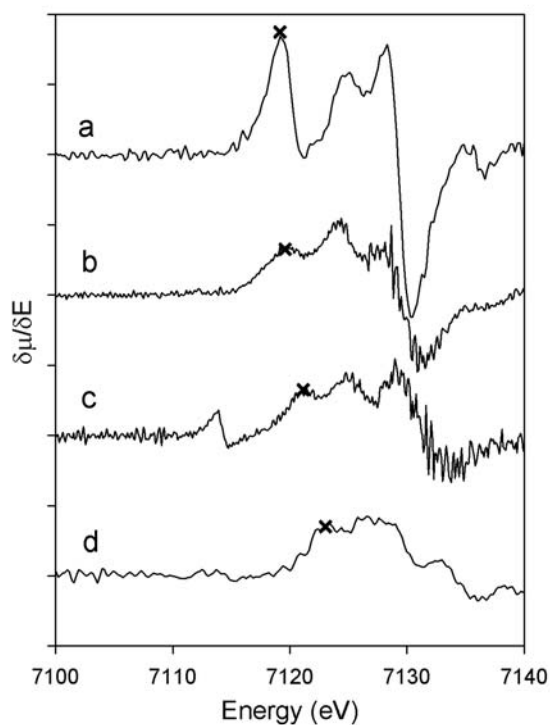


Fig. 3.10-2: First derivatives of ferropericlase (a), wüstite (b), magnetite (c), and hematite (d) XANES spectra at 13 GPa. Crosses show the E_{der} position.

b. *New experimental setup for high-pressure/high-temperature gigahertz ultrasonic interferometry (A.P. Kantor, I.Yu. Kantor and L.S. Dubrovinsky, in collaboration with S.D. Jacobsen/Washington DC and H.-J. Reichmann/Potsdam)*

The only direct information about the Earth's interior comes from seismological observations of sound wave velocities. In order to create compositional and mineralogical models from seismological data, knowledge of the elastic properties and crystal chemistry of minerals is necessary. Gigahertz ultrasonic interferometry (GUI) is a relatively new tool that is used to measure single-crystal compressional- and shear-wave travel times, which are converted to sound velocities and elastic moduli for direct application to problems in geophysics.

Although the feasibility of simultaneous high-pressure and high-temperature GUI measurements in diamond anvil cells has been demonstrated by earlier studies at temperatures up to 250°C, *in situ* measurements of pressure have not been performed so far. It is necessary to do this simultaneously because usually pressure in the diamond anvil cell changes with temperature. We developed a new experimental setup for simultaneous GUI measurements and pressure determination using a ruby fluorescence scale.

A diamond anvil cell (DAC) was equipped with a miniature internal resistive heater (Fig. 3.10-3) with a thermocouple fixed at a very small distance from the sample chamber. The temperature of the cell was controlled by an automated power supply system with a fluctuation of 1 to 3 K within a temperature interval of 25 - 700 °C. The DAC was mounted on a rotating stage with 5 degrees of freedom (XYZ and two degrees of tilting) that was used in three different settings: on top of a P-buffer rod for compressional wave velocity measurements, on top of a S-buffer rod for shear wave velocity measurements, and under the microscope equipped with a laser and a portable high-resolution spectrometer for ruby fluorescence measurements (Fig. 3.10-4). After heating the sample, the DAC could easily be moved between these three positions, allowing sequential measurements of pressure, S- and P-wave velocities at a given temperature.

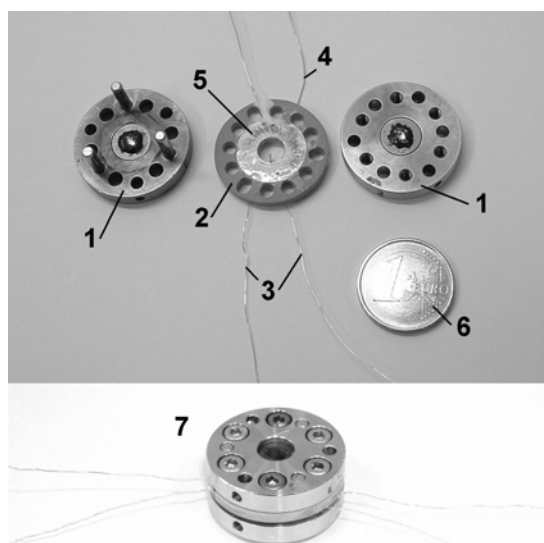


Fig. 3.10-3: Heating assembly for high-pressure/high-temperature GHz experiments: 1 – diamond anvil cell; 2 – pyrophyllite heater; 3 – thermocouple wires; 4 – platinum heater wires; 5 – mica for electrical isolation; 6 – one Euro coin for scale; 7 – entire assembly.

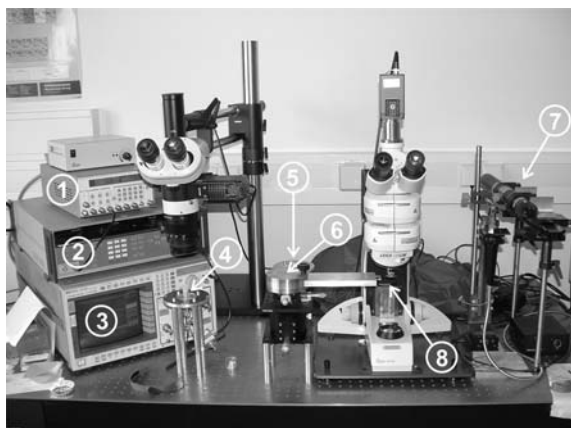


Fig. 3.10-4: Equipment for high-pressure/high-temperature GHz experiments: 1 – pulse generator; 2 – RF signal generator; 3 – sampling oscilloscope; 4 – stage for P-buffer rod; 5 – stage for S-buffer rod; 6 – rotating stage; 7 – laser for pressure calibration; 8 – DAC.

c. High-brilliance X-ray system for *in situ* high-pressure studies: New developments (A.Yu. Kuznetsov, A.V. Kurnosov and L.S. Dubrovinsky)

A high-brilliance X-ray system installed at BGI has been successfully used for various *in situ* high-pressure/high-temperature X-ray diffraction studies as well as for conventional measurements at ambient conditions. In this report, we present some new developments that provide additional possibilities for high-pressure studies.

One development was made towards an improvement of the quality of powder diffraction (powder average) from “poor powders”. One of the main requirements for a successful structural study by means of the X-ray powder diffraction technique is the availability of a sufficient number of randomly oriented crystallites. This requirement is commonly not fulfilled during high-pressure experiments, especially during *in situ* high-pressure synthesis in the diamond anvil cell (DAC), where small sample sizes and melting/recrystallization processes tend to lead to the formation of only a few crystallites. To improve the quality of diffraction patterns from such samples, we developed a technique that allows the sample to be rotated during X-ray analysis. For this purpose, a motorized “STANDA” rotational stage with a 50.8 mm aperture was installed in the diffractometer as a sample holder. The stage performs a 360°-rotation with any type of DAC of up to 50 mm diameter, in a plane perpendicular to the X-ray beam in a Debye-Scherrer geometry. The advantage of this type of rotation in combination with the omega-angle variation is the possibility to average reflections from all available crystallites in as many orientations as possible.

Typical examples of compounds that form “poor powder” samples during synthesis in the DAC are ice and clathrate hydrates. Figure 3.10-5 shows the Debye-Scherrer diffraction pattern of methane clathrate hydrate synthesized in a DAC at 1.6 GPa. As can be seen from the right-hand part of the figure, the number of crystallites formed during the experiment was far too small to provide a true powder average. Sample rotation significantly improves the quality of the diffraction pattern, allowing phase analysis and Rietveld refinement.

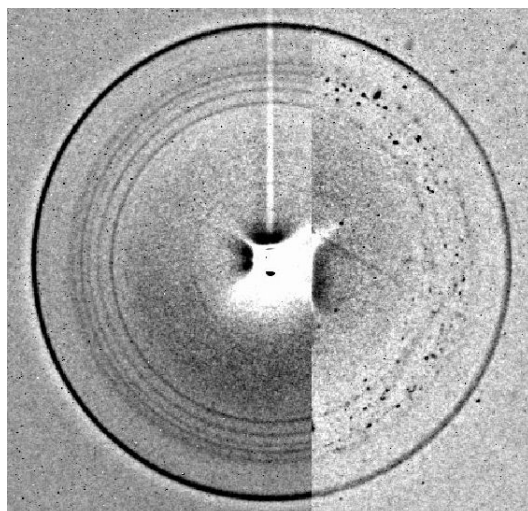


Fig. 3.10-5: Debye-Scherrer diffraction rings of methane clathrate hydrate as recorded on a CCD detector after 30 minutes of exposure. The image obtained from a spinning sample (left) is compared with the image collected from a non-spinning sample (right).

Independently, another method was developed for simultaneous X-ray diffraction and resistance measurements. The experimental setup is adapted for data collection at the BGI X-ray diffractometer system (Fig. 3.10-6). A two-piece rhenium gasket coated by gold is used as a part of the electrical circuit. This allows the use of standard DAC pressure/temperature generation techniques on the one hand, and provides high sensitivities with respect to small variations in sample resistance on the other hand. A linear four-point probe scheme is mounted on the diamond plate or the c-BN seat to ensure that only the sensitivity of the sample is measured. Diamond or corundum powder provides a reliable isolation of the two halves of the gasket at high pressures, while the sample in the gasket hole closes the circuit.

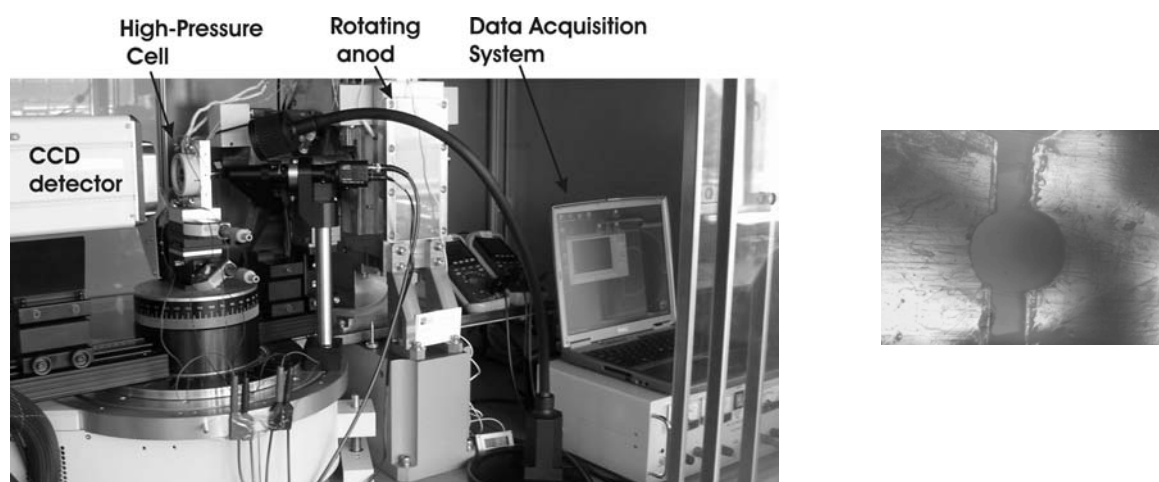


Fig. 3.10-6: Experimental setup for combined X-ray diffraction and resistance measurements in the diamond anvil cell (left). Gasket configuration for resistance measurements (right)

Figure 3.10-7 shows the results of simultaneous high-pressure/high-temperature X-ray diffraction and conductivity measurements on Pr metal. Anomalies in the electrical conductivity of the sample can easily be related to different stages of the *fcc* to *dhcp* phase transition.

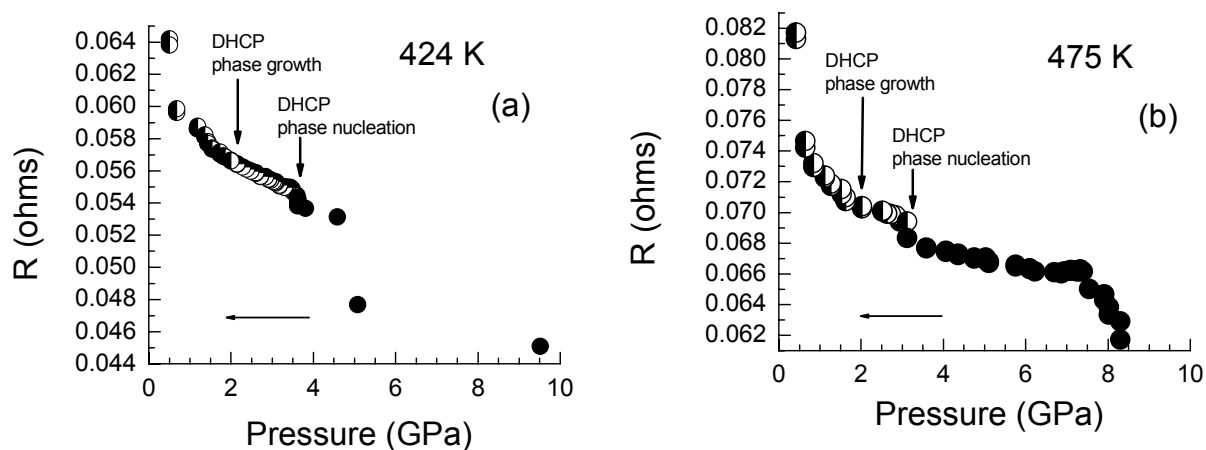


Fig. 3.10-7: Electrical resistance of Pr metal as a function of confining pressure (a) at 424 K and (b) at 475 K. Solid circles: *fcc* phase; Half-filled circles: mixture of *fcc* and *dhcp* phases, as revealed by X-ray diffraction.

d. Raman spectroscopy in laser-heated diamond anvil cells (L.S. Dubrovinsky, A.V. Kurnosov, I.Yu. Kantor and A.Yu. Kuznetsov)

The laser-heated diamond anvil cell (LHDAC) technique is a unique method to reach ultrahigh static pressure and temperature conditions, including those that prevail in deep planetary interiors, up to $P > 100$ GPa and $T > 3000$ K. We have now coupled a Raman spectroscopy system with a Nd:YLF laser heating facility for the DAC (Fig. 3.10-8). As a whole, the system includes a two-stage Dilor XY Raman spectrometer operating with a Ar laser (514 nm and 488 nm), a 50 W CW TEM00 Quantronix Nd:YLF laser, a 3D stage for mounting DACs, and an optical “superhead” connected to the spectrometer through optical fibre lines.

Our system allows us to study a variety of materials and to obtain information about structural and dynamical properties of geophysically important compounds under extreme conditions. Samples that are optically transparent to near-infrared radiation could be heated using a laser absorber (platinum or iridium foils), while a number of materials that are interesting for geochemical and planetary science applications (including oxygen, CO_2 , Fe-bearing silicates, etc.) could be heated directly by NIR laser radiation.

We tested the new facility by studying phase transformations and melting in the $\text{CH}_4\text{-H}_2\text{O-NH}_3$ system (Fig. 3.10-9). Knowledge of the high-pressure behaviour of this system is required in order to model, for example, Titan’s interior. So far only data on the ammonia-

water phase diagram were available and were used to constrain previous models of Titan's interior. We have now demonstrated that water-methane hydrate should be stable in Titan's mantle and that partial decomposition of the hydrate phase could explain the presence of CH₄ in Titan's atmosphere (see section 3.6 e).



Fig. 3.10-8a

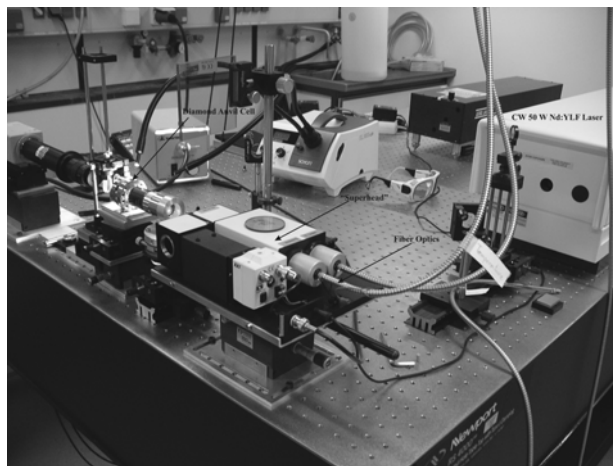


Fig. 3.10-8b

Fig. 3.10-8: General view (a) and enlarged picture (b) of the system for Raman spectroscopy in laser-heated diamond anvil cells. The main component of the system is an optical "superhead" which connects the laser-heating set up and Raman spectrometer through optical fibre lines.

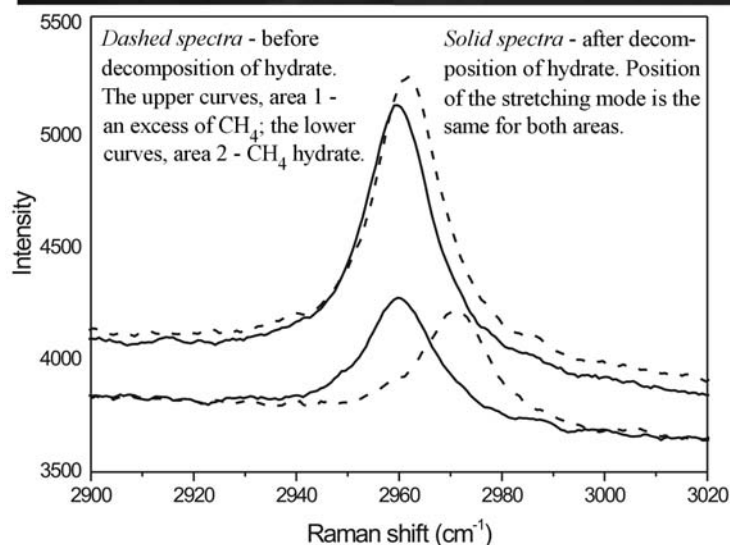
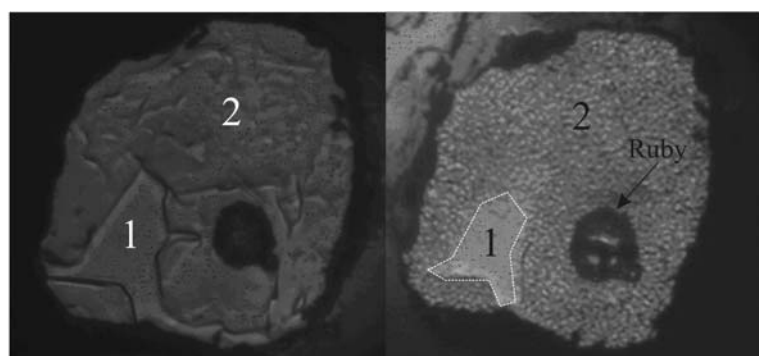


Fig. 3.10-9: Photographs of a sample containing the CH₄-H₂O-NH₃ mixture at 2.7-3.0 GPa and different temperatures before (left) and after (right) decomposition of the methane hydrate phase. The lower panel shows the corresponding Raman spectra collected *in situ*.

e. *Synthesis of large MgSiO₃ perovskite samples for use in shock-wave equation-of-state measurements (J. Mosenfelder/Pasadena, D.J. Frost, D.C. Rubie, P. Asimow/Pasadena and T. Ahrens/Pasadena)*

Improved constraints on the equation-of-state (EoS) of MgSiO₃ perovskite and high-pressure MgSiO₃ melt can facilitate a greater understanding of the dynamics of the lower mantle. Shock-wave experiments provide data at pressures and temperatures unobtainable using laser-heated diamond anvil cells. Such experiments may therefore help to resolve discrepancies in the EoS and melting behaviour of MgSiO₃. Furthermore, thermal parameters such as the Grüneisen parameter can be determined by comparison of the Hugoniot of low-pressure phases and their previously-synthesized high-pressure equivalents, which are shocked to lower temperatures at equivalent pressure. The use of high-pressure phases as starting materials also resolves possible ambiguity as to the phase state achieved along the Hugoniot. However, in order to avoid edge effects and achieve sufficient accuracy using the currently installed streak camera diagnostic system at Caltech, samples with dimensions of ~ 1 mm in thickness and ~ 3 mm in diameter are required. This presents a challenge for synthesis using the multianvil apparatus.

We synthesized five such samples of MgSiO₃ perovskite using a specially modified 18/8 assembly in the 5000-tonne press. The starting material for the experiments was enstatite crystallized from a glass at 1 atm. Hot-pressing experiments were run at ~ 23 GPa and 1800 °C. The recovered samples are cylindrical, polycrystalline disks with final dimensions of ~ 2.7 mm diameter and 2 mm in length. The presence of the perovskite phase in all samples (\pm majorite) was confirmed using Raman spectroscopy. The density of one sample, measured by Archimedes' method, is 3.98 ± 0.02 g/cm³, which is 3 % lower than the theoretical value of 4.103 g/cm³. This discrepancy is most likely due to the presence of majorite. Other samples need to be more fully evaluated.

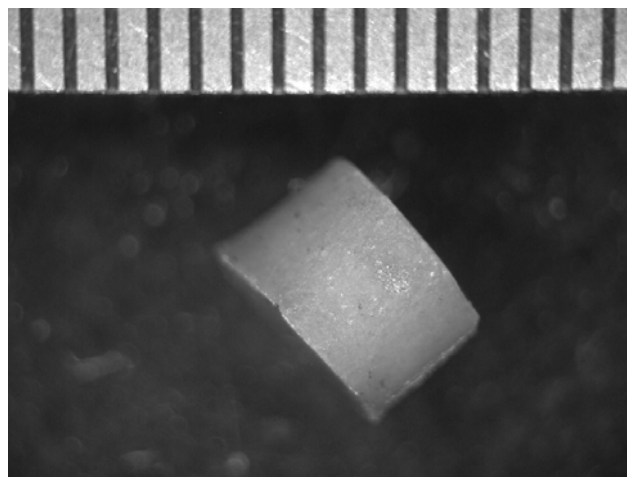


Fig. 3.10-10: Largest MgSiO₃-perovskite sample on the surface of the Earth? Specimen recovered from ~ 23 GPa and 1800 °C. The scale bar is 0.5 mm per tick.

These may be the largest volume MgSiO₃ perovskite samples ever produced. Shock-wave EoS experiments will be conducted using the 25-mm two-stage light gas gun at Caltech. This apparatus is capable of impacting targets at velocities up to 7.5 km/s, which should enable pressures up to ~ 250 GPa to be obtained in the samples.

f. Development of a goniometer stage for single crystal Mössbauer measurements (C. Tennant, C.A. McCammon and F. Nestola, in collaboration with H. Spiering/Mainz)

Mössbauer spectroscopy is traditionally performed on absorbers with diameters of approximately one cm, but a simple modification of the spectrometer combined with the use of a high specific activity source (“point source”) can reduce the diameter by nearly two orders of magnitude without significant loss of signal quality. This dramatic improvement in spatial resolution allows detailed studies of single crystals, where crystallographic orientation information can be combined with hyperfine data to extract fundamental parameters such as the orientation of the electric field gradient tensor and recoil-free fraction anisotropy. Both of these parameters have significant effects on the relative areas of quadrupole doublet components; hence their knowledge is critical to the deconvolution of heavily overlapped spectral components in Mössbauer spectra.

We developed a stage for single crystal measurements to satisfy several criteria: (1) the ability to reproducibly position the crystal within $\pm 1^\circ$ over a large range of different orientations with respect to the direction of the gamma ray beam; and (2) an absorber thickness that remains constant regardless of orientation. To achieve these goals, we designed a stage containing a one-circle goniometer oriented at 45° to the gamma-ray beam (Fig. 3.10-11). The crystal is affixed behind a hole of appropriate diameter in Ta foil that is mounted on the goniometer. The stage is positioned such that the point source is approximately 2 mm distant from the crystal, which ensures a reasonable solid angle of radiation. By rotating the goniometer the gamma beam traces out a cone in the crystal, producing a large set of orientations which considerably over-determine the extraction of Mössbauer hyperfine parameters.

In order to test the apparatus we are measuring the recoil-free fraction anisotropy in a crystal of near end-member almandine garnet. Preliminary calculations based on the X-ray determined mean-squared displacements indicated that rotating a crystal about the axis [101] on the 45° stage should produce a measurable variation in component relative areas from which the recoil-free fraction anisotropy could be determined. X-ray methods were used to orient the crystal, which was then prepared as a doubly polished slice with the [101] direction in the plane of the slab. Spectra are being collected in 20° intervals around the 360° rotation of the stage, and so far suggest an angular dependence of area ratios that is consistent with an anisotropic recoil-free fraction. The final analysis of the data will be carried out by

simultaneous fitting of all spectra, including a numerical treatment of thickness and polarisation and a correction for background.

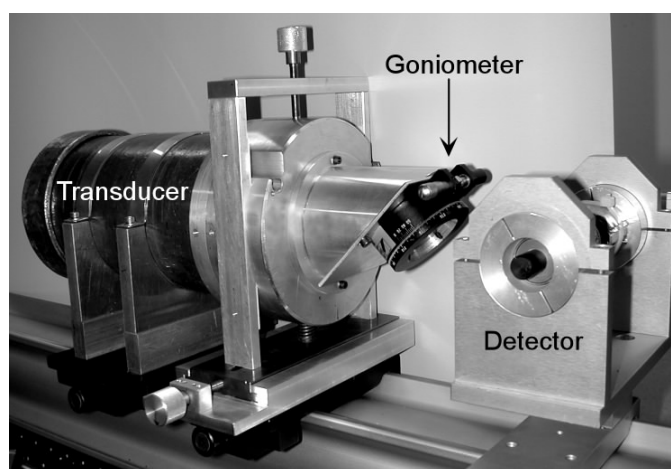


Fig. 3.10-11: (a) Photograph of the single-crystal stage mounted on the Mössbauer spectrometer. The source is attached to a rod (not visible) and is situated approximately 2 mm away from the crystal, which is mounted at the centre of the one-circle goniometer.

g. *A preparation method for TEM specimens using combined techniques of Focused Ion Beam milling and conventional Ar-milling (N. Miyajima, Y. Asahara, L.S. Dubrovinsky, D.J. Frost and D.C. Rubie, in collaboration with C. Holzapfel/Saarbrücken)*

Focused Ion Beam (FIB) milling has recently evolved into one of the most effective techniques for preparing specimens for the transmission electron microscope (TEM). The technique offers new capabilities beyond those available when using conventional Ar ion milling. The advantages include site-specificity at the sub-micrometer scale and homogeneous thinning of samples consisting of multi-layers of different phases or containing two-phase interfaces. However, several difficulties still remain for applications of High Resolution TEM (HRTEM) and Electron Energy Loss Spectroscopy (EELS): (1) surface contamination and damage caused by the Ga^+ beam; (2) sample thinning to less than 100 nm thickness. In order to overcome these problems, we have combined the application of both FIB milling and conventional Ar-milling for the preparation of TEM specimens from high-pressure samples.

The specimen examined in this report consists of quenched molten iron coexisting with magnesiowüstite, and was synthesized in a laser heated diamond anvil cell (DAC) experiment. The recovered sample was mechanically polished and milled to leave a foil of about 1 μm thickness through the region of interest using a FIB milling system equipped a micromanipulator at Universität des Saarlandes. As shown in Fig. 3.10-12, removing the foil from the host sample and gluing it onto the Cu grid are performed *in situ* under vacuum using a tungsten needle driven by the micromanipulator. Following the FIB milling, conventional Ar-milling was used at 3 kV to reduce the thickness to 40 nm for EELS qualitative analysis.

Transmission electron microscopy of the foil was performed with a *Philips CM20FEG* TEM operating at 200 kV. The relative thickness of the foil was estimated from the ratio of zero-loss and low-loss intensities in EELS spectra acquired with a *Gatan 666 PEELS* system, assuming that the inelastic mean free path in iron is 115 nm.

The foil prepared by the FIB technique was transparent to the electron beam. The thickness was fairly uniform over the whole area containing metallic iron and magnesiowüstite (Fig. 3.10-13a). However, the thickness of about 130 nm is too thick for quantitative EELS analysis. In the process of Ar re-thinning, the thickness of the edge decreased gradually from 130 nm to 40 nm (Fig. 3.10-13b and 3.10-13c), which is thin enough to obtain a good signal to noise ratio in the core-loss region of *O-K* edge and *Fe-L* edge spectra. As revealed by energy dispersive X-ray spectroscopy, Ga impregnation into the surface was also significantly removed during this process. The combination of focused ion beam milling with conventional Ar-milling is important for HRTEM applications and EELS qualitative analysis of oxygen in molten iron, for which very thin and clean TEM foils are needed.

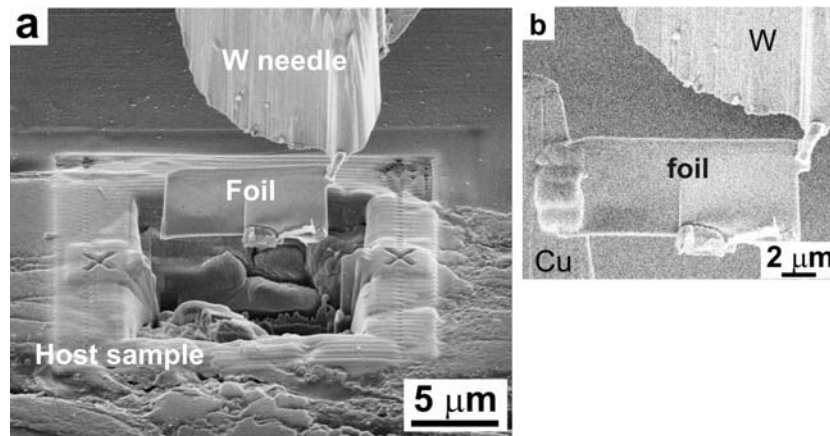


Fig. 3.10-12: SEM micrographs of the TEM specimen at different stages of extraction and deposition using a Focused Ion Beam (FIB) milling system. (a) Extraction of a site-specific foil from the host sample using a Tungsten needle (upper middle), (b) Chemical deposition of the foil onto a bar of Cu grid (left).

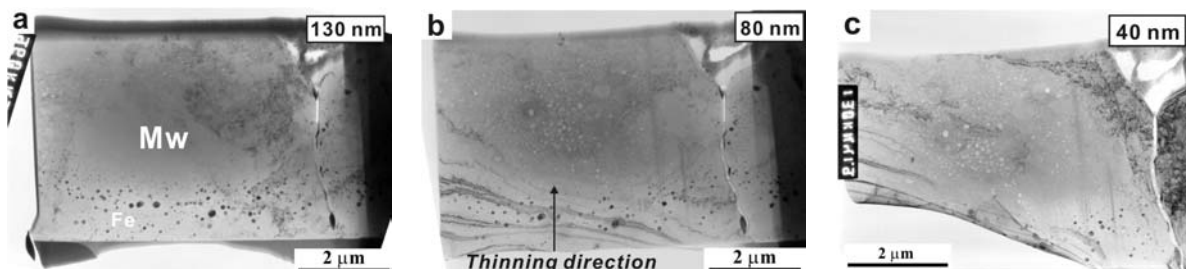


Fig. 3.10-13: TEM micrographs of molten iron (black particles) coexisting with magnesiowüstite (matrix), indicating variations of the thickness of a TEM foil in the Ar-thinning process after the FIB milling. The figures in the upper right are the sample thickness of the eroded edge, assuming that the inelastic mean free path in iron is 115 nm.

h. Preparation of a natural hemo-ilmenite sample for magnetic experiments using a combination of crystallographic, magnetic and polishing techniques (S.A. McEnroe and P. Robinson/Trondheim, A. Hirt/Zurich and F. Heidelberg)

The lamellar magnetism hypothesis postulates that uncompensated electron spins associated with the interfaces between antiferromagnetic hematite exsolution lamellae and paramagnetic ilmenite hosts (and vice-versa) create a new kind of ferri-magnetism. This magnetism would be strongest in regions with a high density of interfaces associated with the finest and lowest temperature exsolution lamellae. TEM images show that such fine exsolution microstructures, with lamellae as thin as 1-2 nm, are particularly well developed close to the interfaces between coarse, high-temperature lamellae and their hosts. The lamellar magnetism hypothesis was developed to explain the strong and very stable remanent magnetization determined in bulk rhombohedral oxides with such exsolution features, but to date there have been only few experiments on natural samples capable of determining the spatial distribution and orientation of magnetization. As a result of discussions with colleagues at the National Institute of Standards in Washington, such determinations are planned, making use of a specially prepared scanning electron microscope and the property of spin polarization of secondary electrons. This technique is reported to have a spatial resolution of 10 nm. The discussion here concerns the advanced work completed in 2005 that produced a “single-crystal” sample with an oriented polished surface considered ideal for these experiments.

The sample chosen is from a drill core in the famous Lac Tio massive ilmenite ore body near Allard Lake, Quebec. It was provided by the late R. B. Hargraves, who characterized it first as part of his 1959 Ph.D. thesis. The polycrystalline sample has hematite exsolution lamellae up to 40 μm thick in an ilmenite host, with many generations of smaller exsolution lamellae, both in the ilmenite and in the hematite. The very low magnetic susceptibility and high natural remanent magnetization (NRM) demonstrates the absence of magnetite, unlike many other hemo-ilmenite samples from the same district and elsewhere.

The first problem was to identify small volumes within the polycrystalline sample that could be considered as single crystals. To do this, a slice of the drill core about 1 cm thick was cut and specially polished on the front and back faces. The slice was then subjected to electron backscatter diffraction (EBSD) with a scanning electron microscope at Bayreuth, which permits exact determination of the crystallographic orientation on the polished faces. From this work, five areas were selected as most promising for having similar orientations on both the front and back faces of the polished slice. From each of these areas a small diamond drill core was taken for further magnetic work, though only two of these areas contained orientation values sufficiently close to be considered seriously. Before drilling, the front polished face of the slice was scratched with parallel lines so that the EBSD crystallographic relationships would be known for each small core.

Following EBSD identification and separation of oriented cores, the NRM direction of each was measured with the cryogenic magnetometer at Zurich. It needs to be remembered that the NRM is a measurement averaged over the entire bulk of the small core; whereas the EBSD

only measured orientation on the front and back faces. Fortunately the NRM orientations of several samples lay close to the average (0001) basal plane of the hemo-ilmenite, as expected for a rhombohedral oxide, and was particularly good for Crystal #19. Furthermore, the NRM vector proved to be reasonably close to a crystallographic a axis as determined by EBSD, a property that has now been observed in a number of other oriented single crystals.

At Zurich the same crystals were also subjected to low-field determinations of the anisotropy of magnetic susceptibility (AMS), also a bulk sample property. As expected for a rhombohedral oxide, the direction of minimum magnetic susceptibility, k3, proved to lie quasi-parallel to the crystallographic c-axes; whereas the intermediate and strong axes of susceptibility, k2 and k1, proved to lie close to the average (0001) basal plane. In addition, especially for Crystal #19, the k2 axis proved to be quasi-parallel to the NRM. This is a property we have observed in a number of lamellar magnetic materials, with its significance still being investigated.

The results of EBSD, NRM and AMS measurements for Crystal #19 were compiled, and from this a special cut and new polished surface orientation was decided. This surface includes the NRM vector and the k3 axis of the AMS. It exactly bisects the angle between the crystallographic c-axes and is normal to the average (0001) basal plane that is the dominant contact plane of (0001) exsolution lamellae. In addition, the k2 axis of the AMS lies 3 degrees away from this plane, and the crystallographic a2 axis determined by the EBSD of the front face of the core lies 13 degrees from the polished surface.

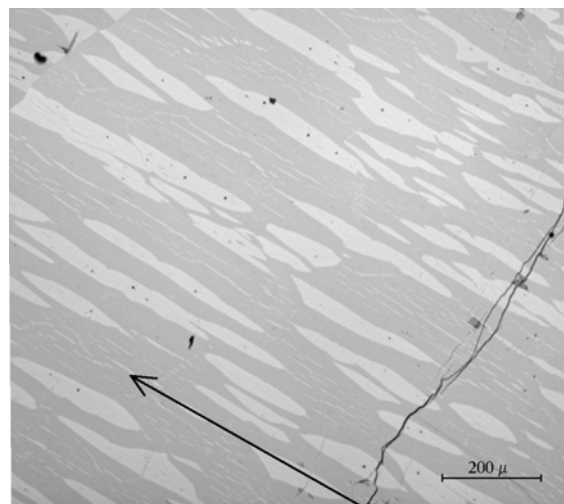


Fig. 3.10-14: BSE image of oriented polished surface of hemoilmenite; the arrow indicates the direction of the magnetic vector.

The core of crystal #19 was cut and polished at Bayreuth along the selected oriented surface. It is shown in the electron backscatter image of Fig. 3.10-14, which includes part of the new polished surface closest to the original front face of the small core. The large bright lamellae

are of hematite with higher mean atomic number, in a host of darker ilmenite with lower mean atomic number. Both the hematite and the ilmenite contain abundant finer exsolution lamellae. Because of the EBSD crystallographic work, we know that the predominant lamellar interfaces on (0001) are here being viewed edge on, and that the crystallographic c axis is in the plane of the section and normal to the interfaces. From the NRM measurements, we know that the mean NRM direction lies along the polished section, with the magnetic vector in the direction of the arrow. Thus, through a unique combination of crystallographic, magnetic, and technical expertise, we now have a sample surface that appears completely ready for a detailed study of the spatial distribution and orientation of remanent magnetic vectors relative to exsolution interfaces down to a resolution of 10 nm, using spin polarization of secondary electrons.

4. International Graduate School "Structure, Reactivity and Properties of Oxide Materials"

The interdisciplinary Graduate School is funded by the State of Bavaria for an initial period of four years (2005-2008). This program encompasses three cooperating institutes: Bayerisches Geoinstitut (BGI), Institute of Inorganic Chemistry I (LAC), both in Bayreuth, and the Fraunhofer Institute for Silicate Research (ISC) in Würzburg. These institutes provide their research facilities, complementary expertise in basic and applied material research, and commitment to capitalize on synergies as well as international contacts to other leading research institutes all over the world.

The theme of the program "Structure, Reactivity and Properties of Oxide Materials" reflects the importance of oxides in nature and in many industrial applications. They exist in a wide variety of chemical compositions, crystal structures, synthesis paths and resulting properties. The study of oxides is providing both an intellectual challenge as well as being a practical necessity, and consequently provides an outstanding basis for the training of young students in the sciences. In this Graduate School educational training and research focus on the interactions between stability, crystal structure, texture, reaction kinetics and physical-chemical properties. For research unconventional synthesis methods under extreme pressures and temperatures and by *chemie douce* are combined with state-of-the-art analytical methods such as spectroscopic, diffraction or microbeam techniques or supplemented with computer simulations ranging from the atomic to the macroscopic scale.

The Graduate School is chaired by Prof. David Rubie, Ph.D. (BGI). It includes seven other faculty members and one coordinator. Enrollment in 2005 was 8 doctoral students on a full-time basis at all 3 institutes (BGI, LAC, ISC) and, in addition, 7 doctoral students have associate status in the school which provides them with full access to all educational activities. Research projects include element partitioning between silicate materials and core-forming alloys at high pressures, thermodynamics of mantle phases, hydroxyl defects in minerals, synthesis of new layer silicates and mesoporous oxide substances as well as experimental and computer simulations of liquid-phase sintering.

In 2005, the following doctoral students were enrolled in the Graduate School and based at the Bayerisches Geoinstitut:

Eva Holbig
since 01.01.2005



TiO₂-ZrO₂ solid solution at high pressure
(for project description see section 3.9l and 3.9m)

Supervisors:

L. Dubrovinsky, G. Steinle-Neumann (BGI)
G. Müller (ISC)

Ute Mann
since 15.10.2004



Phase relations and element partitioning in the system Fe-S-O-Si (for project description see section 3.2f)

Supervisors:

D. Rubie, H. Keppler (BGI)
J. Breu (LAC)

Ashima Saikia
since 01.10.2004



Thermodynamic properties of garnet and silicate perovskite solid solutions at high pressure and temperature

(for project description see section 3.1c)

Supervisors: D. Rubie (BGI), F. Langenhorst (Jena),
J. Breu (LAC) in cooperation with
D. Frost (BGI)

Two new students have been accepted to the program during 2005:

Polina Gavrilenko
since 01.05.2005



Hydroxyl point defects in clinopyroxenes

Supervisors: H. Keppler, D. Rubie (BGI)
J. Breu (LAC)

Anastasia Kantor
since 15.07.2005



Gigahertz ultrasonic interferometry in the diamond anvil cell: Thermoelastic parameters of mantle minerals (for project description see section 3.3k, 3.10b)

Supervisors: L. Dubrovinsky (BGI)
S. Jacobsen (Carnegie Institution, Geophysical Laboratory, Washington D.C.)

Associate students based at the Bayerisches Geoinstitut are: Innokenty Kantor, Alexander Korschak, Jun Liu, Deborah Schmauß-Schreiner and Emil Stoyanov.

Descriptions of the student projects can be found in Chapter 3 of this report. Students presented their research results in publications and at international conferences such as the annual Fall Meeting of the American Geophysical Union in San Francisco/USA, the General Assembly of the European Geosciences Union in Vienna/Austria, and the Joint AIRAPT – EHPRG International Conference on High Pressure Science and Technology in Karlsruhe/Germany. A list of publications and presentations is given in Chapter 5 of this yearbook.

All students undergo an intensive training program, in addition to their research project, that encompasses lectures, short courses, a research colloquium, a graduate seminar, seminars by invited leading experts and weekend seminars on soft skills such as scientific writing, ethics and team work. Seven invited speakers from overseas and Europe presented new results and novel experimental techniques and methods in a series of lectures during last year. The following weekend seminars were held in 2005:

Presentation and communication skills, 15.04.-17.04.2005, Bronnbach bei Würzburg

This workshop was hosted by the branch of the Fraunhofer Institut für Silicatforschung and focused on techniques of scientific presentations: lecture and poster design and professional speech. The program was complemented by a site visit of the Fraunhofer Institut für Silicatforschung in Würzburg which provided students, postdocs and visitors from BGI and LAC with an opportunity to establish new contacts with various laboratories and units of the ISC.

Excursion to the Ries impact crater, 30.09.-02.10.2005, Nördlingen

This 3-day geological excursion to the Ries impact crater was guided by Prof. F. Langenhorst (University of Jena) and Prof. Jay Melosh (University of Arizona), a leading expert on impacts and numerical modelling of impact processes. The Ries crater in southern Germany is a flat, semi-filled impact basin with a diameter of about 25 km with several unique features such as the presence of melt fragments in local rocks ("suevites"), occurrences of coesite in impact breccias and many other extreme-pressure phenomena. Participants have examined numerous outcrops of impact rocks with shock metamorphic phenomena. They have also visited a cement producing plant (raw material, excavating, processing of the products of the impact – "Ries-Trass"), the Ries Crater Museum and the Ries Research Center in Nördlingen.



Joint workshop of the Oxides and Thesis program, 12.11.-14.11.2005, Thurnau

This initiative aimed at creating contacts between two Elite programs devoted to Earth and material sciences: Oxides (BGI, LAC, ISC) and Thesis (Earth & Environmental Sciences, Ludwig-Maximilian-University of Munich). During this workshop, students and faculty members presented their research results in the form of talks and posters, and participated in one field trip to high-pressure mafic rocks of the Münchberger Gneissmasse and on the history of gold mining in the Goldkronach region. The workshop was financially supported by the Elite Network Division of the Bavarian State Ministry for Research, Science and Arts.

Additional information on the Graduate School "Structure, Reactivity and Properties of Oxide Materials" can be found at <http://www.uni-bayreuth.de/elitenetzwerk/oxides>.

5. Publications, Conference Presentations, Seminars

5.1 Publications (published)

Supplement to **2004** (papers published at the end of 2004):

COUVY, H.; FROST, D.J.; HEIDELBACH, F.; NYILAS, K.; UNGÁR, T.; MACKWELL, S.; CORDIER, P. (2004): Shear deformation experiments of forsterite at 11 GPa – 1400 °C in the multianvil apparatus. *European Journal of Mineralogy* 16, 877-890

2005

a) Refereed international journals

AKBER-KNUTSON, S.; STEINLE-NEUMANN, G.; ASIMOW, P.D. (2005): Effect of Al on the sharpness of the MgSiO₃ perovskite to post-perovskite phase transition. *Geophysical Research Letters* 32, L14303, doi: 10.1029/2005GL023192

ALLWARDT, J.R.; STEBBINS, J.F.; SCHMIDT, B.C.; FROST, D.J.; WITHERS, A.C.; HIRSCHMANN, M.M. (2005): Aluminum coordination and the densification of high-pressure aluminosilicate glasses. *American Mineralogist* 90, 1218-1222

ASAHARA, Y.; OHTANI, E.; KONDO, T.; KUBO, T.; MIYAJIMA, N.; NAGASE, T.; FUJINO, K.; YAGI, T.; KIKEGAWA, T. (2005): Formation of metastable cubic-perovskite in high-pressure phase transformation of Ca(Mg, Fe, Al)Si₂O₆. *American Mineralogist* 90, 456-457

AUDÉTAT, A.; KEPPLER, H. (2005): Solubility of rutile in subduction zone fluids, as determined by experiments in the hydrothermal diamond anvil cell. *Earth and Planetary Science Letters* 232, 393-402

BECHMANN, M.; FOERSTER, H.; MAISEL, H.; SEBALD, A. (2005): Double-quantum filtered 1H MAS NMR spectra. *Solid State Nuclear Magnetic Resonance* 27, 174-179

BECHMANN, M.; SEBALD, A. (2005): MAS NMR with and without double-quantum filtration at and near the $n = 0$ rotational resonance condition. *Journal of Magnetic Resonance* 173, 296-304

BECHMANN, M.; DUSOLD, S.; GEIPEL, F.; SEBALD, A.; SELLMANN, D. (2005): Magnitudes and orientations of 31P chemical shielding tensors in Pt(II)-phosphine complexes and other four-fold coordinated phosphorus sites. *Journal of Physical Chemistry A* 109, No. 24, 5275-5280

BOTCHARNIKOV, R.; KOEPKE, J.; HOLTZ, F.; MCCAMMON, C.A.; WILKE, M. (2005): The effect of water activity on the oxidation and structural state of Fe in a ferro-basaltic melt. *Geochimica et Cosmochimica Acta* 69, 5071-5085

BROMILEY, G.D.; HILAIRET, N. (2005): Hydrogen and minor element incorporation in synthetic rutile. *Mineralogical Magazine* 69(3): 345-358

- CHAKHMOURADIAN, A.R.; MCCAMMON, C.A. (2005): Schorlomite: a discussion of the crystal chemistry, formula, and inter-species boundaries. *Physics and Chemistry of Minerals* 32, 277 - 289
- COMODI, P.; FUMAGALLI, P.; NAZZARENI, S.; ZANAZZI, P.F. (2005): The 10 Å phase: Crystal structure from single-crystal X-ray data. *American Mineralogist* 90, 1012-1016
- CORGNE A.; LIEBSKE, C.; WOOD, B.J.; RUBIE, D.C.; FROST, D.J. (2005): Silicate perovskite-melt partitioning of trace elements and geochemical signature of a deep perovskitic reservoir. *Geochimica et Cosmochimica Acta* 69, 485-496
- DAHL, P.S.; HAMILTON, M.A.; JERCINOVIC, M.J.; TERRY, M.P.; WILLIAMS, M.L.; FREI, R. (2005): Comparative isotopic and chemical geochronometry of monazite, with implications for U-Th-Pb dating by electron microprobe: An example from metamorphic rocks of the eastern Wyoming. *American Mineralogist* 90, 619-638
- DELLA VENTURA, G.; REDHAMMER, G.J.; IEZZI, G.; HAWTHORNE, F.C.; PAPIN, A.; ROBERT, J.-L. (2005): A Mössbauer and FTIR study of synthetic amphiboles along the magnesioriebeckite – ferri-clinoholmquistite join. *Physics and Chemistry of Minerals* 32, 103-113
- DELLA VENTURA, G.; IEZZI, G.; REDHAMMER, G.J.; HAWTHORNE, F.C.; SCAILLET, B.; NOVEMBRE, D. (2005): Synthesis and crystal-chemistry of alkali amphiboles in the system Na₂O-MgO-FeO-Fe₂O₃-SiO₂-H₂O as a function of *f*O₂. *American Mineralogist* 90, 1375-1383
- DEMOUCHY, S.; DELOULE, E.; FROST, D.J.; KEPPLER, H. (2005): Pressure and temperature-dependence of water solubility in Fe-free wadsleyite. *American Mineralogist* 90, 1084-1091
- DOLEJŠ, D.; BAKER, D.R. (2005): Thermodynamic modeling of melts in the system Na₂O-NaAlO₂-SiO₂-F₂O₁. *Geochimica et Cosmochimica Acta* 69, 5537-5556
- DUBROVINSKAIA, N.A.; DUBROVINSKY, L.S. (2005): Internal and external electrical heating in diamond anvil cells. – In: CHEN, J., et al. (Eds.): *Advances in High-Pressure Technology for Geophysical Applications*, Elsevier Publishing, 487-501
- DUBROVINSKAIA, N.A.; DUBROVINSKY, L.S.; CRICHTON, W.; LANGENHORST, F.; RICHTER, A. (2005): Aggregated diamond nanorods, the densest and least compressible form of carbon. *Applied Physics Letters* 87, 083106
- DUBROVINSKAIA, N.A.; DUBROVINSKY, L.S.; LANGENHORST, F.; JACOBSEN, S.D.; LIEBSKE, C. (2005): Nanocrystalline diamond synthesized from C₆₀. *Diamond & Related Materials* 14, 16-22
- DUBROVINSKY, L.S.; DUBROVINSKAIA, N.A.; KANTOR, I.Yu.; MCCAMMON, C.A.; CRICHTON, W.; URUSOV, V. (2005): Decomposition of ferropericlase (Mg_{0.80}Fe_{0.20})O at high pressures and temperatures. *Journal of Alloys and Compounds* 390, 41-45
- DUBROVINSKY, L.S.; DUBROVINSKAIA, N.A.; KUZNETSOV, A.; KANTOR, I.Yu. (2005): Chemistry at extreme conditions: Approaching the Earth's major interface. – In: Chen, J., et al. (Eds.): *Advances in High-Pressure Technology for Geophysical Applications*, Elsevier Publishing, 289-315

- DUBROVINSKY, L.S.; DUBROVINSKAIA, N.A.; GATTA, G.D.; NESTOLA, F. (2005): High-brilliance X-ray system for high-pressure in-house research. Proceedings of the Joint 20th AIRAPT – 43rd EHPRG Conference on Science and Technology of High Pressure, Forschungszentrum Karlsruhe, ISBN 3-723704-49-6
- GAILLARD, F.; IACONO MARZIANO, G. (2005): Electrical conductivity of magma in the course of crystallization controlled by their residual liquid composition. *Journal of Geophysical Research* 110, B06204, doi: 10.1029/2004JB003282
- GATTA, G.D.; BOFFA BALLARAN, T.; IEZZI G. (2005): High-pressure and Raman study of a ferrian magnesian spodumene. *Physics and Chemistry of Minerals* 32, 132-139
- GATTA, G.D.; COMODI, P.; ZANAZZI, P.F.; BOFFA BALLARAN, T. (2005): Anomalous elastic behavior and high-pressure structural evolution of zeolite lewyne. *American Mineralogist* 90, 645-652
- GUIDOTTI, C.V.; SASSI, F.P.; COMODI, P.; ZANAZZI, P.F.; BLENCOE, J.G. (2005): Slaty cleavage: does the crystal chemistry of layer silicates play a role in its development? *Canadian Mineralogist* 43, 311-325
- HACKER, B.R., RUBIE, D.C., KIRBY S.H., BOHLEN, S.R. (2005): The calcite → aragonite transformation in low-Mg marble. *Journal of Geophysical Research* 110, B03205, doi: 10.1029/2004JB003302
- HEIDELBACH, F.; HOLTZMAN, B.; HIER-MAJUMDER, S.; KOHLSTEDT, D.L. (2005): Textures in experimentally deformed olivine aggregates: the effects of added water and melt. – In: van Houtte, P.; Kestens, L. (Eds.): Proceedings of the 14th International Conference on Textures of Materials 1, 63-68
- HOLZAPFEL, C.; RUBIE, D.C.; FROST, D.J.; LANGENHORST, F. (2005): Fe-Mg interdiffusion in (Mg,Fe)SiO₃ perovskite and lower mantle reequilibration. *Science* 309, 1707-1710
- IEZZI, G.; GATTA, G.D.; KOCKELMANN, W.; DELLA VENTURA, G.; RINALDI, R.; SCHÄFER, W.; PICCININI, M.; GAILLARD, F. (2005): Low-*T* neutron powder-diffraction and synchrotron-radiation IR study of synthetic amphibole Na(NaMg)Mg₅Si₈O₂₂(OH)₂. *American Mineralogist* 90, 695-700
- IEZZI, G.; BOFFA BALLARAN, T.; MCCAMMON, C.A.; LANGENHORST, F. (2005): The CaGeO₃-Ca₃Fe₂Ge₃O₁₂ garnet solid solution. *Physics and Chemistry of Minerals* 32, 197-207
- JACOBSEN, S.D.; DEMOUCHEY, S.; FROST, D.J.; BOFFA BALLARAN, T. (2005): A systematic study of OH in hydrous wadsleyite from polarized FTIR spectroscopy and single-crystal X-ray diffraction: Oxygen sites for hydrogen storage in Earth's interior. *American Mineralogist* 90, 61-70
- KANTOR, A.P.; DUBROVINSKY, L.S.; DUBROVINSKAIA, N.A.; KANTOR, I.Yu.; GONCHARENKO, I (2005): Phase transitions in MnO and FeO at low temperatures: A neutron powder diffraction study. *Journal of Alloys and Compounds* 401, 42-45
- KANTOR, I.Yu.; DUBROVINSKY, L.S.; KANTOR, A.P.; URUSOV, V.S.; MCCAMMON, C. (2005): Trigonal distortion of ferropericlasite (Mg_{0.8}Fe_{0.2})O at high pressures. *Doklady Physics* 50, 343-345

- KEPPLER, H.; SMYTH, J.R. (2005): Optical and near infrared spectra of ringwoodite to 21.5 GPa: Implications for radiative heat transport in the mantle. *American Mineralogist* 90, 1209-1212
- KONZETT, J.; YANG, H.X.; FROST, D.J. (2005): Phase relations and stability of magnetoplumbite- and crichtonite-series phases under upper-mantle P-T conditions: an experimental study to 15 GPa with implications for LILE metasomatism in the lithospheric mantle. *Journal of Petrology* 46, 749-781
- LIEBSKE, C.; CORGNE, A.; FROST, D.J.; RUBIE, D.C.; WOOD, B.J. (2005): Compositional effects on element partitioning between Mg-silicate perovskite and silicate melts. *Contributions to Mineralogy and Petrology* 149, 113-128
- LIEBSKE, C. SCHMICKLER, B., TERASAKI, H., POE, B.T., SUZUKI, A., FUNAKOSHI, K., ANDO, R., RUBIE, D.C. (2005): Viscosity of peridotite liquid up to 13 GPa: Implications for magma ocean viscosities. *Earth and Planetary Science Letters* 240, 589-604
- LUNDEGAARD, L.F.; MAKOVICKY, E.; BOFFA BALLARAN, T.; BALIC-ZUNIC, T. (2005): Crystal structure and cation lone electron pair activity of Bi_2S_3 between 0 and 10 GPa. *Physics and Chemistry of Minerals* 32, 578-584
- MAINPRICE, D.; TOMMASI, A.; COUVY, H.; CORDIER, P.; FROST, D.J. (2005): Pressure sensitivity of olivine slip systems and seismic anisotropy of Earth's upper mantle. *Nature* 433, 731-733
- MANGHNANI, M.H.; AMULELE, G.; SMYTH, J.R.; HOLL, C.M.; CHEN, G.; PRAKAPENKA, V.; FROST, D.J. (2005): Equation of state of hydrous Fo(90) ringwoodite to 45 GPa by synchrotron powder diffraction. *Mineralogical Magazine* 69, 317-323
- MARTON, F.C.; SHANKLAND, T.J.; RUBIE, D.C.; XU, Y. (2005): Effects of variable thermal conductivity on the mineralogy of subducting slabs and implications for mechanisms of deep earthquakes. *Physics of the Earth and Planetary Interiors* 149, 53-64
- MASHKINA, E.; BAIER, M.; MAGERL, A.; GÖBBELS, M.; SEIFERT F. (2005): Resistivity relaxation, a new approach to study ionic mobility in perovskite mixed conductors like $\text{CaTi}_{0.7}\text{Fe}_{0.3}\text{O}_{3-\delta}$. *Ionics* 11, 269-274
- MCCAMMON, C.A. (2005): Mantle oxidation state and oxygen fugacity: Constraints on mantle chemistry, structure and dynamics. – In: VAN DER HILST, R.D.; BASS, J.; MATAS, J.; TRAMPERT., J. (Eds.): *Earth's Deep Mantle: Structure, Composition, and Evolution*, American Geophysical Union, Washington D.C., 221-242
- MCCAMMON, C.A. (2005): The paradox of mantle redox. *Science* 308, 807-808 and 309, 1816
- NESTOLA, F.; BOFFA BALLARAN, T.; TRIBAUDINO, M.; OHASHI, H. (2005): Compressional behaviour of $\text{CaNiSi}_2\text{O}_6$ clinopyroxene: bulk modulus systematic and cation type in clinopyroxenes. *Physics and Chemistry of Minerals* 32, 222-227
- O'NEILL, C., MÜLLER, D.; STEINBERGER, B. (2005): On the uncertainties in hot spot reconstructions and the significance of moving hot spot reference frames. *Geochemistry Geophysics Geosystems* 6, Q04003, doi:10.1029/2004GC000784

- PETTKE, T.; AUDÉTAT, A.; SCHALTEGGER, U.; HEINRICH C.A. (2005): Magmatic-to-hydrothermal crystallization in the W-Sn mineralized Mole Granite (NSW, Australia): Part II: Evolving zircon and thorite trace element chemistry. *Chemical Geology* 220, 191-213
- PRAKAPENKA, V. B.; SHEN, G.Y.; RIVERS, M.L.; Sutton, S.R.; Dubrovinsky, L.S. (2005): Grain-size control *in situ* at high pressures and high temperatures in a diamond anvil cell. *Journal of Synchrotron Radiation* 12, 560-565
- ROZENBERG, G.K.; PASTERNAK, M.P.; XU, W.M.; DUBROVINSKY, L.S.; CARLSON, S.; TAYLOR, R.D. (2005): Consequences of pressure-instigated spin crossover in $R\text{FeO}_3$ perovskites; a volume collapse with no symmetry modification. *Europhysics Letters* 71, 228-234
- SANDBAKKEN, P.T.; LANGENHORST, F.; DYPVIK H. (2005): Shock metamorphism of quartz at the submarine Mjølner impact crater, Barents Sea. *Meteoritics & Planetary Science* 40, 1363-1375
- SANLOUP, C.; SCHMIDT, B.C.; CHAMORRO PEREZ, E.M.; JAMBON, A.; GREGORYANZ, E.; MEZOUAR, M. (2005): Retention of xenon in quartz and Earth's missing xenon. *Science* 310, 1174-1177
- SCHALTEGGER, U.; PETTKE, T.; AUDÉTAT, A.; REUSSER, E.; HEINRICH, C.A. (2005): Magmatic-to-hydrothermal crystallization in the W-Sn mineralized Mole Granite (NSW, Australia): Part I: Crystallization of zircon and REE-phosphates over three million years – a geochemical and U-Pb geochronological study. *Chemical Geology* 220, 215-235
- SHINOVA, E.; ZHECHEVA, E.; STOYANOVA, R.; BROMILEY, G.D. (2005): High-pressure synthesis of solid solutions between trigonal LiNiO_2 and monoclinic $\text{Li}[\text{Li}_{1/3}\text{Ni}_{2/3}]\text{O}_2$. *Journal of Solid State Chemistry* 178: 1661-1669
- SHINOVA, E.; ZHECHEVA, E.; STOYANOVA, R.; BROMILEY, G.D.; ALCANTARA, R.; TIRADO, J.L. (2005): High-pressure synthesis and electrochemical behavior of layered $(1-x)\text{LiNi}_{1-y}\text{Al}_y\text{O}_2 \cdot x\text{Li}[\text{Li}_{1/3}\text{Ni}_{2/3}]\text{O}_2$ oxides. *Journal of Solid State Chemistry* 178(9): 2692-2700
- SHIRYAEV, A.A.; SPIVAK, A.V.; LITVIN, Yu.A.; URUSOV, V.S. (2005): Formation of nitrogen *A*-defects in diamond during growth in carbonate-carbon solutions-melts: Experiments at 5.5-8.5 GPa. *Doklady Earth Sciences* 403A, No. 6, 908-911
- SMYTH, J.R.; HOLL, C.M.; LANGENHORST, F.; LAUSTSEN, H.M.; ROSSMAN, G.R.; KLEPPE, A.; MCCAMMON, C.A.; KAWAMOTO, T.; VAN AKEN, P.A. (2005): Crystal chemistry of wadsleyite II and water in the Earth's interior. *Physics and Chemistry of Minerals* 31, 691-705
- SWAMY, V.; DUBROVINSKY, L.S.; DUBROVINSKAIA, N.A.; LANGENHORST, F.; SIMIONOVICI, A.S.; DRAKOPOULOS, M.; DMITRIEV, V.; WEBER, H.P. (2005): Size effects on the structure and phase transition behavior of baddeleyite TiO_2 . *Solid State Communications* 134, 541-546
- SWAMY, V.; KUZNETSOV, A.; DUBROVINSKY, L.S.; CARUSO, R.A.; SHCHUKIN, D.G.; MUDDLE, B.C. (2005): Finite-size and pressure effects on the Raman spectrum of nanocrystalline anatase TiO_2 . *Physical Review B* 71, 184302

- TALYZIN, A.V.; LANGENHORST, F.; DUBROVINSKAIA, N.A.; DUB, S.; DUBROVINSKY, L.S. (2005): Structural characterization of the hard fullerite phase obtained at 13 GPa and 830 K. *Physical Review B* 71, 115424
- TALYZIN, A.V.; LANGENHORST, F.; DUBROVINSKAIA, N.A.; DUBROVINSKY, L.S.; DUB, S. (2005): Structural characterization of the "hard fullerite" phase obtained at 13 GPa and 830K. *Fullerenes Nanotubes and Carbon Nanostructures* 13, 83-89
- TARANTINO, S.C.; GHIGNA, P.; MCCAMMON, C.A.; AMANTEA, R.; CARPENTER, M.A. (2005): Local structural properties of (Mn,Fe)Nb₂O₆ from Mössbauer and X-ray absorption spectroscopy. *Acta Crystallographica B* B61, 250-257
- TENNANT, W.C.; CLARIDGE, R.F.C.; MCCAMMON, C.A.; SMIRNOV, A.I.; BECK, R.J. (2005): Structural studies of New Zealand pounamu using Mössbauer spectroscopy and electron paramagnetic resonance. *Journal of the Royal Society of New Zealand* 35, No. 4, 385-398
- TERASAKI, H.; FROST, D.J.; RUBIE, D.C.; LANGENHORST, F. (2005): The effect of oxygen and sulphur on the dihedral angle between Fe-O-S melt and silicate minerals at high pressure: Implications for Martian core formation. *Earth and Planetary Science Letters* 232, 379-392
- VERNOOIJ, M.G.C.; LANGENHORST, F. (2005): Experimental reproduction of tectonic deformation lamellae in quartz and comparison to shock-induced planar deformation features. *Meteoritics & Planetary Science* 40, Nr. 9/10, 1353-1361
- WALTE; N.P.; BONS, P.D.; PASSCHIER, C.W. (2005): Deformation of melt-bearing systems – Insight from *in situ* grain-scale analogue experiments. *Journal of Structural Geology* 27, 1666-1679
- WILLIAMS, H.M.; PESLIER, A.H.; MCCAMMON, C.A.; HALLIDAY, A.N.; TEUTSCH, N.; LEVASSEUR, S.; BURG, J.-P. (2005): Iron isotope fractionation in mantle minerals and the effects of partial melting and oxygen fugacity. *Earth and Planetary Science Letters* 235, 435-452

b) Monographs

- KEPPLER, H.; AUDÉTAT, A. (2005): Fluid-mineral interaction at high pressure. – In: MILETICH, R. (Ed.): *Mineral Behaviour at Extreme Conditions*, European Mineralogical Union Lecture Notes in Mineralogy, Vol. 7, 225-251
- KEPPLER, H.; FROST, D.J. (2005): Introduction to minerals under extreme conditions. – In: MILETICH, R. (Ed.): *Mineral Behaviour at Extreme Conditions*, European Mineralogical Union Lecture Notes in Mineralogy, Vol. 7, 1-30

5.2 Publications (submitted, in press)

- AUDÉTAT, A.; PETTKE, T.: Evolution of a porphyry-Cu mineralized magma system at Santa Rita, New Mexico (USA). *Journal of Petrology* (submitted)

- BESTMANN, M.; RICE, A.H.N.; LANGENHORST, F.; GRASEMANN, B.; HEIDELBACH, F.: Subglacial bedrock welding associated with ice quakes. Geological Society of London Special Publications (submitted)
- BOFFA BALLARAN, T.; WOODLAND, A.B.: Local structure of ferric iron-bearing garnets deduced by IR-spectroscopy. Chemical Geology (in press)
- BOLFAN-CASANOVA, N.; MCCAMMON, C.A.: Water in transition zone and lower mantle minerals. – In: JACOBSEN, S.D.; VAN DER LEE, S. (Eds.): Earth's Deep Water Cycle, American Geophysical Union, Washington D.C. (submitted)
- BROMILEY, G.D.; SHIRYAEV, A.A.: Neutron irradiation and post-irradiation annealing of rutile (TiO_{2-x}): effects on hydrogen incorporation and optical absorption. Physics and Chemistry of Minerals (submitted)
- BROMILEY, G.D.; BROMILEY, F.A.: High-pressure phase transitions and hydrogen incorporation in MgSiO_3 enstatite. American Mineralogist (submitted)
- BROMILEY, G.D.; BROMILEY, F.A.; BROMILEY, D.W.: Hydration of stishovite and the fate of subducting slabs. Geophysical Research Letters (submitted)
- BYSTRICKY, M.; HEIDELBACH, F.; MACKWELL, S.J.: Large-strain deformation and strain partitioning in polyphase rocks: dislocation creep of olivine-magnesiowüstite aggregates. Tectonophysics (submitted)
- COMODI, P.; CERA, F.; FUMAGALLI, P.; DUBROVINSKY, L.S.; NAZZARENI, S.: The high pressure behaviour of 10 Å phase: a spectroscopic and diffractometric study up to 42 GPa. Earth and Planetary Science Letters (submitted)
- DEMOUCHY, S.; MACKWELL, S.J.: Solubility and diffusivity of hydrogen in iron-bearing olivine. Phys. Chem. Minerals (submitted)
- DEMOUCHY, S.; JACOBSEN, S.D.; GAILLARD, F.; STERN, C.R.: Rapid magma ascent recorded by water diffusion profiles in olivine from Earth's mantle. Geology (submitted)
- DMITRIEV, V.P.; DUBROVINSKY, L.S.; LE BIHAN, T.; BASHKIN, I.; KUZNETSOV, A.; PONYATOVSKY, E.; WEBER, H.-P.: Compressing TiZr: from the electron driven collapse to the phonon triggered expansion. Physical Review B (re-submitted)
- DOLEJŠ, D.; BAKER, D.R.: Melting equilibria in the system $\text{K}_2\text{O}-\text{Na}_2\text{O}-\text{Al}_2\text{O}_3-\text{SiO}_2-\text{F}_2\text{O}-1-\text{H}_2\text{O}$ to 100 MPa: I. Silicate-fluoride liquid immiscibility in anhydrous systems. Journal of Petrology (submitted)
- DOLEJŠ, D.; BAKER, D.R.: Melting equilibria in the system $\text{K}_2\text{O}-\text{Na}_2\text{O}-\text{Al}_2\text{O}_3-\text{SiO}_2-\text{F}_2\text{O}-1-\text{H}_2\text{O}$ to 100 MPa: II. Differentiation paths of fluorosilicic magmas in hydrous systems. Journal of Petrology (submitted)
- DOLEJŠ, D.; BAKER, D.R.: Fluorite solubility in hydrous haplogranitic melts at 100 MPa. Chemical Geology (in press)
- DOLEJŠ, D.; BAKER, D.R.: Phase transitions and volumetric properties of cryolite, Na_3AlF_6 : Differential thermal analysis to 100 MPa. American Mineralogist (in press)
- DUBROVINSKAIA, N.A.; DUBROVINSKY, L.S.: High-pressure high-temperature amorphous ice. Physical Review Letters (submitted)
- DUBROVINSKAIA, N.A.; DUBROVINSKY, L.S.: Melting of Ice VII and new high-pressure high-temperature amorphous ice. – In: Ohtani, E. (Ed.): "GSA monograph" (in press)

- DUBROVINSKAIA, N.A.; ESKA, G.; SHESHIN, G.A.; BRAUN, H.: Superconductivity in polycrystalline boron-doped diamond synthesized at 20 GPa and 2700 K. *Journal of Applied Physics* (submitted)
- DUBROVINSKY, N.A.; DUBROVINSKAIA, L.S.; KANTOR, I.Yu.; CRICHTON, W.A.; VITOS, L.; AHUJA, R.; ABRIKOSOV, I.A.: Beating the miscibility barrier between iron group elements and magnesium by high-pressure alloying. *Physical Review Letters* (in press)
- GALADÍ-ENRÍQUEZ, E.; ZULAUF, G.; HEIDELBACH, F.; ROHRMÜLLER, J.: Insights into the deformation history of a dyke-host association showing contrasting rheologies and inconsistent shear-sense indicators: the Saunstein granite dyke (Bavarian Forest, SE Germany, European Variscides). *Journal of Structural Geology* (submitted)
- GLASMACHER, U.A.; LANG, M.; KEPPLER, H.; LANGENHORST, F.; NEUMANN, R.; SCHARDT, D.; TRAUTMANN, C.; WAGNER, G.A.: Phase transitions in solids stimulated by simultaneous exposure to high pressure and relativistic heavy ions. *Physical Review Letters* (submitted)
- GOTOU, H.; YAGI, T.; FROST, D.J.; RUBIE, D.C.: An opposed-anvil type high-pressure and high-temperature apparatus using sintered diamond. *Review of Scientific Instruments* (in press)
- IEZZI, G.; DELLA VENTURA, G.; TRIBAUDINO, M.: Synthetic P21/m amphiboles in the system $\text{Li}_2\text{O}-\text{Na}_2\text{O}-\text{MgO}-\text{SiO}_2-\text{H}_2\text{O}$ (LNMSH). *American Mineralogist* (in press)
- IEZZI, G.; TRIBAUDINO, M.; DELLA VENTURA, G.; NESTOLA, F.; BELLATRECCIA, F.: High-T phase transition of $\text{ANaB}(\text{LiMg})\text{CMg}_5\text{Si}_8\text{O}_{22}(\text{OH})_2$ amphibole: an X-ray synchrotron powder diffraction and FTIR spectroscopic study. *Physics and Chemistry of Minerals* (in press)
- KANTOR, A.P.; DUBROVINSKY, L.S.; DUBROVINSKAIA, N.A.; KANTOR, I.Yu.; GONCHARENKO, I.N.: Phase transitions in MnO and FeO at low temperatures: a neutron powder diffraction study. *Journal of Alloys and Compounds* (in press)
- KANTOR, I.Yu.; DUBROVINSKY, L.S.; MCCAMMON, C.A.; KANTOR, A.P.; PASCARELLI, S.; AQUILANTI, G.; CRICHTON, W.; MATTESINI, M.; AHUJA, R.; ALMEIDA, J.; URUSOV, V.: Pressure-induced phase transition in $\text{Mg}_{0.8}\text{Fe}_{0.2}\text{O}$ ferropericlase. *Physics and Chemistry of Minerals* (in press)
- KANTOR, I.Yu.; DUBROVINSKY, L.S.; MCCAMMON, C.A.: Spin crossover in ferropericlase: A new Mössbauer spectroscopic study and a reinterpretation of existing X-ray emission spectroscopic data. *Physical Review B* (submitted)
- KUZNETSOV, A.Yu.; DE ALMEIDA, J.S.; DUBROVINSKY, L.S.; AHUJA, R.; KWON, S.K.; KANTOR, I.Yu.; KANTOR, A.; GUIGNOT, N.: High pressure synthesis and physical properties of an orthorhombic phase of chromium dioxide. *Journal of Applied Physics* (submitted)
- LEE, K.K.M.; STEINLE-NEUMANN, G.: High-pressure alloying of iron and xenon: 'Missing' Xe in the Earth's core? *Journal of Geophysical Research* (in press)
- MACKENZIE, K.J.D.; TEMUJIN, J.; MCCAMMON, C.A.; SENNA, M.: Mechanochemical activation of wolframite, FeWO_4 , studied by ^{57}Fe Mössbauer spectroscopy. *Journal of the European Ceramical Society* (in press)

- MELOSH, H.J.: A hydrocode equation of state for SiO₂. *Icarus* (submitted)
- MIERDEL, K.; KEPPLER, H.; SMYTH, J.R.; LANGENHORST, F.: The origin of the Earth's asthenosphere. *Nature* (submitted)
- MIYAJIMA, N.; OHGUSHI, K.; ICHIHARA, M.; YAGI, T.: Crystal morphology and dislocation microstructures of CaIrO₃. A TEM study of an analogue of the MgSiO₃ post-perovskite phase. *Geophysical Research Letters* (submitted)
- MLYNARCZYK, M.S.J.; WILLIAMS-JONES, A.E., DOLEJŠ, D.: Geology and geochemistry of alteration at the San Rafael Sn-Cu deposit, SE Peru. *Economic Geology* (submitted)
- O'NEILL, H.S.C.; BERRY, A.J.; MCCAMMON, C.A.; JAYASURIYA, K.D.; CAMPBELL, S.J.; FORAN, G.: A direct experimental determination of the effect of pressure on the Fe³⁺/Fe²⁺ ratio of an anhydrous silicate melt to 3.0 GPa. *American Mineralogist* (in press)
- ROBINSON, P.; HEIDELBACH, F.; HIRT, A.; MCENROE, S.A.; BROWN, L.L.: Crystallographic-magnetic correlations in single crystal hemo-ilmenite: New evidence for lamellar magnetism. *Geophysical Journal International* (in press)
- ROUQUETTE, J.; HAINES, J.; BORNAND, V.; PINTARD, M.; PAPET, Ph.; SAUVAJOL, J.L.: Use of Resonance Raman Spectroscopy to study the phase diagram of PbZr_{0.52}Ti_{0.48}O₃. *Physical Review B* (submitted)
- SHAW, C.S.J.; HEIDELBACH, F.: The origin of reaction textures in mantle peridotite xenoliths from Sal Island, Cape Verde: the case for 'metasomatism' by the host lava. *Contributions to Mineralogy and Petrology* (submitted)
- SHCHEKA, S.S.; WIEDENBECK, M.; FROST, D.J.; KEPPLER, H.: Carbon solubility in mantle minerals. *Earth and Planetary Science Letters* (submitted)
- STEINBERGER, B.: Effect of latent heat release at phase boundaries on flow in the Earth's mantle, phase boundary topography and dynamic topography at the Earth's surface. *Physics of the Earth and Planetary Interiors* (submitted)
- TALYZIN, A.V.; DZWILEWSKI, A.; SUNDQVIST, B.; TSYBIN, Y.; MARSHALL, A.G.; PURCELL, J.M.; SHULGA, Y.; MCCAMMON, C.A.; DUBROVINSKY, L.S.: High pressure high temperature hydrogenation of C₆₀. *Chemical Physics* (submitted)
- TERASAKI, H.; FROST, D.J.; RUBIE, D.C.; LANGENHORST, F.: Percolative core formation in planetesimals. *Earth and Planetary Science Letters* (submitted)
- ZEDGENIZOV, D.A.; SHIRYAEV, A.A.; SHATSKY, V.S.; KAGI, H.: Water related IR characteristics in natural fibrous diamonds. *Mineralogical Magazine* (submitted)

5.3 Presentations at scientific institutions and at congresses

- AKBER-KNUTSON, S.; STEINLE-NEUMANN, G.; ASIMOW, P.D.: 24.-29.04.2005, EGU General Assembly 2005, Vienna, Austria^{*1}: "On the sharpness of the perovskite/post-perovskite phase transition in the Earth's mantle", *Geophysical Research Abstracts* 7, 00254

- AKBER-KNUTSON, S.; STEINLE-NEUMANN, G.; ASIMOW, P.: 20.-25.05.2005, Goldschmidt Conference, Moscow, USA: "On the sharpness of the perovskite/post-perovskite transition in the Earth's mantle", Conference Supplement to *Geochimica et Cosmochimica Acta*, A255, 2005
- AKBER-KNUTSON, S.; STEINLE-NEUMANN, G.; ASIMOV, P.: 27.06.-01.07.2005, Joint 20th AIRAPT – 43rd EHPRG, Karlsruhe, Germany^{*2}: "Al, Fe incorporation into post-perovskite from first principles"
- AKBER-KNUTSON, S.; STEINLE-NEUMANN, G.; ASIMOW, P.: 03.-05.10.2005: International Workshop on the Post-perovskite Phase Transition in the Earth's Deep Mantle, Tokyo, Japan: "On the sharpness of the perovskite/post-perovskite transition in the Earth's mantle"
- ALÉON, J.; EL GORESY, A.; ZINNER, E.: Workshop on Oxygen in the Earliest Solar Systems, Gatlinburgh, USA: "First evidence for co-existing ¹⁶O-poor and ¹⁶O-rich gases in the early solar nebula inferred from a compound Ca-Al-rich inclusion from Efremovka"
- ALLWARDT, J.R.; STEBBINS, J.F.; DU, L.; FROST, D.J.; WITHERS, A.C.; HIRSCHMANN, M.M.: 05.-09.12.2005, AGU Fall Meeting, San Francisco, USA^{*4}: "Aluminum coordination and density of 4 and 5 component high-pressure aluminosilicate glasses", *EOS Trans. AGU*, 86(52), Fall Meet. Suppl., Abstract MR11A-05, 2005
- ASAHARA, Y.; FROST, D.J.; RUBIE, D.C.: 22.-26.05.2005, Japan Earth and Planetary Science Joint Meeting, Makuhari, Japan: "Oxygen partitioning between magnesiowüstite and liquid Fe-rich metal at high pressure and high temperature"
- ASAHARA, Y.; OHTANI, E.; KONDO, T.; DUBROVINSKY, L.S.; RUBIE, D.C.; LANGENHORST, F.; FROST, D.J.: 22.-26.05.2005, Japan Earth and Planetary Science Joint Meeting, Makuhari, Japan: "Partitioning coefficients in the Allende meteorite at high pressures obtained by laser heated diamond anvil cell experiments"
- ASAHARA, Y.; FROST, D.J.; RUBIE, D.C.; LANGENHORST, F.: 05.-09.12.2005, AGU Fall Meeting, San Francisco, USA^{*4}: "Oxygen partitioning between magnesiowüstite and liquid Fe-rich metal at high pressure and high temperature", *EOS Trans. AGU*, 86(52), Fall Meet. Suppl., Abstract MR13A-0050, 2005
- BAIER, J.; AUDÉTAT, A.; KEPLER, H.: 05.-09.12.2005, AGU Fall Meeting, San Francisco, USA^{*4}: "Origin of the negative niobium tantalum anomaly in subduction zone magmas", *EOS Trans. AGU*, 86(52), Fall Meet. Suppl., Abstract V33C-06, 2005
- BOFFA BALLARAN, T.: 16.-19.10.2005, MSA Awardee Lecture at the Geological Society of America Annual Meeting, Salt Lake City, USA: "Local strain heterogeneity in mineral solid solutions: the relationship between line broadening in IR spectra and excess enthalpy"
- BYSTRICKY, M.; HEIDELBACH, F.; MACKWELL, S. (2005): 01.-04.05.2005, 15th International Conference on Deformation mechanisms, Rheology and Tectonics, Zürich: "Large strain deformation of olivine-magnesiowüstite mixtures"
- CHAKHMOURADIAN, A.R.; MCCAMMON, C.A.; MACBRIDE, L.; CAHILL, C.L.: 15.-18.05.2005, 2005 Joint Annual Meeting of the Geological Association of Canada, Mineralogical Association of Canada, Canadian Society of Petroleum Geologists and the Canadian Society of Soil Science, Halifax, Canada: "Titaniferous garnets in carbonatites: Their significance and place in the evolutionary history of host rocks"

- COMODI, P.; FUMAGALLI, P.; NAZARENI, S.; ZANAZZI, P.F.: 9.-11.02.2005, Micas@Italy, Rimini, Italy: "The 10 Å phase: A high pressure phyllosilicate with a mica-like structure"
- COMODI, P.; FUMAGALLI, P.; NAZZARENI, S.; ZANAZZI, P.F.: 24.-29.04.2005, EGU General Assembly 2005, Vienna, Austria^{*1}: "The structure of the 10 Å phase from X-ray single crystal diffraction data", Geophysical Research Abstracts 7, 08085, 2005
- COUVY, H.; CORDIER, P.; FROST, D.J.; HEIDELBACH, F.; MAINPRICE, D.; TOMMASI, A.: 05.-09.12.2005, AGU Fall Meeting, San Francisco, USA^{*4}: "Pressure sensitivity of olivine deformation mechanisms and implications for seismic anisotropy of deep upper mantle", EOS Trans. AGU, 86(52), Fall Meet. Suppl., Abstract DI41A-1258, 2005
- DOBSON, D.P.; ALFREDSON, M.; BRODHOLT, J.P.; HOLZAPFEL, C.: 05.-09.12.2005, AGU Fall Meeting, San Francisco, USA^{*4} (*invited*): "Grain-boundary enrichment of iron in MgSiO₃ perovskite", EOS Trans. AGU, 86(52), Fall Meet. Suppl., Abstract MR14A-01, 2005
- DOLEJŠ, D.: 11.-13.05.2005, Short course 'Lower mantle mineralogy, high pressure phase behaviour', Ludwig-Maximilians-Universität München, Germany: "Thermodynamics in mineralogy and petrology"
- DOLEJŠ, D.: 11.-13.05.2005, Short course 'Lower mantle mineralogy, high pressure phase behaviour', Ludwig-Maximilians-Universität München, Germany: "Thermodynamic modelling"
- DOLEJŠ, D.: 19.-26.06.2005, 7th European Mineralogical Union School 'Mineral Behaviour at Extreme Conditions', Heidelberg, Germany: "Transport of silica in the Earth's interior: The role of fluorine"
- DOLEJŠ, D.: 18.-21.09.2005, 83. Jahrestagung der DMG, Aachen, Germany^{*3}: "Fluorine solubility in granitic magmas: Role of melt composition and mineral buffering", Beihefte zum European Journal of Mineralogy 17, 29
- DOLEJŠ, D.; WAGNER, T.: 18.-21.09.2005, 83. Jahrestagung der DMG, Aachen, Germany^{*3}: "Fluid-rock interactions in the temperature-composition space: Thermodynamic modeling of non-ideal mineral-aqueous systems. Beihefte zum European Journal of Mineralogy 17, 29
- DUBROVINSKAIA, N.A.; DUBROVINSKY, L.S.; CRICHTON, W.; LANGENHORST, F.; RICHTER, A.: 11.-14.05.2005, ICNDST-10: The 10th International Conference on New Diamond Science and Technology, Tsukuba, Japan: "Aggregated diamond nanorods, the new densest and least compressible form of carbon"
- DUBROVINSKAIA, N.A.; DUBROVINSKY, L.S.: 11.-14.05.2005, ICNDST-10: The 10th International Conference on New Diamond Science and Technology, Tsukuba, Japan: "Bulk superhard semiconducting C-B composites"
- DUBROVINSKAIA, N.A.: 06.06.2005, L.P.M.T.M.-C.N.R.S., Institute Galilee, Université Paris, France: "Heavily boron-doped diamonds, synthesis and properties"
- DUBROVINSKAIA, N.A.: 27.06.-01.07.2005, Joint 20th AIRAPT – 43rd EHPRG, Karlsruhe, Germany^{*2} (*invited*): "Bulk superhard semiconducting C-B composites"

- DUBROVINSKAIA, N.A.; DUBROVINSKY, L.S.; ABRIKOSOV, I.: 05.-09.12.2005, AGU Fall Meeting, San Francisco, USA^{*4}: "Iron-magnesium alloy in the Earth's core", EOS Trans. AGU, 86(52), Fall Meet. Suppl., Abstract MR23A-0046, 2005
- DUBROVINSKY, L.S.; KANTOR, I.Yu.; KANTOR, A.P.; MCCAMMON, C.A.; CRICHTON, W.: 05.-09.12.2005, AGU Fall Meeting, San Francisco, USA^{*4}: "Phase transitions in transition metal monoxides: Interplay between structural, magnetic and electronic properties", EOS Trans. AGU, 86(52), Fall Meet. Suppl., Abstract MR34A-07, 2005
- DUC-TIN, Q.; AUDÉTAT, A.; KEPPLER, H.: 18.-21.09.2005, 83. Jahrestagung der DMG, Aachen, Germany^{*3}: "Solubility of tin in magmatic-hydrothermal fluids: a LA-ICP-MS study of synthetic fluid inclusions", Beihefte zum European Journal of Mineralogy 17, 31
- EBERT, E.; GROVE, T.: 24.-29.04.2005, EGU General Assembly 2005, Vienna, Austria^{*1}: "Systematics of garnet peridotite melting: New experimental constraints", Geophysical Research Abstracts 7, 08306, 2005
- EIMER, B.; KIEFER, B.; STEINLE-NEUMANN, G.: 05.-09.12.2005, AGU Fall Meeting, San Francisco, USA^{*4}: "Ab initio study of iron at intermediate pressure", EOS Trans. AGU, 86(52), Fall Meet. Suppl., Abstract MR34A-04, 2005
- EL GORESY, A.; CHEN, M.; GILLET, PH.; DUBROVINSKY, L.S.: 12.-16.09.2005, 68th Annual Meeting of the Meteoritical Society, Gatlinburgh, USA: "Two distinct olivine-ringwoodite phase transition mechanisms in shocked L-chondrites: Genetic implications"
- EL GORESY, A.; CHEN, M.; GILLET, Ph.; DUBROVINSKY, L.S.: 18.-21.09.2005, 83. Jahrestagung der DMG, Aachen, Germany^{*3}: "Two distinct olivine-ringwoodite phase transition mechanisms in shocked chondrites: Genetic implications", Beihefte zum European Journal of Mineralogy 17, 34
- FROST, D.J.; SMYTH, J.R.: 24.-29.04.2005, EGU General Assembly 2005, Vienna, Austria^{*1}: "The effects of temperature and water concentration on the olivine to wadsleyite transformation", Geophysical Research Abstracts 7, 06398
- FROST D.J.: 12.05.2005, Institut für Mineralogie, Münster, Germany: "Evidence and implications concerning the existence of metallic Fe in the Earth's lower mantle"
- FROST D.J.: 12.-17.06.2005, Gordon Research Conference on the Interior of the Earth, Mount Holyoke College, South Hadley, USA: "Experimental constraints on the depth and sharpness of seismic discontinuities in the transition zone"
- FROST D.J.: 07.11.2005, Friedrich-Schiller-Universität Jena, Institut für Geowissenschaften, Jena, Germany: "Experimental constraints on the depth and sharpness of seismic discontinuities in the transition zone"
- FROST D.J.: 12.-14.11.2005, Joint Workshop of OXIDES and THESIS, Thurnau, Germany: "Experimental constraints on the depth and sharpness of the 410 km seismic discontinuity"
- FROST, D.J.: 05.-09.12.2005, AGU Fall Meeting, San Francisco, USA^{*4}: "The effect of water on the structure and sharpness of the olivine to wadsleyite transformation", EOS Trans. AGU, 86(52), Fall Meet. Suppl., Abstract DI41A-1257, 2005
- FROST, D.J.: 05.-09.12.2005, AGU Fall Meeting, San Francisco, USA^{*4} (*invited*): "The effect of ferric iron on the olivine to wadsleyite transformation: Implications for the sharpness of the "410" km discontinuity", EOS Trans. AGU, 86(52), Fall Meet. Suppl., Abstract MR14A-02, 2005

- HEIDELBACH, F.; TERRY, M.P.: 16.-19.10.2005, Geological Society of America Annual Meeting, Salt Lake City, USA: "Inherited fabric in a symplectite: a key to deformation history?"
- HEIDELBACH, F.; TERRY, M.; BYSTRICKY, M.; HOLZAPFEL, C.: 24.-29.04.2005, EGU General Assembly 2005, Vienna, Austria^{*1}: "A dynamic diffusion experiment in ferropericlasite", Geophysical Research Abstracts 7, 07547, 2005
- HEIDELBACH, F.: 04.07.2005, DFH-UFA Summerschool 'Textures and Microstructures in the Earth Sciences', Freiberg, Germany: "Texture analysis of geological materials experimentally deformed at high pressure and temperature"
- HOLL, C.M.; SMYTH, J.R.; FROST, D.J.: 05.-09.12.2005, AGU Fall Meeting, San Francisco, USA^{*4}: "Structure and hydroxyl bonding environment in hydrous wadsleyite", EOS Trans. AGU, 86(52), Fall Meet. Suppl., Abstract MR41A-0905, 2005
- HUNT, S.A.; BRODHOLT, J.; DOBSON, D.P.; FROST, D.J.: 05.-09.12.2005, AGU Fall Meeting, San Francisco, USA^{*4}: "Deformation DIA experiments on the relative strength of pyrope - majorite garnets", EOS Trans. AGU, 86(52), Fall Meet. Suppl., Abstract MR23C-0082, 2005
- KANTOR, A.P.; KANTOR, I.Yu.; DUBROVINSKY, L.S.; GONCHARENKO, I.N.: 27.06.-01.07.2005, Joint 20th AIRAPT – 43rd EHPRG, Karlsruhe, Germany^{*2}: "Magnetization of MnO and FeO at high pressures: a powder neutron diffraction study"
- KANTOR, A.P.; KANTOR, I.Yu.; DUBROVINSKY, L.S.; JACOBSEN, S.D.: 05.-09.12.2005, AGU Fall Meeting, San Francisco, USA^{*4}: "New Experimental Setup for High-Pressure High-Temperature Gigahertz Ultrasonic Interferometry", EOS Trans. AGU, 86(52), Fall Meet. Suppl., Abstract MR31A-0138, 2005
- KANTOR, I.Yu.; DUBROVINSKY, L.S.; MCCAMMON, C.A.: 27.06.-01.07.2005, Joint 20th AIRAPT – 43rd EHPRG, Karlsruhe, Germany^{*2}: "Mössbauer spectroscopy at elevated pressures and temperatures: Spin transition in (Mg_{0.8}Fe_{0.2})O ferropericlasite"
- KANTOR, I.Yu.; DUBROVINSKY, L.S.; KANTOR, A.P.; MCCAMMON, C.A.: 05.-09.09.2005, International Conference on the Applications of the Mössbauer Effect, Montpellier, France: "High-pressure phase transitions in FeO and (Mg,Fe)O"
- KANTOR, I.Yu.; DUBROVINSKY, L.S.; MCCAMMON, C.A.: 05.-09.12.2005, AGU Fall Meeting, San Francisco, USA^{*4}: "Spin transition in ferropericlasite at high pressures and temperatures: Mössbauer spectroscopic study", EOS Trans. AGU, 86(52), Fall Meet. Suppl., Abstract MR23A-0038, 2005
- KEGLER, Ph.; HOLZHEID, A.; RUBIE, D.C.; FROST, D.J.; PALME, H.: 14.-18.03.2005, 36th Lunar and Planetary Science Conference, Houston, USA: "New results of metal/silicate partitioning of Ni and Co at elevated pressures and temperatures"
- KEPPLER, H.; AUDÉTAT, A.: 19.-26.06.2005, 7th European Mineralogical Union School 'Mineral Behaviour at Extreme Conditions', Heidelberg, Germany: "Fluid-mineral interaction at high pressure"
- KEPPLER, H.; FROST, D.J.: 19.-26.06.2005, 7th European Mineralogical Union School 'Mineral Behaviour at Extreme Conditions', Heidelberg, Germany: "Introduction to minerals under extreme conditions"

- KUZNETSOV, A.Yu.; DUBROVINSKY, L.S.; DMITRIEV, V.: 27.06.-01.07.2005: Joint 20th AIRAPT – 43rd EHPRG, Karlsruhe, Germany^{*2}: "In situ combined X-ray diffraction and conductivity measurements of Pr metal: Evidence of the isostructural phase transition"
- KUZNETSOV, A.Yu.; PEREIRA, A.S.; HAINES J.; DUBROVINSKY L.S.; DMITRIEV, V.; PATTISON, P.: 27.06.-01.07.2005: Joint 20th AIRAPT – 43rd EHPRG, Karlsruhe, Germany^{*2}: "Structural changes and pressure-induced chemical decomposition of boric acid"
- KUZNETSOV, A.Yu.; DMITRIEV, V.; LANGENHORST, F.; ESTEVEZ-RAMS, E.; DUBROVINSKY, L.S.: 23.-31.08.2005, XX Congress of the International Union of Crystallography, Florence, Italy: "Stacking faults and internal strains in DHCP phase of La", Abstracts of the XX IUCr Congress, Acta Crystallographica, A61, C451
- KUZNETSOV, A.Yu.; DUBROVINSKY, L.S.; DE ALMEIDA, J.S.; PEREIRA, A.S.; KURNOSOV, A.; KANTOR, I.Yu.; KANTOR, A.; DMITRIEV V.: 25.10.2005, Advanced Photon Source, Argonne National Laboratory, Argonne, USA: "High-pressure *in situ* synthesis and studies of simple crystalline solids"
- LEE, K.K.M.; STEINLE-NEUMANN, G.: 05.-09.12.2005, AGU Fall Meeting, San Francisco, USA^{*4}: "Pressure- and chemistry-dependent electron capture radioactive decay", EOS Trans. AGU, 86(52), Fall Meet. Suppl., Abstract V41F-1528, 2005
- LIU, J.; BOFFA BALLARAN, T.; DUBROVINSKY, L.S.; FROST, D.J.: 24.-29.04.2005, EGU General Assembly 2005, Vienna, Austria^{*1}: "Effect of Na substitution into KAlSi₃O₈ hollandite type structure", Geophysical Research Abstracts 7, 06529, 2005
- LIU, J.; BOFFA BALLARAN, T.; DUBROVINSKY, L.S.; FROST, D.J.: 19.-26.06.2005, 7th European Mineralogical Union School 'Mineral Behaviour at Extreme Conditions', Heidelberg, Germany: "High pressure study of K-Na hollandite solid solution"
- LIU, J.; BOFFA BALLARAN, T.; DUBROVINSKY, L.S.; FROST, D.J.: 05.-09.12.2005, AGU Fall Meeting, San Francisco, USA^{*4}: "High pressure study of K-Na hollandite solid solution", EOS Trans. AGU, 86(52), Fall Meet. Suppl., Abstract MR31A-0125, 2005
- MANN, U.; MARKS, M.; MARKL, G.: 04.-06.03.2005, PERALK 2005, Workshop on Peralkaline Rocks, Tübingen, Germany: "Unusual mineral compositions in highly oxidized peralkaline igneous rocks: The Katzenbuckel volcano, Southwest Germany"
- MANN, U.; FROST, D.J.; RUBIE, D.C.: 24.-29.04.2005, EGU General Assembly 2005, Vienna, Austria^{*1}: "The effect of Si on dihedral angles between metallic Fe-rich liquids and forsterite and magnesium silicate perovskite", Geophysical Research Abstracts 7, 06674
- MANN, U.; FROST, D.J.; RUBIE, D.C.: 19.-26.06.2005, 7th European Mineralogical Union School 'Mineral Behaviour at Extreme Conditions', Heidelberg, Germany: "The effect of Si on dihedral angles between metallic Fe-rich liquids and silicate mantle minerals at high pressure", Book of Abstracts, 7
- MANN, U.; FROST, D.J.; RUBIE, D.C.; SHEARER, C.K.; AGEE, C.B.: 05.-09.12.2005, AGU Fall Meeting, San Francisco, USA^{*4}: "Constraints on oxygen fugacity during core formation – metal-silicate partitioning of nominally lithophile elements", EOS Trans. AGU, 86(52), Fall Meet. Suppl., Abstract MR13A-0052, 2005

MCCAMMON, C.A.; MCENROE, S.A.; ROBINSON, P.: 05.-09.09.2005, International Conference on the Applications of the Mössbauer Effect, Montpellier, France: "The nature of iron in ferrimagnetic nanolayers"

MCCAMMON, C.A.: 05.-07.10.2005, ESF Exploratory Workshop: The Reactivity of Iron Minerals in Natural Aquatic Systems, Thurnau, Germany: "Mössbauer spectroscopy at the BGI in Bayreuth, European Research Infrastructure: Transnational Access"

MCCAMMON, C.A.: 12.-14.11.2005, Joint Workshop of OXIDES and THESIS, Thurnau, Germany: "Iron in mantle phases: Influence on mantle properties and dynamics"

MCCAMMON, C.A.; MCENROE, S.; ROBINSON, P.: 05.-09.12.2005, AGU Fall Meeting, San Francisco, USA^{*4} (*invited*): "Applications of Mössbauer spectroscopy to lamellar magnetism", EOS Trans. AGU, 86(52), Fall Meet. Suppl., Abstract GP43B-02, 2005

MELOSH, H.J.: 18.-21.09.2005, 83. Jahrestagung der DMG, Aachen, Germany^{*3} (*Invited Plenary Lecture*): "Impact mineralogy: Behavior of silicates at ultrahigh pressures and temperatures"

MELOSH, H.J.: 13.10.2005, Paneth Kolloquium, Nördlingen, Germany (*Invited Keynote Talk*): "High speed ejection of rocks from planetary surfaces"

MIYAJIMA, N.; OHGUSHI, K.; ICHIHARA, M.; YAGI, T.; FROST, D. J.; RUBIE, D. C.: 05.-09.12.2005, AGU Fall Meeting, San Francisco, USA^{*4}: "Crystal morphology and dislocation textures of the CaIrO₃ phase – TEM study of an analogue of the post-perovskite phase", EOS Trans. AGU, 86(52), Fall Meet. Suppl., Abstract MR23B-0069, 2005

PIAZZONI, A.; BUNGE, H.-P.; STEINLE-NEUMANN, G.: 05.-09.12.2005, AGU Fall Meeting, San Francisco, USA^{*4}: "Towards driving mantle convection by mineral physics", EOS Trans. AGU, 86(52), Fall Meet. Suppl., Abstract V32B-05, 2005

POE, B.T.; ROMANO, C.; NESTOLA, F.; RUBIE, D.C.: 05.-09.12.2005, AGU Fall Meeting, San Francisco, USA^{*4}: "Electrical conductivity of hydrous single crystal San Carlos olivine", EOS Trans. AGU, 86(52), Fall Meet. Suppl., Abstract MR41A-0895, 2005

ROBINSON, P.; HARRISON, R.; MCENROE, S.; LANGENHORST, F.; HEIDELBACH, F.; HIRT, A.: 05.-09.12.2005, AGU Fall Meeting, San Francisco, USA^{*4}: "Lamellar magnetism: Ferrimagnetic effect of cation monolayers at interfaces of nanoscale exsolution lamellae", EOS Trans. AGU, 86(52), Fall Meet. Suppl., Abstract GP41A-0860, 2005

RUBIE, D.C.: 11.01.2005, Universität Münster, Institut für Geophysik, Münster, Germany: "Mechanisms of metal-silicate equilibration during core formation in terrestrial planets"

RUBIE, D.C.: 19.01.2005, ETH Zürich, Switzerland: "Mechanisms of metal-silicate equilibration during core formation on terrestrial planets"

RUBIE, D.C.: 24.01.2005, University of Oxford, Department of Earth Sciences, Oxford, UK: "Mechanisms of metal-silicate segregation during core formation in terrestrial planets"

RUBIE, D.C.; LIEBSKE, C.; TERASAKI, H.; REID, J.E.; ASAHARA, Y.: 11.03.2005, Workshop on the Earth's Core, Tokyo Institute of Technology, Tokyo, Japan: "Mechanisms of core formation on Earth and Mars"

RUBIE, D.C.: 16.06.2005, Institut de Physique du Globe de Paris, France: "Mechanisms of core formation on Earth and Mars"

- RUBIE, D.C.; LIEBSKE, C.; SCHMICKLER, B.; TERASAKI, H.; POE, B.; SUZUKI, A.; FUNAKOSHI, K.; ANDO, R.: 21.-23.07.2005, COMPRES Workshop on High-P Melts, Albuquerque, USA: "The transport properties of depolymerized silicate melts at high pressure"
- RUBIE, D.C.; FROST, D.J.; LANGENHORST, F.: 29.08.2005, 3rd DFG Colloquium on Mars and the Terrestrial Planets, Berlin, Germany: "Oxygen solubility in Fe-Ni alloy at high pressure and implications for the formation and compositions of planetary cores"
- RUBIE, D.C., LANGENHORST, F., ASAHARA, Y., FROST, D.J.: 18.-21.09.2005, 83. Jahrestagung der DMG, Aachen, Germany^{*3}: "A new model for oxygen solubility in liquid Fe as a function of pressure and temperature", Beihefte zum European Journal of Mineralogy 17, 114
- RUBIE, D.C.: 28.09.2005, Department of Geology and Geophysics, Yale University, New Haven, USA: "Core formation in terrestrial planets"
- RUBIE, D.C.: 30.09.2005, Department of Geological Sciences, Northwestern University, Evanston, USA: "Processes of core formation on Earth and Mars"
- RUBIE, D.C.: 21.10.2005, Forschungskollegium Physik des Erdkörpers (FKPE) Sitzung, Hamburg, Germany: "Core formation on Earth and Mars"
- RUBIE, D.C.; FROST, D.J.; ASAHARA, Y.; LANGENHORST, F.: 05.-09.12.2005, AGU Fall Meeting, San Francisco, USA^{*4}: "A new Model for Oxygen Solubility in Liquid Iron and the Oxygen Content of the Cores of Earth and Mars", EOS Trans. AGU, 86(52), Fall Meet. Suppl., Abstract MR21A-02, 2005
- SAIKIA, A.; FROST, D.J.; RUBIE, D.C.: 24.-29.04.2005, EGU General Assembly 2005, Vienna, Austria^{*1}: "The CaSiO₃ perovskite forming reaction at transition zone and lower mantle conditions", Geophysical Research Abstracts 7, 06786
- SAIKIA, A.; FROST, D.J.; RUBIE, D.C.: 19.-26.06.2005, 7th European Mineralogical Union School 'Mineral Behaviour at Extreme Conditions', Heidelberg, Germany: "The effect of pressure, temperature and composition on CaSiO₃ perovskite solubility in majorite garnet at mantle condition", Book of Abstracts, 8
- SAIKIA, A.; FROST, D.J.; RUBIE, D.C.: 05.-09.12.2005, AGU Fall Meeting, San Francisco, USA^{*4}: "The formation of calcium perovskite from majorite garnet: Implications for splitting of the 520 km seismic discontinuity", EOS Trans. AGU, 86(52), Fall Meet. Suppl., Abstract DI41A-1256, 2005
- SCHMICKLER, B.; LIEBSKE, C.; HOLZAPFEL, C.; RUBIE, D.C.: 05.-09.12.2005, AGU Fall Meeting, San Francisco, USA^{*4}: "Viscosity of peridotite liquid up to 24 GPa: Predictions from self-diffusion coefficients", EOS Trans. AGU, 86(52), Fall Meet. Suppl., Abstract MR11A-06, 2005
- SCHUBERTH, B.; PIAZZONI, A.; BUNGE, H.-P.; IGEL, H.; STEINLE-NEUMANN, G.: 05.-09.12.2005, AGU Fall Meeting, San Francisco, USA^{*4}: "Simulation of 3D global wave propagation through geodynamic models", EOS Trans. AGU, 86(52), Fall Meet. Suppl., Abstract NG43B-0570, 2005
- SHIRYAEV, A.; GRAMBOLE, D.; RIVERA, A.; FOLLKER, H.: 12.-16.09.2005, 7th National Semiconductor Physics Conference, Moscow region, Russia: "Experimental investigation of hydrogen diffusion in diamonds"

- SHIRYAEV, A.; DEMBO, K.: 14.-19.11.2005, 5th National Conference on Applications of X-rays, Neutrons and Electrons for Solid State Research, Moscow, Russia: "Small-angle X-ray and neutron scattering in diamonds"
- SMYTH, J.R.; NESTOLA, F.; FROST, D.J.; HOLL, C.M.; BROMILEY, G.: 05.-09.12.2005, AGU Fall Meeting, San Francisco, USA*⁴: "Hydration effects on molar volume and compressibility of olivine", EOS Trans. AGU, 86(52), Fall Meet. Suppl., Abstract MR44A-03, 2005
- SPIVAK, A.; SHIRYAEV, A.; NOZHKINA, A.; LITVIN, Yu.: 30.05.-02.06.2005, ICCM'2005, International Conference on Crystal Materials, Kharkov, Ukraine: "Carbonate-synthetic diamond: crystal growth and properties"
- STEINLE-NEUMANN, G.: 19.10.2005: Department of Earth Sciences, Ruhr-Universität Bochum, Germany: "Squeezing spin: Magnetism in Earth materials"
- STEINLE-NEUMANN, G.: 30.11.2005, Scripps Institute of Oceanography, University of California at San Diego, La Jolla, USA: "Squeezing spin: Magnetism in Earth materials"
- STOYANOV, E.; STEINLE-NEUMANN, G.; LANGENHORST, F.: 19.-26.06.2005, 7th European Mineralogical Union School 'Mineral Behaviour at Extreme Conditions', Heidelberg, Germany: "Cr – L_{2,3} electron energy loss near-edge structures of Cr-bearing phases: fingerprint to the valence state and the coordination of Cr", Book of Abstracts, 13
- STOYANOV, E.; STEINLE-NEUMANN, G.; LANGENHORST, F.: 18.-21.09.2005, 83. Jahrestagung der DMG, Aachen, Germany*³: "Cr – L_{2,3} electron energy loss near-edge structures of Cr-bearing phases: fingerprint to the valence state and the coordination of Cr", Beihefte zum European Journal of Mineralogy 17, 135
- STOYANOV, E.; LANGENHORST, F.; STEINLE-NEUMANN, G.; FROST, D.J.: 05.-09.12.2005, AGU Fall Meeting, San Francisco, USA*⁴: "Titanium – L_{3,2} and O-K electron energy loss near-edge structures of Ti_xO_y phases: fingerprints to the valence state and site geometry", EOS Trans. AGU, 86(52), Fall Meet. Suppl., Abstract V31B-0607, 2005
- TERASAKI, H.; RUBIE, D.C.; FROST, D.J.; LANGENHORST, F.: 11.03.2005, Workshop on the Earth's Core, Tokyo Institute of Technology, Tokyo, Japan: "Connectivity of liquid Fe-S-O alloy and solubility of oxygen in Fe-alloy under high pressure: Possibility of percolative core formation"
- TERASAKI, H.; RUBIE D.C.; MANN, U.; FROST, D.J.; LANGENHORST, F.: 14.-18.03.2005, 36th Lunar and Planetary Science Conference, Houston, USA: "The effects of oxygen, sulphur and silicon on the dihedral angles between Fe-rich liquid metal and olivine, ringwoodite and silicate perovskite: Implications for planetary core formation"
- UVAROVA, Y.; MCCAMMON, C.A.; SOKOLOVA, E.; HAWTHORNE, F.C.; LOBANOV, K.V.; KAZANSKY, V.I.: 15.-18.05.2005, Joint Annual Meeting of the Geological Association of Canada, Mineralogical Association of Canada, Canadian Society of Petroleum Geologists and the Canadian Society of Soil Science, Halifax, Canada: "Fe³⁺ content and Ti⁴⁺ ordering in amphiboles from the Kola superdeep borehole: Correlation of crystal-chemical and Mössbauer measurements"
- WALTE, N.P.; FROST, D.J.; RUBIE, D.C.: 02.-04.05.2005, Deformation mechanisms, Rheology and Tectonics Meeting, ETH Zürich, Switzerland: "The role of deformation on the interconnection of Fe-S melts in olivine aggregates"

- WALTE, N.P.; FROST, D.J.; RUBIE, D.C. (2005): 01.-04.10.2005 'Sheared Magmas in Nature and Experiment: Bridging the Brittle and Ductile Fields' Conference, Kloster Seeon/München, Germany: "Melt distribution and non-continuous melt migration during deformation of a crystalline aggregate that contains a high-dihedral angle melt phase (Olivine- FeS)"
- WALTE, N.P.; FROST, D.J.; RUBIE, D.C.: 05.-09.12.2005, AGU Fall Meeting, San Francisco, USA^{*4}: "Is core-formation enhanced by deformation? Olivine-FeS melt experiments with the Deformation-DIA", EOS Trans. AGU, 86(52), Fall Meet. Suppl., Abstract T33F-05, 2005
- WALTE, N.P.; Keppler, H.: 05.-09.12.2005, AGU Fall Meeting, San Francisco, USA^{*4} (*invited*): "*In situ* optical observation of high-temperature geological processes with the Moissanite Cell", EOS Trans. AGU, 86(52), Fall Meet. Suppl., Abstract MR13B-05, 2005
- WENZEL, M.J.; STEINLE-NEUMANN, G.: 27.06.-01.07.2005: Joint 20th AIRAPT – 43rd EHPRG, Karlsruhe, Germany^{*2}: "Absence of charge localization in compressed magnetite from first principles computations"
- WENZEL, M.J.; STEINLE-NEUMANN, G.: 05.-09.12.2005, AGU Fall Meeting, San Francisco, USA^{*4}: "Absence of charge localization in magnetite under pressure", EOS Trans. AGU, 86(52), Fall Meet. Suppl., Abstract MR23A-0040, 2005
- WESTRAADT, J.E.; NEETHLING, J.H.; DUBROVINSKAIA, N.A.; SIGALAS, I.: The South African Microscopy Conference, July 2005: "Processing and characterization of heat resistant polycrystalline diamond with calcium carbonate as sintering aid"
- ZEDGENIZOV, D.; SHIRYAEV, A.; KAGI, H.; FEDOROVA, E.: 05.-06.03.2005, COE-21 International Symposium on 'Origin, Evolution and Dynamics of the Earth', Misasa, Japan: "Water-related absorption in fibrous diamonds"

^{*1} EGU: European Geosciences Union General Assembly 2005, 24.-29.04.2005, Vienna, Austria, Geophysical Research Abstracts, 7

^{*2} Joint 20th AIRAPT – 43rd EHPRG International Conference on High Pressure Science and Technology, 27.06.-01.07.2005, Karlsruhe, Germany

^{*3} DMG: 83. Jahrestagung der Deutschen Mineralogischen Gesellschaft, 18.-21.09.2005, Aachen, Germany – Beihefte zum European Journal of Mineralogy 17

^{*4} AGU: American Geophysical Union Fall Meeting, 05.-09.12.2004, San Francisco, USA – EOS Transactions, American Geophysical Union, 86(52), AGU Fall Meeting 2005 Supplement

5.4 Lectures and seminars at Bayerisches Geoinstitut

- ABRIKOSOV, I.: 23.09.2005 "First-principles simulations of alloy thermodynamics in megabar pressure range"

- AKBER-KNUTSON, S.: 22.07.2005 "The effect of chemical heterogeneity on the perovskite – post-perovskite phase transition"
- ALLALEN, M.: 03.11.2005 "Magnetic properties and proton-spin lattice relaxation rate T1 of heterometallic wheels"
- AUDÉTAT, A.: 25.05.2005 "Fluids in the Earth"
- BELMONTE, A.E.: 13.05.2005 "Solid state chemistry of the Y₂Si₂O₇-Ln₂Si₂O₇ systems"
- BONS, P.: 23.06.2005 "Numerical modelling of metamorphic and tectonic microstructures with ELLE"
- CARACAS, R.: 22.11.2005 "Exploring the interior of the Earth with theoretical mineralogy"
- DE RONDE, A.: 20.01.2005 "Interactions between metamorphism and deformation: An experimental study on plagioclase-olivine rocks"
- DUBROVINSKAIA, N.A.: 14.04.2005 "Synthesis and properties of new materials in the B-C system"
- FABBRIZIO, A.: 13.01.2005 "Experimental data on biotite + magnetite + sanidine saturated phonolitic melts and application to the estimation of magmatic water fugacity"
- FUJINO, K.: 02.09.2005 "Cation substitution and structural change in silicate perovskites"
- GUDFINSSON, G.: 28.07.2005 "Experimental evidence for continuous gradations among CO₂-rich and CO₂-poor melts in equilibrium with garnet lherzolite at 3-8 GPa"
- HEWINS, R.: 09.06.2005 "Experimental constraints on chondrule formation"
- KANTOR, I.: 01.12.2005 "Spin crossover in ferropericlase: a Mössbauer spectroscopic study"
- KENNETT, B.: 10.06.2005 "The nature of seismic mantle heterogeneity"
- KESHAV, S.: 08.07.2005 "Is the Earth's outer core so giving?"
- KING, S.: 27.05.2005 "Mantle equation of state and convection: Toward a more integrated picture"
- KLOTZ, S.: 20.10.2005 "Neutron diffraction at high pressure"
- KRISCH, M.: 12.01.2005 "Inelastic X-ray scattering from phonons at high pressure: present status and perspectives"
- KURNOSOV, A.: 15.12.2005 "Methane clathrate in Titan's interior"
- LITASOV, K.: 04.05.2005 "Effect of water on the phase relations in the Earth's mantle and deep water cycle"
- MELOSH, H.J.: 10.11.2005 "First results of NASA's Deep Impact experiments"
- MIYAJIMA, N.: 26.01.2005 "Behavior of trivalent ions of the Earth's lower mantle: Analytical Transmission Electron Microscopy"
- PIAZZONI, A.: 27.01.2005 "Towards driving mantle convection by mineral physics"
- ROUQUETTE, J.: 13.01.2005 "Pressure-temperature-composition phase diagram of the lead zirconate titanate solid solution Pb (Zr_{1-x}Ti_x)O₃ (PZT)"
- SHANKLAND, T.J.: 11.08.2005 "Heat transport in upper mantle minerals"
- SHCHEKA, S.: 21.04.2005 "Carbon solubility in major mantle minerals"
- SYASSEN, K.: 24.11.2005 "'Simple' metals at high pressures"
- TAKAFUJI, N.: 04.05.2005 "Chemical reaction between molten iron and silicates and segregation of core melts in the lower mantle"
- TERRY, M.: 31.01.2005 "Geothermobarometry of kyanite eclogites with experimental results in the CMAS system and simultaneous deformation and diffusion in ferropericlase"

UPADHYAY, C.: 10.10.2005 "Fe II-III layered double hydroxides: Green rust and its oxidized forms"

VINOGRAD, V.: 27.10.2005 "Monte Carlo modelling of ordering and mixing in pyrope-majorite solid solution"

WESTRAADT, J.: 28.04.2005 "Synthesis of thermally stable PCD by using non-metallic sintering aids"

WU, X.: 10.03.2005 "The high-pressure behaviour of GdFeO₃-type perovskites and Sr₂RuO₄ superconductor"

ZHANG, A.: 19.01.2005 "Phosphorus in the Earth's interior"

ZIMOVA, M.: 30.06.2005 "Volatiles in aluminosilicate melts"

5.5 Conference organization

16.-20.11.2005, ESF PESC Exploratory Workshop on Novel Superhard Materials, Bayreuth, Germany (DUBROVINSKY, L.S.; DUBROVINSKAIA, N.A.)

6. Visiting scientists

6.1 Visiting scientists funded by the Bayerisches Geoinstitut

- ABRIKOSOV, I.A., Linköping University, Sweden: 22.-24.09.2005
- ALLALEN, M., Universität Osnabrück, Fachbereich Physik, Osnabrück, Germany: 02.-04.11.2005
- ARIESTO, M., Aachen, Germany: 11.-13.07.2005
- BONS, P., Universität Tübingen, Institut für Geowissenschaften, Tübingen, Germany: 23.-24.06.2005
- CARACAS, R., Carnegie Institution of Washington, Geophysical Laboratory, Washington DC, USA: 21.-25.11.2005
- DE RONDE, A.A., Universität Basel, Geologisch-Paläontologisches Institut, Basel, Switzerland: 19.-21.01.2005
- ECSEDI, Z., "Politehnica" University of Timisoara, Romania: 14.-18.02.2005
- FABBRIZIO, A., Università degli Studi di Camerino, Dipartimento di Scienze della Terra, Camerino, Italy: 10.-14.01.2005
- GATTA, G.D., Università degli Studi di Milano, Dipartimento di Scienze della Terra, Milano, Italy: 09.-21.05.2005, 28.05.-10.06.2005
- GUDFINNSSON, G., Carnegie Institution of Washington, Geophysical Laboratory, Washington DC, USA: 26.-31.07.2005
- HEWINS, R., Rutgers, The State University of New Jersey, New Brunswick, USA: 09.-10.06.2005
- JACOBSEN, S.D., Carnegie Institution of Washington, Geophysical Laboratory, Washington DC, USA: 27.01.-13.02.2005
- JOSEPH, S., Mahatma Gandhi University Kerala, Kottayam, India: 25.-30.01.2005
- KENNETT, B., The Australian National University, Research School of Earth Sciences, Earth Physics, Canberra, Australia: 09.-11.06.2005
- KESHAV, S., Carnegie Institution of Washington, Geophysical Laboratory, Washington DC, USA: 06.-10.07.2005
- KING, S., Purdue University, Department of Earth & Atmospheric Sciences, West Lafayette, USA: 26.-28.05.2005
- KLOTZ, S., Université Pierre et Marie Curie, Paris, France: 19.-21.10.2005
- KOZLENKO, D.P., Frank Laboratory for Neutron Physics, Joint Institute for Nuclear Research, Dubna, Moscow Region, Russia: 12.09.-11.10.2005
- KRISCH, M., ESRF Grenoble, France: 12.-13.01.2005
- LITASOV, K., Tohoku University, Institute of Mineralogy, Petrology and Economic Geology, Sendai, Japan: 02.-04.05.2005
- LIU, X., Beijing University, Department of Geology, Beijing, China: 17.-24.04.2005
- MIYAJIMA, N., University of Tokyo, Institut for Solid State Physics, Tokyo, Japan: 24.-30.01.2005
- MOSENFELDER, J., California Institute of Technology, Pasadena, USA: 14.09.-03.10.2005

OKUBE, M., Tokyo Institute of Technology, Materials and Structures Laboratory, Yokohama, Japan: 21.-23.08.2005

PFEIFER, C., Universität Mainz, Germany: 30.06.-01.07.2005

QIN, S., Beijing University, Beijing, China: 15.07.-30.08.2005

ROUQUETTE, J., Montpellier II University, Montpellier, France: 12.-16.01.2005

SHCHEKA, S., Universität Tübingen, Mineralogisches Institut, Tübingen, Germany: 20.-22.04.2005

SYASSEN, K., Max-Planck-Institut für Festkörperforschung, Servicegruppe Hochdruck, Stuttgart, Germany: 24.-25.11.2005

SCHMICKLER, B., Göttingen, Germany: 11.-14.07.2005

TAKAFUJI, N., Tokyo Institute of Technology, Japan: 02.-08.05.2005

TENNANT, C., University of Canterbury, Chemistry Department, Christchurch, New Zealand: 21.06.-11.11.2005

UPADHYAY, C., CNRS-Université Henri Poincaré, LCPME, Nancy, France: 09.-14.10.2005

VINOGRAD, V., Universität Frankfurt/M., Kristallographie, Frankfurt/M., Germany: 27.-28.10.2005

WERE, P., Universität Tübingen, Mineralogisches Institut, Tübingen, Germany: 27.-30.11.2005, 05.-09.12.2005

WU, X., Chinese Academy of Sciences, Beijing, China: 08.-13.03.2005

YELAMANCHILI, R.S., Uttar Pradesh, India: 23.-29.01.2005

ZHANG, A., Nanjing University, Department of Earth Sciences, Nanjing, China: 16.-23.01.2005

ZIMOVA, M., Geowissenschaftliches Zentrum Göttingen, Abteilung Mineralogie, Göttingen, Germany: 29.06.-01.07.2005

ZOTOV, N., Forschungszentrum caesar, Bonn, Germany: 05.-06.07.2005

6.2 Visiting scientists supported by other externally funded BGI projects

ADJAOUD, O., Université Mouloud Mammeri, Laboratoire de Physique et Chimie Quantique, Tizi-Ouzou, Algeria: 05.-09.09.2005 (International Graduate School under the Elitenetzwerk Bayern)

AKAOGI, M., Gakushuin University, Tokyo, Japan: *"High temperature calorimetry: New developments of experimental methods"*, *"High temperature calorimetry: Applications to mantle minerals and related substances"*, 21.07.-04.08.2005 (International Graduate School under the Elitenetzwerk Bayern)

AKBER-KNUTSON, S., California Institute of Technology, Pasadena, USA: *"D" and the MgSiO₃ post-perovskite phase"*, 18.-28.07.2005 (International Graduate School under the Elitenetzwerk Bayern)

ALESSANDRI, I., Università degli Studi di Brescia, Italy: *"Crystallization and nanostructuring in glasses for second harmonic generation (SHG)"*, 18.-23.04.2005 (EU "Research Infrastructures: Transnational Access" Programme)

- AUZENDE, A.I., IMPMC, Paris, France: *"Deformation of antigorite serpentinites under subduction conditions"*, 14.-25.03.2005 (EU "Research Infrastructures: Transnational Access" Programme)
- BERGESE, P., Università degli Studi di Brescia, Italy: *"Crystallization and nanostructuring in glasses for second harmonic generation (SHG)"*, 18.-23.04.2005 (EU "Research Infrastructures: Transnational Access" Programme)
- BERRY, A., Imperial College London, Department of Earth Sciences and Engineering, London, U.K.: *"High-resolution ^{17}O NMR studies of high-pressure mantle silicates"*, 20.-30.11.2005 (EU "Research Infrastructures: Transnational Access" Programme)
- BERTHET, S., Université de Marne-la-Vallée, Laboratoire des Geomateriaux, Marne-la-Vallée, France: *"Partitioning of the first series transition metals (Cr, Mn, Fe, Co, Ni) and W among silicate, sulfide and metal under high pressure: implications for the Earth's core formation"*, 27.06.-11.07.2005 (EU "Research Infrastructures: Transnational Access" Programme)
- BRAZHKIN, V., Russian Academy of Sciences, Institute for High Pressure Physics, Troitsk, Moscow Region, Russia: *"Liquid and glassy oxides (SiO_2 , GeO_2 , B_2O_3) under pressure"*, 17.-21.11.2005 (International Graduate School under the Elitenetzwerk Bayern)
- CATLOW, R., The Royal Institution of Great Britain, Davy Faraday Research Laboratory, London, U.K.: *"Predictive modelling in materials chemistry"*, *"Modelling of structural and defect properties of solids"*, 20.-21.07.2005 (International Graduate School under the Elitenetzwerk Bayern)
- CERA, F., Università degli Studi di Perugia, Dipartimento di Scienze della Terra, Perugia, Italy: *"The high-pressure behaviour of 10 \AA phase: in situ microraman and IR spectroscopic investigation"*, 02.-07.05.2005, 13.-22.07.2005 (EU "Research Infrastructures: Transnational Access" Programme)
- CERA, F., Università degli Studi di Perugia, Dipartimento di Scienze della Terra, Perugia, Italy: *"The high-pressure behaviour of 10 \AA phase: in situ microraman and X-ray diffraction investigation"*, 11.-18.12.2005 (EU "Research Infrastructures: Transnational Access" Programme)
- CHEN, S., Tianjin University, Tianjin, China: 10.-12.11.2005 (International Graduate School under the Elitenetzwerk Bayern)
- COMBES, R., Université de Marne-la-Vallée, Laboratoire des Geomateriaux, Marne-la-Vallée, France: *"Partitioning of the first series transition metals (Cr, Mn, Fe, Co, Ni) and W among silicate, sulfide and metal under high pressure: implications for the Earth's core formation"*, 06.-12.07.2005 (EU "Research Infrastructures: Transnational Access" Programme)
- COMODI, P., Università di Perugia, Dipartimento di Scienze della Terra, Perugia, Italy: *"The high-pressure behaviour of 10 \AA phase: in situ microraman and IR spectroscopic investigation"*, 01.-06.05.2005, 13.-22.07.2005 (EU "Research Infrastructures: Transnational Access" Programme)
- DE RONDE, A., University College London, Department of Earth Sciences, London, U.K.: *"Do old faults die? The deformation mechanism of olivine fault"*, 30.10.-05.11.2005 (EU "Research Infrastructures: Transnational Access" Programme)

- DOBSON, D., University College London, Department of Earth Sciences, London, U.K.: *"Do old faults die? The deformation mechanism of olivine fault"*, 30.10.-05.11.2005 (EU "Research Infrastructures: Transnational Access" Programme)
- DUPAS-BRUZEK, C., Université des Sciences et Technologies de Lille 1, Centre d'Etudes et de Recherches, Villeneuve d'Ascq, France: *"Transmission electron microscope investigations of natural intracrystalline ringwoodite in olivine in shocked L-6 chondrites"*, 27.06.-01.07.2005, 17.-21.10.2005 (EU "Research Infrastructures: Transnational Access" Programme)
- DZWILEWSKI, A., Umeå University, Experimental Physics, Umeå, Sweden: *"Synthesis of new fullerene materials by extreme hydrogenation at high pressure high temperature conditions and their characterization"*, 27.04.-11.05.2005 (EU "Research Infrastructures: Transnational Access" Programme)
- ESCUADERO, A., Universidad de Sevilla, Instituto de Ciencia de Materiales de Sevilla, Spain: *"Study of phase transitions in the $Y_{2-x}Ln_xSi_2O_7$ system (Ln =lanthanides) at high temperatures and pressures"*, 29.04.-16.05.2005 (EU "Research Infrastructures: Transnational Access" Programme)
- GATTA, G.D., Università degli Studi di Milano, Dipartimento di Scienze della Terra, Milano, Italy: *"Single crystal X-ray diffraction of magnetite Fe_3O_4 at high pressure"*, 28.11.-19.12.2005 (EU "Research Infrastructures: Transnational Access" Programme)
- GROVE, T., Massachusetts Institute of Technology, Cambridge, USA: *"The role of H_2O in subduction zone magmatism: What's happening today and how things were different in the Archean"*, 29.10.-01.11.2005 (International Graduate School under the Elitenetzwerk Bayern)
- GUILLAUME, C., The University of Edinburgh, School of Engineering + Electronics, Edinburgh, U.K.: *"Synthesis of alloys and ceramics at high pressures and temperatures"*, 01.-07.05.2005, 09.-17.10.2005 (EU "Research Infrastructures: Transnational Access" Programme)
- HUANG, X., University of Beijing, Department of Inorganic and Nonmetallic Materials, Beijing, China: 10.-12.11.2005 (International Graduate School under the Elitenetzwerk Bayern)
- HUNT, S., University College London, Department of Earth Sciences, London U.K.: *"Rheology of garnets"*, 11.07.-31.12.2005 (EU Marie Curie Training Site)
- IWANOW, N., Universität Stuttgart, Institut für Fördertechnik und Logistik, Stuttgart, Germany: 10.-12.11.2005 (International Graduate School under the Elitenetzwerk Bayern)
- IUGA, M., Fraunhofer ISC, Würzburg, Germany: 23.-25.05.2005 (International Graduate School under the Elitenetzwerk Bayern)
- JACOBSEN, S.D., Carnegie Institution of Washington, Geophysical Laboratory, Washington DC, USA: *"New techniques in experimental geophysics: revealing the lower-mantle mineralogy"*, *"Bridging experimental and observational geophysics: identifying hydration in Earth's interior"*, 07.-23.10.2005 (International Graduate School under the Elitenetzwerk Bayern)
- KALO, H., University of Aleppo, Syria: 23.-30.07.2005 (International Graduate School under the Elitenetzwerk Bayern)

- KERTSER, M.; Tel Aviv University, School of Physics & Astronomy, Tel Aviv, Israel: *"Structural, electronic, and magnetic properties of high-pressure phases of the Spin-Frustrated Mott insulator $AFeO_2$ ($A=Cu, Ag, Na$) delafossites"*, 10.-23.07.2005 (EU "Research Infrastructures: Transnational Access" Programme)
- KÖHL, M., Andernach, Germany: 06.-08.03.2005 (International Graduate School under the Elitenetzwerk Bayern)
- KURAKEVYCH, O., Université Paris Nord, LPMTM-CNRS, Institut Galilée, Villetaneuse, France: *"High-pressure high-temperature synthesis and structural studies of novel superhard phases in the B-C system"*, 03.-14.07.2005 (EU "Research Infrastructures: Transnational Access" Programme)
- LIEBSKE, C., ETH Zürich, Institut für Mineralogie und Petrographie, Zürich, U.K.: *"Melting relations along the join $MgO-SiO_2$ at transition zone and lower mantle pressure"*, 01.-09.10.2005 (EU "Research Infrastructures: Transnational Access" Programme)
- MALAVERGNE, V., Université de Marne-la-Vallée, Laboratoire des Geomateriaux, Marne-la-Vallée, France: *"Partitioning of the first series transition metals (Cr, Mn, Fe, Co, Ni) and W among silicate, sulfide and metal under high pressure: implications for the Earth's core formation"*, 27.06.-03.07.2005 (EU "Research Infrastructures: Transnational Access" Programme)
- MARIANI, E., University of Liverpool, Department of Earth and Ocean Sciences, Liverpool, U.K.: *"Electrical conductivity of rocks during recrystallization"*, 04.02.-04.03.2005 (EU "Research Infrastructures: Transnational Access" Programme)
- MCENROE, S., Geological Survey of Norway, Trondheim, Norway: *"The influence of pressure on the magnetic properties of the ilmenite-hematite solid solution"*, 17.-23.10.2005 (EU "Research Infrastructures: Transnational Access" Programme)
- MCMILLAN, P., University College London, Department of Chemistry, London, U.K.: *"High pressure materials chemistry"*, *"Amorphous polymorphism and liquid-liquid phase transitions"*, 13.-16.11.2005 (International Graduate School under the Elitenetzwerk Bayern)
- MECKLENBURGH, J., University of Manchester, School of Earth, Atmospheric and Environmental Sciences, Manchester, U.K.: *"Electrical conductivity of rocks during recrystallization"*, 04.02.-04.03.2005 (EU "Research Infrastructures: Transnational Access" Programme)
- PAVÓN, E., Universidad de Sevilla, Instituto de Ciencia de Materiales de Sevilla, Spain: *"Study of phase transitions in the $Y_{2-x}Ln_xSi_2O_7$ system ($Ln=lanthanides$) at high temperatures and pressures"*, 02.-16.05.2005 (EU "Research Infrastructures: Transnational Access" Programme)
- PIAZZONI, A.S., Università degli Studi di Milano, Dipartimento di Scienze della Terra "Ardito Desio", Milano, Italy: *"Self-consistent mantle modelling using geodynamic mantle flow simulation and mineral physics"*, 01.01.-31.01.2005 (EU Marie Curie Training Site)
- PIAZZONI, A., Ludwig-Maximilians-Universität München, Department für Geo- und Umweltwissenschaften, München, Germany: 05.-08.09.2005 (International Graduate School under the Elitenetzwerk Bayern)

- PLATTNER, C., Ludwig-Maximilians-Universität München, Lehrstuhl für Geographie, München, Germany: 23.-24.05.2005 (International Graduate School under the Elitenetzwerk Bayern)
- POE, B., Università degli Studi "G. d'Annunzio", Chieti, Italy: *"Synthesis and electrical conductivity measurement of hydrous olivine single crystals"*, 04.-26.07.2005 (EU "Research Infrastructures: Transnational Access" Programme)
- ROBINSON, P., Geological Survey of Norway, Trondheim, Norway: *"The influence of pressure on the magnetic properties of the ilmenite-hematite solid solution"*, 20.-26.10.2005 (EU "Research Infrastructures: Transnational Access" Programme)
- ROMANO, C., Università degli Studi "G. d'Annunzio", Chieti, Italy: *"Synthesis and electrical conductivity measurement of hydrous olivine single crystals"*, 04.-26.07.2005 (EU "Research Infrastructures: Transnational Access" Programme)
- ROZENBERG, G.; Tel Aviv University, School of Physics & Astronomy, Tel Aviv, Israel: *"Structural, electronic, and magnetic properties of high-pressure phases of the Spin-Frustrated Mott insulator $AFeO_2$ ($A=Cu, Ag, Na$) delafossites"*, 10.-23.07.2005 (EU "Research Infrastructures: Transnational Access" Programme)
- SCHMIDT, P., TU Dresden, Institut für Anorganische Chemie, Dresden, Germany: *"Existence of inorganic solids dependent on the partial pressure: Thermodynamic calculations and experiments"*, 24.-25.10.2005 (International Graduate School under the Elitenetzwerk Bayern)
- SHINOVA, E., Bulgarian Academie of Sciences, Sofia, Bulgaria: *"High-pressure synthesis of electrode materials for Lithium-Ion batteries III. Formation of solid solutions between layered $LiNiO_2$ and monoclinic $Li(Li_{1/3}Mn_{2/3})O_2$ under high-oxygen pressure"*, 06.-13.05.2005 (EU "Research Infrastructures: Transnational Access" Programme)
- SMYTH, J.R., University of Colorado, Boulder, USA: 28.-31.01.2005 (EU "Research Infrastructures: Transnational Access" Programme)
- SOLOZHENKO, V., Université Paris Nord, LPMTM-CNRS, Institut Galilée, Villetaneuse, France: *"High-pressure high-temperature synthesis and structural studies of novel superhard phases in the B-C system"*, 03.-14.07.2005 (EU "Research Infrastructures: Transnational Access" Programme)
- STOYANOVA, R., Bulgarian Academie of Sciences, Sofia, Bulgaria: *"High-pressure synthesis of electrode materials for Lithium-Ion batteries III. Formation of solid solutions between layered $LiNiO_2$ and monoclinic $Li(Li_{1/3}Mn_{2/3})O_2$ under high-oxygen pressure"*, 02.-09.05.2005 (EU "Research Infrastructures: Transnational Access" Programme)
- STOYANOVA, R., Bulgarian Academie of Sciences, Sofia, Bulgaria: *"High-pressure synthesis of novel compositions in the $LiNiO_2$ - $Li[Li_{1/3}Ti_{2/3}]O_2$ " system"*, 25.10.-11.11.2005 (EU "Research Infrastructures: Transnational Access" Programme)
- TALYZIN, A., Umeå University, Experimental Physics, Umeå, Sweden: *"Synthesis of new fullerene materials by extreme hydrogenation at high pressure high temperature conditions and their characterization"*, 27.04.-11.05.2005 (EU "Research Infrastructures: Transnational Access" Programme)

- TOMLINSON, E., University College London, Department of Earth Sciences, London, U.K.:
"Superdeep diamond: Morphology, growth and nitrogen content", 13.-22.11.2005 (EU
 "Research Infrastructures: Transnational Access" Programme)
- WANG, Y., Technical University of Denmark, Department of Chemistry, Lyngby, Denmark:
"Synthesis and characterization of bulk metallic glasses in zirconium and titanium",
 22.10.-01.11.2005 (EU "Research Infrastructures: Transnational Access" Programme)
- YONCHEVA, M., Bulgarian Academie of Sciences, Sofia, Bulgaria: *"High-pressure
 synthesis of novel compositions in the "LiNiO₂-Li[Li_{1/3}Ti_{2/3}]O₂" system"*, 25.10.-11.11.2005
 (EU "Research Infrastructures: Transnational Access" Programme)

6.3 Visitors (externally funded)

- ANDREOZZI, G.B., Università degli Studi di Roma "La Sapienza", Dipartimento di Scienze
 della Terra, Roma, Italy: 03.-06.07.2005
- BECHMANN, M., Universität Dortmund, Fachbereich Physik, Dortmund, Germany: 15.-
 17.06.2005
- CHAMPALLIER, R., C.N.R.S., Institut des Sciences de la Terre d'Orléans, France: 02.-
 03.03.2005
- CORDIER, P., Université des Sciences et Technologies de Lille, Laboratoire de Structure et
 Propriétés de l'Etat Solide, Villeneuve d'Ascq, France: 28.02.-01.03.2005, 10.04.-
 23.04.2005, 18.-30.07.2005
- COSTA, F., Ruhr-Universität, Bochum, Institut für Geologie, Mineralogie, und Geophysik,
 Bochum, Germany: 23.-25.11.2005
- COUVY, H., Université des Sciences et Technologies de Lille, Laboratoire de Structure et
 Propriétés de l'Etat Solide, Villeneuve d'Ascq, France: 28.02.-05.03.2005
- DOBSON, D., University College London, Department of Earth Sciences, London, U.K.: 08.-
 12.08.2005, 22.-26.08.2005
- GALADÍ ENRÍQUES, E., Universität Frankfurt/M., Institut für Geowissenschaften,
 Frankfurt/M., Germany: 21.-24.11.2005
- GOLDIN, T., University of Arizona, Lunar and Planetary Laboratory, Tucson, USA: 03.09.-
 31.12.2005
- GROSS, T., Technische Universität Darmstadt, Fachbereich Materialwissenschaft,
 Darmstadt, Germany: 04.-08.04.2005
- HANSEN, U., Westfälische Wilhelms-Universität Münster, Institut für Geophysik, Münster,
 Germany: 07.-08.07.2005
- HOLZHEID, A., Westfälische Wilhelms-Universität Münster, Institut für Mineralogie,
 Münster, Germany: 25.-28.01.2005, 10.-11.08.2005
- HUSTOFT, J., University of Minnesota, Department of Geology & Geophysics, Minneapolis,
 USA: 09.-21.05.2005
- KEGLER, P., Universität Köln, Germany: 17.-31.01.2005

KONZETT, J., Universität Innsbruck, Institut für Mineralogie und Petrographie, Innsbruck, Austria: 14.-24.02.2005, 12.-25.09.2005

LANG, M., Gesellschaft für Schwerionenforschung mbH, Darmstadt, Germany: 04.-08.04.2005

LEROUX, H., Université des Sciences et Technologies de Lille, Laboratoire de Structure et Propriétés de l'Etat Solide, Villeneuve d'Ascq, France: 28.02.-01.03.2005

LIEBERMANN, R., Stony Brook University, Mineral Physics Institute, Stony Brook, USA: 03.-04.05.2005

LINNEN, R., University of Waterloo, Department of Earth Sciences, Waterloo, Canada: 01.-03.12.2005

LITVIN, Y., Institute of Experimental Mineralogy, Chernogolovka, Russia: 18.09.-02.10.2005

LOCHERER, T., Technische Universität Darmstadt, Fachbereich Materialwissenschaft, Darmstadt, Germany: 04.-08.04.2005

LONGO, M., Università di Roma "La Sapienza", Dipartimento di Scienze della Terra, Roma, Italy: 10.01.-29.07.2005

MEZOUAR, M., ESRF Grenoble, France: 20.-23.10.2005

NAKAMOTO, Y., Osaka University, Japan: 31.08.-02.09.2005

NEUFELD, K., Universität Mainz, Institut für Geowissenschaften, Mainz, Germany: 02.-04.02.2005, 31.03.-05.04.2005, 06.-11.10.2005, 10.-14.11.2005

NJIEKAK, G., Universität Frankfurt/M., Institut für Geowissenschaften, Frankfurt/M., Germany: 22.-28.08.2005

PEREIRA, A.S., Universidade Federal do Rio Grande do Sul, Porto Alegre, Brasil: 22.-26.06.2005

PICHAVANT, M., C.N.R.S., Institut des Sciences de la Terre d'Orléans, France: 02.-03.03.2005

PISTORINO, M., Università degli Studi di Pavia, Dipartimento di Scienze della Terra, Pavia, Italy: 20.-24.06.2005

REICHMANN, H.-J., GeoForschungsZentrum Potsdam, Germany: 27.-29.04.2005

SEBALD, A., Universität Dortmund, Fachbereich Physik, Dortmund, Germany: 15.-17.06.2005

SHANKLAND, T., GeoForschungsZentrum Potsdam, Germany: 11.-13.08.2005

SHUSHKANOVA, A., Institute of Experimental Mineralogy, Chernogolovka, Russia: 18.-28.09.2005

SIMAK, S., Linköpings University, Sweden: 22.-24.09.2005

SWAMY, V., Monash University, School of Physics & Material Engineering, Victoria, Australia: 16.-23.03.2005, 19.-25.11.2005

TAKEMURA, K., NIMS Tsukuba, Japan: 16.-18.06.2005

VOLKOVA, Y., Ural State University, Ekaterinburg, Russia: 09.10.-26.11.2005

WESTRAADT, J., Element6, Johannesburg, South Africa: 14.-20.03.2005, 31.03.-30.04.2005

7. Additional scientific activities

7.1 Patents

DUBROVINSKAIA, N.A.; DUBROVINSKY, L.S.: Superhard aggregated diamond nanorods (ADNRs) with improved wear coefficient. Deutsche Patentanmeldung, submitted 03.11.2005

KEPPLER, H.; WALTE, N.: Hochtemperatur-Moissanitsichtzelle. Deutsche Patentanmeldung 10 2005 056 977.3, 30.11.2005

7.2 Ph.D. theses

Bechmann, M.: MAS NMR of Nuclei with Spin $S = \frac{1}{2}$ in Polycrystalline Powders: Experiments and Numerical Simulations

Couvy, H.: Experimental deformation of forsterite, wadsleyite and ringwoodite: Implications for seismic anisotropy of the Earth's mantle

Liebske, C.: Mantle-Melting at High Pressure – Experimental Constraints on Magma Ocean Differentiation

7.3 Honours and awards

Tiziana BOFFA BALLARAN received the 2005 MSA Award of the Mineralogical Society of America

Jérôme ROUQUETTE received the 2005 Jamieson Award of the International Association for the Advancement of High Pressure Science and Technology (AIRAPT)

7.4 Editorship of scientific journals

MCCAMMON, C.A. Editor "Physics and Chemistry of Minerals"

SEBALD, A. Editorial Board of "Solid State Nuclear Magnetic Resonance"

RUBIE, D.C. Editor-in-Chief, Physics of the Earth and Planetary Interiors

SEIFERT, F. Editorial Advisory Board of "Physics and Chemistry of Minerals"

7.5 Membership of scientific advisory bodies

BOFFA BALLARAN, T. Kraus Crystallography Award Committee of the Mineralogical Society of America

KEPPLER H.	Chairman, Section for Crystallography, Physics and Chemistry of Minerals, German Mineralogical Society
MCCAMMON, C.A.	MSA Lecture Program Committee of the Mineralogical Society of America Advisory Board of "Mössbauer Information Exchange" International Advisory Board of the Mössbauer Effect Data Center
RUBIE, D.C.	AGU Mineral and Rock Physics Executive Committee Chair of AGU Mineral and Rock Physics Awards Committee Urey Medal Committee SPring-8 Beamline Review Committee (BL04B1) Forschungskollegium Physik des Erdkörpers (FKPE)
SEIFERT, F.	Committee for Glaciology, Bavarian Academy of Sciences Forschungskollegium Mineralogie Mitglied des Kuratoriums des Geo-Zentrums an der KTB e. V. Academia Europaea, London Deutsche Akademie der Naturforscher Leopoldina, Halle (Senate 2003-2006) Bayerische Akademie der Wissenschaften, München Akademie der Wissenschaften, Göttingen

8. Scientific and Technical Personnel

Name		Position	Duration in 2005	Funding source
ASAHARA, Yuki	Dr.	Stipendiatin	to 31.03.	JSPS
		Wiss. Angestellte	from 01.04.	DFG
AUDÉTAT, Andreas	Dr.	Wiss. Assistent		BGI
BAUMGARTNER, Alexander	Dipl.-Chem.	Wiss. Mitarbeiter	from 04.10.	BGI/IGS ⁷
BECHMANN, Matthias	Dipl.-Phys.	Wiss. Angestellter	to 30.04.	DFG ¹
BÖHM, Ulrich		Mechaniker		BGI
BÖSS, Wolfgang	RAR	Verwalt. Beamter		BGI
BOFFA BALLARAN, Tiziana	Dr.	Akad. Rätin		BGI
BUCHERT, Petra		Fremdsprachen- sekretärin		BGI
COUVY, Hélène	Dipl.-Geol.	Wiss. Angestellte	to 16.01.	DFG
DOLEJŠ, David	Dr.	Wiss. Angestellter		BGI/IGS
DUBROVINSKAIA, Natalia	Dr.	Wiss. Angestellte	to 31.07.	BGI/VP
DUBROVINSKY, Leonid	PD Dr.	Akad. Oberrat		BGI
EL GORESY, Ahmed	Prof. Dr.		from 01.06.	BGI/VP ²
FISCHER, Heinz		Mechaniker		BGI
FROST, Daniel	Dr.	Akad. Oberrat		BGI
FUJINO, Kiyoshi	Prof. Dr.	Gastprofessor	10.06.-09.09.	DFG
GATTA, Giacomo Diego	Dr.	Wiss. Angestellter	to 31.01.	BGI/VP
GAVRILENKO, Polina	Dipl.-Geol.	Wiss. Mitarbeiterin	from 01.05.	BGI/IGS
GOLLNER, Gertrud		Chem.-Techn. Assistentin		BGI
HEIDELBACH, Florian	Dr.	Wiss. Assistent		BGI
HOLBIG, Eva	Dipl.-Min.	Wiss. Mitarbeiterin		BGI/IGS
KANTOR, Anastasia	Dipl.-Geol.	Wiss. Angestellte	to 10.07. from 11.07.	DFG BGI/IGS
KANTOR, Innokenty	Dipl.-Geol.	Wiss. Angestellter	to 30.09. from 01.10.	DFG BGI/VP
KEPPLER, Hans	Prof. Dr.	Stellvertr. Leiter		BGI
KEYSSNER, Stefan	Dr.	Akad. Oberrat		BGI
KISON-HERZING, Lydia		Sekretärin		BGI
KLASINSKI, Kurt	Dipl.-Ing. (FH)	Techn. Angestellter		BGI
KONSCHAK, Alexander	Dipl.-Geol.	Wiss. Angestellter	01.04.-30.09. from 01.10.	DFG ³ BGI/VP
KRAUßE, Detlef	Dipl.-Inform. (FH)	Techn. Angestellter		BGI

KRIEGL, Holger		Haustechniker		BGI
KURNOSOV, Alexander	Dr.	Wiss. Angestellter	from 24.01.	BGI/VP
KUZNETSOV, Oleksii	Dr.	Wiss. Angestellter		BGI/VP
LEE, Kanani	Dr.	Stipendiatin	01.07.-30.09.	AvH ⁴
LEITNER, Oskar		Präparator		BGI
LINHARDT, Sven		Elektroniker		BGI
LIU, Jun	Dipl.-Min.	Stipendiatin	to 31.07.	AvH ⁵
		Wiss. Angestellte	from 01.08.	DFG
MANN, Ute	Dipl.-Geol.	Wiss. Mitarbeiterin		BGI/IGS
MCCAMMON, Catherine	Dr.	Akad. Oberrätin		BGI
MELOSH, Jay	Prof. Dr.	Forschungspreisträger	from 21.09.	AvH
MIYAJIMA, Nobuyoshi	Dr.	Wiss. Assistent	from 01.09.	BGI
NESTOLA, Fabrizio	Dr.	Forschungsstipendiat	to 31.10.	AvH
NÖTH, Andreas	Dipl.-Min.	Wiss. Mitarbeiter	to 31.05.	BGI/IGS ⁶
POTZEL, Anke		Chem.-Techn. Assistentin	from 01.03.	DFG ³
RAMMING, Gerd		Elektroniker		BGI
RAUSCH, Oliver		Mechaniker		BGI
REHBEIN, Alexander	Dipl.-Phys.	Wiss. Mitarbeiter	01.04.-31.08.	BGI/IGS ⁶
ROUQUETTE, Jérôme	Dr.	Wiss. Angestellter	from 01.04.	BGI/VP
RUBIE, David C.	Prof. Dr.	Leiter		BGI
SAIKIA, Ashima	M.Sc. (Geol.)	Wiss. Mitarbeiterin		BGI/IGS
SCHMAUß-SCHREINER, Deborah	Dipl.-Geophys.	Wiss. Angestellte	01.05.-30.09. from 01.10.	DFG ³ BGI/VP
SCHMICKLER, Bettina	Dr.	Wiss. Angestellte	to 16.05.	DFG
SCHULZE, Hubert		Präparator		BGI
SEIFERT, Friedrich	Prof. Dr.	Stellvertr. Leiter		BGI
SHCHEKA, Svyatoslav	Dr.	Wiss. Angestellter	from 01.10.	BGI/VP
SHIRYAEV, Andrei	Dr.	Forschungsstipendiat	to 31.03.	AvH
SKÁLA, Roman	Dipl.-Geol.	Wiss. Angestellter	to 28.02.	DFG
STEINLE-NEUMANN, Gerd	Dr.	Akad. Rat z.A.		BGI
STOYANOV, Emil	Dipl.-Chem.	Wiss. Angestellter	to 30.04.	DFG
TERRY, Michael	Dr.	Wiss. Angestellter		BGI/VP
ÜBELHACK, Stefan		Mechaniker	to 06.10. from 07.10.	EU BGI
WALTE, Nicolas	Dipl.-Geol.	Wiss. Angestellter		BGI/VP
YELAMANCHILI, Ram Sai	Dipl.-Chem.	Wiss. Mitarbeiter	from 01.04.	BGI/IGS ⁷

Abbreviations/explanations:

AvH	Alexander von Humboldt Foundation
BGI	Staff Position of Bayerisches Geoinstitut
BGI/VP	Visiting Scientists' Program of Bayerisches Geoinstitut
DFG	German Science Foundation
EU	European Union
IGS	International Graduate School under the Elitenetzwerk Bayern "Structure, Reactivity and Properties of Oxide Materials"
JSPS	Japanese Society for the Promotion of Science

¹ project granted to Prof. B. Wrackmeyer, Bayreuth

² partially funded by the Visiting Scientists' Program of Bayerisches Geoinstitut

³ Leibnitz-Preis Prof. Keppler

⁴ Summer Research Fellowship for U.S. Scientists and Scholars

⁵ Sofia Kovalevskaja-Preis

⁶ Fraunhofer ISC Würzburg

⁷ Lst. f. Anorganische Chemie I, Prof. Breu

Index

Abrikosov, I.A.	37
Ahrens, T.	173
Ahuja, R.	37
Akber-Knutson, S.	28
Aléon, J.	33
Allwardt, J.R.	100
Amulele, G.M.	70
Asahara, Y.	35, 175
Asimow, P.D.	28, 173
Audétat, A.	50, 86
Baier, J.	50
Berthet, S.	42
Bestmann, M.	120
Bockmeyer, M.	153
Boffa Ballaran, T.	52, 54, 55, 57, 62, 71, 153
Braun, H.	142
Bromiley, D.W.	95
Bromiley, F.A.	95
Bromiley, G.D.	93, 95, 126
Bruno, M.	55
Bystricky, M.	73
Caruso, R.A.	147
Cera, F.	59
Combes, R.	42
Comodi, P.	59
Couvy, H.	126
Crichton, W.A.	37, 134
DeRonde, A.	108
Dmitriev, V.	77, 144
Dobson, D.P.	108
Dolejš, D.	30, 84, 89
Du, L.-S.	100
Dubrovinskaia, N.A.	37, 67, 77, 134, 136, 140, 142, 149
Dubrovinsky, L.S.	37, 59, 62, 63, 65, 67, 77, 80, 82, 104, 134, 138, 139, 140, 142, 144, 147, 149, 151, 153, 154, 156, 157, 165, 168, 169, 171, 175
Duc-Tin, Q.	86
Dzwilewski, A.	138, 139
El Goresy, A.	33
Eska, G.	142

Esquinazi, P.	139
Estevez-Rams, E.	144
Frost, D.J.	20, 22, 23, 35, 42, 44, 46, 48, 62, 70, 82, 91, 93, 100, 113, 154, 160, 162, 163, 173, 175
Fuess, H.	162
Fujino, K.	60
Galadi-Enriquez, E.	121
Gatta, G.D.	57, 71
Goncharenko, I.N.	67, 80
Gross, T.	162
Guillaume, C.	160, 163
Habler, G.	120
Heidelbach, F.	73, 108, 110, 117, 118, 120, 121, 126, 128, 130, 177
Hirschmann, M.M.	100
Hirt, A.	177
Holbig, E.	153, 154
Holl, C.M.	70, 93
Holzappel, C.	73, 98, 175
Holzheid, A.	46
Hustoft, J.	110
Izumi, H.	60
Jacobsen, S.D.	168
Jirák, Z.	156
Kantor, A.P.	67, 168
Kantor, I.Yu.	37, 63, 65, 67, 77, 80, 82, 165, 168, 171
Kegler, P.	46
Keppler, H.	25, 50, 86, 91, 102, 103, 115
Kohlstedt, D.	110
Konschak, A.	102
Kozlenko, D.P.	156
Krogh, T.	126
Kroke, E.	162
Kühn, A.	128
Kurakevych, O.O.	140
Kurnosov, A.V.	77, 104, 169, 171
Kuznetsov, A.Yu.	77, 140, 144, 147, 151, 157, 169, 171
Langenhorst, F.	25, 35, 48, 60, 134, 144, 149
Lee, K.K.M.	39
Liebske, C.	54, 98
Liu, J.	62
Locherer, T.	162

Löbmann, P.	153
Longo, M.	52, 56
Malavergne, V.	42
Manghnani, M.H.	70
Mann, U.	44
Marshall, A.G.	138
McCammon, C.A.	22, 52, 56, 63, 65, 73, 75, 82, 138, 154, 165, 174
McEnroe, S.	75, 177
McMillan, P.F.	151
Meredith, P.	108
Mierdel, K.	25
Miyajima, N.	153, 175
Mornioli, J.P.	160, 163
Mosenfelder, J.	173
Muddle, B.C.	147, 151
Neethling, J.H.	136
Nestola, F.	52, 54, 55, 56, 57, 71, 93, 174
Neufeld, K.	128
Njiekak, G.	130
Palme, H.	46
Piazzoni, A.S.	30
Poe, P.T.	98
Prakapenka, V.B.	70
Purcell, J.M.	138
Reichmann, H.-J.	168
Richter, A.	134
Riedel, R.	162
Ring, U.	128
Robinson, P.	75, 124, 177
Rouquette, J.	63, 82
Rubie, D.C.	23, 35, 44, 46, 60, 98, 113, 173, 175
Saikia, A.	23
Savenko, B.N.	156
Schmauß-Schreiner, D.	103
Schmickler, B.	98
Schwarz, M.	162
Sekar, M.	70
Serghiou, G.	160, 163
Setzer, A.	139
Shcheka, S.	91
Shchukin, D.G.	147

Shen, G.	70
Sheshin, G.A.	142
Shiryayev, A.	157
Shulga, Y.	138
Sigalas, I.	136
Smyth, J.R.	25, 70, 93
Solozhenko, V.L.	140
Spiering, H.	174
Stebbins, J.F.	100
Steinle-Neumann, G.	28, 30, 39, 79
Stoyanov, E.	48
Sundqvist, B.	138
Swamy, V.	147, 149, 151
Talyzin, A.V.	138, 139
Tennant, C.	174
Terry, M.P.	73, 117, 118, 124, 126
Thoeni, M.	120
Thomson, A.	163
Tribaudino, M.	55
Tsybin, Y.O.	138
Vitos, L.	37
Volkova, Y.	77
Wagner, T.	89
Walte, N.P.	113, 115
Weber, H.-P.	144
Wenzel, M.J.	79
Westraadt, J.E.	136
Wiedenbeck, M.	91
Withers, A.C.	100
Zinner, E.	33
Zulauf, G.	121, 130